

**ÉCOLE DOCTORALE DES SCIENCES CHIMIQUES**  
**Institut de Science et d'Ingénierie Supramoléculaires**

**THÈSE** présentée par :

**Ricardo TOTOVAO**

soutenue le : 17 Février 2017

pour obtenir le grade de : **Docteur de l'université de Strasbourg**

Discipline/ Spécialité : Chimie

**Stimuli-responsive breakable hybrid  
organic/inorganic silica nanoparticles  
for biomedical applications**

**THÈSE dirigée par :**

**M<sup>me</sup> DE COLA Luisa**

Professeur, Université de Strasbourg

**RAPPORTEURS :**

**M. CORRADINI Roberto**

**M<sup>me</sup> VENTOSA Nora**

Professeur, Università degli Studi di Parma (Italie)  
Docteur et directrice de recherche, Institut de  
Ciència de Materials de Barcelona – Universitat  
Autònoma de Barcelona (Espagne)

---

**AUTRE MEMBRE DU JURY :**

**M<sup>me</sup> BEGIN-COLIN Sylvie**

Professeur, Université de Strasbourg

# Table of Contents

|   |           |
|---|-----------|
| <b>Table of Contents</b> .....  | <b>1</b>  |
| <b>Résumé de thèse</b> .....  | <b>3</b>  |
| <b>Summary of the thesis</b> .....  | <b>15</b> |
| <b>Chapter 1 General introduction</b> .....   | <b>30</b> |
| <b>Abstract</b> .....   | <b>30</b> |
| <b>1.1 Nanoparticles (NPs) as promising delivery vectors in nanomedicine</b> .....  | <b>31</b> |
| 1.1.1 Physicochemical features affecting NPs efficiency .....   | 32        |
| <b>1.2 Silica nanoparticles in nanomedicine</b> .....   | <b>35</b> |
| 1.2.1 Amorphous silica spheres .....  | 36        |
| 1.2.2 Bioglasses .....  | 37        |
| 1.2.3 Ordered mesoporous silica (OMS) .....   | 38        |
| <b>1.3 Aim of the thesis</b> .....  | <b>43</b> |
| <b>1.4 References</b> .....   | <b>46</b> |
| <b>Chapter 2 pH-Breakable hybrid mesoporous silica nanoparticle: synthesis, characterisation and breakability studies</b> ..... | <b>50</b> |
| <b>Abstract</b> .....   | <b>50</b> |
| <b>2.1 Introduction</b> .....   | <b>52</b> |
| <b>2.2 Synthesis and characterisation of the diiminosilane linker</b> .....   | <b>54</b> |
| <b>2.3 Synthesis and characterisation of the hybrid mesoporous silica nanoparticle</b> .....                                    | <b>56</b> |
| <b>2.4 Kinetic studies of the breakability of the particle</b> .....  | <b>62</b> |
| 2.4.1 Monitoring by SEM .....   | 63        |
| 2.4.2 Monitoring by TEM .....   | 65        |
| 2.4.3 Monitoring by <sup>1</sup> H NMR spectroscopy .....   | 68        |
| 2.4.4 Monitoring by dye release .....   | 72        |
| <b>2.5 Conclusion</b> .....   | <b>77</b> |
| <b>2.6 Experimental Section</b> .....   | <b>78</b> |
| 2.6.1 Materials .....   | 78        |
| 2.6.2 Instruments .....   | 78        |
| 2.6.3 Syntheses .....   | 79        |
| 2.6.4 Chemical biodegradability tests .....   | 82        |
| <b>2.7 References</b> .....   | <b>83</b> |
| <b>Chapter 3 <i>In vitro</i> studies: delivery of paclitaxel into living cells for breast cancer treatment</b> .....            | <b>87</b> |
| <b>Abstract</b> .....   | <b>87</b> |
| <b>3.1 Introduction</b> .....   | <b>88</b> |
| <b>3.2 Cellular uptake of BMONPs</b> .....  | <b>90</b> |
| <b>3.3 Cytotoxicity evaluation of MSNPs</b> .....   | <b>94</b> |

|  |            |
|--|------------|
| 3.4 Cytotoxicity evaluation of BMONPs .....  | 99         |
| 3.5 Cytotoxicity evaluation of paclitaxel loaded MSNPs (Pac@MSNPs) .....   | 101        |
| 3.6 Cytotoxicity evaluation of paclitaxel loaded BMONPs (Pac@BMONPs) .....   | 104        |
| 3.7 Conclusion .....   | 107        |
| 3.8 Experimental section .....   | 107        |
| 3.8.1 Materials .....  | 107        |
| 3.8.2 Preparation of the systems .....   | 108        |
| 3.8.3 In vitro experiments .....   | 109        |
| 3.9 References .....   | 111        |
| <b>Chapter 4 Encapsulation and <i>in vitro</i> delivery of an antibody and a chemotherapeutic agent for cancer treatment .....</b> | <b>114</b> |
| <b>Abstract .....</b>  | <b>114</b> |
| <b>4.1 Introduction .....</b>  | <b>116</b> |
| <b>4.2 Encapsulation of monoclonal anti-E6 antibody .....</b>  | <b>119</b> |
| 4.2.1 Morphology of the resulted particles .....   | 120        |
| 4.2.2 Colloidal stability in cell culture medium .....   | 122        |
| 4.2.3 Biocompatibility enhancement: PEG-5000 post-grafting.....  | 125        |
| 4.2.4 Cell internalisation and localisation studies by confocal microscopy.....  | 127        |
| <b>4.3 Encapsulation of doxorubicin .....</b>  | <b>131</b> |
| 4.3.1 Morphology of the resulted particles .....   | 132        |
| 4.3.2 Kinetic studies of the release .....   | 133        |
| 4.3.3 Cell internalisation studies by confocal microscopy .....  | 141        |
| 4.3.4 Determining the activity towards cancer cells .....  | 142        |
| <b>4.4 Conclusion .....</b>  | <b>145</b> |
| <b>4.5 Experimental section .....</b>  | <b>145</b> |
| 4.5.1 Materials .....  | 145        |
| 4.5.2 Instruments .....  | 146        |
| 4.5.3 Synthesis .....  | 146        |
| 4.5.4 In vitro experiments .....   | 149        |
| <b>4.6 References .....</b>  | <b>150</b> |
| <b>Chapter 5 Instrumental techniques .....</b>   | <b>154</b> |
| <b>Abstract .....</b>  | <b>154</b> |
| <b>5.1 <sup>1</sup>H Nuclear magnetic resonance (NMR) spectroscopy .....</b>   | <b>155</b> |
| <b>5.2 Infrared (IR) spectroscopy .....</b>  | <b>156</b> |
| <b>5.3 X-ray photoelectron spectroscopy (XPS) .....</b>  | <b>158</b> |
| <b>5.4 Electrospray Ionisation-Mass Spectrometry (ESI-MS) .....</b>  | <b>159</b> |
| <b>5.5 Scanning electron microscopy (SEM) and energy-dispersive X-ray spectroscopy (EDX) .....</b>                                 | <b>161</b> |
| 5.5.1 Scanning electron microscopy (SEM) .....   | 161        |
| 5.5.2 Energy-dispersive X-ray spectroscopy (EDX) .....   | 162        |
| <b>5.6 Transmission electron microscopy (TEM) .....</b>  | <b>162</b> |
| <b>5.7 Fluorescence confocal microscopy and z-stack processing .....</b>   | <b>164</b> |
| 5.7.1 Fluorescence confocal microscopy .....   | 164        |
| 5.7.2 Z-stack processing .....   | 166        |
| <b>5.8 Fluorescence spectroscopy .....</b>   | <b>166</b> |
| <b>5.9 Dynamic light scattering (DLS) .....</b>  | <b>167</b> |
| <b>5.10 Zeta potential .....</b>   | <b>169</b> |
| <b>5.11 Thermogravimetric analysis (TGA) .....</b>   | <b>170</b> |
| <b>5.12 References .....</b>   | <b>171</b> |
| <b>Acknowledgements .....</b>  | <b>172</b> |

# Résumé de thèse

Un des grands défis en médecine est d'avoir un meilleur relargage de médicaments insolubles dans l'eau, un ciblage plus efficace, la protection de biomolécules fragiles et, enfin, dans le cas de l'utilisation de vecteurs, l'élimination du transporteur. Plusieurs chercheurs ont exploré l'utilisation de nanomatériaux pour relarguer des médicaments, oligonucléotides, protéines ou autres substances dans des types de cellules spécifiques, en particulier, des cellules cancéreuses.<sup>1</sup> La plupart des systèmes capables d'agir comme des nanoconteneurs ont été décrits dans la littérature tels que des micelles ou des vésicules basées sur des polymères,<sup>2</sup> liposomes,<sup>3</sup> des charpentes métallo-organiques (MOFs),<sup>4</sup> des nanotubes de carbone,<sup>5</sup> des silices poreuses.<sup>6</sup> Comme problème général pour des nanovecteurs inorganiques, le problème d'excrétion complète et sûre du système biologique après avoir accompli leurs fonctions de diagnostic ou thérapeutiques n'a pas encore été entièrement élucidé<sup>7</sup> et demeure l'un des obstacles majeurs entravant leur translation clinique potentielle en tant que vecteurs de médicaments, outils d'imagerie ou agents thérapeutiques *in situ*. Le relargage total des médicaments ou des molécules piégés à l'intérieur des systèmes poreux n'a pas été résolu puisqu'un pourcentage plutôt bon des molécules reste piégé dans les matériaux soit à cause de leur faible solubilité dans la phase aqueuse soit dû à des interactions avec les murs des pores.

La silice est un matériau idéal pour la construction de nanoparticules poreuses et celle de nanocapsules. En effet, l'incorporation de motifs organiques dans la charpente de silice pour obtenir des nanoparticules d'organosilice (OSi-NPs), initiée par Inagaki *et al.*,<sup>8</sup> attire de l'intérêt dans différents domaines incluant la nanomédecine.<sup>6</sup> L'approche par l'hybridation du noyau a été employé avec efficacité pour surmonter l'un des principaux défis en nanomédecine, la dite dégradation efficace d'OSi-NPs dans l'environnement biologique. En effet, malgré la biodégradabilité clamée de particules de silice,<sup>9</sup> des problèmes d'élimination incomplète et de bioaccumulation demeurent des obstacles majeurs encombrant leur application clinique.<sup>10</sup> Une stratégie possible pour surmonter ces problèmes consiste en l'introduction d'un lien clivable dans la charpente de la particule.<sup>10-12</sup> La cassabilité des OSi-NPs pourrait aussi être déclenchée dans l'environnement biologique causant la destruction des particules et empêchant leur accumulation dans des cellules et des tissus.<sup>13</sup>

*Le but de cette thèse est de développer des systèmes cassables capables de piéger des médicaments ou des biomolécules pour des applications thérapeutiques.*

De tels systèmes peuvent être développés par l'incorporation d'un lien répondant à un *stimulus* dans la charpente de silice. Précédemment, des liens sensibles à de la réduction basés sur des fonctions disulfures ont été reportés.<sup>11-13</sup> Par exemple, notre groupe a introduit du disulfure de bis[3-(triéthoxysilyl)propyl] (**Figure 1 gauche**). Dans cette thèse, nous discutons de l'incorporation d'un lien répondant au pH base sur une fonction imine. Plus précisément, la molécule est le N,N'E/Z,N,N'E/Z)-N,N'-(1,4-phenylenebis(methanylylidene))bis(3-(triéthoxysilyl)propan-1-amine) (**Figure 1 droite**) Ainsi, la nanoparticule (NP) contenant l'imine est capable de se désintégrer à un pH inférieur à 5,5, le pH trouvé dans la matrice extracellulaire des cellules cancéreuses.<sup>14,15</sup> Dans notre concept, suite à sa désintégration, le matériau va relarguer sa charge et, grâce à sa fragmentation en petits morceaux, nous nous attendons à ce qu'il soit excrété de l'animal/du corps du patient. L'incorporation du lien organique dans la charpente d'une silice mésoporeuse et d'une capsule de silice toutes deux sphériques avec un diamètre allant de 60 à 150 nm a été explorée.

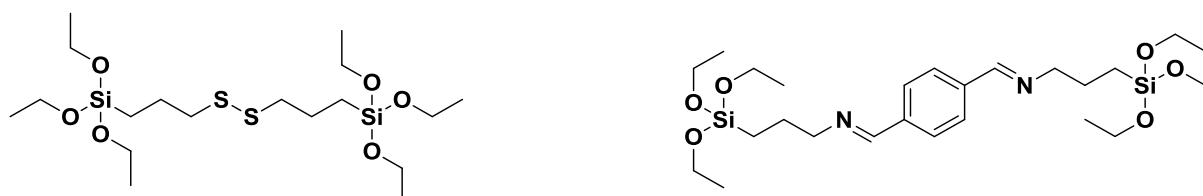


**Figure 1** Structures (**gauche**) du disulfure de bis [3-(triéthoxysilyl)propyl], le lien sensible à la réduction précédemment incorporé dans la charpente du matériau dans le groupe et (**droite**) de N,N'E/Z,N,N'E/Z)-N,N'-(1,4-phenylenebis(methanylylidene))bis(3-(triéthoxysilyl)propan-1-amine), le lien répondant au pH discuté dans cette thèse.

### **Nanoparticule hybride mésoporeuse d'iminosilice sensible au pH: synthèse, caractérisations et études cinétiques de la désintégration *in chemico* :**

En se basant sur des méthodologies développées dans le groupe pour des matériaux poreux contenant du disulfure, dans la première partie de cette thèse, nous nous sommes focalisés sur des nanoparticules d'organosilice mésoporeuses hybrides contenant un motif basé sur une imine comme lien organique clivable. Le principe du système étudié est représenté sur le **schéma 1**.

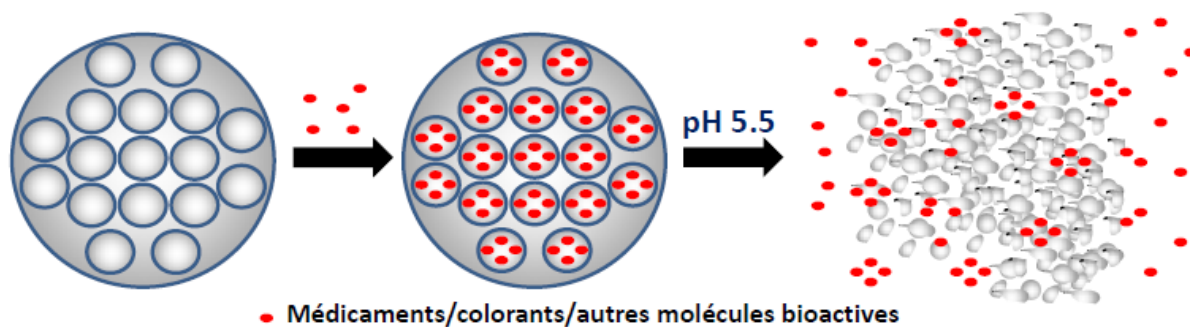


**Schéma 1** Représentation du système étudié dans la première partie de la thèse

### Synthèse et caractérisations du lien diiminosilane

Selon les méthodes rapportées par Bhaumik's *et al*, du téréphtaldialdéhyde a été mis en réaction avec du 3-(triéthoxysilyl)propan-1-amine, communément connu sous 3-aminopropyltriéthoxysilane (APTES), dans l'éthanol anhydre à 80 °C (reflux) pour donner le produit désiré ayant l'aspect d'une huile jaune limpide avec un rendement quantitatif. Une caractérisation par spectroscopie infra-rouge à transformée de Fourier avec réfléchissement total atténué (ATR-FTIR) indique une bande intense correspondant à la liaison imine à  $\sim 1648 \text{ cm}^{-1}$ , alors que le carbonyle de l'aldéhyde de départ présente un signal fort à  $\sim 1678 \text{ cm}^{-1}$ . Par ailleurs, l'analyse par spectroscopie RMN du proton indique la haute pureté du lien organique. En particulier, nous pouvons remarquer l'apparition du pic de l'imine à 8,28 ppm qui a remplacé le signal du carbonyle de l'aldéhyde utilisé comme réactif de départ à 10,23 ppm.

### Synthèse et caractérisations de la nanoparticule d'organosilice mésoporeuse cassable (BMONP)

La nanoparticule de silice cassable avec le pH (BMONP) a été synthétisée via une méthode sol-gel avec un mélange d'orthosilicate de tétraéthyle (TEOS) et le lien diiminosilane en présence d'ammoniac et de butanol et en utilisant du bromure d'ammonium de cetyltriméthyle (CTAB) comme surfactant (**Figure 2A**) ; avec un ratio molaire de TEOS/diiminosilane de 5 : 3. Ce ratio est l'un de ceux possibles afin de s'assurer que les particules se casseront correctement en temps contrôlable.

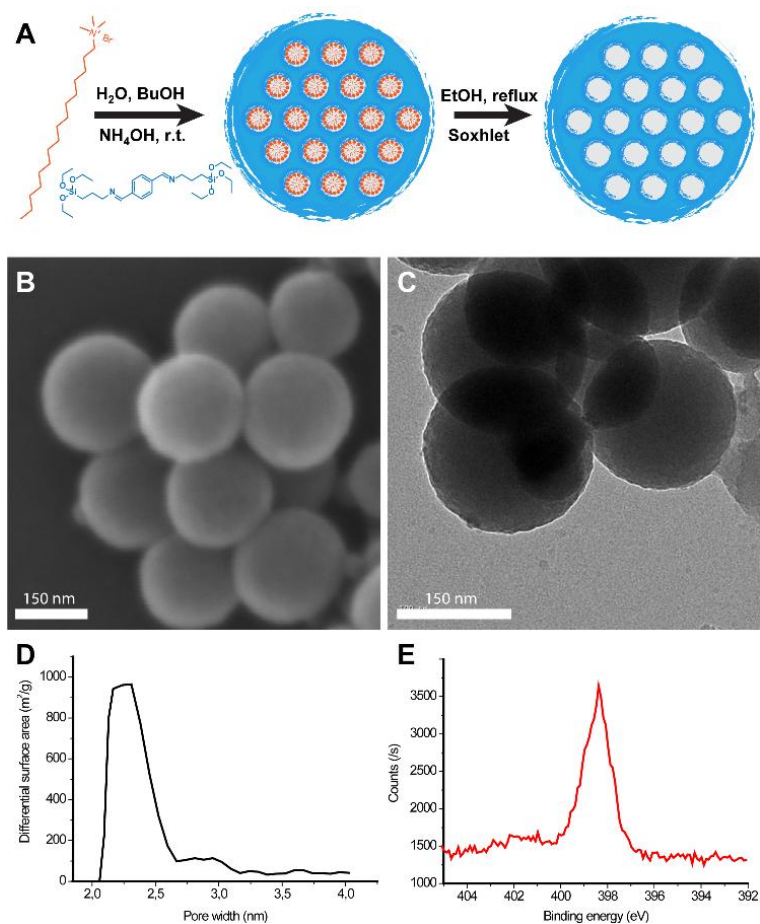


**Figure 2** (A) Schéma représentatif de la synthèse des BMONPs. (B) Photos au MEB et (C) MET des BMONPs. (D) Distribution de la taille des pores des BMONPs. L'expérience a été réalisée avec une technique d'adsorption/désorption de  $N_2$ . (E) Balayage élémentaire de l'atome d'azote sur les BMONPs par XPS.

Les molécules de surfactant ont été extraites par une technique d'extraction au soxhlet, dans un premier temps, des caractérisations morphologiques du matériau hybride ont été effectuées par microscopies électroniques à balayage (MEB) et à transmission (MET) (**Figure 2B** et **C** respectivement). Les images présentent la morphologie sphérique du matériau avec un bon degré de monodispersité de la taille des particules avec un diamètre moyen de 150 nm. Une taille similaire (165 nm) a été mesurée par diffusion dynamique de la lumière sur une suspension des particules dans l'eau. De la cartographie *in situ* par spectroscopie à rayons X à dispersion d'énergie (EDX) d'une BMONP seule met en évidence la distribution homogène de l'atome d'azote dans la structure entière de la particule. Les isothermes d'adsorption/désorption de  $N_2$  de l'échantillon sont de type IV bien définis avec des boucles d'hystérésis de type H1, qui est caractéristique pour des matériaux mésoporeux ayant des

mésostructures de type cylindrique avec une largeur de pore de 2,3 nm (**Figure 2D**). Par ailleurs, un balayage de l'azote effectué par spectroscopie photoélectronique à rayons X (XPS) indique aussi une valeur d'énergie de liaison attribuée à une liaison imine localisée à 398,57 eV (**Figure 2E**).

### **Etudes de cassabilité**

Afin d'évaluer la cinétique de désintégration de la BMONP à travers l'hydrolyse des groupements imines, nous avons effectué un suivi de la libération du téréphtaldialdéhyde de départ, suite à l'hydrolyse de l'imine. Les particules ont été dispersées en milieu acide (pH 5,5) (**Figure 3A**) avec une agitation vigoureuse et l'aldéhyde libéré est suivi par son spectre RMN du proton en le piégeant dans un solvant organique deutéré. Le résultat démontre une rapide libération de l'aldéhyde et qui s'estompe au bout de 24 heures d'expérience (**Figure 3C, courbe noire**). Parallèlement, la suspension de BMONPs en milieu à pH physiologique résulte en une très faible dégradation (**Figure 3C, courbe rouge**). Par ailleurs, la particule a été fonctionnalisée avec un colorant par une liaison covalente de celui-ci à la charpente. Un échantillon des matériaux a ensuite été suspendu en milieu acide (pH = 5,5). Les cinétiques de désintégration ont été suivies en analysant la solution surnageant à l'aide d'un fluorimètre, en faisant un suivi de l'émission du colorant libéré. Selon le profil de libération du colorant (**Figure 3D**), nous pouvons voir que, à temps  $t_0$ , il n'y a aucune émission, comme attendu. Après quelques minutes, nous pouvons déjà observer l'émission du colorant dans la solution, qui augmente ensuite avec le temps. Après 24 heures, l'émission atteint un plateau, confirmant la libération de la totalité des colorants dans l'échantillon. Il est important de noter que ce comportement est en accord avec des changements morphologiques mis en évidence par analyse au MEB et au MET de l'échantillon, indiquant la destruction du matériau. Comme expérience de contrôle, les particules ont été suspendues dans la solution à pH 7,4 et, selon, le profil de libération, nous pouvons constater que la plupart des particules ne se casse pas. De la même manière, nous avons préparé et analysé des particules non cassables dépourvues du motif imine (MSNPs). Ils présentent une morphologie et une taille très similaires mais ne mettent en évidence aucun signe de dégradation en milieu acide, ni même en milieu à pH neutre (**Figure 3B**).

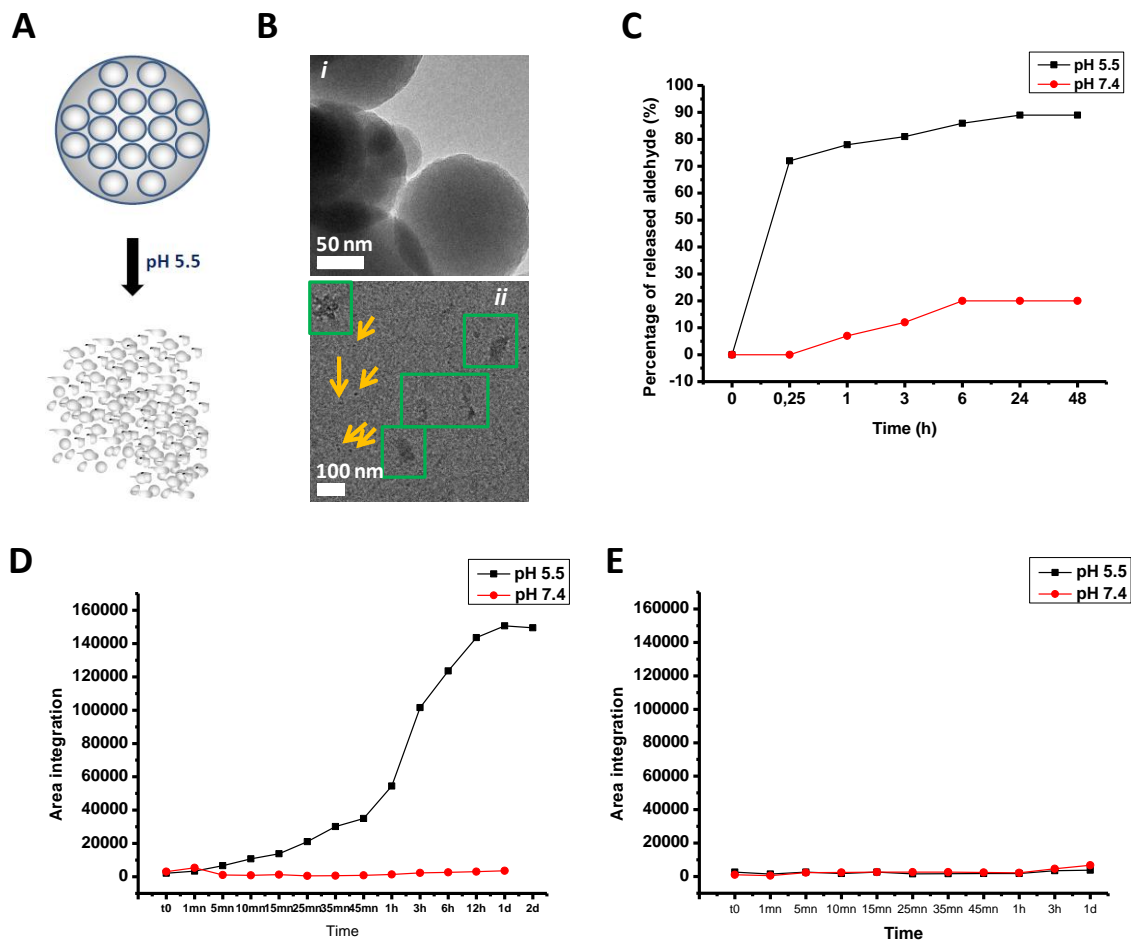


**Figure 3** (A) Représentation schématique des expériences de cassabilité réalisées sur les particules. (B) Images de BMONPs suivies par MET suite à une dispersion dans une solution aqueuse à pH 5 aux temps 0 (i) et 2d (ii) ; les encadrements en vert et flèches jaunes indiquent de très petits morceaux de BMONPs. (C) Profil de libération du téréphthalaldéhyde suite à une suspension de BMONPs dans du PBS à (courbe noire) pH 5,5 et à (courbe rouge) pH 7,4 ; l’aldéhyde libéré est piégé dans du Tol-*d8* et en utilisant du 1,4-diméthoxybenzène comme standard interne. Données obtenues à partir d’une spectroscopie RMN <sup>1</sup>H dans du Tol-*d8*. Profil de libération de sulfo-cyanine 5 après attachement covalent avec (D) BMONPs et (E) nanoparticules de silice mésoporeuses (MSNPs), suite à une suspension aqueuse à (courbe noire) pH 5,5 et (courbe rouge) à pH 7,4.  $\lambda_{exc} = 575$  nm.

### Etudes *in vitro* : internalisation cellulaire, évaluation de la cytotoxicité et relargage de paclitaxel dans des cellules vivantes pour le traitement du cancer du sein

Avant d’employer la BMONP dans des expériences de relargage de médicaments *in vivo*, nous devons enquêter sur leur internalisation par les cellules et leur cytotoxicité. Nous avons

employé les cellules Hs578T et MCF-10 qui sont respectivement les versions cancéreuses et saines de cellules de sein humain.

L'internalisation du matériau a été suivie par MEB. Les cellules internalisent rapidement un petit nombre de particules seulement 5 mn après le début de l'incubation et la quantité de matériaux internalisés augmente avec le temps. Les images au confocal et les investigations de Z-stack effectuées 24 heures suivant l'incubation et rapportées dans la **Figure 4** démontrent clairement une internalisation efficace des BMONPs dans les deux lignées cellulaires.

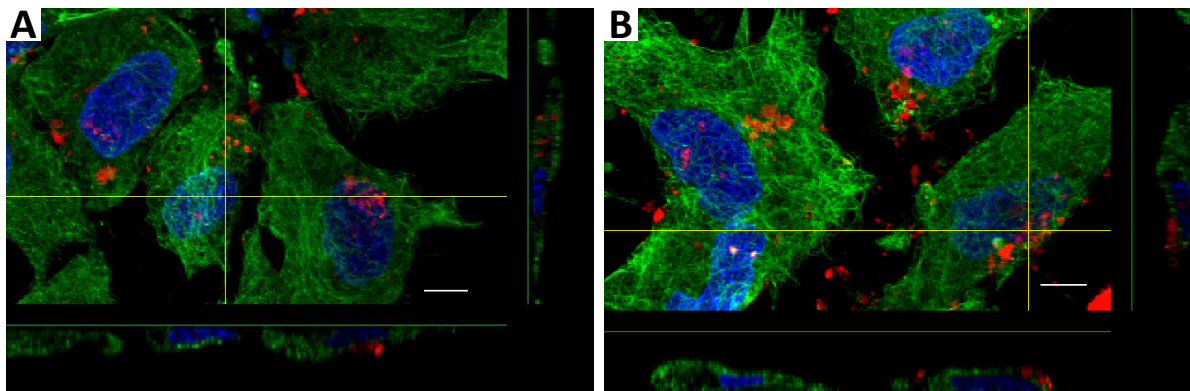


**Figure 4** Images de Z-stack prises au confocal de cellules Hs578T après incubation avec les BMONPs pendant 24h ; les BMONPs ont été colorées avec de la rhodamine B isothiocyanate (**rouge**) pendant que la membrane cellulaire a été colorée avec de l'Alexa Fluor® 647 Phalloïdine (**vert**) et son noyau avec du 4',6-diamidino-2-phénylindole (DAPI) (**bleu**).

Pour évaluer la cytotoxicité de BMONP, les cellules ont été traitées avec la particule à différentes concentrations (0,05 et 0,1 mg/mL) et la viabilité a été mesurée après 48 heures. Une mort cellulaire négligeable a été détectée dans la gamme de concentration testée, indiquant que la particule hybride bio-sensible n'est pas cytotoxique dans les conditions testées (**Figure 5A**).

L'effet bénéfique de la cassabilité de la BMONP dans l'activité de relargage de médicaments a été testé *in vitro*. Comme médicament de choix, nous avons adopté le paclitaxel (Pac), un agent chimiothérapeutique hydrophobe puissant pour le cancer du sein. Des expériences de contrôle sur des cellules incubées uniquement avec du Pac ont été incluses dans l'étude, en maintenant constante la quantité totale de médicament. Comme il est illustré dans la **Figure**

**5B**, le système Pac@BMONP est capable de réduire jusqu'à près de 40 % la viabilité des cellules lorsqu'elles sont incubées avec 0,1 mg/mL de particule. Cependant, la réduction de viabilité cellulaire induite par le paclitaxel seul est négligeable en considérant même une volontairement exagérée de médicaments. Cette différence en comportement peut être attribuée à la meilleure internalisation ainsi qu'à la cinétique de relargage plus rapide de la BMONP. Par ailleurs, des études réalisées sur un système de relargage basé sur une particule analogue conventionnelle non cassable démontrent une cytotoxicité négligeable.

Dans le chapitre suivant, nous discuterons de l'utilisation du lien diiminosilane dans l'élaboration d'un système de relargage de médicaments base sur des nanocapsules de silice, dépourvue de toute porosité.

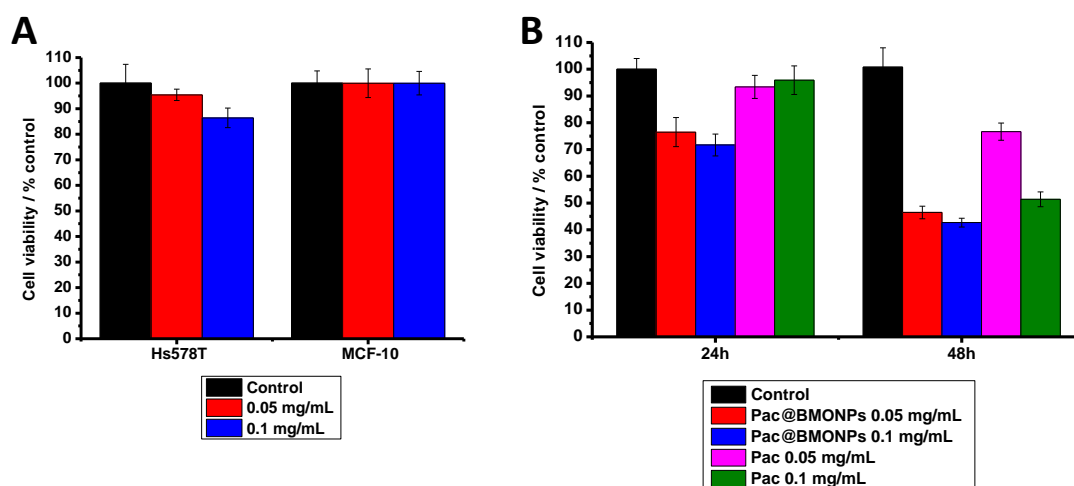


**Figure 5** Tests de viabilité cellulaire des BMONP vide, BMONP chargée avec du paclitaxel (Pac@BMONP) et de solution de paclitaxel seul (Pac). **(A)** Viabilité cellulaire de Hs578T et de MCF-10 suite à une incubation avec BMONP à des concentrations de 0,05 et 0,1 mg/mL pendant 48h. **(B)** Viabilité cellulaire de Hs578T suite à une incubation avec Pac@BMONP et une suspension aqueuse de Pac pendant 24h et 48h à des concentrations de 0,05 et 0,1 mg/mL. Expériences réalisées avec des tests à la sulforhodamine B.

### Nanocapsule d'organosilice cassable pour le relargage de médicaments, d'autres biomolécules et d'anticorps

Afin d'accommoder des molécules de plus grande taille tels que des protéines, des gènes ou des anticorps, l'utilisation de nanoparticules d'organosilice hybrides de type coquille a été explorée. Le principe de ce système est représenté sur le schéma 2. L'encapsulation de

protéines ou de petites molécules dans des nanocapsules offrent plusieurs avantages tels que la protection complète de ces agents bioactifs pendant leurs transports *in vitro* aussi bien qu'*in vivo*. Cela permet, d'une part, de conserver leur intégrité et, d'autre part, d'éviter des relargages prématurés des petites molécules que l'on peut rencontrer dans le cas des systèmes basés sur des particules poreuses (dus à des interactions supramoléculaires instables avec les pores). Nous avons choisi, comme exemple de médicament, de la doxorubicine, un autre agent chimiothérapeutique puissant.

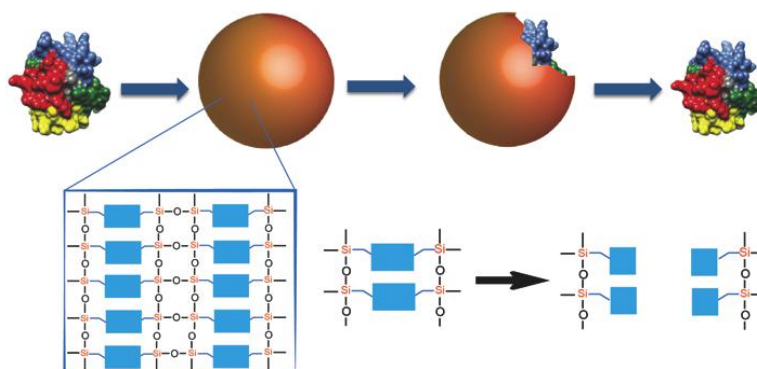


**Schéma 2.** Représentation du système de nanomatériau de type coquille étudié dans le chapitre présent.

### Synthèse et caractérisation de la nanocapsule

Selon une méthode rapportée par notre groupe,<sup>13</sup> une solution aqueuse du médicament a été piégée dans une micelle inverse dans une émulsion eau-dans-huile composée de cyclohexane comme huile. Du TEOS a été mis en réaction avec le lien organique autour de la micelle inverse avec de l'ammoniac servant de base pour initier l'hydrolyse du précurseur de silice (**Figure 6A**). Après précipitation et une série de lavages, la nanocapsule a été obtenue sous forme de matériau sphérique avec un diamètre allant de 60 à 90 nm (**Figure 6B-C**). Pour servir de contrôle, une nanocapsule non cassables ont aussi été synthétisées avec uniquement du TEOS comme précurseur de la charpente.

Le pourcentage d'encapsulation de doxorubicine a été déterminé à 10 % en masse. A partir d'ici, nous appellerons le système cassable Dox@imine-SiO<sub>2</sub>-NC et le non-cassable Dox@SiO<sub>2</sub>-NC.

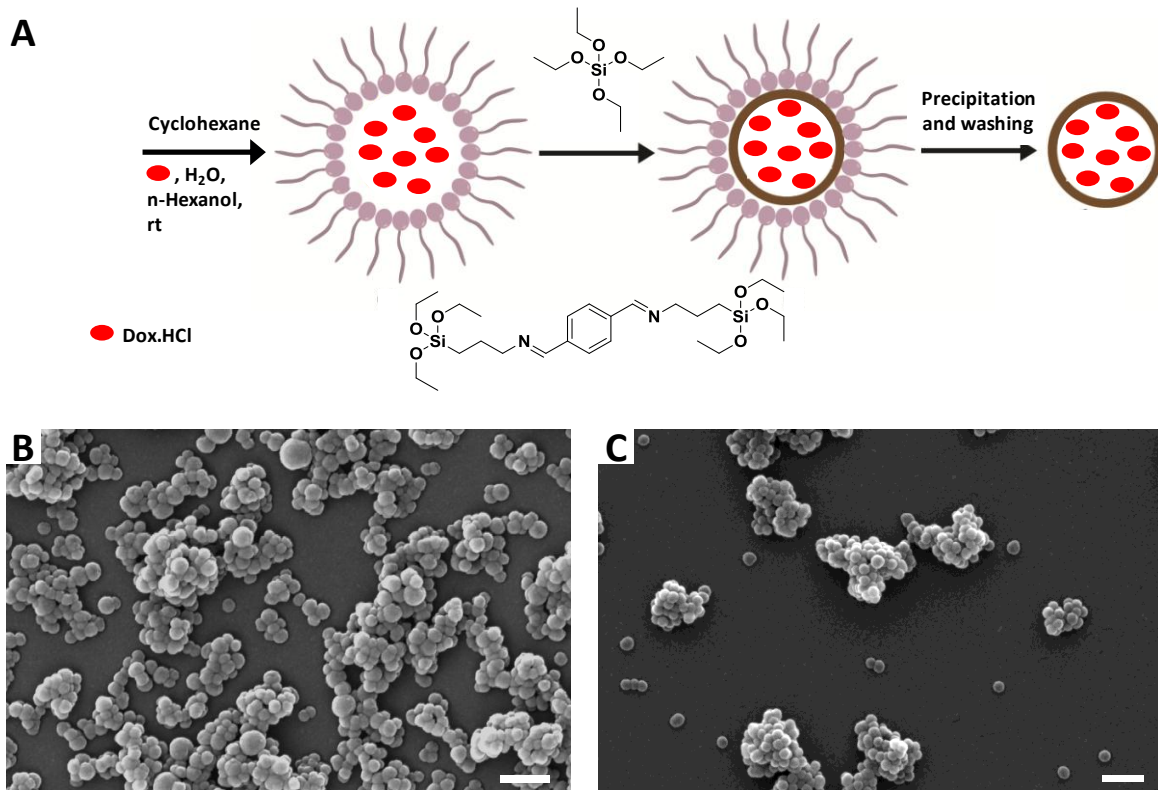


**Figure 6 (A)** Schéma représentatif de la procédure pour l'encapsulation de la doxorubicine. Images au MEB de nanocapsules de **(B)** dox@imine-SiO<sub>2</sub>-NCset **(C)** dox@SiO<sub>2</sub>-NCs.

### Etudes de cassabilité

La cassabilité des matériaux a été étudiée en les dispersant dans un milieu acide (pH 5,5). Un fluorimètre a été utilisé pour faire un suivi de l'émission de doxorubicine libérée suite à la désintégration des particules. Par comparaison, la même expérience a été réalisée dans des milieux à pH neutre. Les profils de libération du médicament démontrent un relargage rapide et qui augmente au fil du temps avant de s'arrêter au bout d'un jour.

Des études *in vitro* réalisées sur des cellules cancéreuses provenant du col de l'utérus (HeLa) se révèlent positives vis-à-vis de l'efficacité du système contre les cellules cancéreuses (**Figure 7**). On observe ainsi près de 50 % de mort cellulaire 48 heures après un traitement avec le système cassable à une concentration de 1 mg/mL (**Figure 7A**). Simultanément, un traitement avec l'analogue non-cassable et une solution aqueuse de doxorubicine induit une toxicité négligeable (**Figure 7A et B**).

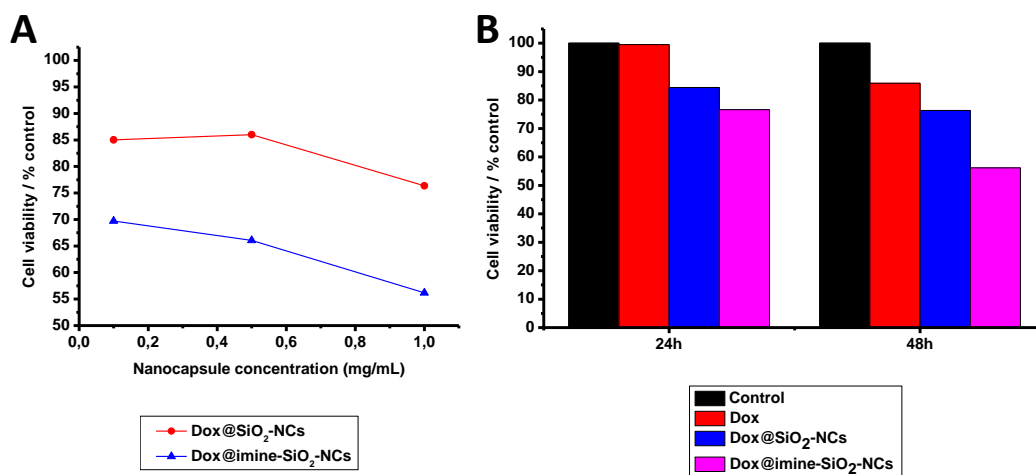


**Figure 7** HeLa cell Tests de viabilité de cellules HeLa avec les nanocapsules chargées en doxorubicine : **(A)** résultats obtenus après 48h de traitement. Les concentrations en nanocapsule utilisés pour les expériences sont 0,1, 0,5 et 1 mg/mL; **(B)** résultats obtenus avec des nanocapsules chargées en doxorubicine et une solution aqueuse de doxorubicine. Les cellules sont incubées avec les nanocapsules à la concentration de 1 mg/mL et avec la solution de doxorubicine à la concentration de 0,1 mg/mL pour être en accord avec le pourcentage d'encapsulation. La viabilité cellulaire est déterminée après 24 et 48h. Mesures effectuées avec du test au bleu alamar.

En conclusion, nous pouvons dire que nous avons développé une nanoparticule d'organosilice hybride pH-responsive cassable (30 % de motifs organiques), capable de répondre à un *stimulus* de pH avec un comportement d'autodestruction unique et une performance de relargage de médicaments améliorée. La particule a été démontrée comme biocompatible et dégradable à la fois dans des conditions simulant celles physiologiques et *in vitro*. Par conséquent, les BMONPs chargées au paclitaxel présentent une efficacité létale améliorée vis-à-vis de cellules cancéreuses *in vitro*. La même propriété de cassabilité, en addition à celle répondant à un agent réducteur, a été exploitée pour synthétiser des nanocapsules capables d'encapsuler *in situ* un agent anti-cancéreux d'une manière efficace sans altérer l'activité de la molécule. Par ailleurs, ces nanocapsules ont aussi été utilisées pour encapsuler, avec efficacité, des substrats de plus grande taille tels que des anticorps.

## Références

1. Riehemann, K. *et al.* Nanomedicine-Challenge and Perspectives. *Angew. Chem. Int. Ed.* **48**, 872–897 (2009).

2. Blanz, A., Armes, S. P. & Ryan, A. J. Self-Assembled Block Copolymer Aggregates: From Micelles to Vesicles and their Biological Applications. *Macromol. Rapid Commun.* **30**, 267–277 (2009).
3. Gokhale, P. C. *et al.* An improved method of encapsulation of doxorubicin in liposomes: pharmacological, toxicological and therapeutic evaluation. *Br. J. Cancer* **74**, 43 (1996).
4. Horcajada, P. *et al.* Porous metal–organic-framework nanoscale carriers as a potential platform for drug delivery and imaging. *Nat. Mater.* **9**, 172–178 (2010).
5. Lu, F. *et al.* Advances in Bioapplications of Carbon Nanotubes. *Adv. Mater.* **21**, 139–152 (2009).
6. Li, Z., Barnes, J. C., Bosoy, A., Stoddart, J. F. & Zink, J. I. Mesoporous silica nanoparticles in biomedical applications. *Chem. Soc. Rev.* **41**, 2590 (2012).
7. Kunzmann, A. *et al.* Toxicology of engineered nanomaterials: Focus on biocompatibility, biodistribution and biodegradation. *Biochim. Biophys. Acta BBA - Gen. Subj.* **1810**, 361–373 (2011).
8. Inagaki, S., Guan, S., Ohsuna, T. & Terasaki, O. An ordered mesoporous organosilica hybrid material with a crystal-like wall structure. *Nature* **416**, 304–307 (2002).
9. Lu, J., Li, Z., Zink, J. I. & Tamanoi, F. In vivo tumor suppression efficacy of mesoporous silica nanoparticles-based drug-delivery system: enhanced efficacy by folate modification. *Nanomedicine Nanotechnol. Biol. Med.* **8**, 212–220 (2012).
10. Quignard, S., Mosser, G., Boissière, M. & Coradin, T. Long-term fate of silica nanoparticles interacting with human dermal fibroblasts. *Biomaterials* **33**, 4431–4442 (2012).
11. Croissant, J. *et al.* Biodegradable Ethylene-Bis(Propyl)Disulfide-Based Periodic Mesoporous Organosilica Nanorods and Nanospheres for Efficient In-Vitro Drug Delivery. *Adv. Mater.* **26**, 6174–6180 (2014).
12. Maggini, L. *et al.* Breakable mesoporous silica nanoparticles for targeted drug delivery. *Nanoscale* **8**, 7240–7247 (2016).
13. Prasetyanto, E. A. *et al.* Breakable Hybrid Organosilica Nanocapsules for Protein Delivery. *Angew. Chem. Int. Ed.* **55**, 3323–3327 (2016).
14. Montcourrier, P., Silver, I., Farnoud, R., Bird, I. & Rochefort, H. Breast cancer cells have a high capacity to acidify extracellular milieu by a dual mechanism. *Clin. Exp. Metastasis* **15**, 382–392 (1997).
15. Kato, Y. *et al.* Acidic extracellular microenvironment and cancer. *Cancer Cell Int.* **13**, 89–89 (2013).

## Summary of the thesis

One of the big challenge in medicine is to have better delivery of water insoluble drugs, a more effective targeting, the protection of fragile biomolecules and finally in case of the use of carriers, the elimination of the transporter. Many researchers explored the use of nanomaterials to deliver drugs, oligonucleotide, protein or other substances to specific types of cells, in particular cancerous cells.<sup>1</sup> Most of the systems able to act as nanocontainers have been described in the literature such as polymer-based micelles or vesicles,<sup>2</sup> liposomes,<sup>3</sup> metal–organic frameworks (MOFs),<sup>4</sup> carbon nanotubes,<sup>5</sup> porous silica.<sup>6</sup> As general problem for inorganic nanovectors, the issue of complete and safe excretion from the biological system after accomplishing their diagnostic or therapeutic functions has not yet been entirely addressed<sup>7</sup> and remains one of the major obstacles impeding their potential clinical translation as drug carriers, imaging tools or *in-situ* therapeutic agents. Also the full delivery of the drug or molecules entrapped inside porous systems has not been solved since a rather good percentage of the molecules remain entrapped in the materials either due to their low solubility in the water phase or because of interactions with the walls of the pores.

Silica is an ideal material for the construction of porous nanoparticles and capsules. Indeed, the incorporation of organic moieties in the silica framework, to obtain organosilica nanoparticles (OSi-NPs), pioneered by Inagaki *et al.*,<sup>8</sup> is attracting interest in different fields including nanomedicine.<sup>6</sup> The core hybridization approach has been effectively employed to overcome one of the main challenges in nanomedicine, namely the efficient degradation of OSi-NPs in the biological environment. Indeed, despite the claimed biodegradability of silica particles,<sup>9</sup> incomplete elimination and bioaccumulation issues remain as major obstacles hindering their clinical application.<sup>10</sup> A possible strategy to overcome those issues consists in the introduction of a cleavable linker in the particle framework.<sup>10–12</sup> The breakability of the OSi-NPs could also be triggered directly in the biological environment causing the destruction of the particles and preventing their accumulation in cells and tissues.<sup>13</sup>

*The aim of this thesis is to develop breakable systems able to entrap drugs or biomolecules for therapeutic applications.*

Such systems can be developed by the incorporation of stimulus responsive linker in the silica framework. Previously, reduction sensitive linkers based on disulfide functions have been reported.<sup>11–13</sup> For instance, our group introduced bis[3-(triethoxysilyl)propyl] disulfide (**Figure 1 left**). In this thesis, we discuss the incorporation of a pH-responsive linker based on an imine function. More precisely, the molecule is N,N'E/Z,N,N'E/Z)-N,N'-(1,4-phenylenebis(methanylylidene))bis(3-(triethoxysilyl)propan-1-amine) (**Figure 1 right**) Thus, the imine containing nanoparticle (NP) is able to break down at pH lower than 5.5., the pH found in the extracellular matrix of the cancerous cells.<sup>14,15</sup> In our design, upon breaking, the material will deliver the payload and, due to its fragmentation into very small, it is expected to be excreted from the animal/patient's body. The incorporation of the organic linker into the framework of a spherical mesoporous silica and a capsule with a diameter size ranging from 60 to 150 nm has been explored.

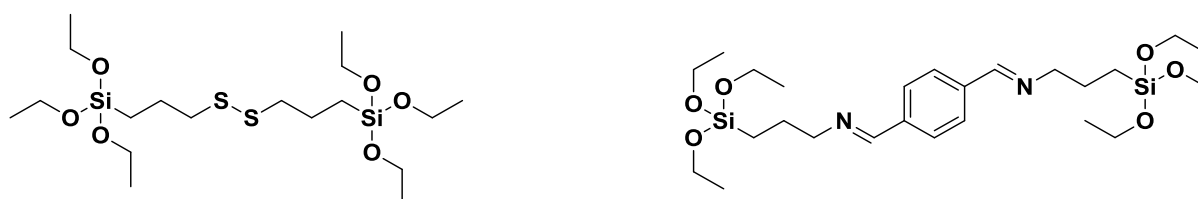


**Figure 1.1** Structures of (**left**) bis [3-(triethoxysilyl)propyl] disulfide, the reduction sensitive linker previously incorporated in the material framework in the group and (**right**) N,N'E/Z,N,N'E/Z)-N,N'-(1,4-phenylenebis(methanylylidene))bis(3-(triethoxysilyl)propan-1-amine), the pH responsive linker discussed in this thesis.

Due to the low pH in the tumour sites (see **chapter 1**), many pH-responsive mesoporous silica nanoparticles (MSNPs) have been developed for controlled drug delivery into cancerous tissues.<sup>16–19</sup> These systems have demonstrated relatively considerable efficiency towards cancerous sites *in vitro* as well as *in vivo*. However, depending on the level of hydrophobicity of the chemotherapeutic agent, the release and, thus, the efficiency of the system can be altered. Moreover, most of pH-responsive properties of these systems regard either electrostatic interactions between the pore walls and the payload or the pore “door” where macromolecular or polymeric systems serve as gatekeepers by supramolecular interactions. In both cases, the interactions are disrupted upon arrival in the acidic environment of the cancerous sites. Nevertheless, in some cases, highly hydrophobic drugs tend to be retained

inside MSNPs. Furthermore, the vector is not biodegradable and its elimination remains an unavoidable issue.

*In the chapter 2, we report the synthesis of a pH-breakable hybrid mesoporous silica nanoparticle which is not only pH-responsive but also what we call pH-breakable.*

Such a particle specifically responds to low pH to trigger its breaking into small pieces. The system is obtained by incorporating an organic linker based on a pH-cleavable function in the particle framework. For this purpose, knowing the pH-sensitivity of imine functions and the fact that their hydrolysis rate can be influenced by substituents on the adjacent positions, we used (N,N'E/Z,N,N'E/Z)-N,N'-(1,4-phenylenebis(methanylylidene))bis(3-(triethoxysilyl)propan-1-amine) that we cited in the **introductory chapter** and that we will abbreviate as diiminosilane. The synthesis and the breakability studies of the particles are herein discussed.

### **Synthesis and characterisation of the diiminosilane linker**

According to the methods reported by Bhaumik's *et al*, terephtaldialdehyde was reacted with 3-(triethoxysilyl)propan-1-amine, commonly known as 3-Aminopropyltriethoxysilane (APTES), in dry ethanol at 80 °C (reflux) to afford the desired product as a yellowish limpid oil in quantitative yield. A characterization by attenuated total reflectance Fourier transform infrared spectroscopy (ATR-FTIR) shows an intense band corresponding to the imine bond at  $\sim 1648\text{ cm}^{-1}$ , while the carbonyl of the starting aldehyde displays a strong signal at  $\sim 1678\text{ cm}^{-1}$ . Furthermore, the NMR analysis shows the high purity of the organic linker. In particular, we can notice the appearance of the imine peak at 8.28 ppm which replaced the carbonyl signal of the aldehyde used as starting material at 10.23 ppm.

### **Synthesis and characterisation of BMONP**

The pH-breakable mesoporous organosilica nanoparticle (BMONP) has been synthesized via sol-gel synthesis method with a mixture of tetraethyl orthosilicate (TEOS) and the diiminosilane linker in the presence of ammonia and butanol (**Figure 2.1A**); with a TEOS/diiminosilane molar ratio of 5:3. This ratio is one of those possible to ensure that the particle will break properly in controllable time. Hexadecyltrimethylammonium bromide also known as cetyltrimethylammonium bromide (CTAB) serves as surfactant template. The

reaction occurs at room temperature over 1 day and, after removing the surfactant by Soxhlet method and drying in the ambient air, the particle is obtained in a white powder aspect.

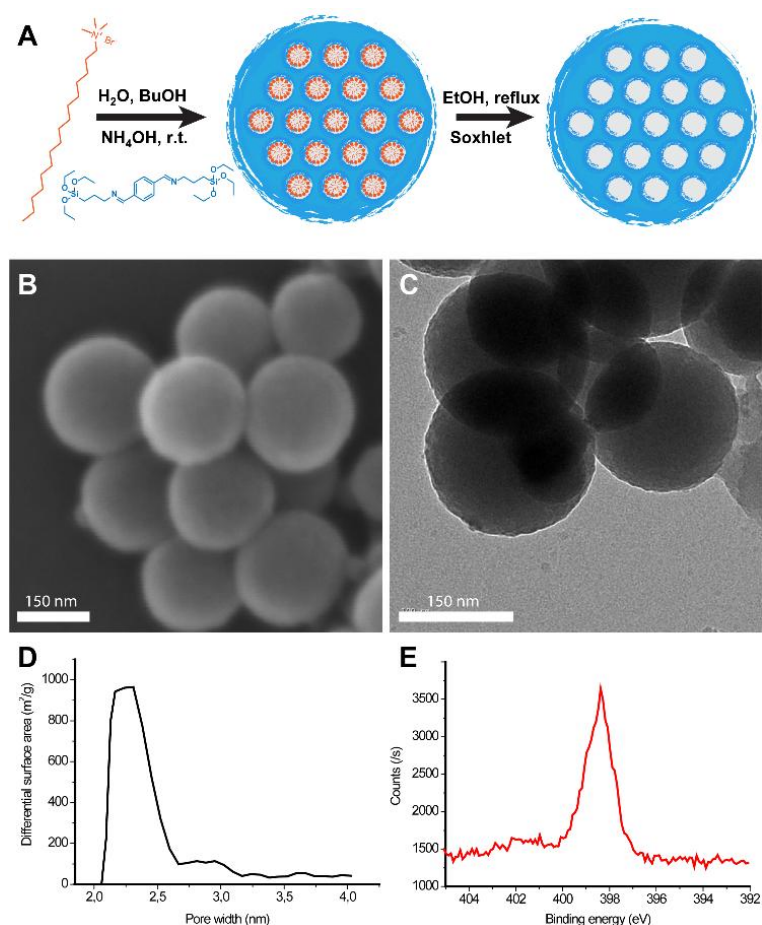


**Figure 2.1** (A) Representative scheme of the synthesis of BMONPs. (B) SEM and (C) TEM pictures of BMONPs. (D) Pore size distribution of BMONPs. The experiment was carried with  $N_2$  adsorption/desorption technique. (E) Nitrogen elemental scan on BMONPs by XPS.

Morphological characterisation of the hybrid materials has first been performed by scanning and transmission electron microscopy (SEM and TEM), (**Figure 2.1B** and **C** respectively). The images display the spherical morphology of the material with a good degree of monodispersity of the particles size, with an average diameter of 150 nm. A similar size (165 nm) is measured by dynamic light scattering (DLS) measurements on a suspension of the particles in phosphate buffer saline (PBS) solution. The nitrogen adsorption–desorption isotherms of the sample exhibits well-defined type IV features with H1-type hysteresis loops, which is characteristic for mesoporous material having cylindrical type mesostructures with an average pore width of 2.3 nm (**Figure 2.1D**).<sup>20–25</sup> Furthermore, nitrogen scan performed

with X-ray photoelectron spectroscopy (XPS) also exhibits a binding energy value attributed to an imine bond located at 398.57 eV (**Figure 2.1E**).<sup>26–29</sup>

To evaluate the breaking kinetics of the BMONPs through the hydrolysis of the imine groups, we have taken the advantage of the presence of the imine function to monitor its hydrolysis by <sup>1</sup>H NMR spectroscopy, liberating the starting aldehyde. The particles are suspended in aqueous acidic medium (pH 5.5) (illustration of **Figure 2.2A**) with a vigorous stirring and the released aldehyde is entrapped in a deuterated organic solvent which is analysed by NMR. The release profile of the aldehyde is represented in **Figure 2.2C** where we can see a fast liberation before reaching a plateau after 24 hours of reaction (**Figure 2.2C, black curve**). As comparison, the same experiment has been performed in the physiological conditions (pH 7.4) where only a few amount of aldehyde is released (**Figure 2.2C, red curve**).

To understand the kinetic release of guest molecules such as drugs, oligonucleotides and others, we have simulated this with dye release measured by photoluminescence spectroscopy. For this purpose, the particles have been functionalised with a dye called sulfo-cyanine 5 by its covalent linkage on the framework. The materials are then suspended in acidic media (pH = 5.5) with a gentle stirring. The breaking kinetics is followed by analysing the supernatant solution with a fluorimeter, monitoring the emission of released dye. From the dye release profile (**Figure 2.2D, black curve**), we can see that, at time 0, there is no emission as expected. After few minutes, we can already observe the emission of the dye in the solution, which then increases with time. After 24 hours, the emission reaches a plateau confirming the release of the totality of the dye in the sample. It is worth to notice that this behaviour is in agreement with morphology change evidenced by TEM analysis of the sample, indicating the destruction of the material (**Figure 2.2B**). As controlled experiment, the particles are suspended in the pH 7.4 solution and, from the release profile, we can see that most of the particles do not break apart. Also, in an analogous manner we have prepared and analysed a suspension of the non-breakable particles which lack the imine moieties. They show very similar size and morphology but do not display any degradation in the same acidic media nor in the neutral pH one (**Figure 2.2E**).

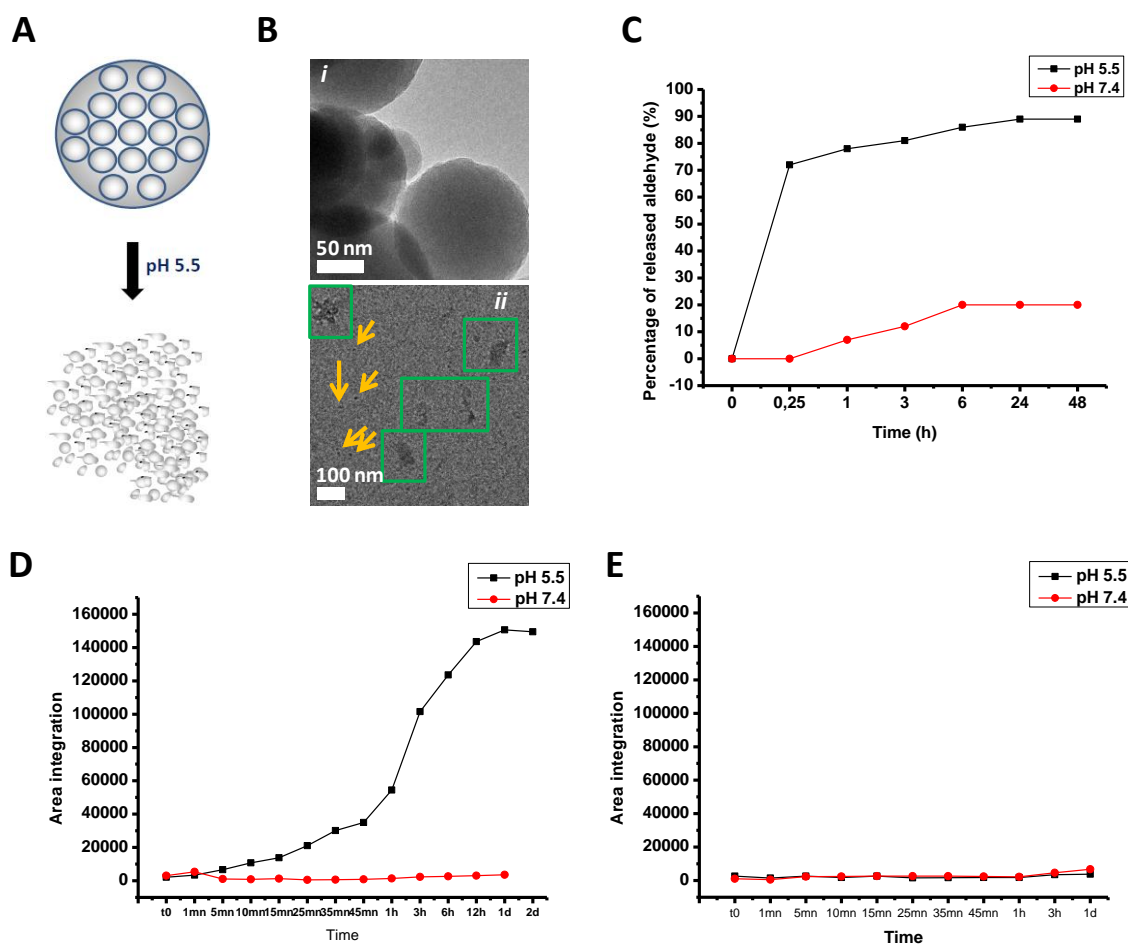


**Figure 2.2** (A) Schematic representation of the breaking experiments performed on the particles. (B) Images of BMONPs monitored by TEM upon dispersion in aqueous solution at pH 5 at times 0 (*i*) and 2d (*ii*); the **green squares** and **yellow arrows** indicate very small pieces of BMONPs. (C) Release profile of the aldehyde upon dispersion in PBS at (**black curve**) pH 5.5 and at (**red curve**) pH 7.4; the released aldehyde is entrapped into a Tol-*ds* solvent and using 1,4-dimethoxybenzene as internal standard. Data obtained from <sup>1</sup>H NMR spectroscopy in Tol-*ds*. Sulfo-cyanine 5 release profile from a covalent attachment to (D) BMONPs and (E) (MSNPs).

The pH-breakable hybrid mesoporous silica nanoparticles have been synthesized using a relatively straightforward method. Moreover, it demonstrated a relatively good stability in physiological conditions while it breaks down in acidic media.

With nearly 1.7 million new cases diagnosed in 2012 (latest data), breast cancer is the most common cancer type in women worldwide and the second most common overall, the first position being occupied by lung cancer.<sup>30,31</sup>

In the attempt to cure breast cancer, as well as to cure all cancer types, several techniques are proposed nowadays, such as surgery, radiation therapy, chemotherapy or immunotherapy. Regarding chemotherapy, a certain number of drugs are available on the market and, among those used to treat breast cancer, paclitaxel, a water insoluble molecule commercially known as Taxol<sup>®</sup>, occupies an important position. Paclitaxel acts as an antimitotic agent by blocking the cell cycle in its G1 or M phases by stabilising the microtubule cytoskeleton against depolymerisation.<sup>32-35</sup>

*The objective of the chapter 3 is to effectively load the hydrophobic paclitaxel into the pores of the pH-breakable mesoporous organosilica nanoparticle and deliver it into human breast cancer cells in order to kill them. Hs578T cell line has been used as model. The effect on a healthy version of human breast is also described by employing MCF-10 cell line. For comparison, non-breakable mesoporous silica nanoparticles (MSNPs) have also been loaded with the same drug and the cytotoxicity effect was studied, as well as the toxic effect of both breakable and non-breakable particles alone.*

Before employing BMONPs for *in vivo* drug delivery experiments, we need to first investigate their uptake and cytotoxicity in cells. For this purpose, we have used Hs578T and MCF-10 cell lines, cancer and healthy versions of human breast cells, respectively.

The internalisation of the material has been followed by SEM. The cells rapidly internalise small numbers of particles only 5 min after starting the incubation, and the amount of materials taken up increase over time. Z-stack investigations images taken 24 hours after incubation by confocal microscopy reported in **Figure 3.1** clearly demonstrate an efficient internalisation of BMONPs Hs578T cell line, with a tendency to localise mainly in the perinuclear region. The same result is obtained with MCF-10 cells.

Furthermore, the non-breakable particle, i.e. MSNPs, induces the same behaviour to those cells.

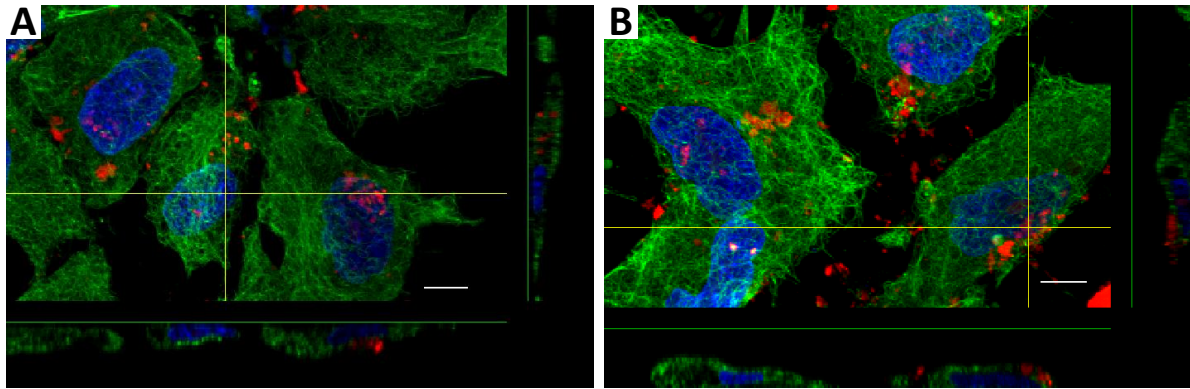


**Figure 3.1** Confocal microscopy on BMONPs - Z-stack analysis: (A) and (B) upon incubation with Hs578T cells at a concentration of 0.05 mg/mL for 24h; BMONPs are labelled with RITC (red) while the cell membrane is stained with Alexa Fluor® 647 Phalloidin (green) and its nucleus with DAPI (blue).

To investigate on the cytotoxicity of BMONPs, Hs578T and MCF-10 cells are treated with the particles at different concentrations (0.05 and 0.1 mg/mL) and the viability is measured after 48 hours. Negligible cell death is detected in the concentrations range tested, indicating that the hybrid bio-responsive particles are non-cytotoxic under the conditions explored (Figure 3.2A).

The beneficial effect of the breakability of BMONPs in the hydrophobic drug release activity has been tested *in vitro* using paclitaxel (Pac) as water-insoluble drug. The chemotherapeutic agent has been loaded into the particles by a weight percentage of 26 %. Control experiments conducted on cells incubated only with aqueous suspensions of Pac have also been included in the study. In this case, the concentration of the drug has been deliberately exaggerated as compared to that loaded in the particles. As shown in Figure 3.2B, the Pac@BMONPs systems are able to reduce the cell viability down to about 40 % when Hs578T cells are treated with 0.1 mg/mL of particles. On the contrary, the decrease in cell viability induced by Paclitaxel alone is negligible considering the exact amount of drug. This difference in behaviour can be attributed to the higher internalisation and the faster kinetic release of BMONPs. Simultaneously, the same experiments have been carried out with the non-breakable particles, i.e. MSNPs and no particular cytotoxicity is observed, most probably due to the fact the highly hydrophobic drug tend to remain inside the particle pores.

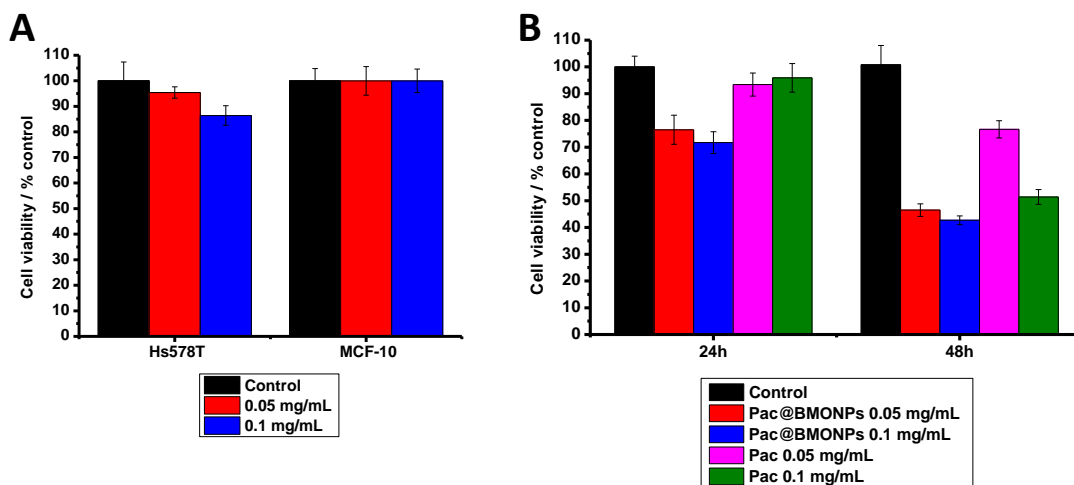


**Figure 3.2** (A) Cell viability assays of BMONPs towards Hs578T and MCF-10 cell lines after 48h of incubation at concentrations of 0.05 and 0.1 mg/mL; (B) Hs578T cell viability tests upon incubation with Pac@BMONPs and aqueous Pac suspensions for 24 and 48h at 0.05 and 0.1 mg/mL. Experiments performed with sulforhodamine B assays.

After being taken up by the breast cancer cell, both of the non-breakable and breakable particles reside in the perinuclear region of the cytoplasm without inducing any particular cytotoxicity. While the DDS based on the conventional MSNP shows a negligible apoptotic effect on the cells, the one based on the imine-doped particle demonstrates a highly cytotoxic effect thanks to the technology based on the pH-breakability of the vector which forces the drug to get into and stay inside the cell.

Intracellular delivery of particular proteins has attracted a great deal of attention in nanomedicine for protein or peptide-based nanotherapeutics and several strategies have been undertaken.<sup>36–38</sup> Nevertheless, the efficient delivery of native, functional proteins or enzymes, in an active conformation to the necessary site of action, still remains a challenge. Under physiological conditions, proteins and peptides tend to undergo degradation by proteolytic enzymes or, in the case of the higher-molecular-weight proteins, may be recognised by neutralising antibodies.<sup>39,40</sup> Some examples of diverse soft and hard host structures have been reported on nanocapsule systems to deliver proteins into cancer cells.<sup>41,42</sup> Very recently, our group reported the use of hard nanoparticles to effectively encapsulate and deliver into C6 glioma cells highly cytotoxic proteins such as TRAIL Apo2 ligand and onconase. Beside this efficient method, one great advantage of the system is its synergic stimuli-responsive and

biodegradability property upon the incorporation of a reduction sensitive organic linker within the framework.<sup>13</sup>

In the present chapter, we report the extension of the stimuli-responsive biodegradability of the silica nanocapsules. For this purpose, we describe herein the incorporation of the pH-responsive diiminosilane linker that we used within the mesoporous silica nanoparticles (MSNPs) in **chapters 2 and 3**.

Simultaneously, another challenge comes up. Is it also possible to effectively encapsulate smaller molecules such as drugs into biodegradable and bio-responsive hard silica nanomaterials and deliver them into cancer cells?

In **chapter 3**, the use of MSNPs towards drug delivery in the field of cancer therapy was discussed. Due to the small size of some drugs or other payload molecules as compared to that of the pores of MSNPs, most of the drug delivery systems (DDS) based on MSNPs suffer from leakage issues leading to premature release and thus severe side effects.<sup>43,44</sup> To overcome these limitations, the novel systems based on non-porous nanocapsules are attracting a great deal of attention. In such systems, the guest is encapsulated inside a nanoshell as described above for the protein encapsulation systems, preventing premature release. Some examples of diverse soft and hard host structures have been reported on nanocapsule systems to deliver drugs into cancer cells.<sup>3,45</sup>

However, to the best of our knowledge, no system of drug encapsulation into bio-responsive and breakable hard silica nanocapsules has been yet reported. Thus, encouraged by our novel technology based on the pH-breakable system, we herein rise to this challenge. We have thus effectively encapsulated doxorubicin, a potent chemotherapeutic agent,<sup>46,47</sup> into the hybrid nanocapsule. The material is able to break down upon contact with acidic medium and deliver the loaded drug to provide effective cytotoxicity towards HeLa cells.

According to a method reported by our group,<sup>13</sup> an aqueous solution of doxorubicin hydrochloride (Dox.HCl) is trapped into a reverse micelle made of Triton™ X-100 in a water-in-oil emulsion composed of cyclohexane as oil and n-hexanol as co-solvent. TEOS is reacted with the diiminosilane linker around the reverse micelle with ammonia as a base to trigger the hydrolysis of the silica precursor (**Figure 4.1A**). After precipitation and several washing steps, the nanocapsule is obtained as spherical materials with a diameter ranging from 60 to 90 nm (**Figure 4.1B,C**). The percentage of drug loading has been determined to be 10 weight %. As a control, a non-breakable nanocapsule has also been synthesized by the mean of only

TEOS as precursor of the framework. From now on, the breakable system will be called as Dox@imine-SiO<sub>2</sub>-NC and the non-breakable one as Dox@SiO<sub>2</sub>-NC.

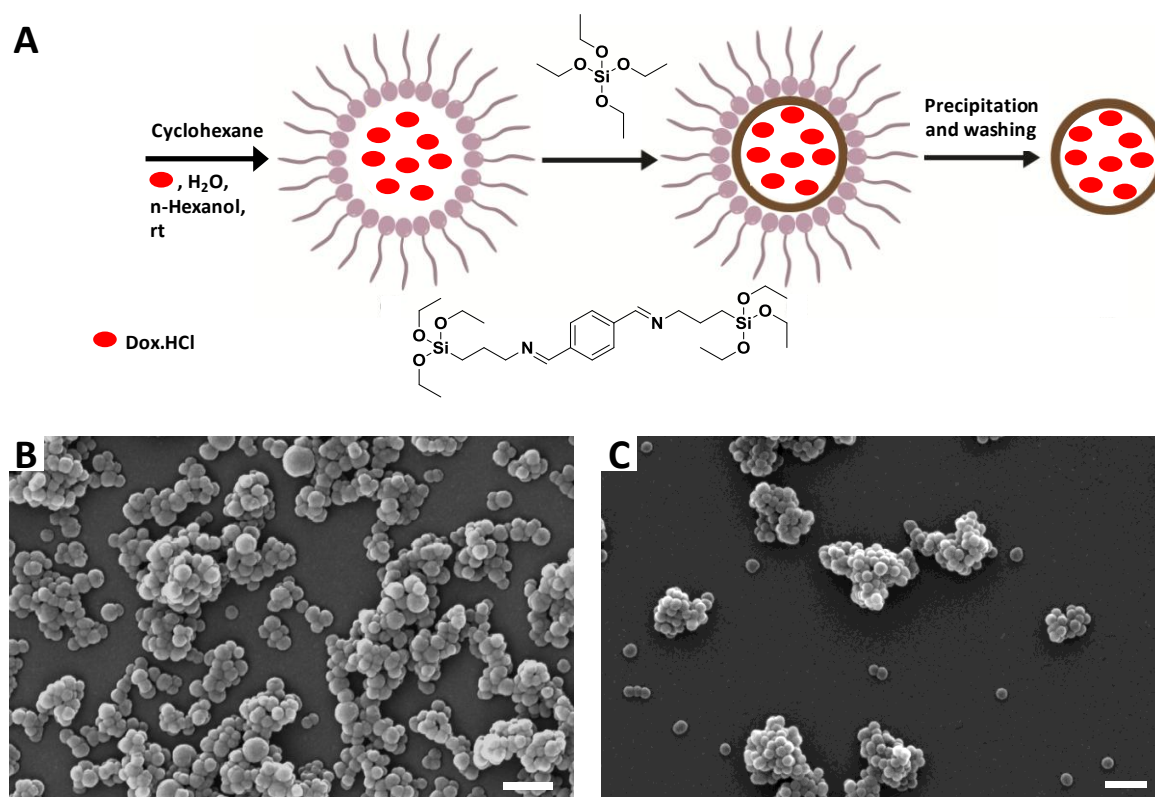


**Figure 4.1** (A) Representative scheme of the procedure for doxorubicin encapsulation. SEM pictures of (B) Dox@imine-SiO<sub>2</sub>-NCs and (C) Dox@SiO<sub>2</sub>-NCs. Scale bar = 300 nm.

The breakability of the materials has been studied by dispersing them in acidic media (pH 5.5). A fluorimeter is used to monitor the emission of the released doxorubicin upon the particles breaking. The release profile of the drug implicates a fast liberation in acidic conditions which stops after 2 days of dispersion. As comparison, the same experiment has been performed in neutral pH media and also with non-breakable shells. In none of the latter cases, we can observe a drug release.

Cell internalisation studies by confocal microscopy enable to observe a fast uptake of both of the breakable and non-breakable particles by HeLa cell line, within 4 hours. The activity has been determined by incubating the cells with the particles at the concentrations of 0.1, 0.5 and 1 mg/mL. We can see from **Figure 4.2A** that, after 48 hours, significant cells death are obtained with Dox@imine-SiO<sub>2</sub>-NCs as compared to Dox@SiO<sub>2</sub>-NCs. Moreover, the same

experiment carried out with an aqueous solution of Dox in the conditions and considering the same percentage as in the capsules lead to negligible cells death as compared to the breakable capsule (**Figure 4.2B**).

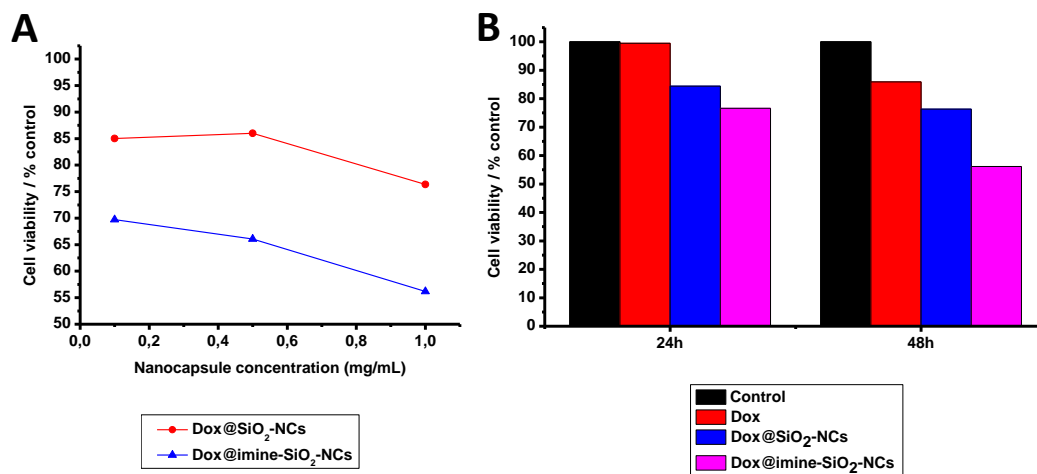


**Figure 4.2** HeLa cell viability tests of doxorubicin loaded nanocapsules: **(A)** results obtained after 48 hours of treatment. The nanocapsules concentrations used for the experiments are 0.1, 0.5 and 1 mg/mL; **(B)** results obtained with doxorubicin loaded nanocapsules and doxorubicin solution. The cells are incubated with the nanocapsules at the concentration of 1 mg/mL and with doxorubicin solution at the concentration of 0.1 mg/mL to be in accordance with the percentage of loading. The cell viability is determined after 24 and 48 hours. Tests performed with alamarBlue assay.

We have been able to extend the reduction sensitive nanocapsule to the pH sensitive one and, simultaneously, we have successfully encapsulated a small drug molecule. The system demonstrates a good stability in physiological conditions and thus enables to avoid premature release of the payload. A rapid internalisation also occurs with HeLa cell line and the particles are retained in the periphery of the nucleus. Eventually, taking advantage of the technology based on the pH-breakability, the nanocapsule can effectively deliver the drug *in vitro* into HeLa cells and leads to the cells apoptosis.

## References

1. Riehemann, K. *et al.* Nanomedicine-Challenge and Perspectives. *Angew. Chem. Int. Ed.* **48**, 872–897 (2009).
2. Blanazs, A., Armes, S. P. & Ryan, A. J. Self-Assembled Block Copolymer Aggregates: From Micelles to Vesicles and their Biological Applications. *Macromol. Rapid Commun.* **30**, 267–277 (2009).

3. Gokhale, P. C. *et al.* An improved method of encapsulation of doxorubicin in liposomes: pharmacological, toxicological and therapeutic evaluation. *Br. J. Cancer* **74**, 43 (1996).
4. Horcajada, P. *et al.* Porous metal–organic-framework nanoscale carriers as a potential platform for drug delivery and imaging. *Nat. Mater.* **9**, 172–178 (2010).
5. Lu, F. *et al.* Advances in Bioapplications of Carbon Nanotubes. *Adv. Mater.* **21**, 139–152 (2009).
6. Li, Z., Barnes, J. C., Bosoy, A., Stoddart, J. F. & Zink, J. I. Mesoporous silica nanoparticles in biomedical applications. *Chem. Soc. Rev.* **41**, 2590 (2012).
7. Kunzmann, A. *et al.* Toxicology of engineered nanomaterials: Focus on biocompatibility, biodistribution and biodegradation. *Biochim. Biophys. Acta BBA - Gen. Subj.* **1810**, 361–373 (2011).
8. Inagaki, S., Guan, S., Ohsuna, T. & Terasaki, O. An ordered mesoporous organosilica hybrid material with a crystal-like wall structure. *Nature* **416**, 304–307 (2002).
9. Lu, J., Li, Z., Zink, J. I. & Tamanoi, F. In vivo tumor suppression efficacy of mesoporous silica nanoparticles-based drug-delivery system: enhanced efficacy by folate modification. *Nanomedicine Nanotechnol. Biol. Med.* **8**, 212–220 (2012).
10. Quignard, S., Mosser, G., Boissière, M. & Coradin, T. Long-term fate of silica nanoparticles interacting with human dermal fibroblasts. *Biomaterials* **33**, 4431–4442 (2012).
11. Croissant, J. *et al.* Biodegradable Ethylene-Bis(Propyl)Disulfide-Based Periodic Mesoporous Organosilica Nanorods and Nanospheres for Efficient In-Vitro Drug Delivery. *Adv. Mater.* **26**, 6174–6180 (2014).
12. Maggini, L. *et al.* Breakable mesoporous silica nanoparticles for targeted drug delivery. *Nanoscale* **8**, 7240–7247 (2016).
13. Prasetyanto, E. A. *et al.* Breakable Hybrid Organosilica Nanocapsules for Protein Delivery. *Angew. Chem. Int. Ed.* **55**, 3323–3327 (2016).
14. Montcourrier, P., Silver, I., Farnoud, R., Bird, I. & Rochefort, H. Breast cancer cells have a high capacity to acidify extracellular milieu by a dual mechanism. *Clin. Exp. Metastasis* **15**, 382–392 (1997).
15. Kato, Y. *et al.* Acidic extracellular microenvironment and cancer. *Cancer Cell Int.* **13**, 89–89 (2013).
16. He, Q. *et al.* A pH-responsive mesoporous silica nanoparticles-based multi-drug delivery system for overcoming multi-drug resistance. *Biomaterials* **32**, 7711–7720 (2011).
17. Meng, H. *et al.* Autonomous in Vitro Anticancer Drug Release from Mesoporous Silica Nanoparticles by pH-Sensitive Nanovalves. *J. Am. Chem. Soc.* **132**, 12690–12697 (2010).
18. Yuan, L. *et al.* Preparation of pH-Responsive Mesoporous Silica Nanoparticles and Their Application in Controlled Drug Delivery. *J. Phys. Chem. C* **115**, 9926–9932 (2011).
19. Yao, X., Chen, X., He, C., Chen, L. & Chen, X. Dual pH-responsive mesoporous silica nanoparticles for efficient combination of chemotherapy and photodynamic therapy. *J Mater Chem B* **3**, 4707–4714 (2015).

20. Sing, K. S. W. *et al.* in *Handbook of Heterogeneous Catalysis* (Wiley-VCH Verlag GmbH & Co. KGaA, 2008).
21. Tang, H. *et al.* Facile synthesis of pH sensitive polymer-coated mesoporous silica nanoparticles and their application in drug delivery. *Int. J. Pharm.* **421**, 388–396 (2011).
22. Harrison Wanyika. Synthesis and characterization of ordered mesoporous silica nanoparticles with tunable physical properties by varying molar composition of reagents. *Afr. J. Pharm. Pharmacol.* **5**, (2011).
23. Wanyika, H. Sustained release of fungicide metalaxyl by mesoporous silica nanospheres. *J. Nanoparticle Res.* **15**, (2013).
24. Rashidi, L., Vasheghani-Farahani, E., Rostami, K., Ganji, F. & Fallahpour, M. Mesoporous silica nanoparticles with different pore sizes for delivery of pH-sensitive gallic acid: mesoporous silica nanoparticles for delivery of gallic acid. *Asia-Pac. J. Chem. Eng.* **9**, 845–853 (2014).
25. Fernando, I. R. *et al.* Esterase- and pH-responsive poly( $\beta$ -amino ester)-capped mesoporous silica nanoparticles for drug delivery. *Nanoscale* **7**, 7178–7183 (2015).
26. Lee, T. H. & Rabalais, J. W. X-ray photoelectron spectra and electronic structure of some diamine compounds. *J. Electron Spectrosc. Relat. Phenom.* **11**, 123–127 (1977).
27. Snauwaert, P., Lazzaroni, R., Riga, J., Verbist, J. J. & Gonbeau, D. A photoelectron spectroscopic study of the electrochemical processes in polyaniline. *J. Chem. Phys.* **92**, 2187 (1990).
28. Rosink, J. *et al.* Self-assembly of  $\pi$ -conjugated azomethine oligomers by sequential deposition of monomers from solution. *Langmuir* **16**, 4547–4553 (2000).
29. Luo, Y. *et al.* In Situ Hydrolysis of Imine Derivatives on Au(111) for the Formation of Aromatic Mixed Self-Assembled Monolayers: Multitechnique Analysis of This Tunable Surface Modification. *Langmuir* **28**, 358–366 (2012).
30. Latest world cancer statistics Global cancer burden rises to 14.1 million new cases in 2012: Marked increase in breast cancers must be addressed. *International Agency for Research on Cancer - World Health Organization* (2013).
31. Ferlay, J. *et al.* Cancer incidence and mortality worldwide: Sources, methods and major patterns in Globocan 2012: Globocan 2012. *Int. J. Cancer* **136**, E359–E386 (2015).
32. Schiff, P. B., Fant, J. & Horwitz, S. B. Promotion of microtubule assembly in vitro by taxol. *Nature* **277**, 665–667 (1979).
33. Arnal, I. & Wade, R. H. How does taxol stabilize microtubules? *Curr. Biol.* **5**, 900–908 (1995).
34. Amos, L. A. & Löwe, J. How Taxol® stabilises microtubule structure. *Chem. Biol.* **6**, R65–R69 (1999).
35. Howarth, F. C., Calaghan, S. C., Boyett, M. R. & White, E. Effect of the microtubule polymerizing agent taxol on contraction, Ca<sup>2+</sup> transient and L-type Ca<sup>2+</sup> current in rat ventricular myocytes. *J. Physiol.* **516**, 409–419 (1999).
36. Zhou, H. *et al.* Generation of Induced Pluripotent Stem Cells Using Recombinant Proteins. *Cell Stem Cell* **4**, 381–384 (2009).
37. Schwarze, S. R., Ho, A., Vocero-Akbani, A. & Dowdy, S. F. In Vivo Protein Transduction: Delivery of a Biologically Active Protein into the Mouse. *Science* **285**, 1569 (1999).

38. Shah, A. M. & Mann, D. L. In search of new therapeutic targets and strategies for heart failure: recent advances in basic science. *The Lancet* **378**, 704–712
39. Fu, K., Klibanov, A. M. & Langer, R. Protein stability in controlled-release systems. *Nat Biotech* **18**, 24–25 (2000).
40. Jiskoot, W. *et al.* Protein Instability and Immunogenicity: Roadblocks to Clinical Application of Injectable Protein Delivery Systems for Sustained Release. *J. Pharm. Sci.* **101**, 946–954
41. Yuba, E. *et al.* The application of pH-sensitive polymer-lipids to antigen delivery for cancer immunotherapy. *Biomaterials* **34**, 5711–5721 (2013).
42. Yuba, E., Harada, A., Sakanishi, Y., Watarai, S. & Kono, K. A liposome-based antigen delivery system using pH-sensitive fusogenic polymers for cancer immunotherapy. *Biomaterials* **34**, 3042–3052 (2013).
43. Slowing, I., Viveroescoto, J., Wu, C. & Lin, V. Mesoporous silica nanoparticles as controlled release drug delivery and gene transfection carriers☆. *Adv. Drug Deliv. Rev.* **60**, 1278–1288 (2008).
44. Sun, R., Wang, W., Wen, Y. & Zhang, X. Recent Advance on Mesoporous Silica Nanoparticles-Based Controlled Release System: Intelligent Switches Open up New Horizon. *Nanomaterials* **5**, 2019–2053 (2015).
45. Sanyakamdhorn, S., Agudelo, D. & Tajmir-Riahi, H.-A. Encapsulation of Antitumor Drug Doxorubicin and Its Analogue by Chitosan Nanoparticles. *Biomacromolecules* **14**, 557–563 (2013).
46. Eikenberry, S. A tumor cord model for Doxorubicin delivery and dose optimization in solid tumors. *Theor. Biol. Med. Model.* **6**, 16 (2009).
47. Tacar, O., Sriamornsak, P. & Dass, C. R. Doxorubicin: an update on anticancer molecular action, toxicity and novel drug delivery systems: Doxorubicin cell and molecular biological activity. *J. Pharm. Pharmacol.* **65**, 157–170 (2013).

# Chapter 1

## General introduction

### Abstract

In recent years, the use of nanoparticles has expanded in biomedical research. The use of these nanomaterials in nanomedicine has allowed for more efficient treatments, the quality of life of patients. Among the different nanoparticles available nowadays, silica-based materials have attracted a great deal of attention as promising nanovectors for cancer treatment. Therefore, a great deal of effort has been dedicated to the preparation and optimization of such particles. However, the *in vivo* clearance of such relatively big and inorganic materials remains an important issue, leading to harmful side effects and impeding their clinical translation. In order to overcome this limitation, different smart strategies such as the synthesis of stimuli-responsive hybrid organic/inorganic nanomaterials, have emerged and are currently under investigations. In this thesis, the synthesis of a breakable pH-responsive mesoporous organosilica nanoparticle to fight cancer by a “self-poisoning” strategy is reported. This strategy has also been expanded to the preparation of a nanocapsule to accommodate small sized as well as big sized guests still for cancer treatment.

## 1.1 Nanoparticles (NPs) as promising delivery vectors in nanomedicine

In the field of nanomedicine, nanoparticles (NPs) play an emerging role for targeted delivery of diverse bioactive molecules such as drugs, diagnostic agents, genes or proteins.<sup>1-4</sup> NPs are defined as materials possessing a size ranging from 1 to 100 nm in at least one dimension; nevertheless, when related to drug or gene delivery systems, a size of up to 1000 nm can be considered.<sup>5,2,3</sup> NPs are endowed of diverse properties which led them to be considered as good platforms to serve as nanomedical tools. These properties include: a large surface area, which offers the possibility of loading a high amount of molecules of interest; the relative ease of surface functionalisation, enabling a high degree of surface modification; and their size which is also tunable depending on the purpose. Before employing such materials in the medical field, it is of great importance to consider their physicochemical features in order to gain the highest efficiency possible.

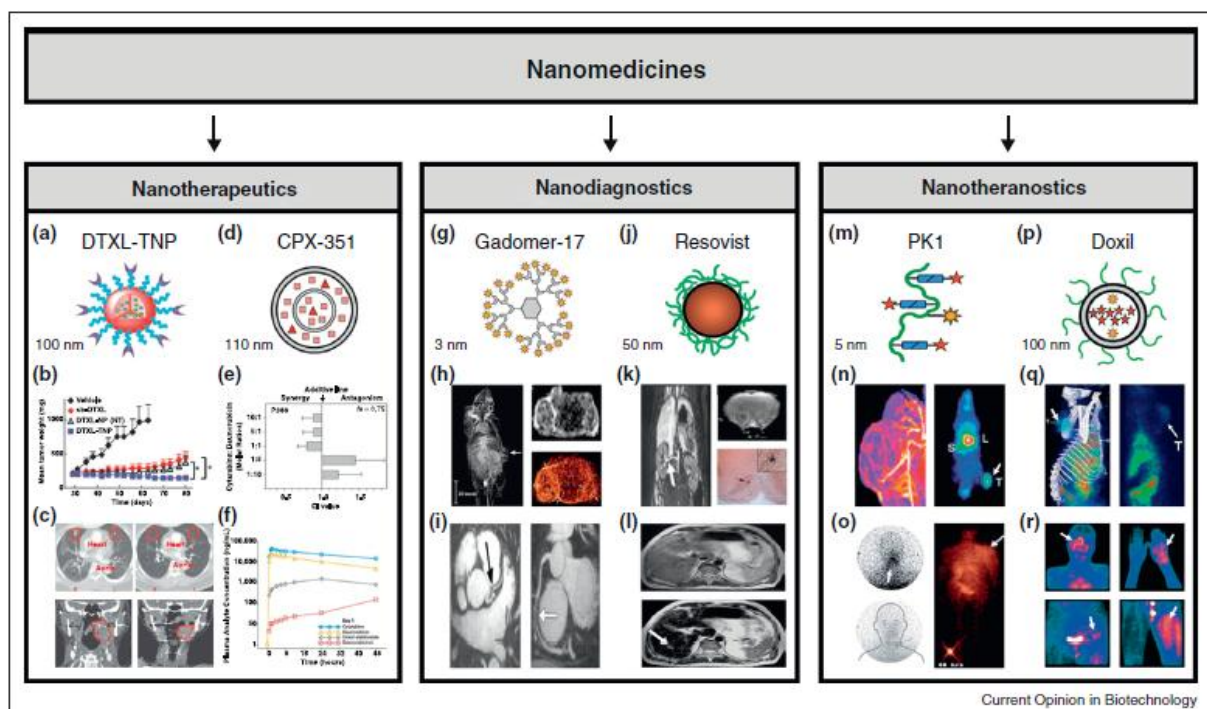


**Figure 1.1** The three different “sub-classes” of nanomedicine. Figure taken from reference 11.

Most of the therapeutic or diagnostic systems available nowadays for diseases treatment suffer from several limitations. The main issue is not the lack of drugs or diagnostic agents, but the efficiency of these molecules to reach properly and exclusively the defective cells.

Indeed, chemotherapeutic or chemodiagnostic molecules suffer from several limitations such as poor solubility in aqueous phase or a lack of specificity, which leads them to not only the defective sites but also the healthy tissues. As a result, often a high dosage is necessary to treat the disease and this leads to severe side effects. To overcome these issues, there had been a crucial need to develop new, more specific and more efficient strategies to better understand (diagnosis) and treat (therapy) the diseases which become more and more complex. It is in these circumstances that nanotechnology has been expanded to medicine. Nanomedicine can thus be defined as a class of medicine which is in very narrow partnership with nanotechnology.<sup>6-10,4</sup> The aim of nanomedicine is to enhance the patient treatment by using more efficient, less invasive and harmful techniques, including the minimisation of the side effects which are mostly highly severe.<sup>4</sup> In this respect, nanoparticles (NPs) have been found to be potentially good platforms to perform what thus called as nanotherapeutics, nanodiagnosis and nanotheranostics (**Figure 1.1**).<sup>11</sup>

### ***1.1.1 Physicochemical features affecting NPs efficiency***

As already mentioned in paragraph **1.1**, NPs present the advantages of large and tunable surface area as well as customisable morphology. Depending on the way these features are tuned, the material can show a very good efficiency towards its purpose. However, if these parameters are not well handled, they can be factors of the reverse effect, leading to non-desired pharmacokinetics, biodistribution and, eventually, increased toxicity. The cytotoxic effect can be observed at different levels, ranging from the cells (*in vitro*) to the body (*in vivo*, clinical) (**Figure 1.2**).<sup>12</sup>

#### ***1.1.1.1 Size***

In the biological media, NPs interact with the cells via the surface of the materials and this interaction can lead to certain cytotoxicity. As the diameter decreases, the surface area of the particle increases exponentially. The surface area of NPs depends on the size, the smaller is the particle, the larger is the surface area. Consequently to this direct relationship, the interaction between the cell and the NP and, thus, the cytotoxicity will depend on the size of the material. The effect of the size on cytotoxicity is independent of the composition of the

NPs. Moreover, the biodistribution of the NPs is also affected by the size.<sup>12</sup> Therefore it is of critical importance to consider the particle size when applied in biomedical field.

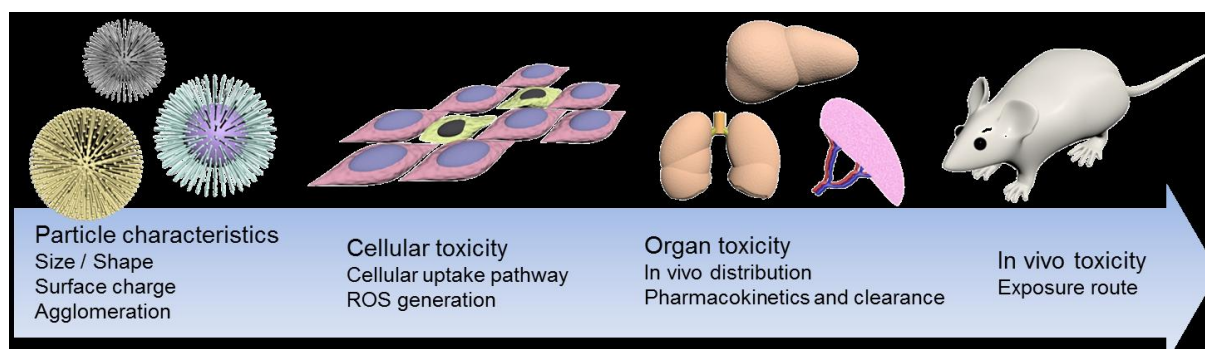


**Figure 1.2** Schematic drawing of nanoparticle induced cytotoxicity. Intrinsic features of nanoparticles, such as size, surface charge, agglomeration, can significantly affect cytotoxicity. Such cytotoxicity can be affected at the levels of the cell, organ and even *in vivo* systems. Figure taken from reference 12.

Upon inhalation, NPs enter the lung parenchyma and the distribution depends on the size. At the cell level, NPs of a size below 100 nm can be easily internalised. Nevertheless, those with sizes up to 500 nm can also be taken up. The mechanism of internalisation differs depending on the size because different interactions with the cell components can occur. Thus, NPs of 40 nm in diameter can penetrate the nucleus membrane. With gold and silica NPs, a decrease in the particle size results in the increase of reactive oxygen species (ROS) and cytotoxicity.

Due to the fact that the immune system takes care of any exogenous material, *in vivo* circulation/residence time is also affected by NPs size. It has been found out that nanomaterials with a size of 1-20 nm have a long residence in the circulatory system.<sup>13,14</sup>

Another important point which needs to be considered is the *in vivo* clearance of the NPs. In this respect, it has been found out that nanomaterials with a diameter above 6 nm are not excreted by the kidneys and tend to accumulate in specific organs, such as the liver and spleen, until being taken in charge by the mononuclear phagocyte system.<sup>13</sup> Due to this lack of clearance, most of those particles lead to important *in vivo* issues.<sup>13</sup>

### *1.1.1.2 Morphology*

The morphology is also an important feature affecting NPs biodistribution and cytotoxicity. In this respect, one critical parameter is the residence time. The biological media interacts with any exogenous material through the immune system and phagocytosis of rod-shaped NPs is faster than that of spherical nanomaterials. Moreover, even without considering the immune system, cell internalisation level is still the highest with rod-like shaped NPs. This order is then followed by spherical, cylindric and cubic NPs (tests performed with HeLa cell line). Nevertheless, the morphology of NPs tends to not strongly affect the cell behaviour when the size is below 100 nm.

### *1.1.1.3 Surface charge*

Due to the possible presence of functional groups on the particle surface, this latter can have surface charges. This feature can be measured by its zeta potential which, in suspension, provides an electric potential value. The surface charge of NPs is of critical importance in respect to their hydrodynamic behaviour in biological media as well their interaction with these media. Depending on the surface charge, the particles can either aggregate or repulse each other. The cell interaction and, thus, cell internalisation are altered by the charge on the particle surface with the highest uptake with positively charged NPs compared to those neutral or negatively charged. This difference in the internalisation rate tends to lead to cytotoxicity rate following the same order.

Another point worth mentioning is the formation of what is called protein corona. This corona is formed because of interactions between the materials and serum proteins or lipids in biological media. This phenomenon is dependent of the charge on the NP surface and alters the initial one. As a consequence, the residence time of the NP in the circulatory system is affected and the efficiency is influenced.

### *1.1.1.4 Surface functionalisation*

The surface is the part of the NP which is exposed to the interactions with its environment, from a chemical point of view, to the *in vivo* and passing by the *in vitro* ones. Therefore it is of great importance to consider this part. To tune the efficiency of the NP, the surface can be

modified by functionalisation with ligands using surface chemistry methods after the particle synthesis (post-grafting method) or by diverse types of chemistry during the NP synthesis. Depending on the purpose, different types of ligand can be attached. As example, PEG can be attached to enhance the biocompatibility. Furthermore, antibodies can be necessary to enhance the specificity to target cancer cells.

According to the composition and the physicochemical properties, numerous different nanoparticles have been developed. In the one hand, we can find soft materials such as virus-based NPs<sup>15-17</sup> or liposomes.<sup>2,18</sup> In the other hand, hard materials have also been reported. As examples, we can cite polymeric NPs,<sup>19</sup> dendrimers,<sup>20</sup> nanocrystals,<sup>21</sup> carbon<sup>22</sup> or metal-based<sup>23</sup> nanoparticles. Some of these platforms have now been translated to clinical stages and some, such as liposomes, have even been put onto the market for drug delivery systems.<sup>18</sup> Among hard NPs, silica-based materials have recently attracted a great attention for biomedical applications.

## **1.2 Silica nanoparticles in nanomedicine**

Silica NPs are inorganic NPs based on silicon dioxide units and they belong to the family of bioactive ceramics (which undergo a specific interaction in the biological medium, enabling the materials integration within the living tissue, by comparison to inert ceramics, which do not)<sup>24</sup>. Indeed, silica-based materials have been the first particles to be classified as bioactive and this is the reason why such materials have attracted great attention towards biomedical field. Bioactivity can be defined as the ability of some materials, with a definite chemical composition and structure, in biological media, to undergo a series of chemical processes in the material-living tissue interface. This property, likely due to the presence of the silanol groups on the surface, leads to the material incorporation into the living tissue.<sup>24</sup> Different classes of silica-based materials have been synthesised for two main purposes: drug delivery systems and bone-tissue regeneration. The main classes are represented in **Figure 1.3**. Nevertheless, these classes can be divided into different sub-classes.

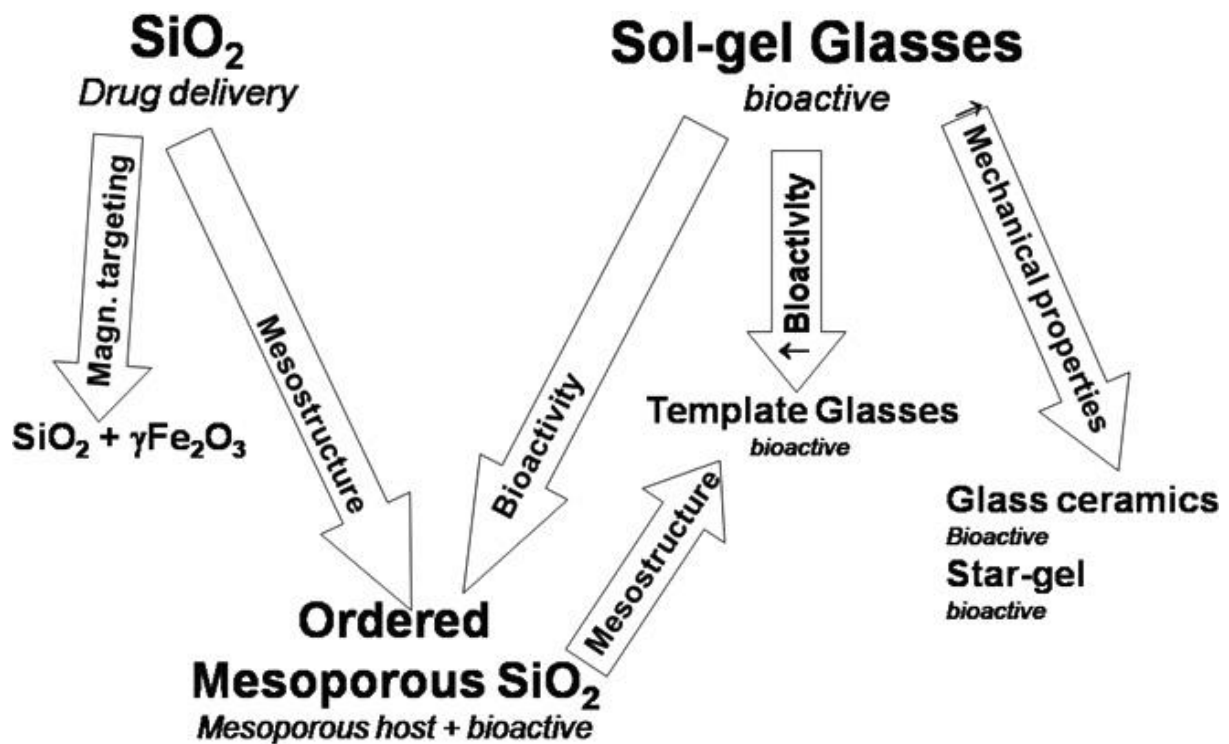


**Figure 1.3** Representative scheme of the main classes of silica-based materials used for biomedical applications. Figure taken from reference 24.

### 1.2.1 Amorphous silica spheres

Amorphous silica spheres are spherical micrometer or sub-micrometer sized silica materials with a high degree of monodispersity. One way to synthesize amorphous silica spheres is the Stöber method. Stöber method consists in the synthesis of silica spheres of uniform size (from nanometer to micrometer scale in diameter size) by hydrolysis of alkyl silicates and subsequent condensation of silicic acid in alcoholic solutions. Ammonia is used as a morphological catalyst.<sup>25</sup> Following this method, the size of the materials can be controlled by tuning the different features of the reaction, i.e., the alkyl silicate structure, the amount of base and the solvent. As we can see in the transmission electron microscopy (TEM) image in **Figure 1.4**, amorphous silica lack porosity.<sup>26</sup> Nevertheless, the possibility of surface functionalisation leads to the possibility of building devices for several applications in nanotechnology including biomedical field.

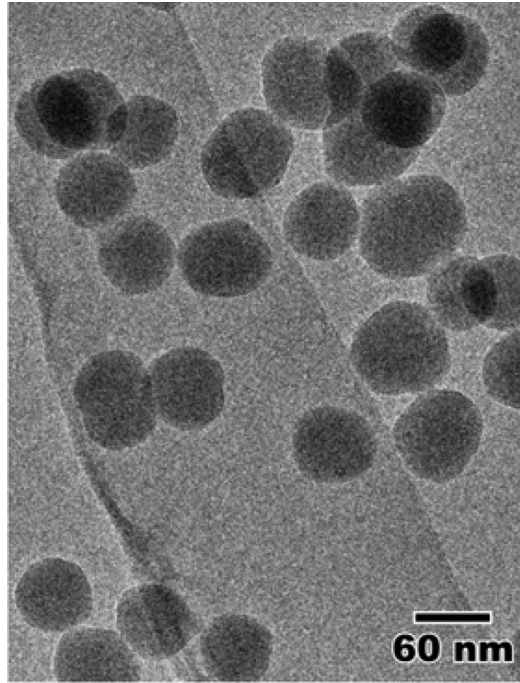


**Figure 1.4** TEM image of amorphous silica spheres. Figure taken from reference 26.

### ***1.2.2 Bioglasses***

Bioglass<sup>®</sup> was discovered by the US army in 1969 and consists in a disodium oxide - silicon dioxide ( $\text{Na}_2\text{O-SiO}_2$ ) matrix. To obtain a matrix with a large amount of calcium oxide (CaO) with some phosphate pentoxide ( $\text{P}_2\text{O}_5$ ), 45% of  $\text{SiO}_2$ , 24.5% of  $\text{Na}_2\text{O}$ , 24.5% of calcium oxide (CaO) and 6%  $\text{P}_2\text{O}_5$  were initially needed in the composition.<sup>27</sup> Bioglasses are amorphous their structure is arranged in a three dimensional network but without periodicity.<sup>24</sup> Initially, Bioglass<sup>®</sup> was employed in the biomedical field as a device for the reparation of bone or other tissues; *in vitro* and *in vivo* studies were led. **Figure 1.5** shows scanning and transmission electron microscopy (SEM and TEM) images of the surface of a bioglass upon incubation a simulated body fluid (SBF) solution for three days.

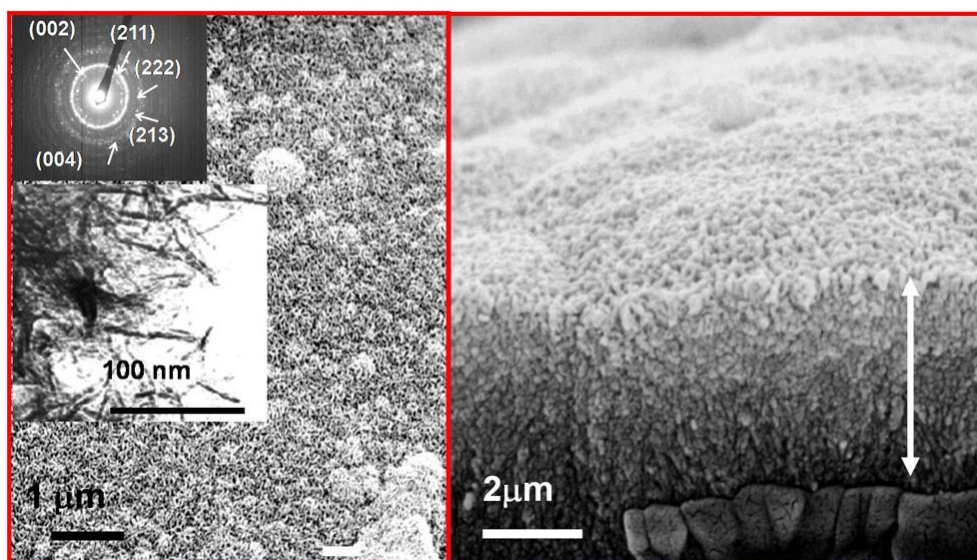


**Figure 1.5** SEM and TEM images of the surface of  $_{80}\text{Si}_{17}\text{Ca}_3\text{P}$  glass after 3 days of soaking in SBF at  $37^\circ\text{C}$ . Right side image shows the transversal cut of the material showing the aggregates of the apatite layer formed on the surface of the bioactive glass. Figure taken from reference 24.

### ***1.2.3 Ordered mesoporous silica (OMS)***

Ordered mesoporous silica consist in silica-based materials which are endowed of porosity. The pores are in the meso scale which means that they can range from 2 to 50 nm and diverse strategies are available to tune them. The mesopores are arranged as channels and cavities with different geometries built up following tetrahedral networks of silica.

A great advantage of OMS, compared to the other types of NPs, is the porosity, which considerably increases the surface area. Depending on the type of OMS, different synthesis methods based on sol-gel chemistry are available.<sup>28</sup> In this chapter, the synthesis of mesoporous silica nanoparticles (MSNPs) using a surfactant template will be described.

#### *Surfactant template synthesis*

One very common way to obtain surfactant template MSNPs consists in the condensation of a hydrolysed silicate, generally, tetraethyl orthosilicate (TEOS), around a surfactant which plays the role of liquid crystal templating. To trigger the hydrolysis of the silicate, a base, usually alkali, is necessary to serve as catalyst. Water is the main solvent of the reaction and an alcoholic co-solvent is also required. In this respect, a very common surfactant is hexadecyltrimethylammonium bromide, usually known as cetyltrimethylammonium bromide

(CTAB). The formation of micelle with CTAB is supposed to occur by self-assembly when the concentration is above the critical micelle concentration (CMC), knowing that the CMC of CTAB in water is 0.9 mM.<sup>29</sup> In these conditions, cylindrical micelles are formed and self-assemble in a hexagonal arrangement. Self-assembly of CTAB leads the silica precursor to condensate at the surface of the surfactant and form silica wall around the polar head region of the micelles. Eventually, to obtain free mesopores, the surfactant is removed by two main techniques; one consists in calcination and the other one in acidic solvent extraction. This procedure is illustrated in **Figure 1.6**. Following such a pathway, MSNPs are obtained with an ordered arrangement of uniform two-dimensional (2D) hexagonal *p6m* mesopores.<sup>30</sup> These pores possess a very high surface area of above 700 m<sup>2</sup>/g and diameter size of about 2 nm.<sup>26</sup>

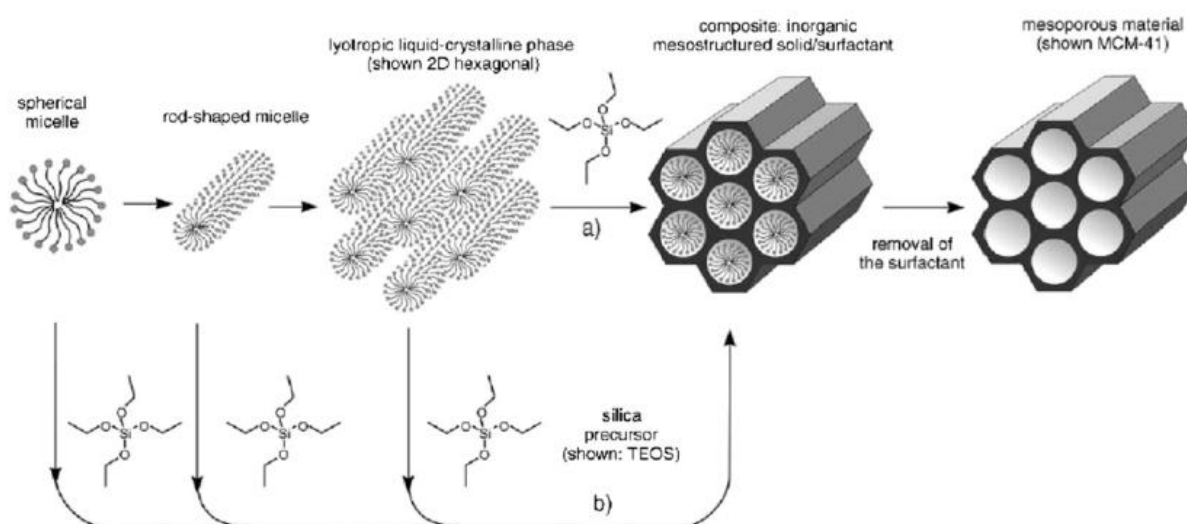


**Figure 1.6** Representative scheme illustrating the synthesis of MSNPs with CTAB surfactant micelles as template and TEOS as silica precursor. Figure taken from reference 28.

The first synthesis of ordered mesoporous silica particles, namely MCM-41, was reported in 1992 (**Figure 1.7**).<sup>31</sup> MCM-41 was prepared by Mobil corporation by using the surfactant of, or sodium metasilicate (Na<sub>2</sub>SiO<sub>3</sub>) as the silica precursors for MCM-41 and SBA-15 respectively.

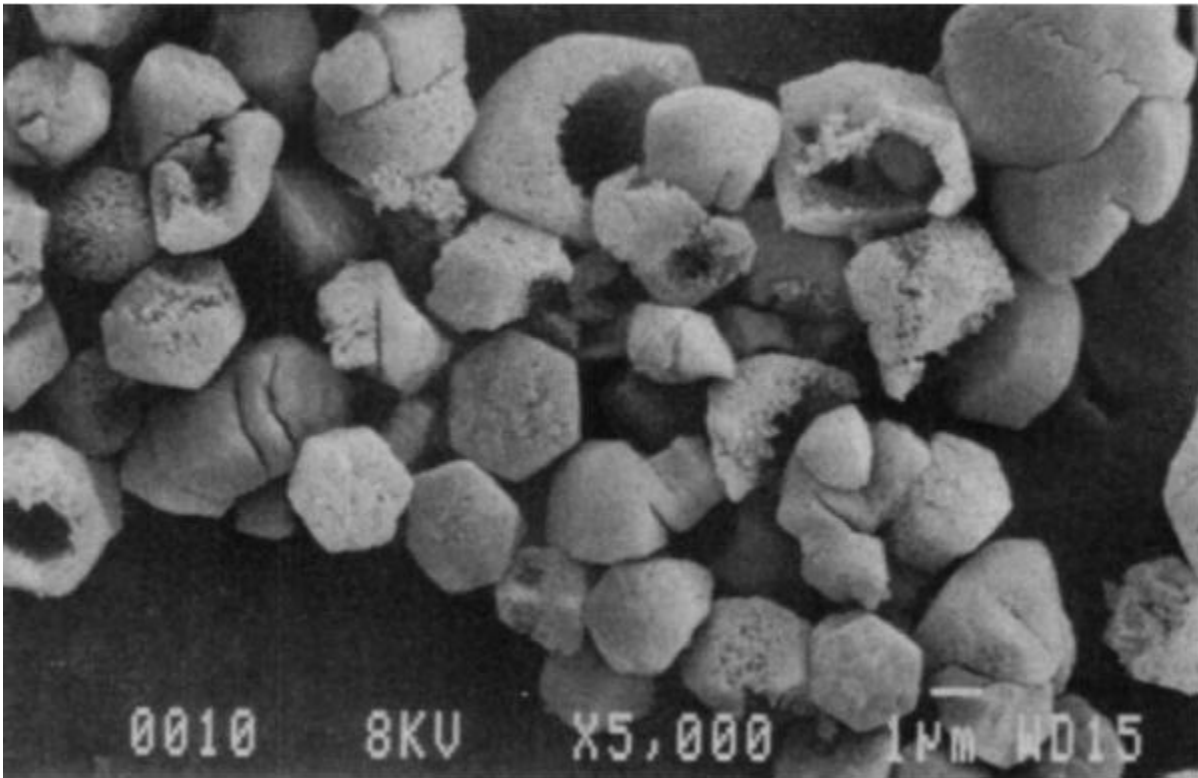


**Figure 1.7** SEM image of MCM-41. Figure taken from reference 31.

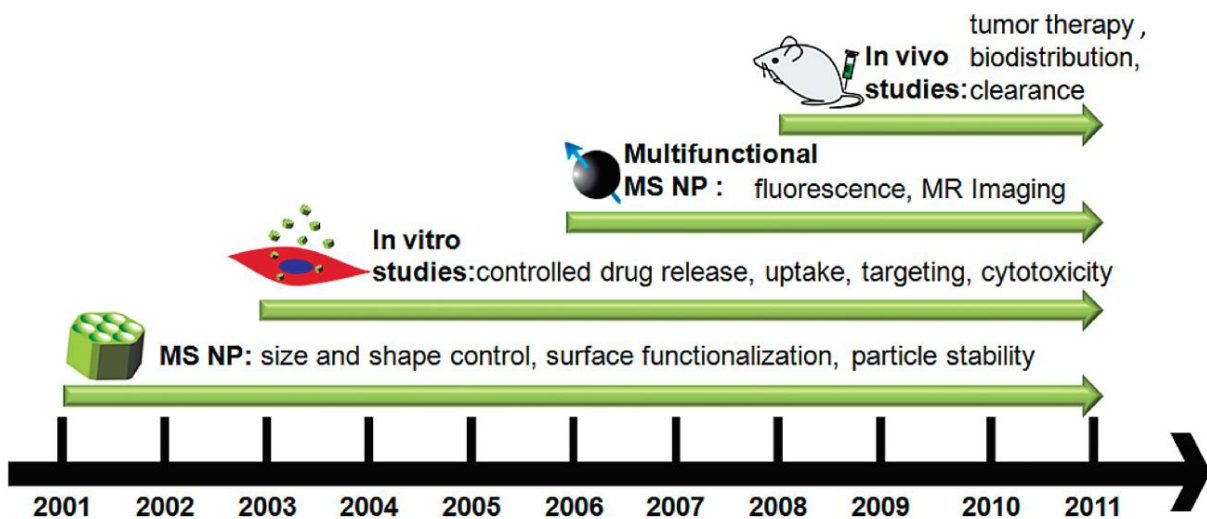


**Figure 1.8** Schematic representation of the evolution of the investigations of MSNPs toward biomedical use. Figure taken from reference 32.

During the following decade, MSNPs were mainly used in catalysis chemistry. However, since 2001, due to the diverse advantages that they can provide, MSNPs have attracted a great

interest in biomedical field. Since the first report on the use of MSNPs for biomedical applications, several different types of MSNPs have been synthesized and numerous optimisations regarding the shape, size, the particle stability and the surface have been brought to get closer and closer to the final aim, which is to improve the quality of the patient life and to obtain a more efficient treatment of the diseases. Thus, *in vitro* investigations have started in 2003 and the first *in vivo* translations have been reported five years later. This evolution of the use of MSNPs in the biomedical field is summarised in **Figure 1.8**.<sup>32</sup>

Being one of the most prevalent diseases in the world, cancer has attracted a great attention in the medical community. In order to help the medical teams to fight this disease, researchers from every field are trying to find a rapid and efficient solution. The main issue is not the lack of drugs or diagnostic agents, but the efficiency of these molecules to reach properly and exclusively the cancer cells. Indeed, chemotherapeutic or chemodiagnostic molecules suffer from several limitations such as poor solubility in aqueous phase or a lack of specificity, which targets not only the tumour site but also the healthy tissue. As a result, often a high dosage is required to treat the tumour and this, unfortunately, leads to severe side effects.

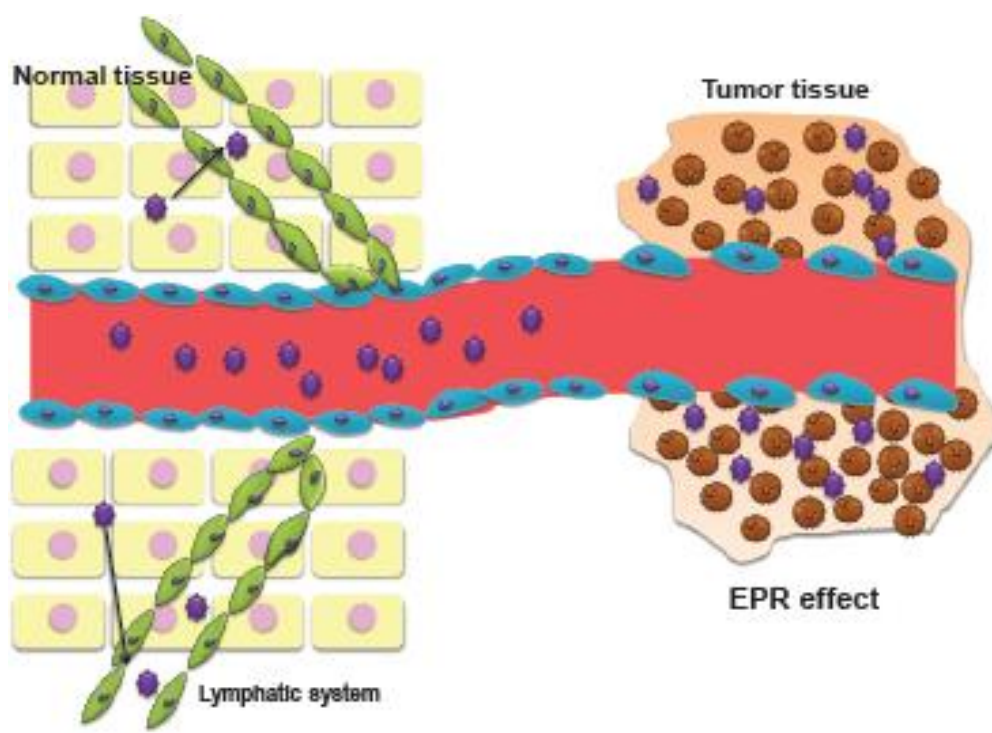


**Figure 1.9** Diagrammatic representation of the EPR effect. Normal blood vessels have surrounding smooth muscle-cell layer with tight cell-cell junctions which macromolecular agents are difficult to extravasate. In contrast, in tumor tissues, blood vessels are always with loose cell-cell junctions, via

which macromolecular agents can escape to tumor tissue. In addition, the defected lymphatic system in tumors leads to the retention of macromolecular agents in tumor tissues.

To overcome these issues, recently, a great attention has been focused on MSNPs which tend, moreover, to naturally reach the tumor sites by a physiological phenomenon called enhanced permeability and retention (EPR) effect (**Figure 1.9**). EPR effect is a phenomenon in which big size exogenous compounds tend to selectively accumulate in tumor tissues, far more than in normal tissues. Moreover, their residence time in the tumor sites is also longer than in the normal ones.

The particles have thus been yet more optimised in order to be the most efficient and most specific possible. Particles with external stimuli-responsive properties have been prepared.<sup>33</sup> Moreover, knowing that the tumor sites show specific physicochemical properties compared to healthy tissues, internal (physiological) stimuli-responsive MSNPs, based on these properties, have been developed.<sup>34</sup> These second class of stimuli-responsive MSNPs are based on either interactions between the payload and the host or on gate systems. In both of the cases, functionalisation with additional molecules either by supramolecular or covalent interactions are needed.

All the systems developed until there showed relative efficiency towards the payload *in vitro* or up to *in vivo* transportation and release. Moreover, these tools were able to more specifically target cancer cells, possibly thanks to surface functionalisation with ligands.

However, the fate of these inorganic materials after performing their function remained uncontrolled for a long time. Indeed, most of these nanoparticles have a size of about 100 nm. In sub-chapter **1.2.1** related to the factors affecting the efficiency of NPs, it was mentioned that particle size of above 6 nm are not excreted through the kidney.<sup>13,14</sup> This lack of clearance leads the 100 nm sized MSNPs to accumulate *in vivo* and thus results in severe side effects. This is now the main reason which impedes the clinical translation of such materials. To overcome this limitation, strategies which consist in synthesizing hybrid organic/inorganic MSNPs are now under investigations. The systems are based on the incorporation of organic cleavable linkers within the particle framework. This linker is responsive to an external or an internal (physiological) stimulus like in the case of the inorganic MSNPs. However, the cleavage of the organic moiety leads to a fast disintegration of the material into fragments small enough to be easily excreted. In this respect, our group as well as Croissant *et al.*

synthesized hybrid organic/inorganic MSNPs based on disulfide functional groups, which are known to undergo a reducing reaction in a reducing agent-rich environment.<sup>35,36</sup> More precisely, the linker used in our group was bis[3-(triethoxysilyl)propyl] disulfide (**Figure 1.10**). The particles have been designed in this way to take advantage of the fact that cancer tissues show a very high concentration of glutathione, which has reducing effect properties, compared to healthy tissues.

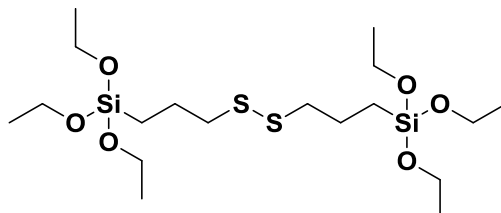


**Figure 1.10** Structure of bis[3-(triethoxysilyl)propyl] disulfide, the reduction-responsive linker incorporated the framework of silica particles in previous studies conducted in our group.

### 1.3 Aim of the thesis

Another physicochemical property which is specific to tumor sites is related to the pH. Indeed, the extracellular matrix of the cancer sites are known to show a low pH of 5.5 compared to that corresponding to the physiological healthy tissues, which is 7.4.<sup>37-40</sup>

*The aim of this thesis is to develop breakable systems able to entrap drugs or biomolecules for therapeutic applications.*

For this purpose, known the numerous advantages of MSNPs and taking advantage of the pH-related physicochemical property of the tumor sites, our strategy consists in developing pH-responsive breakable hybrid organosilica NPs (BMONPs). Such a system is designed based on the incorporation of an organic moiety based on an imine functional group in the particle framework during its synthesis. Imines are known to be pH sensitive. More precisely, the reaction of formation of imines is in constant equilibrium with the reverse reaction, meaning their hydrolysis affording back the carbonyl and the amine groups.<sup>41-46</sup> Nevertheless, in both cases (formation and hydrolysis), the reaction rate can be influenced by the presence of catalysts such as acid/base and imines undergo hydrolysis in acidic medium. More precisely, the imine-based linker is N,N'E/Z,N,N'E/Z)-N,N'-(1,4-phenylenebis(methanylylidene))bis(3-(triethoxysilyl)propan-1-amine) (**Figure 1.11**).

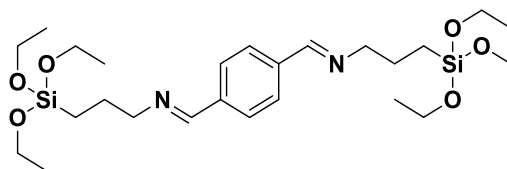


**Figure 1.11** Structure of N,N'E/Z,N,N'E/Z)-N,N'-(1,4-phenylenebis(methanylylidene))bis(3-(triethoxysilyl)propan-1-amine), the pH-cleavable linker incorporated in the framework of silica particles reported in this thesis.

Thus, upon suspension in an acidic environment, due to the imine hydrolysis, BMONPs disintegrate into fragments with a size of about 5-10 nm. The synthesis of the particle is straightforward and occurs in one-pot. Moreover, *in vitro* studies performed with Hs578T, a human breast cancer cell line afford very positive results towards a potent hydrophobic chemotherapeutic agent delivery. The designed system is illustrated in **Figure 1.12**.

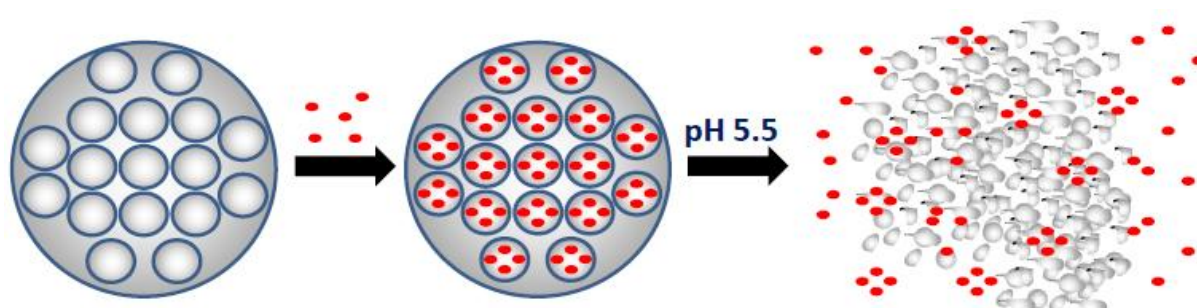


**Figure 1.12** Schematic representation of the designed system, the pH-responsive breakable BMONPs. The red dots correspond to the hydrophobic drug guest.

Another challenge which has recently attracted an important interest in nanomedicine is intracellular delivery of particular proteins for protein or peptide-based nanotherapeutics.<sup>47-49</sup> Nevertheless, the efficient delivery of native, functional proteins or enzymes, in an active conformation to the necessary site of action, still remains a challenge. Under physiological conditions, proteins and peptides tend to undergo degradation by proteolytic enzymes or, in the case of the higher-molecular-weight proteins, may be recognised by neutralising antibodies.<sup>50,51</sup> A possible strategy to overcome these limitations consists in shielding the protein in a nanocapsule, which lacks porosity. This technique provides several advantages such as full protection of the payload and, consequently, its entire stability. Some soft and

hard shells have been developed to deliver proteins or antigens, notably reduction responsive hybrid nanocapsules.<sup>52-54</sup> In our case, having the pH-responsive liner in our hands, we employed it to develop a pH-breakable organosilica nanocapsule for an antibody delivery for cancer treatment.

Furthermore, due to the small size of some drugs or other payload molecules as compared to that of the pores of MSNPs, many drug delivery systems (DDS) based on MSNPs suffer from leakage issues leading to premature release and thus severe side effects.<sup>55,56</sup> Indeed, in case of instable interactions with the pore walls, the payload tends to leak out. Some strategies based on “gatekeeper” systems exist to circumvent this issue; however, in some cases, such systems can induce undesired cytotoxicity.<sup>57-63</sup> To overcome these limitations, the novel systems based on non-porous nanocapsules are attracting a great deal of attention. Such techniques provide several advantages such as full protection of the payload and, consequently, its entire stability, but also the prevention of premature release along the entire circulation of the system until reaching its target *in vivo*.<sup>8</sup> From our side, we prepared the same system as we developed for the antibody delivery to deliver herein a potent chemotherapeutic agent into cancer cells. HeLa cell line was used as model. HeLa is a cell line derived from a woman cervix cancer. The designed nanocapsule system is illustrated in **Figure 1.13**.

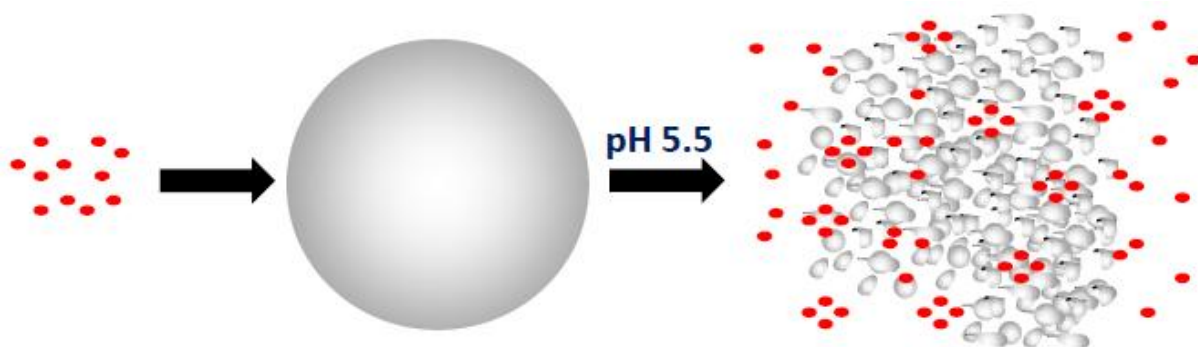


**Figure 1.13** Schematic representation of the designed system of pH-responsive and breakable silica nanocapsule. The red dots correspond to the drug guest.

Based on these two project axes, this thesis has been conducted following three main objectives.

- Development of pH-breakable mesoporous organosilica nanoparticles and breakability evidences.

- Preparation of pH-breakable nanocapsules for the encapsulation of bioactive molecules and kinetic studies of the payload release.
- Studies of the *in vitro* behaviour of the developed nanoparticles towards healthy (MCF-10) and cancer cells (Hs 578T and HeLa).

## 1.4 References

1. Freitas, R. A. What is nanomedicine? *Nanomedicine Nanotechnol. Biol. Med.* **1**, 2–9 (2005).
2. Sanvicens, N. & Marco, M. P. Multifunctional nanoparticles – properties and prospects for their use in human medicine. *Trends Biotechnol.* **26**, 425–433 (2008).
3. De Jong, W. H. & Borm, P. J. Drug delivery and nanoparticles: Applications and hazards. *Int. J. Nanomedicine* **3**, 133–149 (2008).
4. Werengowska-Ciećwierz, K., Wiśniewski, M., Terzyk, A. P. & Furmaniak, S. The Chemistry of Bioconjugation in Nanoparticles-Based Drug Delivery System. *Adv. Condens. Matter Phys.* **2015**, 1–27 (2015).
5. Whitesides, G. Nanoscience, Nanotechnology, and Chemistry. *Small* **1**, 172–179 (2005).
6. Kawasaki, E. S. & Player, A. Nanotechnology, nanomedicine, and the development of new, effective therapies for cancer. *Nanomedicine Nanotechnol. Biol. Med.* **1**, 101–109 (2005).
7. Koo, O. M., Rubinstein, I. & Onyuksel, H. Role of nanotechnology in targeted drug delivery and imaging: a concise review. *Nanomedicine Nanotechnol. Biol. Med.* **1**, 193–212 (2005).
8. Sahoo, S. K., Parveen, S. & Panda, J. J. The present and future of nanotechnology in human health care. *Nanomedicine Nanotechnol. Biol. Med.* **3**, 20–31 (2007).
9. Kim, K. Y. Nanotechnology platforms and physiological challenges for cancer therapeutics. *Nanomedicine Nanotechnol. Biol. Med.* **3**, 103–110 (2007).
10. Kim, B. Y., Rutka, J. T. & Chan, W. C. Nanomedicine. *N. Engl. J. Med.* **363**, 2434–2443 (2010).
11. Rizzo, L. Y., Theek, B., Storm, G., Kiessling, F. & Lammers, T. Recent progress in nanomedicine: therapeutic, diagnostic and theranostic applications. *Curr. Opin. Biotechnol.* **24**, 1159–1166 (2013).
12. Shin, S., Song, I. & Um, S. Role of Physicochemical Properties in Nanoparticle Toxicity. *Nanomaterials* **5**, 1351–1365 (2015).
13. Soo Choi, H. *et al.* Renal clearance of quantum dots. *Nat. Biotechnol.* **25**, 1165–1170 (2007).
14. Alexis, F., Pridgen, E., Molnar, L. K. & Farokhzad, O. C. Factors Affecting the Clearance and Biodistribution of Polymeric Nanoparticles. *Mol. Pharm.* **5**, 505–515 (2008).

15. Sun, J. *et al.* Core-controlled polymorphism in virus-like particles. *Proc. Natl. Acad. Sci.* **104**, 1354–1359 (2007).
16. Koudelka, K. J. & Manchester, M. Chemically modified viruses: principles and applications. *Curr. Opin. Chem. Biol.* **14**, 810–817 (2010).
17. Yildiz, I., Shukla, S. & Steinmetz, N. F. Applications of viral nanoparticles in medicine. *Curr. Opin. Biotechnol.* **22**, 901–908 (2011).
18. Pattni, B. S., Chupin, V. V. & Torchilin, V. P. New Developments in Liposomal Drug Delivery. *Chem. Rev.* **115**, 10938–10966 (2015).
19. Rao, J. P. & Geckeler, K. E. Polymer nanoparticles: Preparation techniques and size-control parameters. *Prog. Polym. Sci.* **36**, 887–913 (2011).
20. Kesharwani, P., Jain, K. & Jain, N. K. Dendrimer as nanocarrier for drug delivery. *Prog. Polym. Sci.* **39**, 268–307 (2014).
21. Junghanns, J.-U. A. & Müller, R. H. Nanocrystal technology, drug delivery and clinical applications. *Int. J. Nanomedicine* **3**, 295 (2008).
22. Lu, F. *et al.* Advances in Bioapplications of Carbon Nanotubes. *Adv. Mater.* **21**, 139–152 (2009).
23. Horcajada, P. *et al.* Porous metal–organic-framework nanoscale carriers as a potential platform for drug delivery and imaging. *Nat. Mater.* **9**, 172–178 (2010).
24. Vallet-Regí, M. & Balas, F. Silica materials for medical applications. *Open Biomed. Eng. J.* **2**, (2008).
25. Stöber, W., Fink, A. & Bohn, E. Controlled growth of monodisperse silica spheres in the micron size range. *J. Colloid Interface Sci.* **26**, 62–69 (1968).
26. de Oliveira, L. F. *et al.* Functionalized Silica Nanoparticles As an Alternative Platform for Targeted Drug-Delivery of Water Insoluble Drugs. *Langmuir* **32**, 3217–3225 (2016).
27. Hench, L. L. The story of Bioglass®. *J. Mater. Sci. Mater. Med.* **17**, 967–978 (2006).
28. Tang, F., Li, L. & Chen, D. Mesoporous Silica Nanoparticles: Synthesis, Biocompatibility and Drug Delivery. *Adv. Mater.* **24**, 1504–1534 (2012).
29. Li, W., Zhang, M., Zhang, J. & Han, Y. Self-assembly of cetyl trimethylammonium bromide in ethanol-water mixtures. *Front. Chem. China* **1**, 438–442 (2006).
30. Martines, M. U. *et al.* Hexagonal mesoporous silica nanoparticles with large pores and a hierarchical porosity tested for HPLC. *Comptes Rendus Chim.* **8**, 627–634 (2005).
31. Kresge, C. T., Leonowicz, M. E., Roth, W. J., Vartuli, J. C. & Beck, J. S. Ordered mesoporous molecular sieves synthesized by a liquid-crystal template mechanism. *Nature* **359**, 710–712 (1992).
32. Lin, Y.-S., Hurley, K. R. & Haynes, C. L. Critical Considerations in the Biomedical Use of Mesoporous Silica Nanoparticles. *J. Phys. Chem. Lett.* 364–374 (2012). doi:10.1021/jz2013837
33. Hocine, O. *et al.* Silicalites and Mesoporous Silica Nanoparticles for photodynamic therapy. *Int. J. Pharm.* **402**, 221–230 (2010).
34. Meng, H. *et al.* Engineered Design of Mesoporous Silica Nanoparticles to Deliver Doxorubicin and P-Glycoprotein siRNA to Overcome Drug Resistance in a Cancer Cell Line. *ACS Nano* **4**, 4539–4550 (2010).

35. Croissant, J. *et al.* Biodegradable Ethylene-Bis(Propyl)Disulfide-Based Periodic Mesoporous Organosilica Nanorods and Nanospheres for Efficient In-Vitro Drug Delivery. *Adv. Mater.* **26**, 6174–6180 (2014).
36. Maggini, L. *et al.* Breakable mesoporous silica nanoparticles for targeted drug delivery. *Nanoscale* **8**, 7240–7247 (2016).
37. Montcourrier, P., Silver, I., Farnoud, R., Bird, I. & Rochefort, H. Breast cancer cells have a high capacity to acidify extracellular milieu by a dual mechanism. *Clin. Exp. Metastasis* **15**, 382–392 (1997).
38. Glunde, K. *et al.* Extracellular Acidification Alters Lysosomal Trafficking in Human Breast Cancer Cells. *Neoplasia N. Y. N* **5**, 533–545 (2003).
39. Iessi, E., Marino, M. L., Lozupone, F., Fais, S. & De Milito, A. Tumor acidity and malignancy: novel aspects in the design of anti-tumor therapy. *Cancer Ther* **6**, 55–66 (2008).
40. Kato, Y. *et al.* Acidic extracellular microenvironment and cancer. *Cancer Cell Int.* **13**, 89–89 (2013).
41. Amaral, L. do, Sandstrom, W. A. & Cordes, E. H. Some Aspects of Mechanism and Catalysis for Carbonyl Addition Reactions1. *J. Am. Chem. Soc.* **88**, 2225–2233 (1966).
42. Willi, A. V. Kinetik der Hydrolyse von Benzalanilin II: Die pH-Abhängigkeit der Reaktionsgeschwindigkeit in ungepufferten Lösungen und die Rolle der Aminoalkohol-Zwischenstufe. *Helvetica Chimica Acta* 1193–1203 (1956).
43. Behme, M. T. A. & Cordes, E. H. Secondary Valence Force Catalysis. I. Kinetics of Schiff Base Hydrolysis in the Presence of Micelle-Forming Detergents1. *J. Am. Chem. Soc.* **87**, 260–265 (1965).
44. Reeves, R. L. On the mechanism, substituent effects, and intramolecular catalysis in Schiff base hydrolysis. *J. Org. Chem.* **30**, 3129–3135 (1965).
45. Prabhu, D. V. & Laxmeshwar, N. B. Kinetics and Reaction Mechanism of Hydrolysis of N-Salicylidene-m-Methyl Aniline Spectrophotometrically. *Asian Journal of Chemistry* 99–106 (1994).
46. Kirdant, A. S., Magar, B. K. & Chondhekar, T. K. Kinetic study of hydrolysis of N-salicylidene-m-methyl aniline spectrophotometrically.
47. Zhou, H. *et al.* Generation of Induced Pluripotent Stem Cells Using Recombinant Proteins. *Cell Stem Cell* **4**, 381–384 (2009).
48. Schwarze, S. R., Ho, A., Vocero-Akbani, A. & Dowdy, S. F. In Vivo Protein Transduction: Delivery of a Biologically Active Protein into the Mouse. *Science* **285**, 1569 (1999).
49. Shah, A. M. & Mann, D. L. In search of new therapeutic targets and strategies for heart failure: recent advances in basic science. *The Lancet* **378**, 704–712
50. Fu, K., Klibanov, A. M. & Langer, R. Protein stability in controlled-release systems. *Nat Biotech* **18**, 24–25 (2000).
51. Jiskoot, W. *et al.* Protein Instability and Immunogenicity: Roadblocks to Clinical Application of Injectable Protein Delivery Systems for Sustained Release. *J. Pharm. Sci.* **101**, 946–954

52. Yuba, E. *et al.* The application of pH-sensitive polymer-lipids to antigen delivery for cancer immunotherapy. *Biomaterials* **34**, 5711–5721 (2013).
53. Yuba, E., Harada, A., Sakanishi, Y., Watarai, S. & Kono, K. A liposome-based antigen delivery system using pH-sensitive fusogenic polymers for cancer immunotherapy. *Biomaterials* **34**, 3042–3052 (2013).
54. Prasetyanto, E. A. *et al.* Breakable Hybrid Organosilica Nanocapsules for Protein Delivery. *Angew. Chem. Int. Ed.* **55**, 3323–3327 (2016).
55. Slowing, I., Viveroescoto, J., Wu, C. & Lin, V. Mesoporous silica nanoparticles as controlled release drug delivery and gene transfection carriers ☆. *Adv. Drug Deliv. Rev.* **60**, 1278–1288 (2008).
56. Sun, R., Wang, W., Wen, Y. & Zhang, X. Recent Advance on Mesoporous Silica Nanoparticles-Based Controlled Release System: Intelligent Switches Open up New Horizon. *Nanomaterials* **5**, 2019–2053 (2015).
57. Slowing, I. I., Trewyn, B. G., Giri, S. & Lin, V. S.-Y. Mesoporous Silica Nanoparticles for Drug Delivery and Biosensing Applications. *Adv. Funct. Mater.* **17**, 1225–1236 (2007).
58. Sun, X. Mesoporous silica nanoparticles for applications in drug delivery and catalysis. (2012).
59. Cui, Y., Dong, H., Cai, X., Wang, D. & Li, Y. Mesoporous Silica Nanoparticles Capped with Disulfide-Linked PEG Gatekeepers for Glutathione-Mediated Controlled Release. *ACS Appl. Mater. Interfaces* **4**, 3177–3183 (2012).
60. Palanikumar, L., Choi, E. S., Cheon, J. Y., Joo, S. H. & Ryu, J.-H. Noncovalent Polymer-Gatekeeper in Mesoporous Silica Nanoparticles as a Targeted Drug Delivery Platform. *Adv. Funct. Mater.* **25**, 957–965 (2015).
61. Hu, C. *et al.* Tannin as a gatekeeper of pH-responsive mesoporous silica nanoparticles for drug delivery. *RSC Adv* **5**, 85436–85441 (2015).
62. Li, Q.-L. *et al.* Mesoporous Silica Nanoparticles Coated by Layer-by-Layer Self-assembly Using Cucurbit[7]uril for in Vitro and in Vivo Anticancer Drug Release. *Chem. Mater.* **26**, 6418–6431 (2014).
63. Mondragón, L. *et al.* Enzyme-Responsive Intracellular-Controlled Release Using Silica Mesoporous Nanoparticles Capped with  $\epsilon$ -Poly- L -lysine. *Chem. - Eur. J.* **20**, 5271–5281 (2014).

# **Chapter 2**

## **pH-Breakable hybrid mesoporous silica nanoparticle: synthesis, characterisation and breakability studies**

### **Abstract**

The pH-responsive breakable silica nanoparticle (BMONP) was synthesized via sol-gel synthesis method with a mixture of tetraethyl orthosilicate (TEOS) and a readily synthesized diiminosilane linker in the presence of ammonia and butanol, with a TEOS/diiminosilane molar ratio of 5:3. Morphological characterisation of the hybrid materials was first performed by scanning and transmission electron microscopy (SEM and TEM respectively). The images display the spherical morphology of the material with a good degree of monodispersity of the particles size. A similar size was measured by dynamic light scattering on a suspension of the particles in phosphate buffered solution. The nitrogen adsorption-desorption isotherms of the sample exhibited characteristic properties of mesoporous material having cylindrical type mesostructures. Furthermore, nitrogen scan performed with X-ray photoelectron spectroscopy also exhibits a binding energy value attributed to an imine bond. To evaluate the breaking kinetics of BMONP through the hydrolysis of the imine group, the particles were suspended in acidic media (pH = 5.5). Aldehyde release resulting from the hydrolysis of the imine was monitored by proton nuclear magnetic resonance spectroscopy. The release profile demonstrated a fast breaking of the particle. Furthermore, BMONP was functionalised with a dye by its covalent linkage on the particle framework. The breaking kinetics in acidic conditions was followed by analysing the supernatant solution with a fluorimeter, monitoring the emission of released dye. The dye release profile followed the same tendency as with that of the aldehyde. This behaviour is in close agreement with a

morphology change evidenced by SEM and TEM analyses of the sample. As control experiment, the particles were suspended in pH 7.4 solution and, from the release profile, we can see that most of the particles did not break apart. Also, in an analogous manner, we prepared and analysed non-breakable particles which lack the imine moieties. They show very similar size and morphology but do not display any degradation in the same acidic medium and neither in the neutral pH one.

## 2.1 Introduction

Due to the low pH in the tumour sites (see **chapter 1**), many pH-responsive mesoporous silica nanoparticles have been reported for controlled drug delivery into cancerous tissues. He *et al.* have reported the use of mesoporous silica nanoparticles-based multi-drug delivery systems for overcoming multi-drug resistance.<sup>1</sup> They have developed a type of pH-responsive nano multi-drug delivery systems (nano-MDDSs) with uniform particle size ( $100\pm 13$  nm) by *in situ* co-self-assembly among water insoluble anti-cancer drug (doxorubicin, DOX), surfactant micelles (CTAB) and silicon precursor forming drugs/surfactant micelles-co-loaded mesoporous silica nanoparticles (drugs@-micelles@MSNs or DOX@CTAB@MSNs) via a micelles-MSNs self-assembly mechanism. The nano-MDDS DOX@CTAB@MSNs have a highly precise pH-responsive drug release behaviour both *in vitro* and *in vivo*. The drug is released in a sustained way within cancer cells through the ion exchanging interaction between  $H^+/H_3O^+$  and positively charged drugs@micelles. Several other investigations have also been reported on the use of organic molecules as gatekeepers on the pore entrance of mesoporous silica nanoparticles which are able to keep the payload within the mesopores until reaching the tumour sites. In 2010, Meng *et al.* reported a spherical ( $\approx 100$  nm in diameter) mesoporous silica nanoparticle delivery system based on the function of  $\beta$ -cyclodextrin ( $\beta$ -CD) nanovalves which are responsive to the endosomal acidic conditions in human differentiated myeloid (THP-1) and squamous carcinoma (KB-31) cell lines.<sup>2</sup> The nanoparticle pores have been covalently functionalised with *N*-methylbenzimidazole, which, under physiological pH (7.4), interacts non-covalently with  $\beta$ -cyclodextrin to block the pores. Under acidic media, the interaction is disrupted due to protonation on the imidazole enabling the release of the payload. The pores ( $\approx 2$  nm) are large enough to contain common dyes and anticancer drugs, yet small enough to be blocked by macrocyclic organic molecules, such as the cyclodextrins. Yuan *et al.* have dealt with Poly(acrylic acid) grafted mesoporous silica nanoparticles (PAA-MSNs) by the amidation between PAA homopolymer and amino group functionalised spherical MSNs of about 150 nm in diameter.<sup>3</sup> Doxorubicin hydrochloride was chosen as a model drug

which, at pH 7.4, is positively charged and binds with the negatively charged PAA to form a DOX@PAA-MSN complex by electrostatic interaction. With the decrease of pH (6.8 and 5.6), most of the PAA is protonated, which would lead to the dissociation of the electrostatic interaction between PAA and DOX, so that most of the incorporated DOX is released. The drug release rate of DOX@PAA-MSN is pH dependent and increases with the decrease of pH. Yao *et al.* have developed a dual pH-responsive mesoporous silica nanoparticle for combination of chemotherapy and photodynamic therapy which can respond to the cancer extracellular and intercellular pH stimuli.<sup>4</sup> The system has been prepared by grafting histidine onto the silica surface and an acid sensitive PEGylated tetraphenylporphyrin zinc (Zn-Por-CA-PEG) has been used as a gatekeeper to block the nanopores of MSNs by the metallo-supramolecular-coordinated interaction between Zn-Por and histidine. This gatekeeper is stable enough to prevent the loaded drug from leaching out in healthy tissue. However, at cancer extracellular pH ( $\approx 6.8$ ), the conjugated acid sensitive cis-aconitic anhydride (CA) between Zn-Por and PEG cleaved and the surface of Zn-Por is amino positively charged to facilitate cell internalization. Furthermore, the metallo-supramolecular-coordination disassemble in intracellular acidic microenvironments ( $\approx 5.3$ ) to release the carried drug and Zn-Por due to the removal of the gatekeeper.

However, from the best of our knowledge, a pH-responsive mesoporous silica nanoparticle on which the responsive system is incorporated within the intrinsic particle framework has not yet been reported.

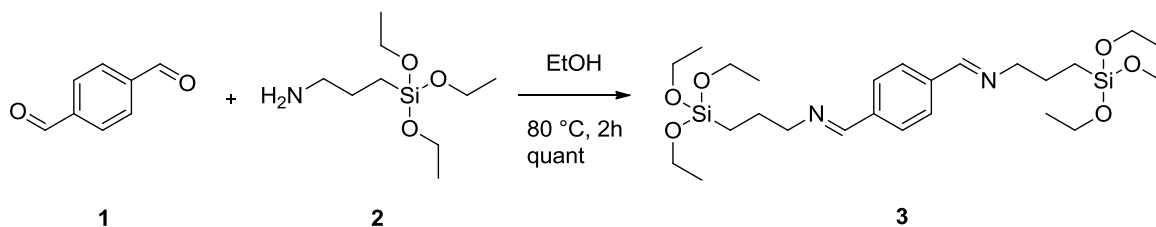
*In the present chapter, we report the synthesis of a pH-breakable hybrid mesoporous silica nanoparticle which is not only pH-responsive but also what we call pH-breakable.*

Such a particle specifically responds to low pH to trigger its fragmentation into small pieces. This technology can be developed by incorporating an organic linker based on a pH-cleavable function such as esters, acetals or amides in the particle framework. Imines are also known to be pH sensitive. More precisely, the reaction of formation of imines is

in constant equilibrium with the reverse reaction, meaning their hydrolysis, affording back the carbonyl and the amine groups.<sup>5-10</sup> Nevertheless, in both cases (formation and hydrolysis), the reaction rate can be influenced by the presence of catalysts such as metal<sup>11</sup> or acid/base<sup>5-10</sup>. The presence of substituents on the adjacent positions can also affect the reaction rate of an imine hydrolysis. Thus, in both acidic and basic conditions, increasing the electron-withdrawing power of the substituent will result in the increase of the reaction rate.<sup>12</sup> Considering those properties, we have chosen (N,N'E/Z,N,N'E/Z)-N,N'-(1,4-phenylenebis(methanylylidene))bis(3-(triethoxysilyl)propan-1-amine) **3** as the organic linker in order to have a hydrolysis in a controllable rate.

## 2.2 Synthesis and characterisation of the diiminosilane linker

The first step to prepare the pH responsive breakable silica nanoparticle is the synthesis of (N,N'E/Z,N,N'E/Z)-N,N'-(1,4-phenylenebis(methanylylidene))bis(3-(triethoxysilyl)propan-1-amine) **3**, which, from now, we call as diiminosilane (**Scheme 2.1**). The linker has been designed to be pH-responsive by the introduction of two Schiff base functional groups. To obtain this compound, according to the methods reported by Bhaumik's group<sup>13</sup>, terephthalaldehyde **1** is reacted with 3-(triethoxysilyl)propan-1-amine **2**, commonly known as 3-Aminopropyltriethoxysilane (APTES), in dry ethanol at 80 °C (reflux) over 2 hours to afford the desired product as a yellowish limpid oil in quantitative yield.



**Scheme 2.1** Synthesis of the pH-cleavable diiminosilane linker.

A characterisation by attenuated total reflectance Fourier transform infrared spectroscopy (ATR-FTIR) shows an intense band corresponding to the imine bond at  $\sim 1648 \text{ cm}^{-1}$ , while the carbonyl of the starting aldehyde displays a strong signal at  $\sim 1678 \text{ cm}^{-1}$  (see **Figure 2.1**). Additionally, the silane groups are very well evidenced with an intense broad band at  $1200\text{-}1100 \text{ cm}^{-1}$ . Furthermore, the proton nuclear magnetic resonance  $^1\text{H}$  NMR spectroscopy analysis shows the high purity of the organic linker (**Figure 2.2**). In particular, we can notice the appearance of the imine peak at 8.28 ppm which replaced the carbonyl signal of the aldehyde used as starting material at 10.23 ppm. We also can see the presence of the signals corresponding to the alkyl chain between 0.7 and 3.8 ppm.

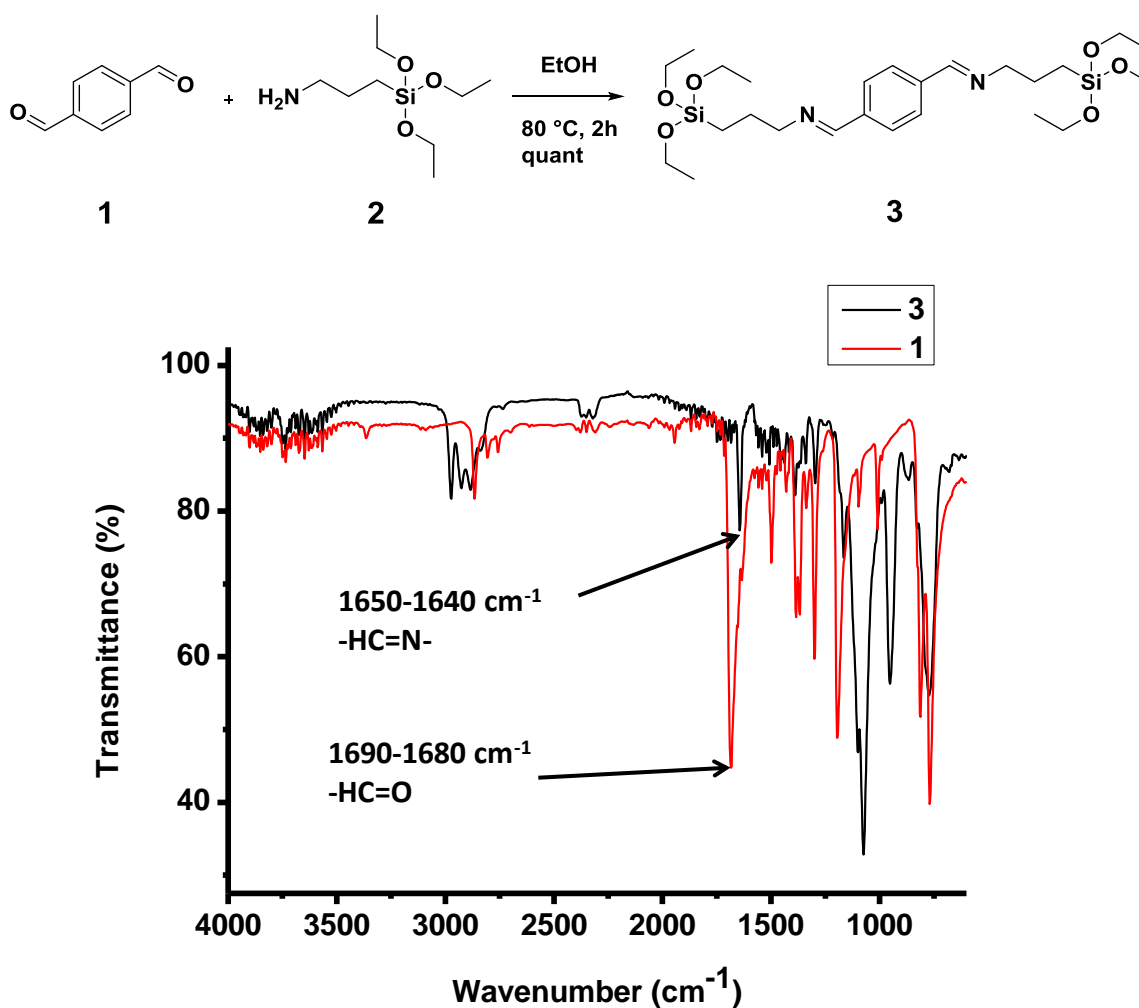


**Figure 2.1** Superimposition of the ATR-FTIR spectra of terephthalaldehyde **1** used as starting material and the diiminosilane linker **3**.

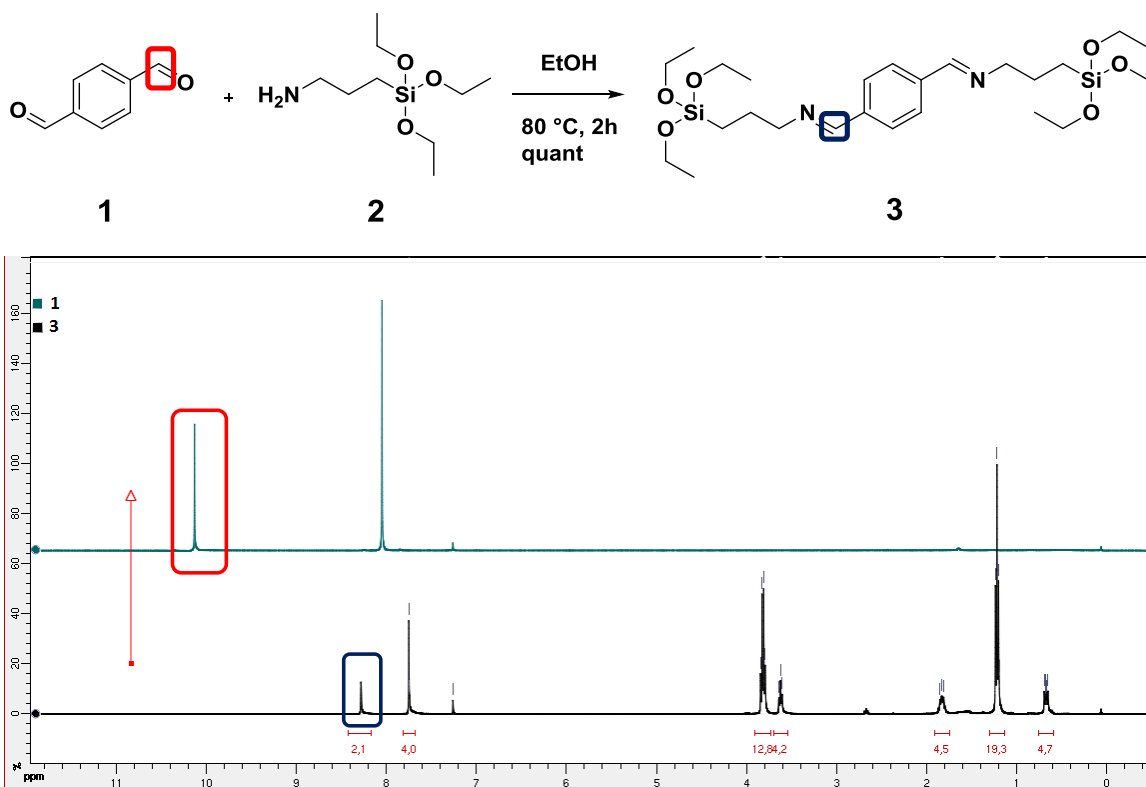


**Figure 2.2** Superimposition of the <sup>1</sup>H NMR spectra of terephthalaldehyde **1** used as starting material and the diiminosilane linker **3** in CDCl<sub>3</sub>.

### 2.3 Synthesis and characterisation of the hybrid mesoporous silica nanoparticle

The pH-breakable mesoporous organosilica nanoparticle (BMONP) has been synthesized via sol-gel synthesis method<sup>14–18</sup> with a mixture of tetraethyl orthosilicate (TEOS) and the diiminosilane linker in the presence of ammonia and butanol (**Figure 2.3A**); with a TEOS/diiminosilane molar ratio of 5:3. This ratio is one of those possible to ensure that the particle will break properly in controllable time. Hexadecyltrimethylammonium bromide also known as cetyltrimethylammonium bromide (CTAB) serves as surfactant template. The reaction occurs at room temperature over 1 day and, after removing the surfactant by Soxhlet method and drying in the ambient air, the particle is obtained in a white powder aspect.

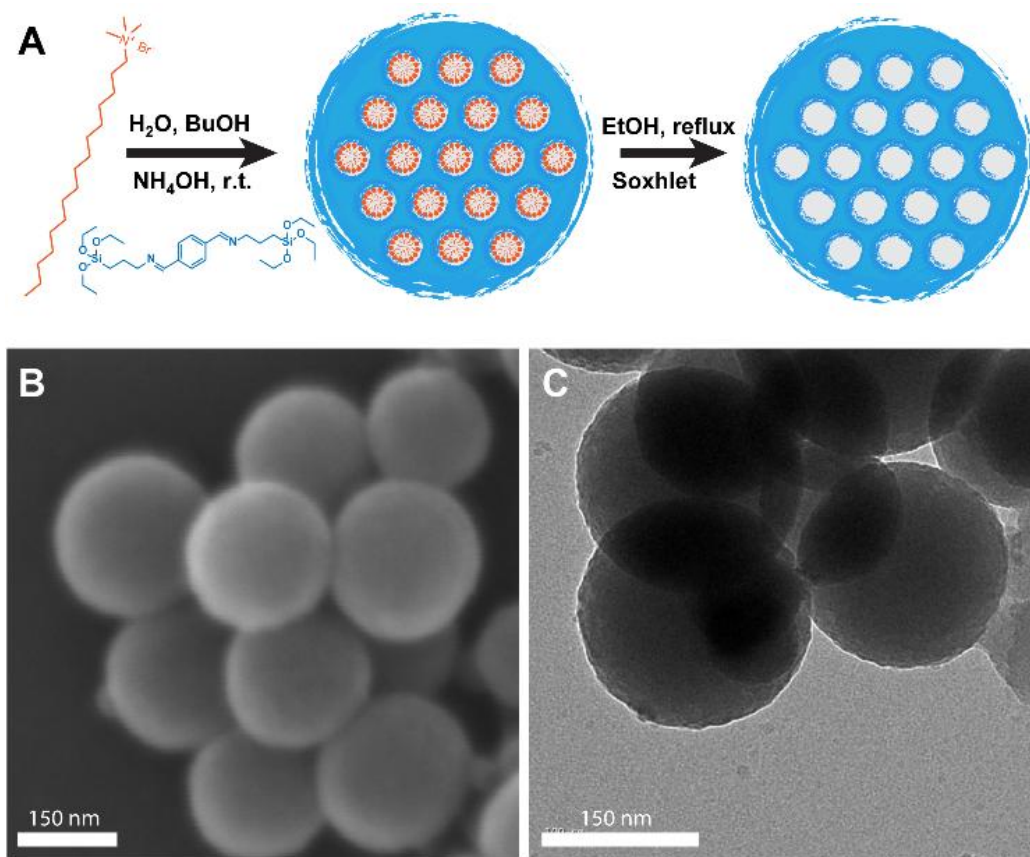


**Figure 2.3** (A) Representative scheme of the synthesis of BMONPs. (B) SEM and (C) TEM pictures of BMONPs.

Morphological characterisation of the hybrid materials has first been performed by scanning and transmission electron microscopy (SEM and TEM) (**Figure 2.3B and C**). The images display the spherical morphology of the material with a good degree of monodispersity of the particles size with an average diameter of 150 nm. A similar diameter size (165 nm) is determined by dynamic light scattering (DLS) measurements on a suspension of the particles in water (**Figure 2.4**).

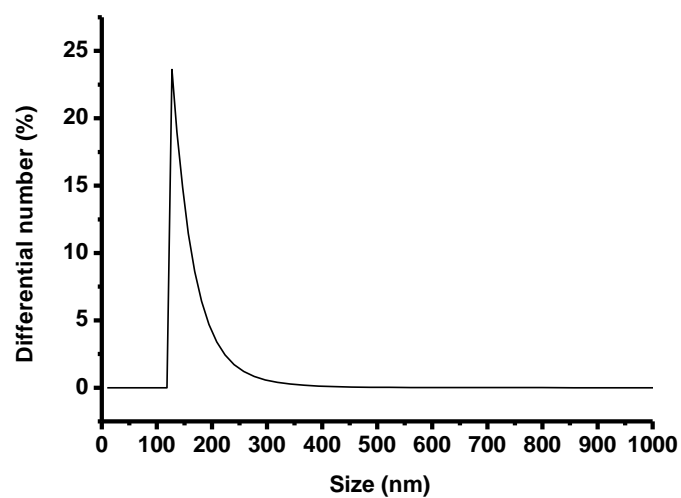


**Figure 2.4** DLS size number distribution of BMONPs. The calculated average size is  $159.1 \pm 41.2$  nm.

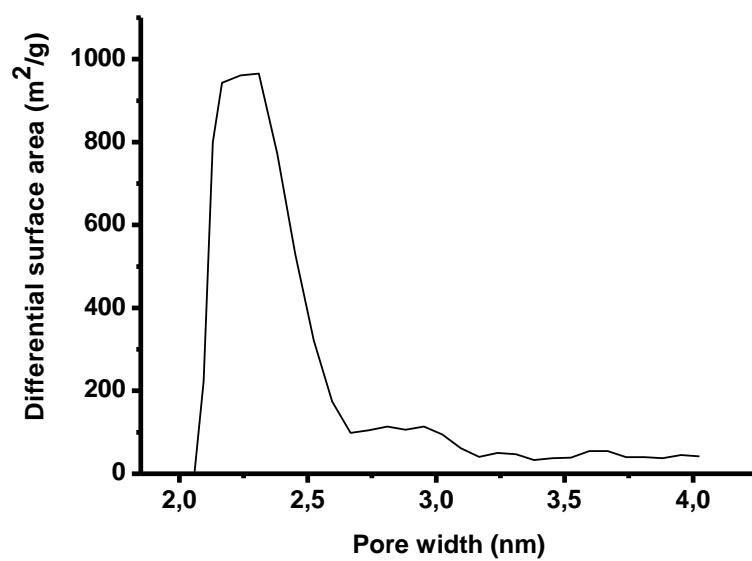


**Figure 2.5 (A)** Pore size distribution of BMONP. The experiment was carried with N<sub>2</sub> adsorption/desorption technique.

The nitrogen (N<sub>2</sub>) adsorption–desorption isotherms of the sample exhibit well-defined type IV features with H1-type hysteresis loops, which is characteristic for mesoporous materials having cylindrical type mesostructures. The average pore size of this mesoporous silica is about 2.3 nm<sup>19–24</sup> (**Figure 2.5**).

A spectrum obtained by energy dispersive X-ray (EDX) shows the presence of all the atoms composing the BMONPs, i.e. silicon, oxygen, carbon and nitrogen (experiment performed under vacuum) (**Figure 2.6**).

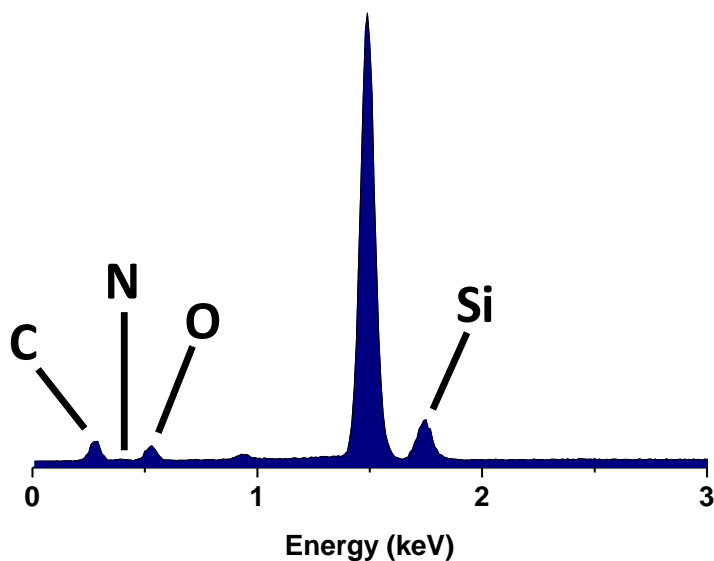


**Figure 2.6** EDX spectrum of BMONP.

Furthermore, a survey obtained with X-ray photoelectron spectroscopy (XPS) also exhibits binding energy values attributed to bonds implying these elements (**Figure 2.7A**) (experiment performed under vacuum). As in the case of the diiminosilane molecule, a characterisation of the material by ATR-FTIR evidences the presence of a silica network at 1200–1100 cm<sup>-1</sup> as well as an imine bond at ~ 1648 cm<sup>-1</sup> (**Figure 2.8A, B**). More interestingly, an elemental scan on the nitrogen atom confirmed the observation done with ATR-FTIR regarding the imine bond, knowing that the binding energy value

attributed to the bond implying this element is 398.57 eV, which corresponds to nitrogen of an imine bond (**Figure 2.7B and Table 2.1**).<sup>25–28</sup>

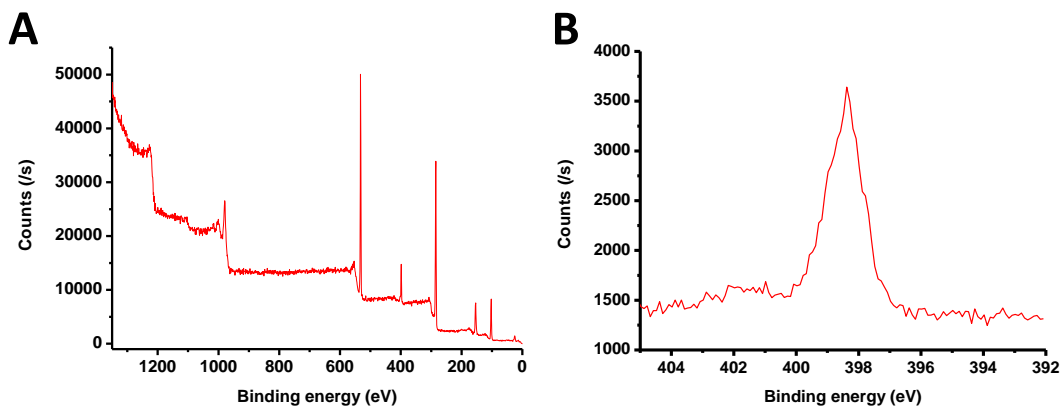


**Figure 2.7.** XPS analyses of BMONPs: (A) Survey of the elements and (B) Nitrogen elemental scan. The experiment has been performed under high vacuum.

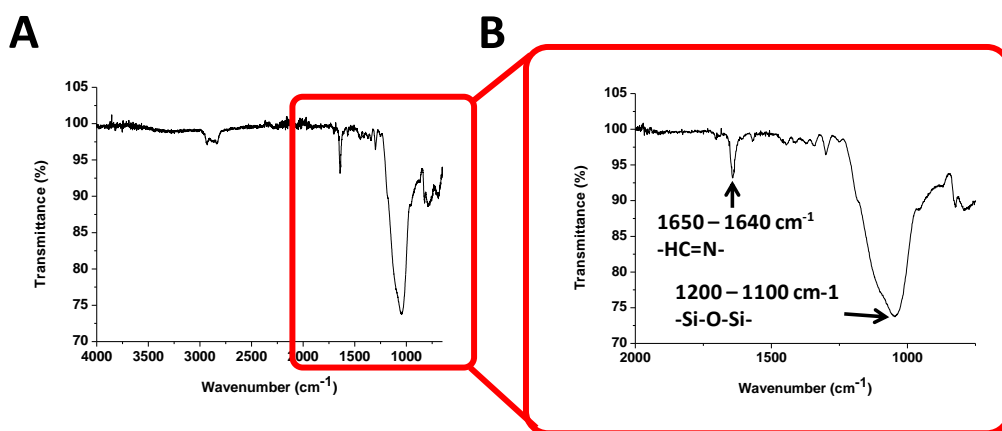


**Figure 2.8** (A) ATR-FTIR spectrum of BMONP and (B) a zoom made on a part of the wavenumber axis.

Zeta potential measurements performed in phosphate saline solution buffered at pH 7.4 reveals a current value of  $-6.75$  mV. This data means that the surface of BMONP is slightly negatively charged due to the presence of  $-\text{Si-O}^-$  groups. This latter is due to the

deprotonation of silanol groups (R-Si-OH) present on the surface of the material at pH 7.4. It is noteworthy to understand that the pKa of silicic acid in the monomer form (Si(OH)<sub>4</sub>) varies between 9.5 and 10.7.<sup>29</sup> This means that, in this pH range, the acid will be present in equilibrium with the conjugated base as illustrated in **Figure 2.9**. However, when incorporated in an oligomer form, such as particles, the pKa of this acid drops to 6.8 and, furthermore, the acid is present as a silanol (R-Si-OH).<sup>29</sup> Consequently, at pH 7.4, the equilibrium will favour the formation of the conjugated base.

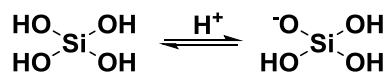


**Figure 2.9** Equilibrium between the acid and the conjugated base of silicic acid.

The question is now about the percentage of imine bonds inserted into the silica framework.

*Has the initial molar ratio of TEOS/diiminosilane linker of 5:3 been maintained during the synthesis?*

**Table 2.1** shows the percentage of each atom composing the material, according to XPS elemental analysis. The extreme right column contains the theoretically calculated percentage of the elements if the ratio of 5:3 had been maintained. When compared to that data, those from XPS analysis correlate very well for each element. Data from EDX measurements (**Table 2.2**) exhibits the same observations. All these results suggest that the initial ratio between TEOS and diiminosilane linker has been very well maintained during the synthesis.

**Table 2.1** Atomic theoretically calculated and experimental percentages of the elements composing BMONPs with related binding energy. Experimental data obtained from XPS

| <b>Element</b> | <b>Binding Energy (eV)</b> | <b>Experimental atomic percentage (%)</b> | <b>Calculated atomic percentage (%)</b> |
|----------------|----------------------------|---|---|
| O1s            | 532.36                     | 26.76                                     | 25.32                                   |
| C1s            | 284.8                      | 52.02                                     | 53.16                                   |
| Si2p           | 102.58                     | 12.86                                     | 13.92                                   |
| N1s            | 398.57                     | 8.35                                      | 7.59                                    |

**Table 2.2** Atomic weight percentage of the elements composing BMONPs with the comparison between the atomic theoretically calculated and experimental percentage of those elements. Experimental data obtained from EDX

| <b>Element</b> | <b>Weight percentage (%)</b> | <b>Experimental atomic percentage (%)</b> | <b>Calculated atomic percentage (%)</b> |
|----------------|------------------------------|---|---|
| O              | 31.62                        | 30.16                                     | 25.32                                   |
| C              | 39.32                        | 49.96                                     | 53.16                                   |
| Si             | 21.59                        | 11.73                                     | 13.92                                   |
| N              | 7.47                         | 8.14                                      | 7.59                                    |
| Total          | 100.00                       | 100.00                                    | 99.99                                   |

## **2.4 Kinetic studies of the breakability of the particle**

After synthesizing and characterising the particle with different techniques, their breakability property upon the pH change has been investigated. Four different methods have been considered to characterise this property.

### ***2.4.1 Monitoring by SEM***

The BMONPs have been dispersed in water at pH 5 in order to mimic the pH of the extracellular matrix of a tumour site. In this case, we use normal water instead of a phosphate buffered saline solution. The purpose to use normal water is to obtain a better quality of the images by SEM. The choice of non-saline solution has been done by preparing an aqueous solution of acetic acid. The experiment has been performed over 48h.

As already mentioned in the introductory chapter, one very important point, which needs to be considered when taking a drug or a drug carrier into an animal or a human body is bio stability. This means that, in our case, once introduced in the body, the particle should be very stable and, thus, no premature delivery should occur before reaching the tumour site. The key is, in the one hand, the stability of BMONP towards its breaking upon the circulatory system and, in the other hand, upon a possible internalisation by a healthy cell. For this reason, we have examined the stability of the particle at pH 7 to mimic the physiological medium. As in the case of the experiment performed in acidic medium, the choice of water instead of a saline solution buffered at pH 7.4 is preferred for the quality of the images by SEM.

To compare our system to the conventional existing one, i.e. MSNP, the experiments cited above have also been performed with such a particle. Furthermore, to minimise the aggregation of the particles, all the samples are vigorously stirred.

**Figure 2.10** illustrates the aspect of BMONPs and MSNPs upon dispersion in acidic medium over 48 hours, compared to the one upon dispersion in a neutral medium. On this figure, we can see that, when dispersed in aqueous medium at pH 5, the BMONPs have a well-defined spherical shape of about 150 nm in diameter at time 0. However, after 48 hours of dispersion, these particles are no more identifiable, only presenting an amorphous layer of silica. Nevertheless, when they are dispersed in neutral pH water, the shape and size are well maintained all along the experiment duration. Regarding the

MSNPs, they kept their original shape and  $\approx 100$  nm size from the beginning to the end of the experiment in acidic medium as well as in the neutral one.

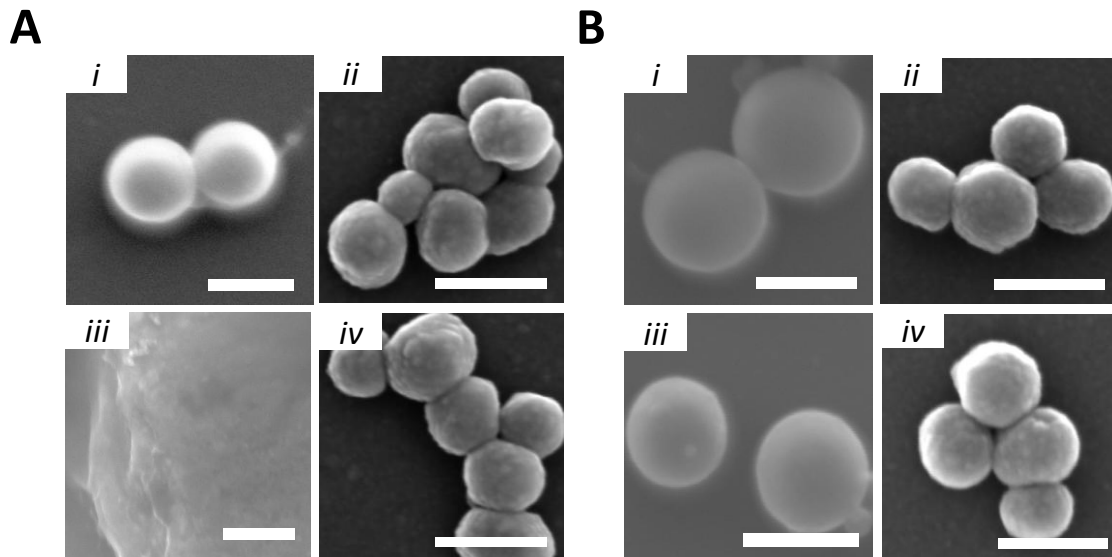


**Figure 2.10.** Breakability and stability studies of the particles monitored by SEM. **(A)** Upon dispersion in aqueous solution at pH 5; at time 0: BMONPs (*i*), MSNPs (*ii*); at time 2d: BMONPs (*iii*), MSNPs (*iv*). **(B)** Upon dispersion in water at pH 7; at time 0: BMONPs (*i*), MSNPs (*ii*); at time 2d: BMONPs (*iii*), MSNPs (*iv*). Scale bar: 200 nm

The breaking process of BMONPs in acidic medium has been studied more deeply by a kinetic method, monitoring at the beginning, 15 minutes, 1 hour, 1 day and 2 days of dispersion (**Figure 2.11**). In this study, we observe that after only 15 minutes of dispersion, the particle shape changes already. It is no more spherical but rather exhibits random shapes. However, the size of the particle is relatively similar to the one at time 0, being 100 - 130 nm (**Figure 2.11B**). After 1 hour, the particle becomes smaller ( $\leq 100$  nm) (**Figure 2.11C**). This result suggests that the disintegration process of the material becomes faster and faster. Between times 1 hour and 1 day, the particle breaks into smaller and smaller pieces to reach a size of 10-20 nm (**Figure 2.11D**). It is noteworthy that, at the magnification set to take those pictures ( $500,000\times$ ), the resolution is extremely low, which means that the size and shape of the pieces observed here are of a

relatively low accuracy. After 2 days of incubation, there is no more piece observed but only a layer of amorphous silica (**Figure 2.11E**), which suggests that the entire particle has been destroyed.

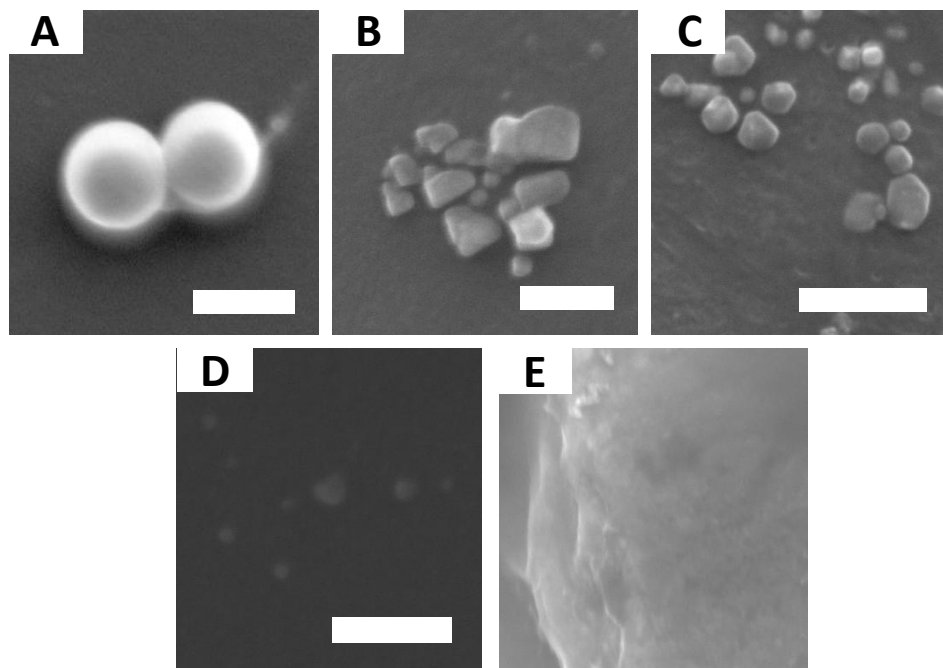


**Figure 2.11 SEM monitoring of the kinetic study of BMONP breaking.** SEM images of BMONPs upon dispersion in an aqueous solution at pH 5 over (A) 0 min, (B) 15 min, (C) 1h, (D) 1d and (E) 2d. Scale bar = 200 nm.

#### ***2.4.2 Monitoring by TEM***

The same conditions as in the case of SEM monitoring have been used to verify the breakability property of BMONP in acidic medium and its stability in neutral pH medium, including the stirring speed. Still like with the SEM technique, the stability of MSNP has been studied. However, the study on this latter has been performed only in acidic medium because it has been assumed that if those particles are stable in acidic medium, this would suggest that they are also in a neutral pH one.

*After 2 days of dispersion in aqueous acidic medium, only very little fragments of size below 10 nm are observed, in addition to some layers of likely amorphous silica.*

On the one hand, on **Figure 2.12Ai**, we can clearly see that, at time 0, BMONPs have a well-defined spherical shape with a diameter size of about 150 nm. Then after 2 days of dispersion in aqueous acidic medium, only very little fragments of about 5 nm or less in size are observed (**Figure 2.12Aiii, yellow arrows**), in addition to some layers of likely amorphous silica (**Figure 2.12Aiii, green boxes**), as already observed in SEM. One very important observation to point out in this result is the size of the fragments obtained due to the particles breaking. In the introductory chapter, it has been mentioned that, to undergo a fast renal clearance, the particles must have a hydrodynamic size below 6 nm.<sup>31</sup> According to that report, we thus can predict that BMONP is supposed to undergo a fast renal clearance if *in vivo* experiments were performed.

On the other hand, **Figure 2.12Bi** and **Bii** illustrates the stability of BMONPs upon dispersion in neutral pH water up to 2 days. Regarding MSNPs, they are, as expected, stable upon dispersion in aqueous medium at pH 5 up to 2 days, maintaining the same size and shape (**Figure 2.12Aii** and **Aiv**).

The breaking process of BMONP in acidic medium has been studied more deeply by a kinetic method, monitoring after 0 minute, 15 minutes, 1 hour, 3 hours, 6 hours and 48 hours of dispersion (**Figure 2.13**). Like in the case of SEM monitoring, already after 15 minutes of dispersion, the particle size and shape differ from those at time 0 and the degradation process seems to start from the periphery of the particles (**Figure 2.13A and B, yellow arrows**). Compared to what observed in SEM, at this time of 15 minutes, the size of the fragments here seem to be smaller, about 90 nm (**Figure 2.13B, yellow arrows**). After 1 hour of dispersion, smaller fragments of 30-40 nm appear (**Figure 2.13C**), which then keep becoming smaller and smaller over time (**Figure 2.13D and E, yellow arrows**). Eventually, at time 48 hours, only very little fragments of about 5 nm or less in size are observed (**Figure 2.13F, yellow arrows**), in addition to some layers of likely amorphous silica (**Figure 2.13F, green boxes**), which suggests that the entire particles have collapsed.

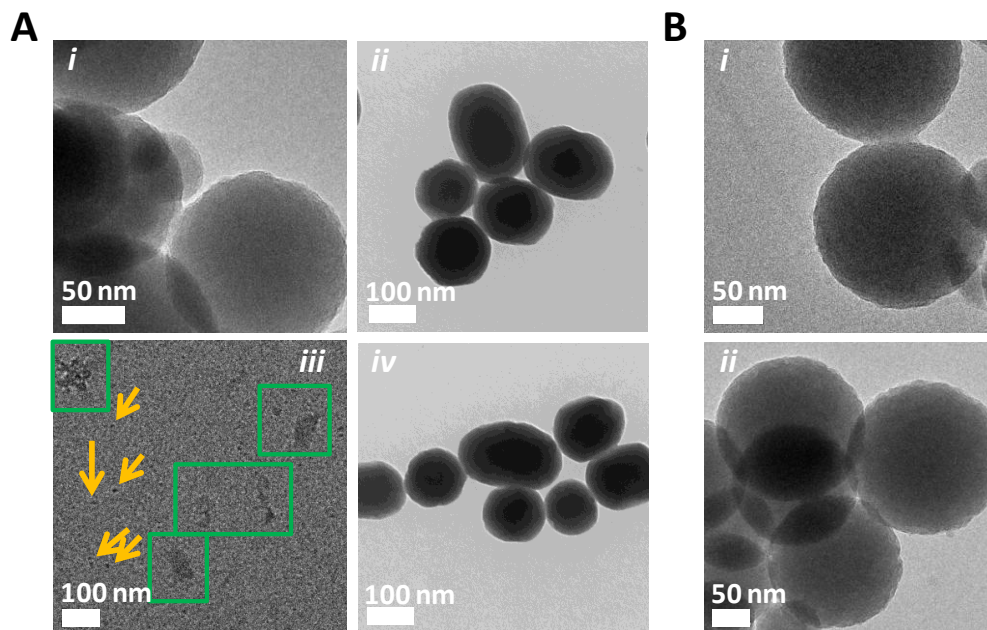


**Figure 2.12** Breakability and stability studies of the particles monitored by TEM. (A) Upon dispersion in aqueous solution at pH 5; at time 0: BMONPs (*i*), MSNPs (*ii*); at time 2d: BMONPs (*iii*), MSNPs (*iv*). (B) BMONPs upon dispersion in water at pH 7; at time 0 (*i*), at time 2d (*ii*).

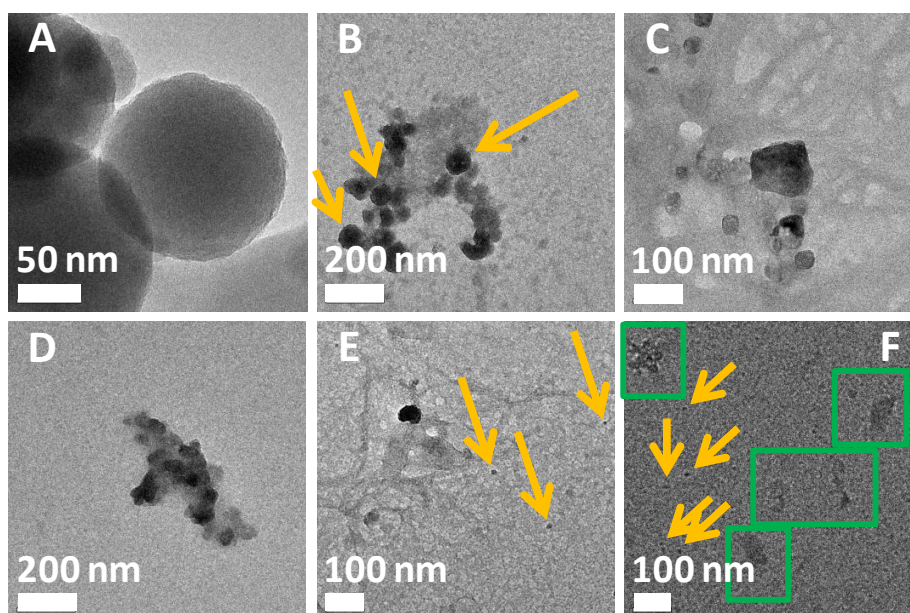


**Figure 2.13** TEM monitoring of the kinetic study of BMONPs breaking. TEM images of BMONPs upon dispersion in an aqueous solution at pH 5 over (A) 0 min, (B) 15 min, (C) 1h, (D) 3h, (E) 6h and (F) 48h.

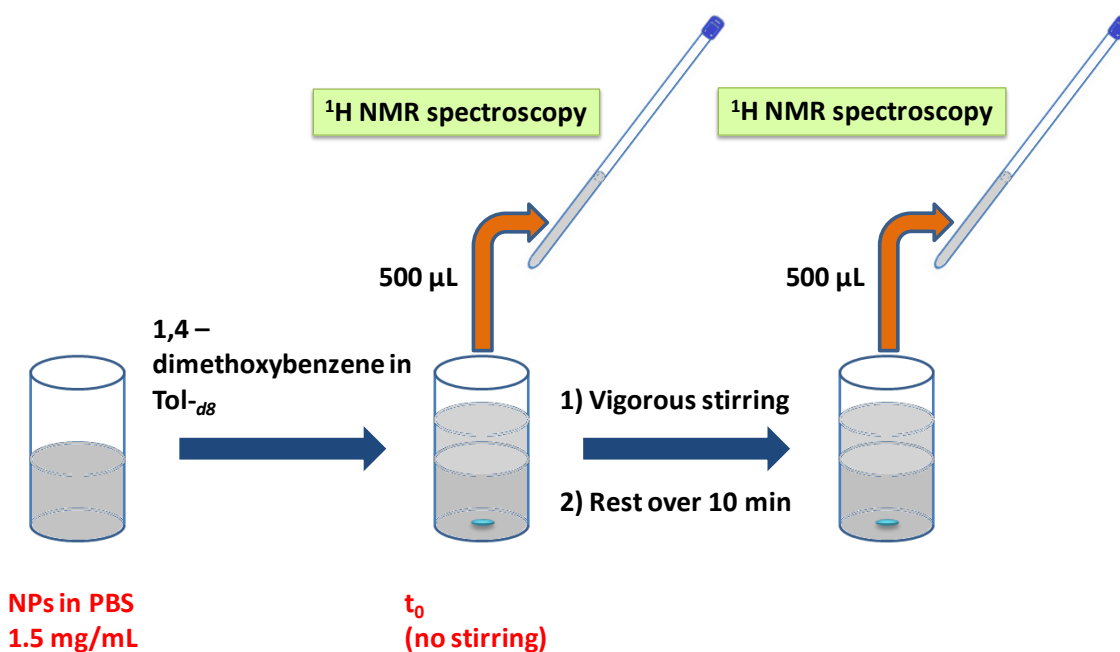
### **2.4.3 Monitoring by $^1\text{H}$ NMR spectroscopy**

To further verify and indisputably prove the breakability of BMONP in acidic medium and its relative stability in physiological conditions,  $^1\text{H}$  NMR spectroscopy has been performed, knowing that BMONP is composed of a silica and diimines network, in another term, a Schiff base. In sub-chapter **2.2**, it was mentioned that Schiff bases formation reaction are known to be in equilibrium with their hydrolysis reaction due to the moisture or water eliminated from the reaction. Thus, when a Schiff base is placed in aqueous medium, it will undergo a hydrolysis reaction, which remains in equilibrium with its formation reaction. However, when an acidic catalyst is added into the medium, the equilibrium will favour the hydrolysis reaction. Taking advantage of this property, BMONPs are dispersed in saline aqueous solution buffered at pH 5.5 to mimic the conditions in the extracellular matrix of a cancerous tissue. Indeed, in these conditions, when the particles collapse, they are expected to liberate the terephthalaldehyde **1** due to the diimine hydrolysis as illustrated in **scheme 2.2**. Deuterated toluene is added into the medium to entrap the liberated terephthalaldehyde and an internal standard is requested as a reference for the  $^1\text{H}$  NMR signaling. This standard is required to exhibit the minimum peak possible and not to be confused with the signals coming from neither the aldehyde nor the solvent. That is why 1,4-dimethoxybenzene in a readily known concentration has been chosen for the experiment. The integrals of  $^1\text{H}$  signals coming from terephthalaldehyde are thus expected to increase over time, which would mean the increase of the concentration of the molecule due to the increasing amount of breaking particles. As in the case of electron microscopy monitoring, the suspensions are vigorously stirred to avoid the aggregation of the particles. All these conditions are illustrated in **Scheme 2.2**.

As a control, the same experiment has been carried out in PBS at pH 7.4 and, in this condition, the liberation of terephthalaldehyde is expected to be far slower than in the acidic medium.

### Determination of liberated terephthalaldehyde

In sub-chapter 2.3, the percentage of diiminosilane linker incorporated in the material's framework was determined. Knowing that, the percentage of terephthalaldehyde, which initially composed the diiminosilane, can be determined as well. Thus, knowing the mass of particles dispersed in the medium for the breakability studies, it is possible to determine, by calculations including atomic mass, the amount of terephthalaldehyde involved in the experiment.



**Scheme 2.2** Representation of the conditions used to monitor the liberation of terephthalaldehyde by <sup>1</sup>H NMR due to BMONPs breaking in PBS.

**Figure 2.14** describes the comparison between the <sup>1</sup>H NMR spectra obtained from both the media at pH 5.5 and 7.4 at times 0 and 15 minutes. On this figure, we can see that, at time 0, only signals coming from the solvent, i.e. deuterated toluene and the internal standard, i.e. 1,4-dimethoxybenzene are present. Those signals are represented by a quintuplet at 2.11 ppm (not shown in the figure) and 3 singlets at 7.00, 7.04 and 7.12 ppm for toluene and 2 other singlets at 3.37 and 6.71 ppm for 1,4-dimethoxybenzene (**Figure**

**2.14A**). However, at time 15 minutes, the spectra are already different depending on the medium. While the one obtained from neutral pH medium is similar to the one at time 0 (**Figure 2.14C**), the spectrum obtained from acidic medium already exhibits signals coming from terephthalaldehyde. Those signals are represented by 2 singlets: one at 7.34 ppm attributed to the protons from the aromatic ring and another one at 9.46 ppm attributed to the proton from the aldehyde function (**Figure 2.14B**).

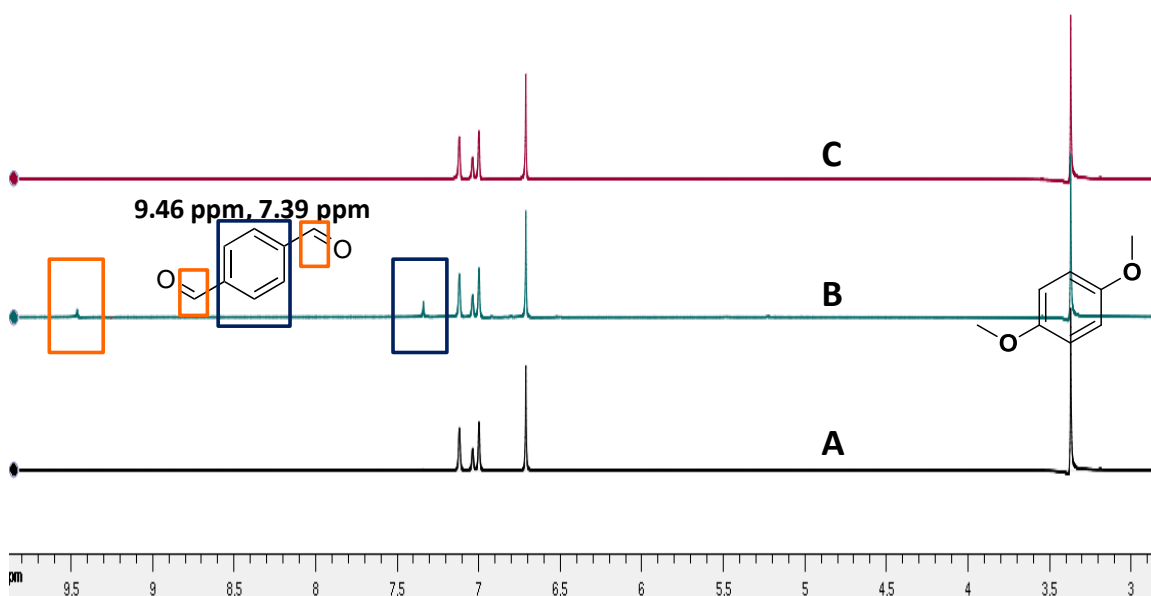


**Figure 2.14**  $^1\text{H}$  NMR spectra obtained from (A) BMONPs in PBS at time 0, (B) BMONPs at time 15 min in PBS at pH 5.5 and (C) BMONPs at time 15 min in PBS at pH 7.4. Spectroscopy performed in  $\text{Tol-}d_8$ .

The aldehyde release has been monitored at times 0, 15 minutes, 1, 3, 6, 24 and 48 hours in both neutral and acidic media. On the one hand, when the spectra obtained over time are superimposed and when the signals attributed to terephthalaldehyde start to appear, the integrals of these signals increase remarkably when BMONPs are dispersed in acidic medium, while this increase is less noticeable when the particles are dispersed in neutral medium. On the other hand, we can see on **Figure 2.15A** the aldehyde release profile upon dispersion in both acidic and neutral media over time. The kinetic of the release is relatively fast and, according to the graph, we can deduce that after only 15 minutes of

dispersion in PBS at pH 5.5, more than 70 % of the aldehyde contained in the particles have been released. The kinetic reaches a plateau at time 6h and nearly 90 % of the aldehyde has been liberated, meaning that almost the totality of the particles has collapsed. Regarding the suspension in neutral pH medium, the kinetic exhibits the same profile but the scale is much smaller. Thus, after 1h of dispersion, only 7 % of the aldehyde has been liberated and a plateau of 20 % is reached at time 6h, which remained stable until the end of the experiment, i.e. 2 days. It is noteworthy to recall here that the suspensions are vigorously stirred and this is likely the reason why the kinetic is so fast in the acidic medium and the amount of collapsed particles is relatively high in the neutral pH one. Nevertheless, the plateau at time 6h in the neutral medium means that the hydrolysis rate of the imine has reached the equilibrium and, consequently, no more particle can break.

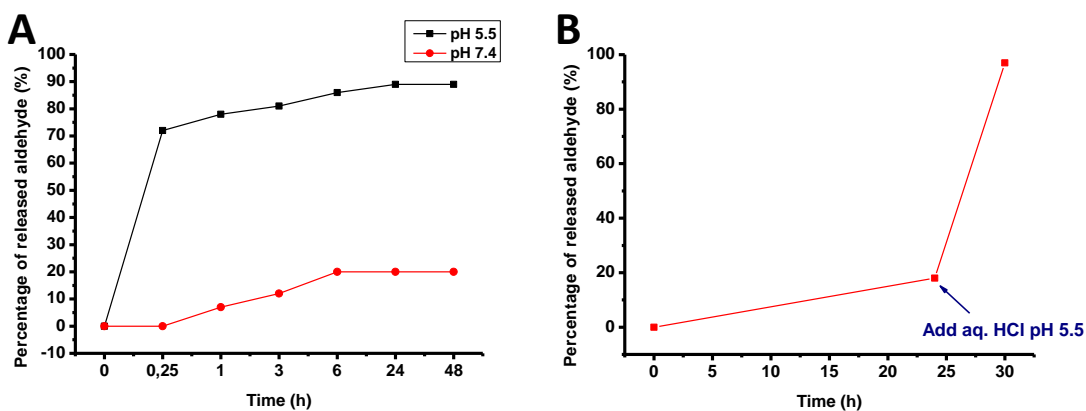


**Figure 2.15** (A) Release profile of the aldehyde upon dispersion in PBS at (**black curve**) pH 5.5 and at (**red curve**) pH 7.4; (B) release profile upon incubation in PBS pH 7.4 for 1d followed by addition of an aqueous HCl solution to drop the pH to 5.5. The released aldehyde was entrapped into a Tol-*d8* solvent and using 1,4-dimethoxybenzene as internal standard. Data obtained from <sup>1</sup>H NMR spectroscopy in Tol-*d8*.

This hypothesis is confirmed on **Figure 2.15B** which represents the release profile of the aldehyde upon a dispersion of BMONPs in PBS at pH 7.4 over 1d, followed by the addition of an aqueous solution of hydrochloric acid until dragging the pH down to 5.5.

The experiment has been performed as the following: BMONPs are dispersed in PBS at pH 7.4 in the same conditions as in the previous experiment cited above; at time 24h, a sample is removed to run  $^1\text{H}$  NMR spectroscopy and, immediately, an aqueous solution of hydrochloric acid is added to the suspension till decreasing the pH to 5.5. The result is in high accordance with our hypothesis related to the equilibrium. Thus, after 1 day of vigorous stirring in PBS at pH 7.4, the amount of particles breaking is relatively low at 18 %. However, only 6 hours after dragging the pH down to 5.5 (time 30h), almost the totality (97 %) of the particles break down suddenly.

#### ***2.4.4 Monitoring by dye release***

To understand the kinetic release of the guest molecules such as drugs, oligonucleotide and others, we have simulated this with dye release, measuring by photoluminescence spectroscopy. Thus, both the breakable and non-breakable particles have been labelled with sulfo-cyanine5 NHS ester by 0.005 % in mole with respect to the content in silane. The dye is grafted on the particles' framework by a covalent bound via an amino group by means of APTES by 20 % in mole with respect to the content in silane. In aqueous solution, the excitation maximum of sulfo-cyanine5 NHS ester is recorded at 646 nm to afford an emission maximum at 662 nm with a molar extinction coefficient of  $2.71 \cdot 10^5 \text{ L}\cdot\text{mol}^{-1}\cdot\text{cm}^{-1\text{ref}}$ . The choice of the dye and its amount have done according to a few criteria. First, the dye can not be pH-sensitive and, second, the amount has to be the minimum possible in order to have reasonable and interpretable emission over time. The labelling process is induced during the particles' synthesis by letting all the reagents react in one pot and keeping the same conditions as for the synthesis of the non-labelled particles. Once obtained, the particles have been characterised by the different techniques as in the case of the non-labelled materials. Electron microscopy such as SEM (**Figure 2.16A-B**) and TEM enable us to see the spherical-like shape of both the breakable and non-breakable particles with a diameter size of about 180 nm for the breakable particles (S-Cy5-BMONPs, **Figure 2.16A**) and about 140 nm for the non-breakable ones (S-Cy5-MSNPs, **Figure 2.16B**).

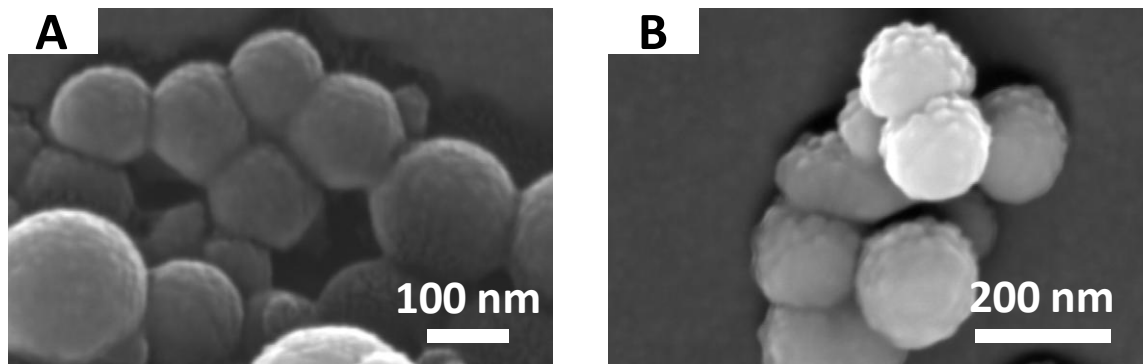


**Figure 2.16** SEM pictures of (A) S-Cy5-BMONPs and (B) S-Cy5-MSNPs.

The diameter size of the particles has been confirmed by DLS measurement where S-Cy5-BMONP exhibits an average size of  $175,65 \pm 71,5$  nm (**Figure 2.17A**) while S-Cy5-MSNPs shows an average size of  $136.8 \pm 16.5$  nm (**Figure 2.17B**).

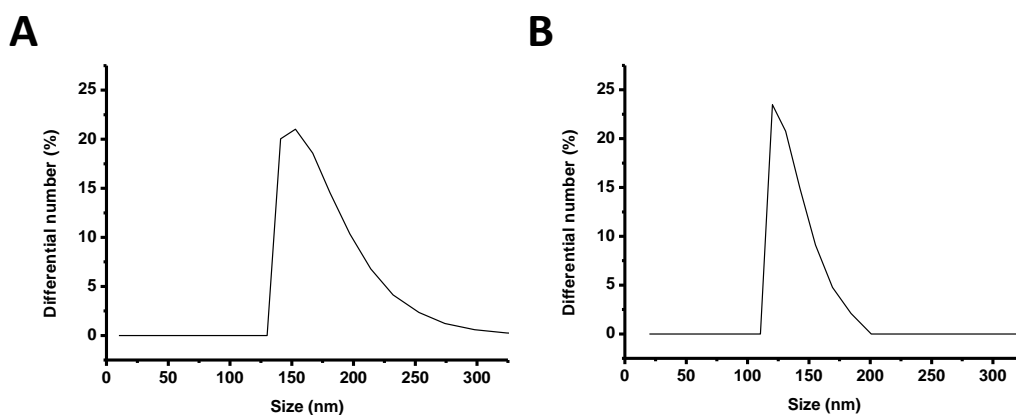


**Figure 2.17** DLS size number distribution of (A) S-Cy5-BMONPs (average diameter:  $175,65 \pm 71,5$  nm) and (B) S-Cy5-MSNPs ((average diameter:  $136.8 \pm 16.5$  nm).

Furthermore, from thermogravimetric analyses (TGA), we can determine the mass percentage of sulfo-cyanine5 together with APTES which have been grafted on the particles with respect to the total mass of the materials. On **Figure 2.18A**, we can see that 50 % of the mass of S-Cy5-BMONPs is due to the dye combined with APTES and the

organic linker. At the same time, **Figure 2.18B** enables us to determine that the organic moiety (dye + APTES) participates to 10 % of the total mass of S-Cy5-MSNPs.

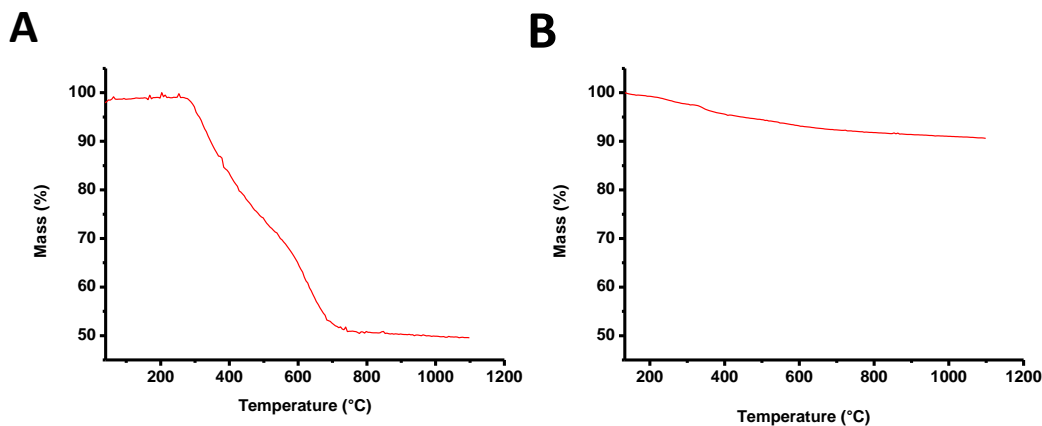


**Figure 2.18** TGA of (A) S-Cy5-BMONPs and (B) S-Cy5-MSNPs.

Regarding the release kinetics of the dye, the particles are first thoroughly washed with water and ethanol in order to get rid of the excess of dye which has not reacted covalently. To verify this process, emission spectra of the supernatants from the particles' suspension after centrifugation are realised and, as we can see in **Figure 2.19A**, for both the breakable and non-breakable particles, the spectra show flat lines close to 0 along the abscissa axis. Nevertheless, if we get closer on the spectra, we can see that the emission is not totally non-existent (**Figure 2.19B**). The reason is that, actually, no matter how long and strong was the centrifugation, there is still very few particles in the supernatant but in a negligible amount. To perform the kinetic experiments of the release of sulfo-cyanine5 upon the particles' breaking in acidic medium, S-Cy5-BMONPs are dispersed in PBS at pH 5.5 at the concentration of 0.1 mg/mL and stirred very gently. The reaction is monitored at times 0, 1 min, 5 min, 10 min, 15 min, 25 min, 35 min, 45 min, 1h, 3h, 6h, 12h, 1d and 2d. At each time point, an aliquot is removed from the suspension followed by a centrifugation and an emission spectrum of the supernatant is realised. This way, the particle is expected to slowly break down and liberate a water soluble molecule containing the dye whose emission could be monitored in time. By measuring the emission from the supernatant, we can be sure that the photoluminescence

is only due to the soluble molecule and not from the particles. Nevertheless, as already observed previously, no matter how strong is the centrifugation, there is still very few particles in the supernatant, but in a negligible amount affording a negligible emission compared to the soluble molecule. To verify the stability of S-Cy5-BMONP in neutral pH medium, the same experiment has been performed in PBS at pH 7.4. The same way, as comparison, the same experiments have been performed with S-Cy5-MSNPs in PBS at pH 5.5 and 7.4. The excitation wavelength is set at 575 nm all along all the experiments and the spectra are recorded from 610 to 800 nm.

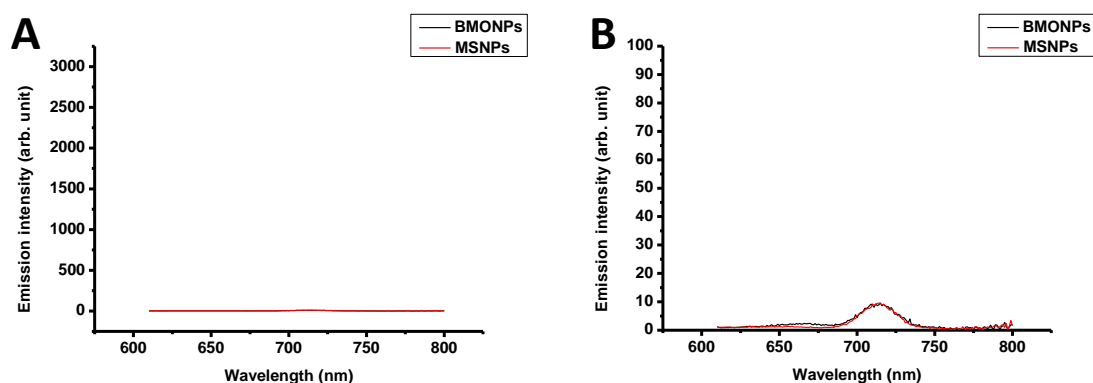


**Figure 2.19** (A) Emission obtained from the supernatant after washing the particles and a (B) zoom. The Y axis was set for direct comparison with **Figure 2.20**.

The results follow the way we expect them to go. The raw data represented on **Figure 2.20A** indicate the result obtained from S-Cy5-BMONPs dispersed in PBS at pH 5.5. In this result, we can see that the emission is almost non-existent at time 0 then it starts to be visible at time 1 min and more at time 5 min. The emission intensity keeps increasing in time, reaches the maximum at time 1d and no more evolution is observed until time 2d. Regarding the data from the same particles upon dispersion in PBS at pH 7.4, the emission is almost non-existent at the beginning of the experiment and is barely visible at the end. The emission spectra collection is stopped after 1d of dispersion without any particular observation all along the experiment (**Figure 2.20B**). Furthermore, the same observation as for S-Cy5-BMONPs in neutral medium is done on the suspension of S-Cy5-MSNPs in both neutral and acidic media (**Figure 2.20C-D**).

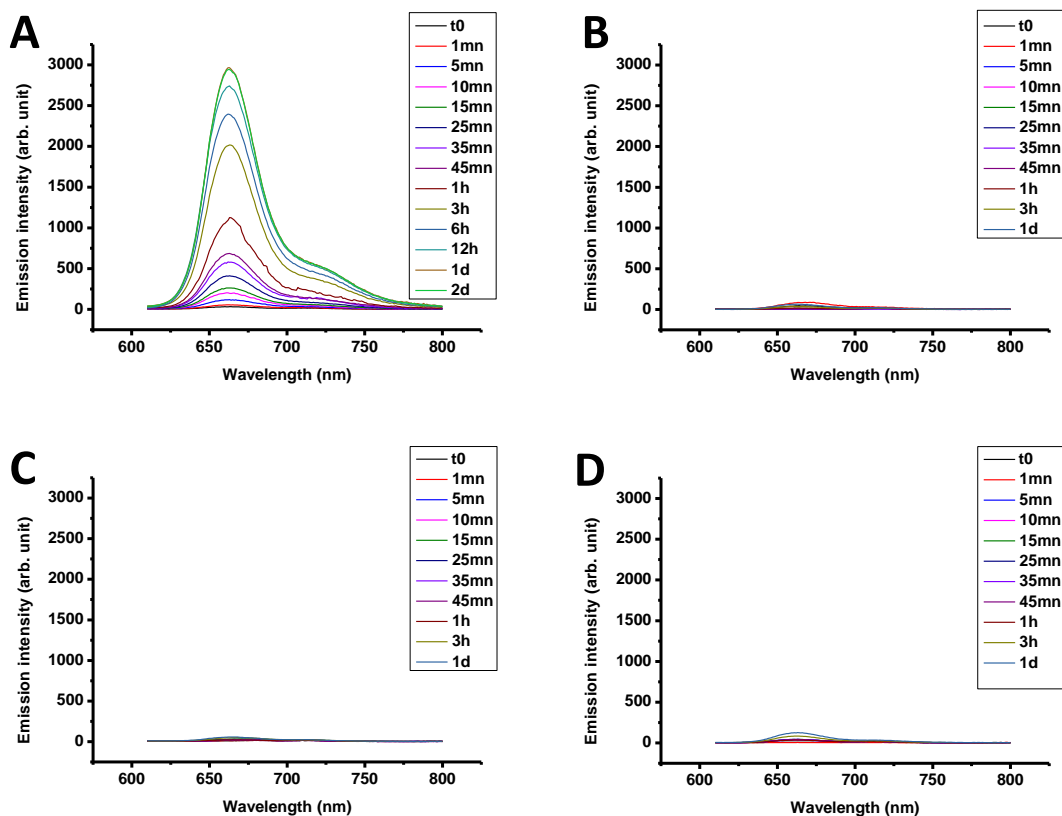


**Figure 2.20** Raw data over time from the emission measurement of the supernatant from suspensions of S-Cy5-BMONPs in PBS at (A) pH 5.5 and (B) pH 7.4 and of S-Cy5-MSNPs at (C) pH 5.5 and (D) pH 7.4.

To better study the phenomenon, the area integration of the emission spectra over time have been plotted. On **Figure 2.21**, we can clearly notice the differences depending on the particles and the conditions. When the breakable particles are dispersed in acidic medium (**Figure 2.21A, black curve**), the area integration of the emission spectra is very low and close to 0 at the beginning of the experiment. After 5 min of dispersion, this feature reaches 4 % of its maximum value then it increases to 9 % at time 15 min and this value keeps increasing until reaching a plateau after 1d of dispersion where the maximum value is observed. When these particles are dispersed in PBS at pH 7.4 (**Figure 2.21A, red curve**), the plot of the area integration of the emission spectra over time exhibits a flat line close to 0. After 1d experiment, the recorded value is only 2 % of the maximum of the value recorded in PBS at pH 5.5. To investigate deeper, we have compared the area

integration to the maximum intensity of the emission and the observations correlate perfectly (**Figure 2.21B**). Regarding the non-breakable particles, as expected, the evolution of both the area integration and the intensity maximum of the emission is very monotone over time, remaining close to 0 for both the experiments performed in neutral and acidic media.

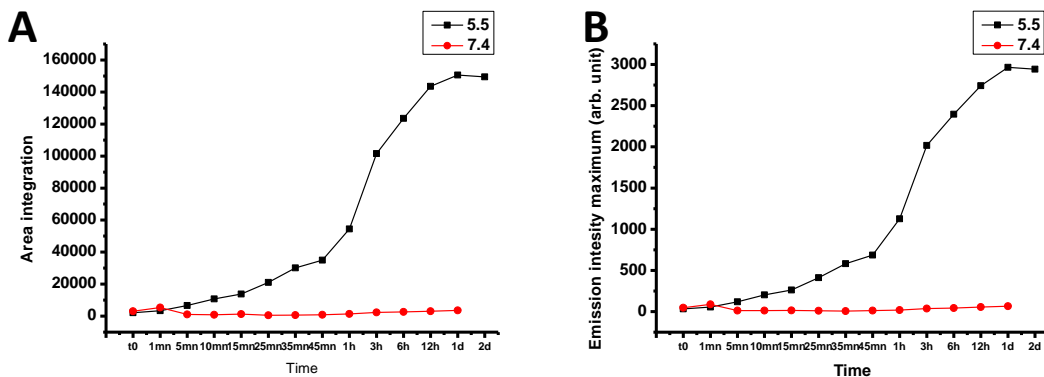


**Figure 2.21** (A) Area integration of the emission over time from the supernatant of a suspension of S-Cy5-BMONPs in PBS and (B) the emission maximum intensity over time.

These observations lead us to conclude that grafting the very low mole percentage of sulfo-cyanine5 on the particles followed by the gentle stirring during the breakability experiments enable to obtain a breakability meant by the dye release in a controllable manner and which can be monitored in a short time scale by emission spectroscopy.

## 2.5 Conclusion

The pH-breakable hybrid mesoporous silica nanoparticle has been synthesized using a relatively straightforward method. Moreover, it demonstrates a relatively good stability in physiological conditions while it breaks down in acidic media. As comparison, the non-breakable particle remains intact in both conditions tested.

## 2.6 Experimental Section

### 2.6.1 Materials

All commercial solvents and reagents were used as received without further purification. Tetraethyl orthosilicate (TEOS), (3-aminopropyl)triethoxysilane (APTES), phosphate buffered saline tablets, 1,4-dimethoxybenzene and chloroform-*d* were purchased from Sigma Aldrich. Toluene-*d*<sub>8</sub> was purchased from Euriso-top.

### 2.6.2 Instruments

#### *<sup>1</sup>H nuclear magnetic resonance (NMR) spectroscopy*

The <sup>1</sup>H NMR spectroscopy was performed with Bruker 400 ultrasield™ at 400 MHz, 16 scans and using deuterated solvents.

#### *Attenuated total reflectance Fourier transform infra-red (ATR-FTIR) spectroscopy*

ATR-FTIR measurements were performed on an ATR IR Affinity-1 instrument (Shimadzu Scientific Instruments). The samples were directly deposited, as so, onto the sample plate surface.

#### *Scanning electron microscopy (SEM)*

To perform the SEM, the samples were drop-casted onto a round glass coverslip of 12 mm in diameter (purchased from R. Langenbrinck) and allowed to dry at 1 atm and room temperature. Gold (using Emitech K575X peltier cooled, 60 mA) was sputtered on the top of the specimen and the samples were observed with a FEI Quanta FEG 250 SEM (FEI corporate, Hillsboro, Oregon, USA) with an acceleration voltage of 20-30 kV.

#### *Transmission electron microscopy (TEM)*

The samples were drop-casted onto a Formvar coated copper grids (400 mesh, purchased from Agar Scientific, Stansted, UK) and allowed to dry at room temperature and 1 atm. The pictures were then recorded with a Hitachi 7500 TEM at an acceleration voltage of 80 kV.

#### *X-ray photoelectron spectroscopy (XPS)*

The samples were drop-casted onto a glass coverslip (the same as for SEM) precoated with gold (Emitech K575X peltier cooled, 60 mA). XPS analyses were performed using a K-Alpha™+ XPS System (Thermo Scientific). Monochromatic Al K alpha X-rays were used (15 keV, 72 W, 200 mm spot diameter). Spectra were measured using a pass energy of 200 eV for survey spectra and 50 eV for core level spectra.

#### *Dynamic light scattering (DLS) and zeta potential (ZP)*

DLS and ZP measurements were conducted on a Delsa Nano C Particle Analyzer (Beckman Coulter, Brea, CA, USA; operative wavelength 655 nm). All DLS measurements of the nanoparticles were conducted in water ( $\approx 0.1$  mg/mL), ZP analyses were performed in PBS buffer (pH 7.4;  $\approx 0.1$  mg/mL).

#### *Nitrogen adsorption/desorption*

Porosimetry analyses of the samples were performed using a Micromeritics porosimeter (model ASAP-2020). The samples were degassed at 150 °C for 3h and N<sub>2</sub> adsorption/desorption measurement was done at -196 °C. The surface areas and pore volume were calculated by BET method and the pore size distributions were calculated by DFT methods.

### **2.6.3 Syntheses**

#### *Synthesis of the diiminosilane linker*

In a typical procedure, 3-aminopropyltriethoxysilane (APTES, 4.92 mmol) was added dropwise to a solution of terephthalaldehyde (2.24 mmol) in dry ethanol (11 mL) under nitrogen atmosphere. After the addition, the mixture was heated up to reflux temperature and stirred during 2h30. The yellowish limpid solution was then allowed to cool down to room temperature. Anhydrous sodium sulphate was added to the mixture while stirring it during 5 min to remove the moisture. After a filtration using a filter paper, solvent

evaporation and drying under vacuum overnight, the final compound was obtained quantitatively as a yellow oil without any further purification.

*Characterisation:* this linker has been characterised by proton nuclear magnetic resonance ( $^1\text{H}$  NMR), infra-red (IR) spectroscopies and mass spectrometry.

$^1\text{H}$  NMR (300 MHz,  $\text{CDCl}_3$ ):  $\delta$  = 0.68 (t, J = 7.5 Hz, 4H), 1.21 (t, J = 6 Hz, 18H), 1.85 (m, 4H), 3.67 (t, J = 4.5 Hz, 4H), 3.83 (q, J = 7.5 Hz, 12H), 7.77(d, J = 3 Hz, 4H), 8.28 (s, 2H).

IR:  $\nu$  2930, 1648, 1189, 1136, 1038  $\text{cm}^{-1}$ .

ESI/MS: m/z calcd. for  $\text{C}_{26}\text{H}_{48}\text{N}_2\text{O}_6\text{Si}_2$  540.31 Found  $[\text{M} + \text{H}]^+ = 541.31$

#### *Synthesis of the breakable mesoporous organosilica nanoparticles (BMONPs)*

In a typical procedure, cetyltrimethylammonium bromide (CTAB, 29 mg) was suspended in distilled water (13.5 mL) with a vigorous stirring (750 rpm) at 23 °C and 28 % ammonia was added to have a basic medium (60  $\mu\text{L}$ , pH 9). In a separated vial, tetraethyl orthosilicate (TEOS, 26  $\mu\text{L}$ ) was added to a solution of the diiminosilane linker (37 mg) in butanol (1.5 mL) and the mixture was shaken manually to homogenize. The silane solution was then added dropwise to the micelles before adding 60  $\mu\text{L}$  more of 28 % ammonia to keep the same pH value in the medium. After stirring during 1d at 23 °C, the material was recovered by means of centrifugation and washing with water and ethanol once each. Eventually, the surfactant was removed through a soxhlet extraction in ethanol at reflux temperature during 4 days and the recovered particles were dried under vacuum.

*Characterisation:* the material has been characterized by electron microscopy by means of scanning electron microscopy (SEM) and transmission electron microscopy (TEM). Spectroscopy was also performed such as X-ray photo-electronic spectroscopy (XPS) and IR as well as nitrogen sorption and zeta potential measurements.

#### *Synthesis of the mesoporous silica nanoparticles (MSNPs)*

The MSNPs were synthesized by first dissolving cetyl trimethyl ammonium bromide (CTAB, 0.5 g) in a mixture of distilled water (240 mL) and 2 M sodium hydroxide (1.75 mL); the solution was heated to 80°C and stirred vigorously. In a separated vial,

tetraethyl ortho silicate (TEOS, 2.5 mL) was dissolved in dry ethanol (6 mL). Once the temperature of the CTAB solution had stabilized, the ethanolic solution containing TEOS was added dropwise. After 2 h, the solution was cooled down to room temperature and the particles were recovered by means of centrifugation and washing once with ethanol. To remove the surfactant from the pores, the materials were refluxed in ethanol overnight with a few drop of hydrochloric acid 37 % and the particles were obtained after centrifugations, washing 3 times with distilled water and 3 more with ethanol followed by drying under vacuum.

*Characterisation:* the materials have been characterised by electron microscopy by means of scanning electron microscopy (SEM) and transmission electron microscopy (TEM). Analyses by spectroscopy were also performed such as X-ray photo-electronic spectroscopy (XPS) and IR, as well as nitrogen sorption and zeta potential measurements.

*Synthesis of the breakable mesoporous organosilica nanoparticles functionalised with sulfo-cyanine5 NHS ester (S-Cy5-BMONPs)*

In a typical procedure, cetyltrimethylammonium bromide (CTAB, 99 mg) was suspended in distilled water (46 mL) with a vigorous stirring (750 rpm) at 23 °C and 28 % ammonia was added to have a basic medium (204 µL, pH 9). In a separated vial, APTES (15 µL) was added to a solution of sulfo-cyanine5 NHS ester (S-Cy5, 15 µg) in butanol (2.5 mL) and the mixture was stirred at 23 °C during 30 min. In another vial, tetraethyl orthosilicate (TEOS, 88 µL) was added to a solution of the diiminosilane linker (123 mg) in butanol (2.5 mL) and the mixture was shaken manually to homogenize. The silane solution was then added to the APTES/S-Cy5 mixture while stirring for 5 more min. The organic solution was eventually added dropwise to the micelles before adding 204 µL more of 28 % ammonia to keep the same pH value in the medium. After stirring during 1d at 23 °C, the material was recovered by means of centrifugation and washing with water and ethanol once each. Eventually, the surfactant was removed through a soxhlet extraction in ethanol at reflux temperature during 4 days and the recovered particles were dried under vacuum.

*Characterisation:* the materials have been characterized by electron microscopy by means of scanning electron microscopy (SEM) and transmission electron microscopy

(TEM). Analyses by spectroscopy were also performed such as X-ray photo-electronic spectroscopy (XPS) and IR, as well as nitrogen sorption and zeta potential measurements.

*Synthesis of the mesoporous silica nanoparticles functionalised with sulfo-cyanine5 NHS ester (S-Cy5-MSNPs)*

S-Cy5-MSNPs were synthesized by first dissolving cetyl trimethyl ammonium bromide (CTAB, 200 mg) in a mixture of distilled water (96 mL) and 2 M sodium hydroxide (700 $\mu$ L); the solution was heated to 80°C and stirred vigorously. In a separated vial, APTES (105  $\mu$ L) was added to a solution of sulfo-cyanine5 NHS ester (S-Cy5, 174  $\mu$ g) in dry ethanol (1,2 mL) and the mixture was stirred at 23 °C during 30 min. Then tetraethyl ortho silicate (TEOS, 1 mL) was added to the APTES/S-Cy5 mixture while stirring for 5 more min. Once the temperature of the CTAB solution had stabilized, the ethanolic solution containing TEOS/APTES/S-Cy5 was added. After 2 h, the solution was cooled down to room temperature and the particles were recovered by means of centrifugation and washing once with ethanol. To remove the surfactant from the pores, the materials were refluxed in ethanol overnight with a few drop of hydrochloric acid 37 % and the particles were obtained after centrifugations, washing 3 times with distilled water and 3 more with ethanol followed by drying under vacuum.

*Characterisation:* the materials have been characterised by electron microscopy by means of scanning electron microscopy (SEM) and transmission electron microscopy (TEM). Analyses by spectroscopy were also performed such as X-ray photo-electronic spectroscopy (XPS) and IR, as well as nitrogen sorption and zeta potential measurements.

#### **2.6.4 Chemical biodegradability tests**

*<sup>1</sup>H NMR monitoring*

To monitor the breaking of the particles by <sup>1</sup>H NMR, BMONPs were dispersed in a phosphate buffer saline (PBS) solution at pH 5.5 and a concentration of 1.5 mg/mL. As an internal standard, deuterated toluene containing a known amount of 1,4-dimethoxybenzene was added to the medium which was then stirred. At time 0, 15 min, 1h, 3h, 6h, 24h and 48h, the medium was left to rest for 10 min to separate the organic

phase from the aqueous one. Then, 500  $\mu\text{L}$  of the upper organic phase was taken out in order to perform  $^1\text{H}$  NMR. For comparison, the same experiment has been carried in a PBS solution at pH 7.4.

#### *Dye release monitoring*

The particles were dispersed in a phosphate buffer saline (PBS) solution at pH 5.5 and a concentration of 0.1 mg/mL. At time 0, an aliquot was removed and centrifuged over 1 min, then the supernatant emission was measured with a fluorimeter ( $\lambda_{\text{exc}} = 575 \text{ nm}$ ). After that, the mixture was stirred gently and the same process (removing an aliquot, centrifugation and measurement of the supernatant emission with a fluorimeter) was repeated at times 1 min, 5 min, 10 min, 15 min, 25 min, 35 min, 45 min, 1h, 3h, 6h, 12h, 1d and 2d. The same experiment was carried out in PBS at pH 7.4.

#### *SEM and TEM monitoring*

The particles were dispersed in distilled water at pH 5 and a concentration of 0.05 mg/mL. The mixture was stirred and a few drop was taken out and drop casted on a coverslip for SEM while it was on a copper grid with Formvar/Carbon film for TEM. The dropcasting procedure followed by a solvent evaporation at 1 atm was done at time 0, 15 min, 1h, 3h 6h, 24h and 48h. For comparison, the same experiment has been carried in distilled water at pH 7 and, furthermore, both BMONPS and NBMSNPs were tested in both media.

## **2.7 References**

1. He, Q., Gao, Y., Zhang, L., Zhang, Z., Gao, F., Ji, X., Li, Y. & Shi, J. A pH-responsive mesoporous silica nanoparticles-based multi-drug delivery system for overcoming multi-drug resistance. *Biomaterials* 32, 7711–7720 (2011).
2. Meng, H., Xue, M., Xia, T., Zhao, Y.-L., Tamanoi, F., Stoddart, J. F., Zink, J. I. & Nel, A. E. Autonomous in Vitro Anticancer Drug Release from Mesoporous Silica Nanoparticles by pH-Sensitive Nanovalves. *J. Am. Chem. Soc.* 132, 12690–12697 (2010).

3. Yuan, L., Tang, Q., Yang, D., Zhang, J. Z., Zhang, F. & Hu, J. Preparation of pH-Responsive Mesoporous Silica Nanoparticles and Their Application in Controlled Drug Delivery. *J. Phys. Chem. C* **115**, 9926–9932 (2011).
4. Yao, X., Chen, X., He, C., Chen, L. & Chen, X. Dual pH-responsive mesoporous silica nanoparticles for efficient combination of chemotherapy and photodynamic therapy. *J Mater Chem B* **3**, 4707–4714 (2015).
5. Amaral, L. do, Sandstrom, W. A. & Cordes, E. H. Some Aspects of Mechanism and Catalysis for Carbonyl Addition Reactions1. *J. Am. Chem. Soc.* **88**, 2225–2233 (1966).
6. Willi, A. V. Kinetik der Hydrolyse von Benzalanilin II: Die pH-Abhängigkeit der Reaktionsgeschwindigkeit in ungepufferten Lösungen und die Rolle der Aminoalkohol-Zwischenstufe. *Helvetica Chimica Acta* 1193–1203 (1956).
7. Behme, M. T. A. & Cordes, E. H. Secondary Valence Force Catalysis. I. Kinetics of Schiff Base Hydrolysis in the Presence of Micelle-Forming Detergents1. *J. Am. Chem. Soc.* **87**, 260–265 (1965).
8. Reeves, R. L. On the mechanism, substituent effects, and intramolecular catalysis in Schiff base hydrolysis. *J. Org. Chem.* **30**, 3129–3135 (1965).
9. Prabhu, D. V. & Laxmeshwar, N. B. Kinetics and Reaction Mechanism of Hydrolysis of N-Salicylidene-m-Methyl Aniline Spectrophotometrically. *Asian Journal of Chemistry* 99–106 (1994).
10. Kirdant, A. S., Shelke, V. A., Shankarwar, S. G. & Chondhekar, T. K. Kinetic study of hydrolysis of N-salicylidene-m-methyl aniline spectrophotomerically. *Journal of Chemical and Pharmaceutical Research* 790–796 (2011).
11. Kumar, S., Jain, S. L. & Sain, B. Thiourea dioxide promoted cobalt-catalyzed hydrolysis of imines: dual activation via organocatalysis and metal catalysis. *RSC Adv* **2**, 789–791 (2012).
12. El-Taher, M. A. E.-D. The effect of electron-withdrawing properties of substituents on the hydrolysis of some Schiff bases. *J. Solut. Chem.* **25**, 401–410 (1996).
13. Paul, M., Pal, N., Rajamohanam, P. R., Rana, B. S., Sinha, A. K. & Bhaumik, A. New organic–inorganic hybrid microporous organosilica having high metal ion adsorption capacity. *Phys. Chem. Chem. Phys.* **12**, 9389 (2010).
14. Hench, L. L. & West, J. K. The sol-gel process. *Chem. Rev.* **90**, 33–72 (1990).
15. Mackenzie, J. D. & Bescher, E. P. Chemical Routes in the Synthesis of Nanomaterials Using the Sol–Gel Process. *Acc. Chem. Res.* **40**, 810–818 (2007).
16. Ramesh, S. Sol-Gel Synthesis and Characterization of Nanoparticles. *J. Nanosci.* **2013**, 1–8 (2013).
17. Danks, A. E., Hall, S. R. & Schnepf, Z. The evolution of ‘sol–gel’ chemistry as a technique for materials synthesis. *Mater Horiz* **3**, 91–112 (2016).
18. Feinle, A., Elsaesser, M. S. & Hüsing, N. Sol–gel synthesis of monolithic materials with hierarchical porosity. *Chem Soc Rev* **45**, 3377–3399 (2016).

19. Sing, K. S. W., Everett, D. H., Haul, R. A. W., Moscou, L., Pierotti, R. A., Rouquerol, J. & Siemieniewska, T. Reporting Physiosorption Data for Gas/Solid Systems, Handbook of Heterogeneous Catalysis (Wiley-VCH Verlag GmbH & Co. KGaA, 2008).
20. Tang, H., Guo, J., Sun, Y., Chang, B., Ren, Q. & Yang, W. Facile synthesis of pH sensitive polymer-coated mesoporous silica nanoparticles and their application in drug delivery. *Int. J. Pharm.* 421, 388–396 (2011).
21. Wanyika, H., Gatebe, E., Kioni, P., Tang, Z. & Gao, Y. Synthesis and characterization of ordered mesoporous silica nanoparticles with tunable physical properties by varying molar composition of reagents. *Afr. J. Pharm. Pharmacol.* 5, (2011).
22. Wanyika, H. Sustained release of fungicide metalaxyl by mesoporous silica nanospheres. *J. Nanoparticle Res.* **15**, (2013).
23. Rashidi, L., Vasheghani-Farahani, E., Rostami, K., Ganji, F. & Fallahpour, M. Mesoporous silica nanoparticles with different pore sizes for delivery of pH-sensitive gallic acid: mesoporous silica nanoparticles for delivery of gallic acid. *Asia-Pac. J. Chem. Eng.* **9**, 845–853 (2014).
24. Fernando, I. R., Ferris, D. P., Frasconi, M., Malin, D., Strekalova, E., Yilmaz, M. D., Ambrogio, M. W., Algaradah, M. M., Hong, M. P., Chen, X., Nassar, M. S., Botros, Y. Y., Vincent L. Cryns, V. L. & Stoddart, J. F. Esterase- and pH-responsive poly( $\beta$ -amino ester)-capped mesoporous silica nanoparticles for drug delivery. *Nanoscale* 7, 7178–7183 (2015).
25. Lee, T. H. & Rabalais, J. W. X-ray photoelectron spectra and electronic structure of some diamine compounds. *J. Electron Spectrosc. Relat. Phenom.* **11**, 123–127 (1977).
26. Snauwaert, P., Lazzaroni, R., Riga, J., Verbist, J. J. & Gonbeau, D. A photoelectron spectroscopic study of the electrochemical processes in polyaniline. *J. Chem. Phys.* **92**, 2187 (1990).
27. Rosink, J., Blauw, M. A., Geerligs, L. J., van der Drift, E., Rousseeuw, B. A. C., & Radelaar, S. Self-assembly of  $\pi$ -conjugated azomethine oligomers by sequential deposition of monomers from solution. *Langmuir* 16, 4547–4553 (2000).
28. Luo, Y., Bernien, M., Krüger, A., Hermanns, C. F., Miguel, J., Chang, Y.-M., Jaekel, S., Kuch, W. & Haag, R. In Situ Hydrolysis of Imine Derivatives on Au(111) for the Formation of Aromatic Mixed Self-Assembled Monolayers: Multitechnique Analysis of This Tunable Surface Modification. *Langmuir* 28, 358–366 (2012).
29. Belton, D. J., Deschaume, O. & Perry, C. C. An overview of the fundamentals of the chemistry of silica with relevance to biosilicification and technological advances: Fundamentals of silica chemistry. *FEBS J.* **279**, 1710–1720 (2012).

30. Kresge, C. T., Leonowicz, M. E., Roth, W. J., Vartuli, J. C. & Beck, J. S. Ordered mesoporous molecular sieves synthesized by a liquid-crystal template mechanism. *Nature* **359**, 710–712 (1992).
31. Choi, S. H., Liu, W., Misra, P., Tanaka, E., Zimmer, J. P., Ipe, B. I., Bawendi, M. G. & Frangioni, J. V. Renal clearance of quantum dots. *Nat. Biotechnol.* **25**, 1165–1170 (2007).

## Chapter 3

### ***In vitro* studies: delivery of paclitaxel into living cells for breast cancer treatment**

#### **Abstract**

The uptake and cytotoxicity effect of BMONPs towards Hs578T and MCF-10 cells were investigated at different concentrations; the viability was measured after 24 and 48 hours of incubation time. Negligible cell death was detected in the concentration range tested, indicating that the hybrid bio-responsive particles were non-cytotoxic under the conditions tested. Comparative experiments performed with MSNPs demonstrated a high toxic effect against both cell lines. The internalisation of the material was first followed by SEM. The cells rapidly internalised small numbers of particles only 5 min after starting the incubation, and the amount of material taken up increased over time. The confocal images and Z-stack investigation taken 4 and 24 hours after incubation clearly demonstrate an abundant uptake of BMONPs by both cell lines, with a tendency to localise mainly in the perinuclear region. Co-localization studies performed to enquire on the internalisation pathway of the particles demonstrated that BMONPs were mainly localised within the lysosomes after 24 hours of incubation. The beneficial effect of the breakability of BMONPs in the drug release activity was tested *in vitro*. As the drug of choice, we chose paclitaxel, a potent chemotherapeutic agent for breast cancer. Control experiments conducted on cells incubated only with paclitaxel were also included in the study, keeping constant the total amount of drug. The Pac@BMONPs were able to remarkably reduce the cell viability. On the contrary, the decrease in cell viability induced by Paclitaxel alone was negligible considering the exact same amount of drug. This difference in behaviour can be attributed to the higher internalisation and the faster kinetic release of BMONPs. Comparative experiments performed with Pac@MSNPs revealed an almost inexistent cell death induced by the system, indicating the lack of efficiency of MSNP to deliver paclitaxel into the cancer cells in an effective way compared to the breakable system.

### 3.1 Introduction

With nearly 1.7 million new cases diagnosed in 2012 (latest data), breast cancer is the most common cancer type in women worldwide and the second most common overall, the first position being occupied by lung cancer.<sup>1,2</sup>

The breast cancer burden, as it is the case for most of the cancers, keeps increasing with the years. A study published by Bray *et al.* on 27 cancer types in the adult population worldwide in 2013 is alarming.<sup>3</sup> Bray and his co-workers investigated these cancers burden over 5 years from 2004 to 2008 in 13 world regions and 184 countries. In the paper, they reported the number of people alive at the end of 2008 and who had been diagnosed with cancer during the 2004-2008 period and they thus counted 28.8 million diagnosed cases. Among all these diseases, breast cancer had the highest rate in women in 145 countries and when combining data from men and women together, breast cancer still exhibited the highest rate in 112 countries with 5.2 million cases (**Figure 1**). This number counts as 18 % of the overall cancer diagnosed.

Otherwise, Curado reported that, for the only year 2008, 1.38 million new cases of breast cancer were diagnosed, which was 23 % of all the diagnosed cancers.<sup>4</sup> Causing 458,000 deaths during that year, this type of cancer was thus the fifth cause of death from all cancers together.

The number of victims of breast cancer keeps increasing within the years. The latest statistics published by the International Agency for Research on Cancer (IARC), the section consecrated to cancer in the World Health Organization (WHO) deals with nearly 1.7 million new diagnosed cases of breast cancer in 2012.<sup>1</sup> When reported to the total number of diagnosed cancers (14.1 million), the proportion is 11.9 % and when compared to the 2008 data, the number of cases of this disease increased by more than 20 %. The mortality trend is not better, causing 522,000 deaths among women worldwide, breast cancer was the most common cause of cancer death during that year. The rise was 14 % compared to the 2008 data.

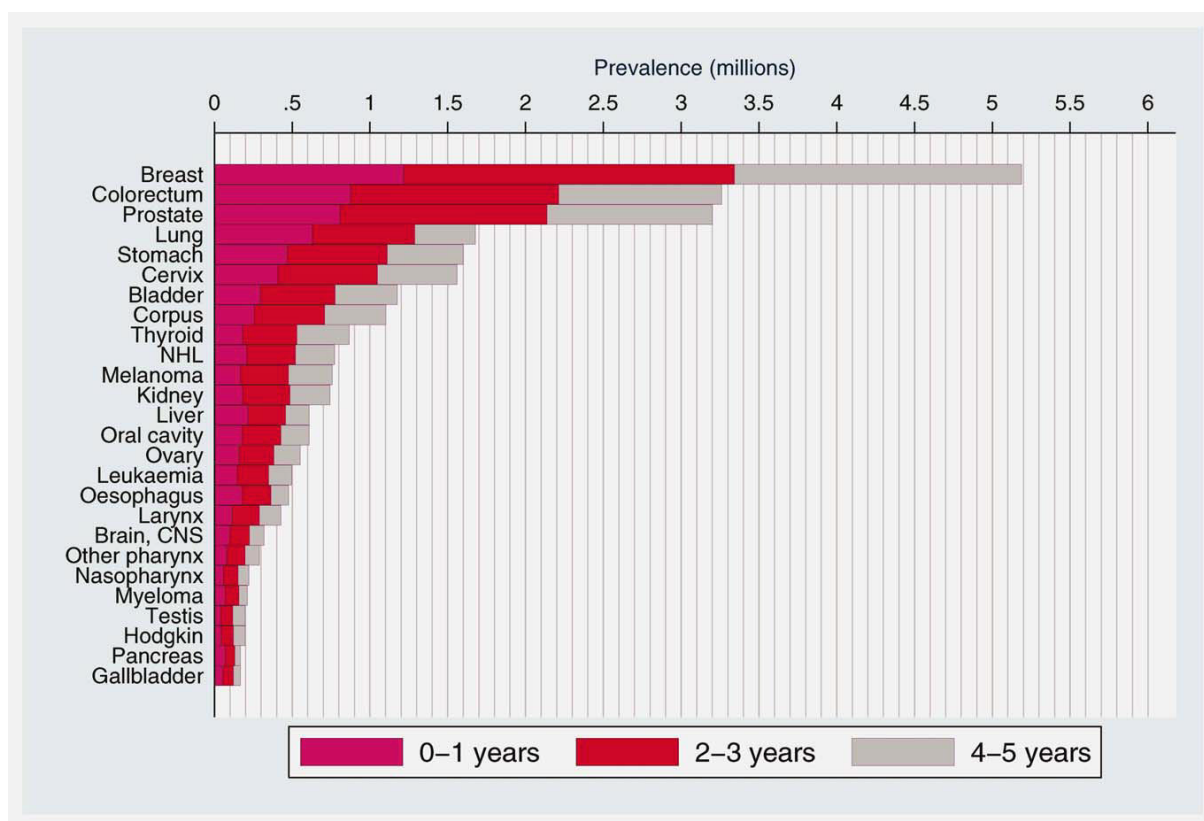


**Figure 3.1** Bar chart of global 5-year cancer prevalence counts (millions) by cancer site; stacked bars denote cancer prevalence among patients alive at the end of 2008 who were diagnosed in 2008, 2006–2007 and 2004–2005, respectively, for example, <1 year, 2–3 and 4–5 years after diagnosis. All cancers combined (except non-melanoma skin cancer), both sexes and aged 15 years and older sorted by magnitude of prevalence counts. Figure taken from reference 2.

In the attempt to cure breast cancer, as well as to cure all cancer types, several techniques are proposed nowadays, such as surgery, radiation therapy, chemotherapy or immunotherapy. Regarding chemotherapy, a certain number of drugs are available on the market and, among those used to treat breast cancer, paclitaxel, a water insoluble molecule commercially known as Taxol<sup>®</sup>, occupies an important position. Paclitaxel acts as an antimetabolic agent by blocking the cell cycle in its G1 or M phases by stabilising the microtubule cytoskeleton against depolymerization.<sup>5–8</sup>

*The objective of the present chapter is to effectively load the hydrophobic paclitaxel into the pores of the pH-breakable mesoporous organosilica nanoparticle and deliver it into human breast cancer cells in order to kill them. Hs578T cell line was used as model. The effect on a healthy version of human breast is also described by employing MCF-10 cell line. For*

comparison, non-breakable mesoporous silica nanoparticles (MSNPs) have also been loaded with the same drug and the cytotoxicity effect was studied, as well as the toxic effect of both breakable and non-breakable particles alone.

### 3.2 Cellular uptake of BMONPs

Before employing the BMONPs in drug delivery experiments, we have first investigated their uptake in Hs578T and MCF-10 cells, the respective cancer<sup>9-11</sup> and healthy versions of human breast cells. The uptake has first been monitored by scanning electron microscopy (SEM) and, in this experiment, the cells are incubated with the particles at a concentration of 0.05 mg/mL for 1 hour. As we can see in **Figure 3.2B**, after only 5 minutes of incubation, a few particles start to be internalised through the cell membrane. The amount of BMONPs taken up then increases within time (**Figure 3.2C-D**).

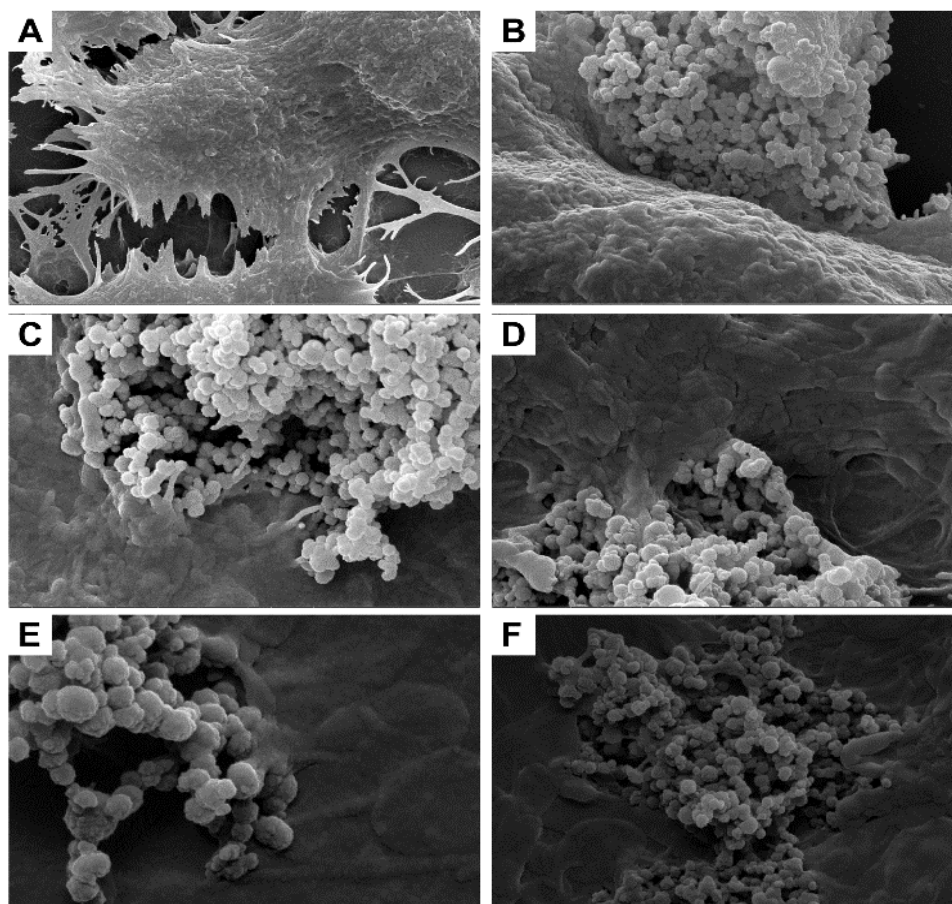


**Figure 3.2** SEM images of the cell uptake of BMONPs at a concentration of 0.05 mg/mL after (A) 0 min, (B) 5 min, (C) 10 min, (D) 30 min and (E), (F) 60 min of incubation.

To push our investigations further, we have performed confocal microscopy. To enable the tracking of the particles, they have been labelled by a covalent attachment of a red emitting dye which is rhodamine B isothiocyanate (RITC). To better observe the particles within the cell, this latter is stained on the membrane with Alexa Fluor® 647 Phalloidin which interacts with the actin of the cytoskeleton. The nucleus is stained with 4',6-diamidino-2-phenylindole, commonly abbreviated as DAPI and which is an intercalating agent for DNA. Both of the cancer and healthy cells have been employed in order to determine their internalisation property towards the particles. The cells are incubated with BMONPs at a concentration of 0.05 mg/mL and the samples are analysed after 4 and 24 hours. As control experiment, the cells are also treated with non-breakable particles which had been readily functionalised with the same dye, i.e. RITC. To acquire images in the best conditions, the different dyes are excited at 488 nm for RITC, 650 nm for Alexa Fluor® 647 Phalloidin and 358 nm for DAPI. **Figure 3.3** illustrates what is occurring when the cells are incubated with BMONPs. We can see that, after 4 hours of incubation, the cells internalise a small amount of particles which seem to be located in the perinuclear region of the cytoplasm (**Figure 3.3B, E**) and this amount increases with time (**Figure 3.3C, F**). This observation is the same with both of Hs578T and MCF-10 cell lines.

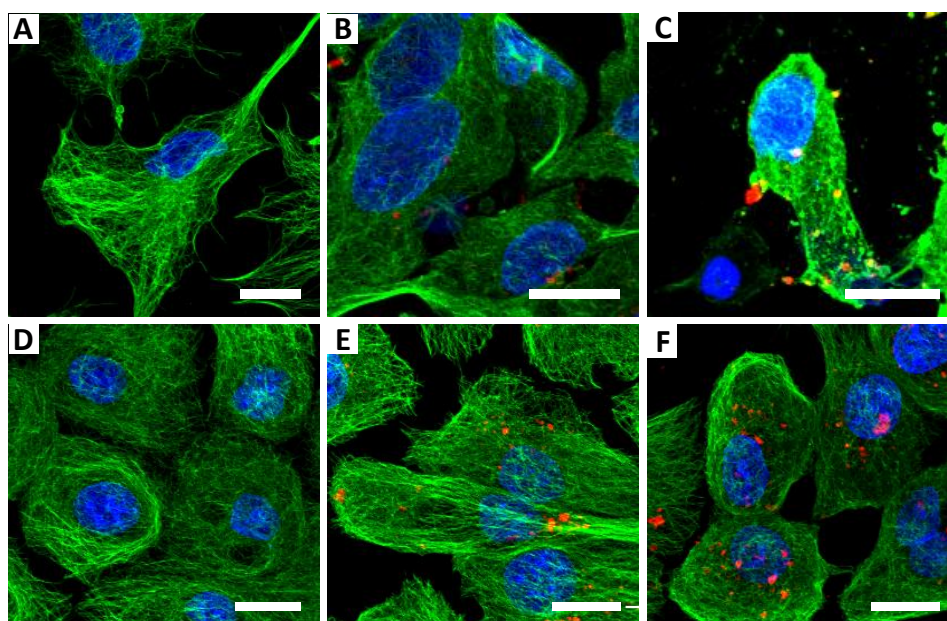


**Figure 3.3** Cell internalisation of BMONPs at a concentration of 0.05 mg/mL monitored by confocal microscopy: images of (A) Hs578T cells alone then after (B) 4h and (C) 24h of incubation with the particles; images of (D) MCF-10 cells alone then after (E) 4h and (F) 24h of incubation with the

particles. BMONPs are labelled with RITC (**red**) while the cell membrane is stained with Alexa Fluor® 647 Phalloidin (**green**) and its nucleus with DAPI (**blue**).

Regarding MSNPs, the experiment affords the same results as compared to BMONPs (**Figure 3.4**). It is noteworthy to mention that at the end of the incubation and before analysis with the confocal microscope, the samples are thoroughly washed to avoid the presence of non-internalised particles in the images. Nevertheless, some particles stick on the support (i.e. glass coverslip) and are impossible to remove; these particles are represented by the red spots/area in the empty dark zones in the pictures.

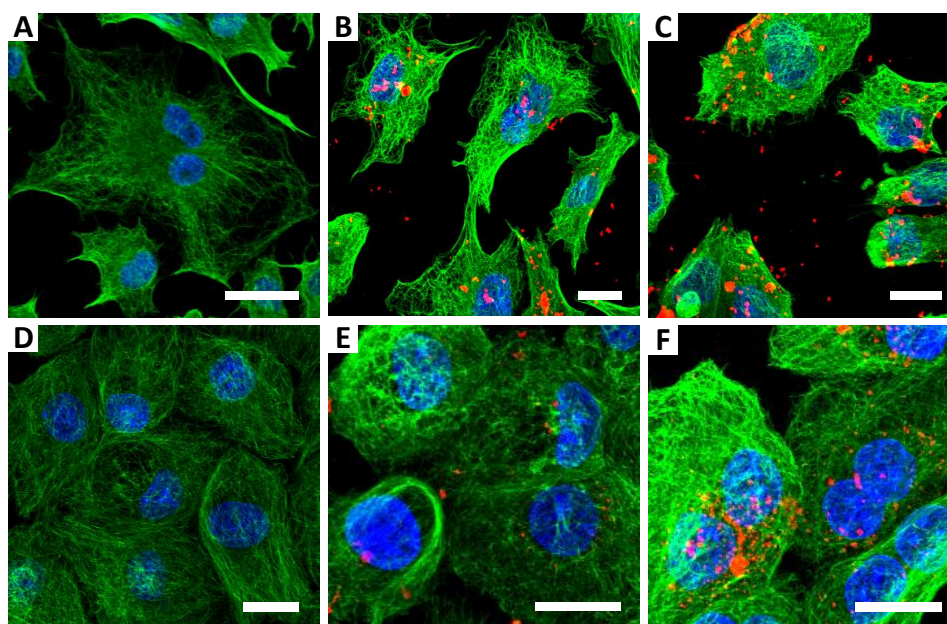


**Figure 3.4** Cell internalization of MSNPs at a concentration of 0.05 mg/mL monitored by confocal microscopy: images of (A) Hs578T cells alone then after (B) 4h and (C) 24h of incubation with the particles; images of (D) MCF-10 cells alone then after (E) 4h and (F) 24h of incubation with the particles. MSNPs are labelled with RITC (**red**) while the cell membrane is stained with Alexa Fluor® 647 Phalloidin (**green**) and its nucleus with DAPI (**blue**).

To verify that the particles have been internalised by the cells and remain inside, Z-stack analysis has also been performed with the confocal microscope. This analysis has been performed *in situ* on the same samples cited above at time 24 hours following the incubation. On **Figure 3.5**, we can see that the breakable particles are perfectly internalised by both the

cancer and the healthy cell lines and they are retained inside. Moreover, as it could already be observed on the two dimensional images, they are located in the cytoplasm in the perinuclear region. Furthermore, as we can see from **Figure 3.6**, the non-breakable particles are perfectly internalised by both Hs578T and MCF-10 cells and they are located in the area surrounding the nucleus.

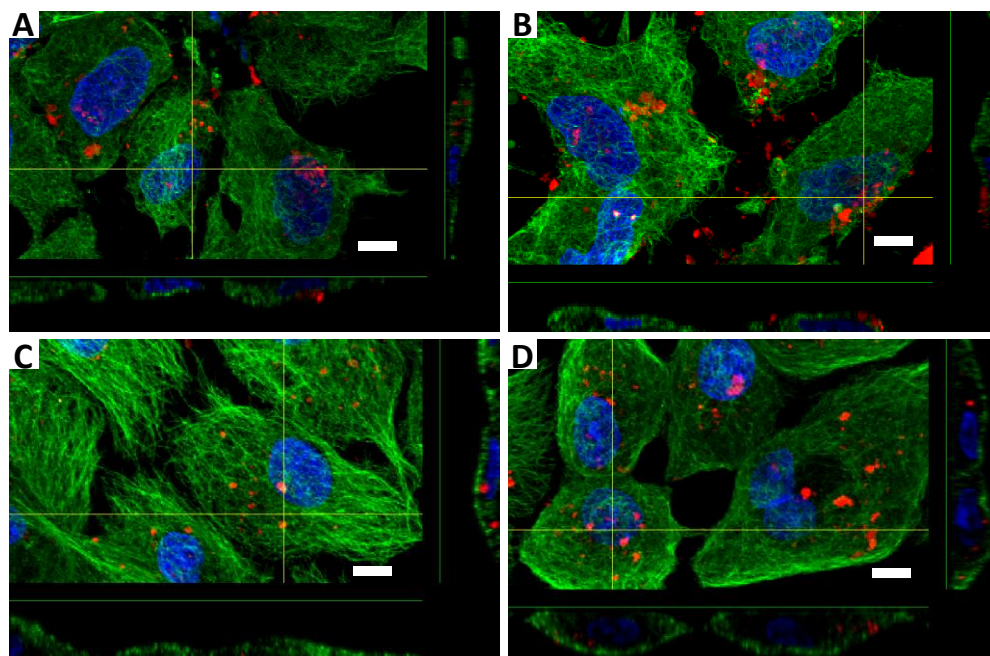


**Figure 3.5** Confocal microscopy on BMONPs - Z-stack analysis: (A) and (B) upon incubation with Hs578T cells at a concentration of 0.05 mg/mL for 24h; (C) and (D) upon incubation with MCF-10 cells at a concentration of 0.05 mg/mL for 24h. BMONPs are labelled with RITC (red) while the cell membrane is stained with Alexa Fluor® 647 Phalloidin (green) and its nucleus with DAPI (blue).

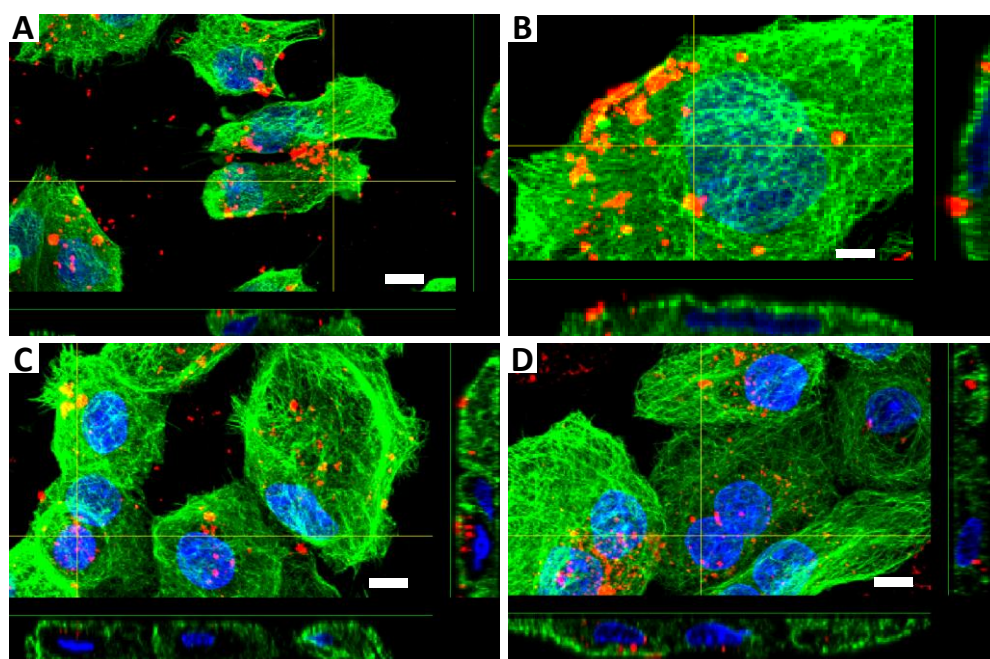


**Figure 3.6** Confocal microscopy on MSNPs - Z-stack analysis: (A) and (B) upon incubation with Hs578T cells at a concentration of 0.05 mg/mL for 24h; (C) and (D) upon incubation with MCF-10 cells at a concentration of 0.05 mg/mL for 24h. MSNPs are labelled with RITC (red) while the cell membrane is stained with Alexa Fluor® 647 Phalloidin (green) and its nucleus with DAPI (blue).

### 3.3 Cytotoxicity evaluation of MSNPs

MSNPs exhibit a relative low cytotoxicity. However, when considering the cell line, the particles concentration and the duration of the incubation, this property becomes debatable. Starting with a MCM-41 type material<sup>12</sup> we can cite the work done by Wang *et al.* on the test of a spherical shaped MCM-41 of a micrometre sized diameter and about 3 nm in pore diameter against Caco-2 cells, which are cells from human colon carcinoma.<sup>13</sup> They have performed experiments at different concentrations of particles ranging from 0.02 to 0.5 mg/mL. They found out that the cytotoxicity is relatively low at low concentrations, displaying less than 10 % of cell death at 0.02 and 0.05 mg/mL. The cells death is still quite negligible upon incubation with the materials at a concentration of 0.1 mg/mL but starts to be slightly more than 10 %. However, at higher concentrations (0.2 and 0.5 mg/mL), they record cells death of more than 20 % and even close to 30 % for 0.5 mg/mL of particles. Hudson *et al.* have investigated the toxic effect of MCM-41 type spherical nanoparticles of 100-150 nm in diameter and about 3 nm in pore diameter towards three cell lines which are human mesothelial cells, mouse peritoneal macrophages and mouse myoblast cells, differentiated

into muscle cells.<sup>14</sup> They incubated the cells with the materials at three different concentrations which are 0.1, 0.3 and 0.5 mg/mL and they measured the cell viability at 3 times points: 1, 3 and 4 days following the incubation. While the particles show no or little toxicity towards mouse peritoneal macrophages, the viability of both human mesothelial and mouse myoblast cells are presented to be dependant of the particles concentration and the duration of the incubation. Upon a 1-day incubation with 0.1 mg/mL of particles, the viability of mouse myoblast cells drops from 100 % (at time 0) to nearly 85 %, this viability goes even down to 75 % with 0.5 mg/mL of particles.

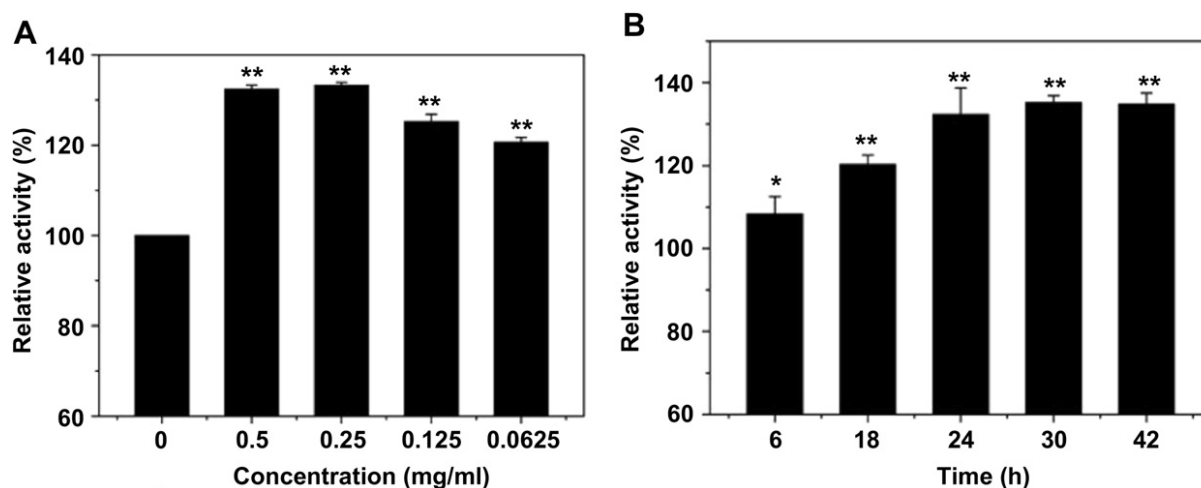


**Figure 3.7** Effect of MSNPs on A375 cell proliferation. Effect of MSNs on cell proliferation (A) after the incubation for 24 h with different concentrations of particles and (B) after the incubation for different times with 0.2 mg/mL particles. Figure taken from reference 17.

Furthermore, when the incubation time is increased to 4 days, the cell viability is, as we could expect, lower, being for instance reaching for instance values close to 70 % at 0.1 mg/mL and 50 % at 0.5 mg/mL of particles concentration. The results obtained with human mesothelial cells are even more dramatic. Despite a value close to 100 % with 0.1 mg/mL of particles up to 4 days, the cell viability drops dramatically to about 45 % with 0.3 mg/mL and to about 25 % at 0.5 mg/mL, both upon 3 days of incubation. Another work reported by Tao *et al.* deals with spherical MCM-41 type particles of 300-350 nm in diameter.<sup>15</sup> In this publication, they talk about an assay of the cytotoxicity of the materials at three different concentrations (0.05, 0.1 and 0.2 mg/mL) against Jurkat cells which are cells from human CD4 T lymphocytes and they conducted the experiments at three different time points including 3, 27 and 51 hours. According to the results, they observed that the particles have no significant toxic effect

against the cells upon 3 hours of incubation for the 3 concentrations tested. However, 27 hours of incubation induce an important cell death of about 25 % and this effect is independent of the particles concentration. Moreover, a similar result is obtained after 51 hours of incubation.

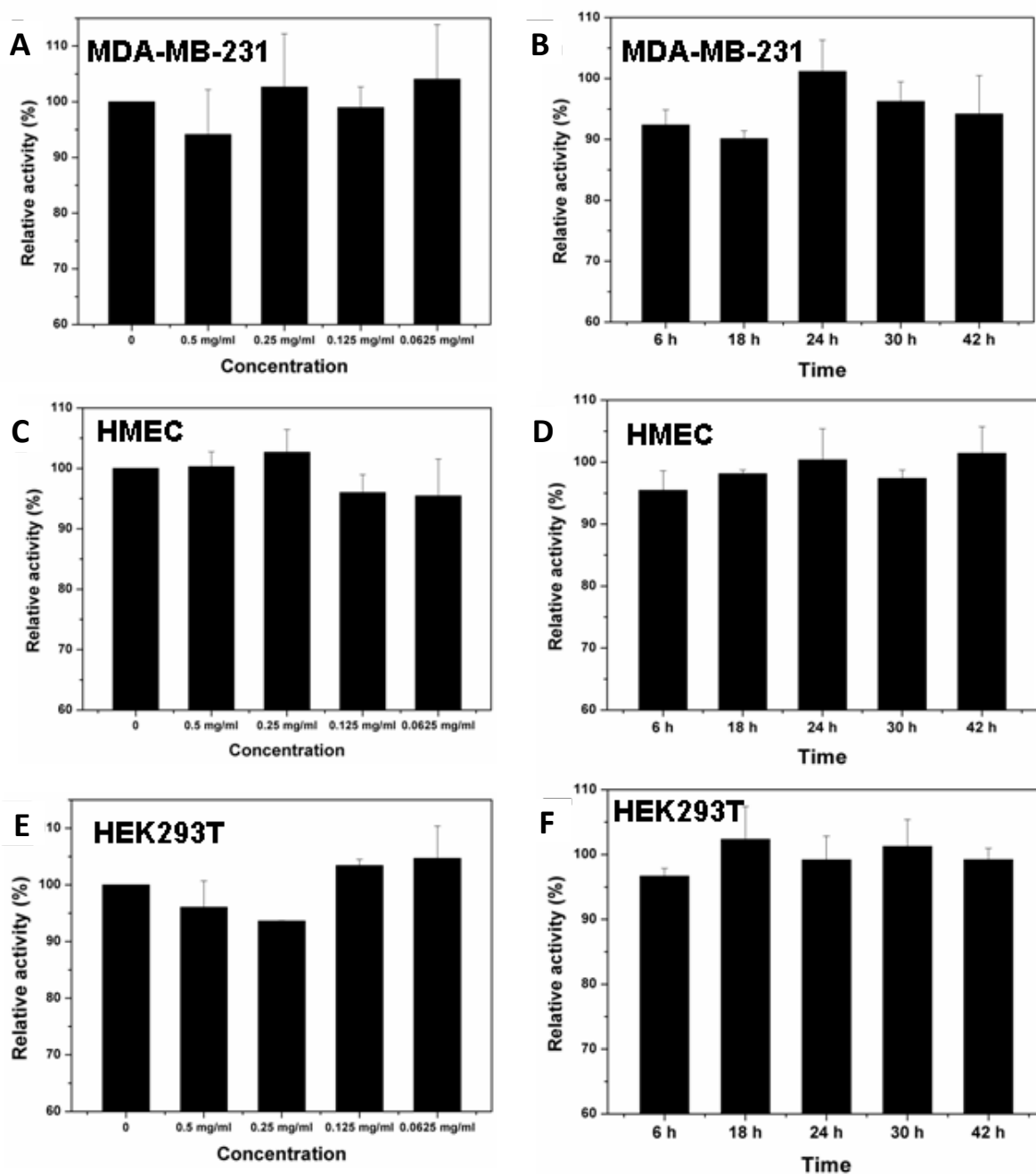


**Figure 3.8** Effect of MSNPs on cell proliferation of different cell lines upon incubation with (A, C, E) the particle at different concentrations and (B, D, F) for 24h at a particle concentration of 0.2 mg/mL. Figure adapted from reference 17.

In another way, MSNPs can induce a reverse effect on some types of tumour, i.e. they can induce the tumour growth. Huang *et al.* reported such an observation upon treatment of a human malignant melanoma tumour with MCM-type MSNPs possessing an average diameter of 110 nm and an average pore size of 2.4 nm.<sup>16</sup> They treated *in vivo* the tumour with the MSNPs and noticed a growth by a factor higher than 2 compared to a control composed of the untreated tumour. *In vitro* studies performed with cell lines from the same tumour type (A375) show the same tendency. In that case, the authors incubated the cells with the particles in increasing concentrations from 0.0625 to 0.5 mg/mL and they observed that the malignant cells proliferate in an increasing rate with increasing the concentration (**Figure 3.7A**). In the same manner, they noticed a time-dependant proliferation rate by performing the experiment up to 42 hours with the same particles concentration, in which a higher rate is obtained at a longer time (**Figure 3.7B**).

However, when the experiments are performed with other cell lines, from healthy as well as cancer versions, the results are totally different. They have thus employed three different cell lines: two healthy versions, which are HEK293T (human embryonic kidney), HMEC (human mammary epithelial cell) and one cancerous version, which is MDA-MB-231 (human breast adenocarcinoma). Experiments performed with those cell lines using the same MSNPs cited above in the same conditions do not afford any particular concentration or time dependency on the cell proliferation (**Figure 3.8**).

*What could this effect be due to?*

Deeper investigations have led the authors to determine that the cell proliferation effect of the MSNPs is mainly associated with a decrease in the reactive oxygen species (ROS) level. ROS are generated species involved in the mechanisms of cellular defence upon xenobiotics internalisation or bacterial invasion.<sup>17,18</sup> In those mechanisms, too high ROS level can be harmful and even lead to the cell death. While several researchers have established the effect of some NPs in the endogeneous ROS level,<sup>20,21</sup> Huang *et al.* have investigated the influence of MSNPs on this feature and they observed that increasing the particle concentration up to 0.5 mg/mL results in the decrease of ROS level (**Figure 3.9A**) in A375 cells. In the same manner, increasing the incubation time for the same particle concentration affords the same tendency in ROS level (**Figure 3.9B**). They have thus concluded that

MSNPs induce A375 cell proliferation by triggering a decrease in the ROS level and the higher is the particle concentration, the higher will be the proliferation rate.

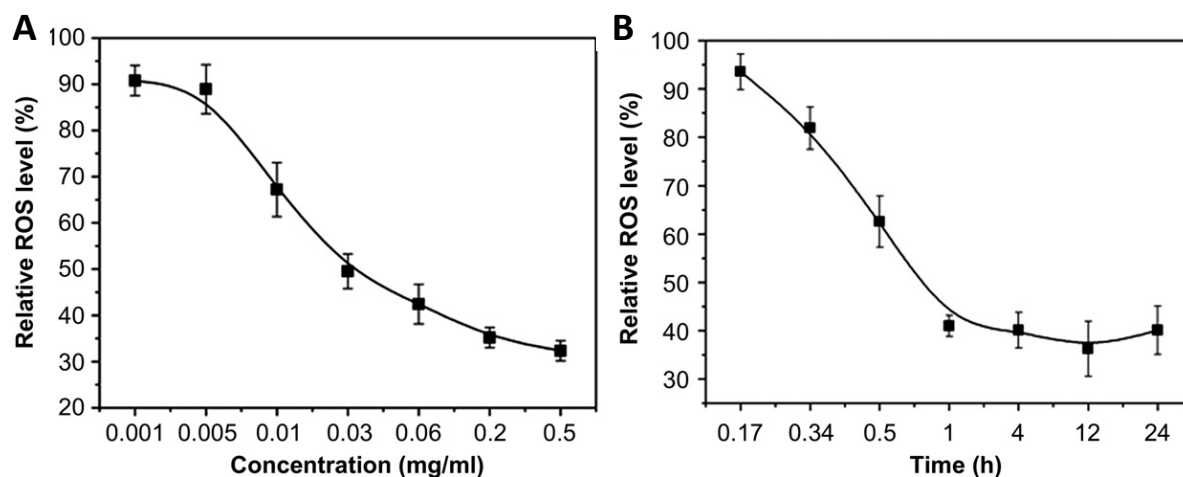


**Figure 3.9** Effect of MSNPs on endogenous reactive oxygen species (ROS) level in A375 cells. (A) Upon incubation for 1h with different particle concentrations and (B) with 0.2 mg/mL of particle for different times. Figure adapted from reference 17.

From the best of our knowledge, no study has been reported on the cytotoxicity of MSNPs towards MCF-10 cell lines. For information, we have also performed experiments with Hs578T cells but, unfortunately, the cells did not survive during the earlier stages of the experiments. In this sub-chapter, we report our results for incubating MCF-10 cells with spherical-like 100-120 nm sized MSNPs at the concentrations of 0.05 and 0.1 mg/mL for 48 hours. Such conditions have been chosen to induce the lowest cytotoxicity according to what we reported from the literature cited at the beginning of this paragraph<sup>13-15</sup> and considering the physic-chemical properties of our MSNPs. The data are illustrated on **Figure 3.10** and what we observe on it is that the cell viability is relatively high and quite similar to that obtained with the control cells. The recorded values are above 86 % for both of the particle concentrations. Nevertheless, less cells death is observed with 0.1 mg/mL particle compared to 0.5 mg/mL. This difference could be due to cell proliferation induced upon MSNPs uptake by the cell triggering ROS decrease, as described above.<sup>16</sup>

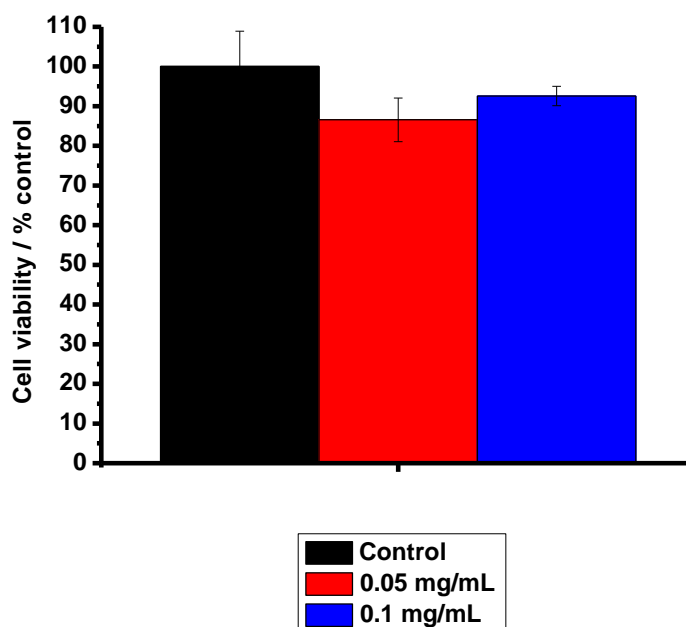


**Figure 3.10** Cell viability assays of MSNPs towards MCF-10 cell line after 48h of incubation at concentrations of 0.05 and 0.1 mg/mL.

We thus can conclude that the MSNPs that we used here induce a negligible toxic effect against MCF-10 cells in the conditions tested. Moreover, the particles rather seem to induce cell proliferation at a relatively high concentration.

### 3.4 Cytotoxicity evaluation of BMONPs

As already mentioned in the introductory chapter, so far, not many hybrid mesoporous silica nanoparticles, with stimuli-cleavable organic moiety within its framework, has been reported in the literature. Nevertheless, in respect to this sub-chapter, we can cite the work done by Croissant *et al.* on ethylene-bis(propyl)disulfide-based periodic mesoporous organosilica nanospheres of 200 nm in diameter.<sup>21</sup> In their investigations, they studied, amongst others, the effect of their particles on MCF-7 cells, which consist in another cancerous version of human breast. They performed the experiment considering particles concentrations ranging from 0 to 0,125 mg/mL and an incubation time of 72 hours. The results that they obtained suggest that, across all the concentrations range, negligible cells death is recorded, being constantly close to 0.

From our side, to evaluate the cytotoxicity of BMONPs, they are incubated with Hs578T and MCF-10 cell lines at two different concentrations (0.05 and 0.1 mg/mL) and the viability is measured after 48 hours. We can see from the data illustrated in **Figure 3.11** that the particles induce a very low cancer cell death of about 4 % at the concentration of 0.5 mg/mL. The Hs578T cells death increases to about 14 % with 0.1 mg/mL but, considering the relatively high concentration, this effect is negligible. Moreover, the toxic effect towards the healthy cells is almost non-existent, where the cell viability is almost 100 % at both concentrations tested. These observations indicate that the hybrid bio-responsive particles are non-cytotoxic under the conditions explored.

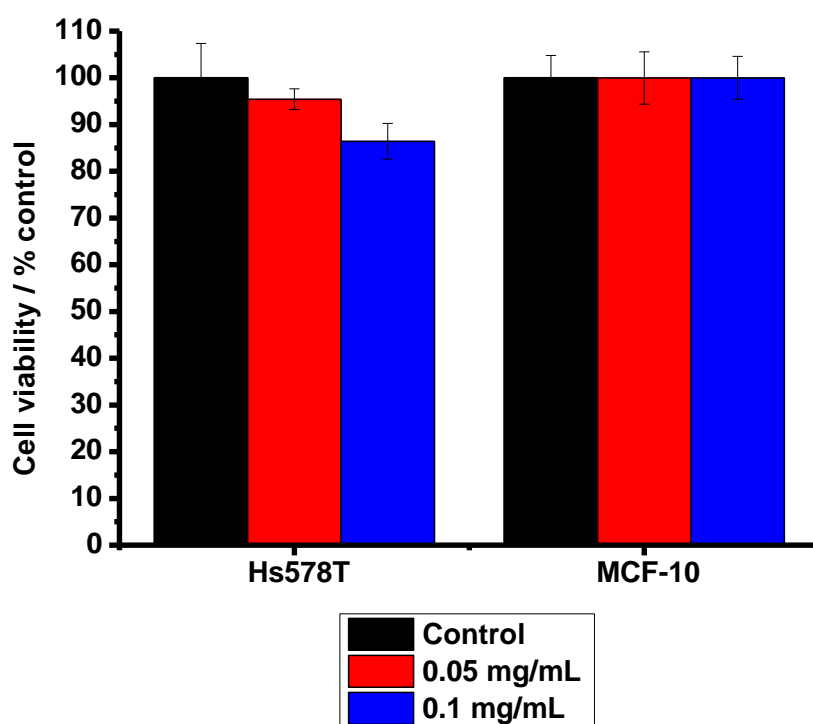


**Figure 3.11** Cell viability assays of BMONPs towards Hs578T and MCF-10 cell lines after 48h of incubation at concentrations of 0.05 and 0.1 mg/mL.

We thus can conclude that our studies, combined with the literature investigations, enable us to say that, up to this thesis, the hybrid stimuli-responsive mesoporous silica nanoparticles with a cleavable organic moiety within its framework exhibit a very low cytotoxicity against a few breast cancer and healthy cells, i.e. MCF-7, MCF-10 and Hs578T lines.

### 3.5 Cytotoxicity evaluation of paclitaxel loaded MSNPs (Pac@MSNPs)

Knowing the high hydrophobicity of paclitaxel, scientists have understood the obvious need to find a more efficient way to deliver such a drug to the site of interest. Several studies have been reported in the literature describing the loading or the adsorption of this chemotherapeutic agent within nanometre sized materials for drug delivery applications towards cancer cells. For instance, we can find the work done by Mugabe *et al.* on the development and *in vitro* characterisation of paclitaxel loaded into spherical hydrophobically derivatised hyperbranched polyglycerols (HPGs) with a diameter of 20 nm.<sup>22</sup> They have tested the toxic effect of the drug loaded material (PTX@HPGs) against a human urothelial carcinoma cell line, KU7, upon exposure with different concentrations of drug (PTX) ranging from 3 to 400 nM for 2 hours and measuring the cell viability 72 hours later. They found out that the cell viability is very dependent of the drug concentration, starting from almost 100 % at 1 nM to reach almost 0 % at 400 nM. However, when they performed a control experiment with PTX alone, the cell viability follows the same profile as with PTX@HPGs, displaying even slightly lower cell viability. Furthermore, Lu *et al.* reported the delivery of PTX from MSNPs into PANC-1 cell line, corresponding to cancer cells from human pancreas.<sup>23</sup> The MSNPs have been designed to have a spherical shape with about 130 nm in diameter and about 2 nm sized porosity. The activity of the system was measured by incubating it with the cancer cells at concentrations of particle ranging from 0.001 to 15 µg/mL, which corresponds to a range of PTX concentrations of 0.001-100 nM. According to the results obtained, it is also possible to mention that the cell viability is dependent of the system concentration. Indeed, the data showed that, at a drug concentration of 0.001 nM, cell viability of about 95 % is observed, while it drops down to about 45 % with 100 nM. Furthermore, there is another point which is worth to emphasize in their studies and it deals with the cytotoxicity induced by PTX alone. When the authors incubated an aqueous suspension of the drug, at any concentration, no cells death is recorded. However, when the cells are treated with a solution of the drug in DMSO, the cell viability followed the same profile as the drug loaded MSN system, showing even slightly lower cell viability. These results leads us to confirm, once more, what is reported in the literature on this drug, i.e., that its lack of efficiency is due to its poor solubility in aqueous phase. On their side, Jia *et al.* have led investigations on loading PTX into the mesopores of MSNPs and on the activity of the designed system against MCF-7 cells.<sup>24</sup> For this purpose, they synthesized spherical MSNPs all possessing the same diameter

in the 200-250 nm range but differ in the pore size, ranging from  $\approx 3$  to 9.7 nm. They have then evaluated the cytotoxicity effect of the different systems at a drug concentration gradient starting from 7.8 and up to 250 ng/mL. The results that they obtained suggest that the inhibitory rate of the systems against the cancer cells is, as we could again expect, dependent of the drug concentration, being about 12 % with MSNPs possessing the smallest pore size at a drug concentration of 7.8 ng/mL to reach almost 100 % with MSNPs having the biggest pore size at a concentration of 250 ng/mL. For each concentration, the same concentration of the drug but alone in solution induces remarkably low inhibitory rate, especially low concentrations.

From our side, we have evaluated the toxic effect of paclitaxel (that we will now abbreviate as Pac) loaded MSNPs (the DDS will be called as Pac@MSNPs) towards MCF-10 cell line. For this purpose, the drug has been loaded into the particle mesopores by diffusion-controlled mechanism where the particles are dispersed in PBS (pH of 7.4) at the concentration of 1 mg/mL. A commercial suspension of Pac is then added while stirring the mixture. Analysis by thermogravimetric analyser (TGA) enables the loading percentage determining which provides a value of 26 weight % (**Figure 3.12**).

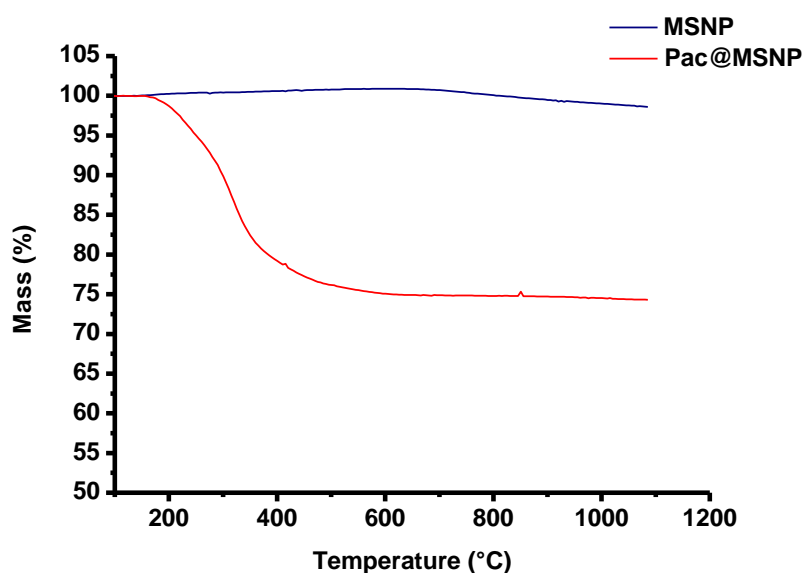


**Figure 3.12** Determining the percentage of Paclitaxel loaded into MSNP. TGA curves of (**blue curve**) as synthesised MSNP after purification and (**red curve**) Pac@MSNPs after washing. The weight loss with Pac@MSNPs compared to MSNP is 26 %.

Once the Pac@MSNP system was obtained, it has been tested with MCF-10 cells at systems concentrations of 0.05 and 0.1 mg/mL. Compared to the case of the cytotoxicity evaluations of the empty materials, in which the cell viability was determined only after 48 hours of incubation time, in the present case, the time points to measure this feature are 24 and 48 hours because it is important for us to know the activity of the system for a long time period as well as for a shorter time. As comparison, suspensions of Pac in PBS (pH 7.4) has also been also used to treat the cells and the concentrations have deliberately been exaggerated to 0.05 and 0.1 mg/mL. The results are summarised in **Figure 3.13** and enable us to first observe that the cell viability profiles correlate with that of empty MSNPs (the higher the NPs concentration, the higher the cell viability, **sub chapter 3.3**). Beside the effect of the MSNP concentration, we also can see that the cytotoxicity of Pac@MSNP is relatively low in the conditions undertaken. The cell viability is higher than 85 % upon a treatment for 24 hours. At the same time, the suspension of Pac alone does not induce a particular toxicity neither where a cell viability higher than 90 % is obtained. Similar results are provided after 48 hours of treatment for both the DDS and the aqueous suspension of Pac, except a little but negligible decrease in the cell viability induced by Pac alone (**Figure 3.13**).

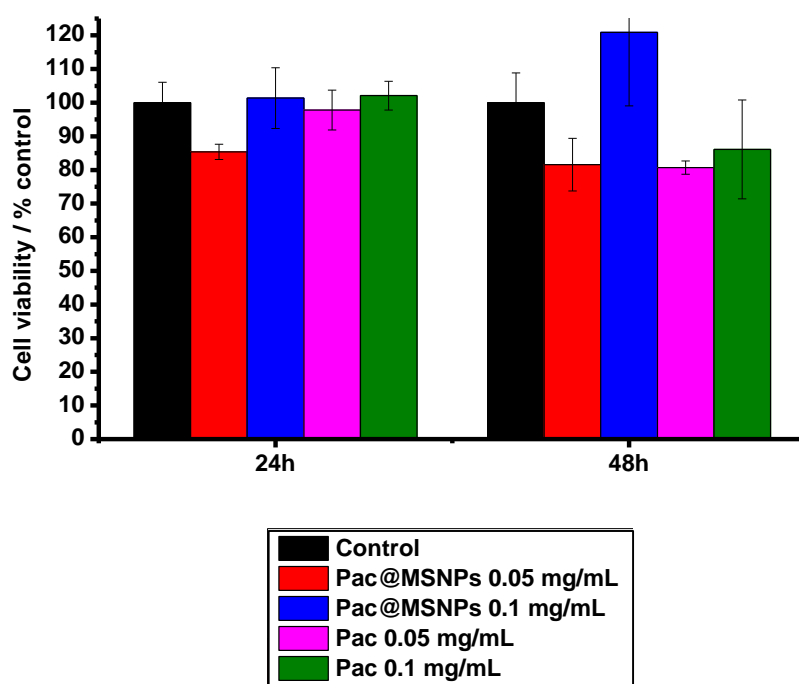


**Figure 3.13** MCF-10 cell viability tests upon incubation with Pac@MSNPs and aqueous Pac suspensions for 24 and 48h at 0.05 and 0.1 mg/mL.

To explain the lack of efficiency of Pac@MSNPs system, we can refer to the drug properties and the mechanism through which it is released. With DDS based on MSNPs where the drug is loaded inside the mesopores via non-covalent bonds, the drug release occurs through a diffusion-controlled mechanism.<sup>25</sup> Therefore, knowing that the biological media are mainly constituted of aqueous phases and that paclitaxel is highly hydrophobic, the release rate can be slowed down, leading to relatively negligible cytotoxic effect.

### 3.6 Cytotoxicity evaluation of paclitaxel loaded BMONPs (Pac@BMONPs)

To evaluate the beneficial effect of the breakability of BMONPs towards cancer treatment via DDS, these particles have been loaded with paclitaxel to obtain a DDS that we will call as Pac@BMONPs. The conditions used are the same as in the case of Pac@MSNPs and the percentage of loaded drug is similar (26 weight %). The human breast cancerous Hs578T cell line has been employed for the *in vitro* experiments. The cells are incubated with Pac@BMONPs at DDS concentrations of 0.05 and 0.1 mg/mL. For comparison, the cells have also been treated with aqueous suspensions of Pac and, as in the case of MSNPs, the drug concentrations have deliberately been exaggerated to 0.05 and 0.1 mg/mL. To determine the effect of our DDS on healthy cells, the same experiments have been performed with the human breast healthy MCF-10 cell line in the same conditions.

**Figure 3.14** reports on the results obtained by treating Hs578T cells with Pac@BMONPs as compared with a treatment with Pac alone. We can see that, after 24 hours of incubation with 0.05 mg/mL of Pac@BMONPs, the cell viability is not very high, displaying a value of 77 % as compared to the control and this value is slightly lower (72 %) with 0.1 mg/mL of DDS. The effect is more visible after 48 hours of incubation. Thus, cell viability of 47 % is obtained upon a treatment with 0.05 mg/mL of Pac@BMONPs and 43 % with 0.1 mg/mL. Regarding the treatment with the suspensions of Pac alone, the results follow an expected trend, knowing that the cells death is always lower as compared to the DDS, showing even 30 % of difference upon incubation for 48 hours at the concentration of 0.05 mg/mL.

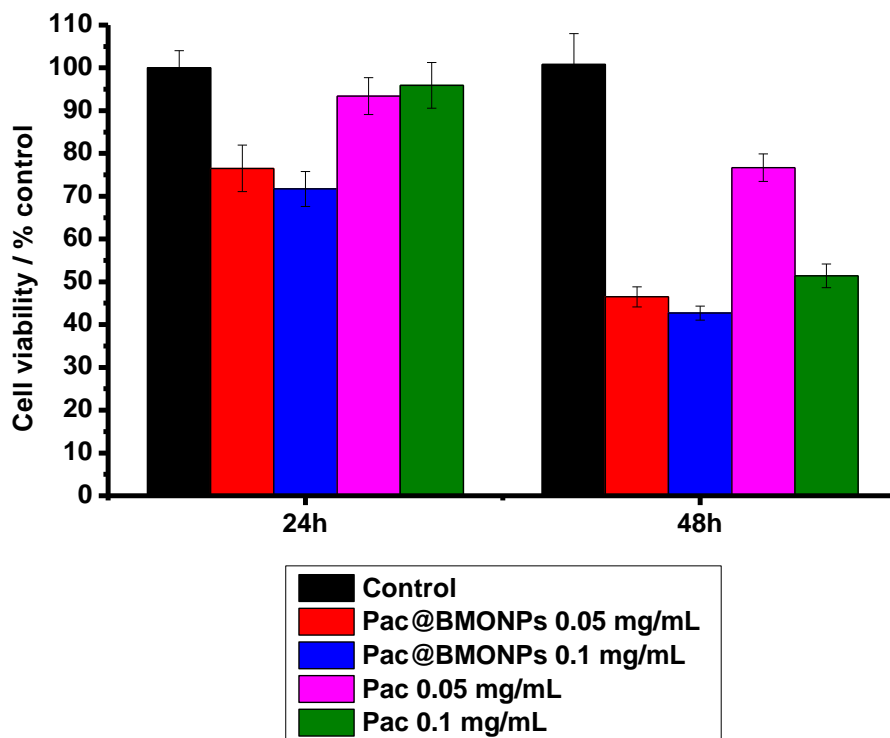


**Figure 3.14** Hs578T cell viability tests upon incubation with Pac@BMONPs and aqueous Pac suspensions for 24 and 48h at 0.05 and 0.1 mg/mL.

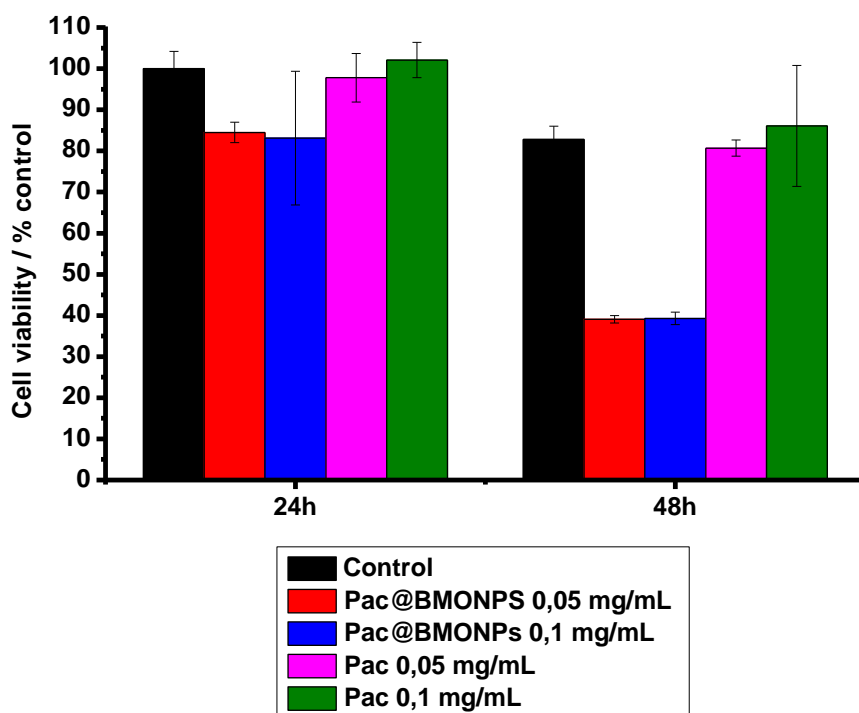


**Figure 3.15** MCF-10 cell viability tests upon incubation with Pac@BMONPs and aqueous Pac suspensions for 24 and 48h at 0.05 and 0.1 mg/mL.

However, the Pac@BMONPs system alters also the viability of the healthy MCF-10 cells as it is shown in **Figure 3.15**. After incubating those cells with 0.05 mg/mL of DDS for 24 hours, 15 % of them died and a similar amount of cells death is obtained with 0.1 mg/mL. As in the case observed for Hs578T cells, a higher cells death is recorded upon a treatment for 48 hours and, thus, 61 % of the cells died with both 0.05 and 0.1 mg/mL of DDS. Nevertheless, the results obtained with the drug alone differ from those observed with the cancer cells. In the present case, no cell death is observed as compared to the control, whether at 0.05 or 0.1 mg/mL of drug concentration, from 24 to 48 hours.

From these results, we thus can report that, thanks to the breakability of BMONPs, it is possible to deliver in an effective way a highly hydrophobic drug such as paclitaxel into a cancer cell. The fact that the particle breaks down forces the payload to reach the interior of the cell and remain inside, leading to its apoptosis. Furthermore, the cytotoxic effect of the drug loaded breakable particles towards the human breast cancerous Hs578T cell line depends not on the concentration but on the duration of the treatment. In this case, a period of 48 hours seems to show the best efficiency. However, due to its very low solubility in aqueous media, the drug alone is poorly effective against these cells. Nevertheless, at the same time, this drug does not alter the activity of the healthy cells in the conditions tested. This statement could be explained by the fact that, due to its relatively high hydrophobic structure, the molecule is hardly internalised by the healthy cells at neutral pH. However, due to the low pH (5.5) in the extracellular matrix of the cancer cells, despite the buffer (pH 7.4) of the culture medium for the *in vitro* experiments, protonations could occur on the molecule, especially on its amino group. This phenomenon could then facilitate the internalisation of the drug by the cancer cell. We also noticed that, towards the healthy MCF-10 cell line, Pac@BMONPs is as cytotoxic as towards Hs578T line. This statement is actually not surprising. In **chapters 1 and 2**, we mentioned that the extracellular matrix of the cancerous cells exhibits a lower pH (5.5) as compared to the physiological one (7.4).<sup>26-30</sup> However, in our case, all the *in vitro* experiments are performed with a phosphate saline solution buffered (PBS) at pH 7.4. Moreover, in sub-chapter **3.2**, we reported that BMONPs are rapidly internalised by the cancer cells (5 minutes) and they seem to go within the lysosomes. These features (PBS 7.4 and fast internalisation) could suggest that, in the conditions of our experiments, the possible acidification of the extracellular matrix of the cancer cells is permanently buffered by the PBS. This phenomenon could prevent the particles to break down and release the drug and the

DDS is thus rapidly internalised by the cell and arrive intact to the lysosomes. It is worth to mention that, whether in healthy or cancer cells, the lysosomes are characterised by a pH of 5.5.<sup>21,22,24,25</sup> According to this information, we could expect that, being pH-responsive, BMONPs will break down and release the loaded drug when arrive within the lysosomes, whether in cancer or healthy cells in the conditions explored, releasing the cytotoxic molecule. Nevertheless, the cytotoxicity effect of Pac@BMONPs can be overcome by minimising its cell uptake. This result can be obtained by functionalising the particle surface with a specific targeting ligand which would interact specifically with the cancer cells. Such a study is under investigations in our group by employing an antibody as a targeting ligand.

### **3.7 Conclusion**

Both of the non-breakable and breakable particles show a high paclitaxel loading capacity and are internalised by both Hs578T and MCF-10 cell lines with a relatively high rate. After being taken up, the materials reside in the perinuclear region of the cytoplasm without inducing any particular cytotoxicity. The DDS based on the conventional MSNP shows a negligible apoptotic effect on MCF-10 cell line due to the weakness of the driving force associated to diffusion-based mechanism to liberate the loaded hydrophobic drug. Whereas the DDS based on the imine-doped particle demonstrates a highly cytotoxic effect thanks to the technology based on the pH-breakability of the vector which forces the drug to get into and stay inside the cell. Moreover, the breakability of the hybrid nanoparticle evidenced in **chapter 2** would facilitate and accelerate the elimination of this vector *in vivo*, thus leading to overcome the critical issue related to its accumulation.

### **3.8 Experimental section**

#### **3.8.1 Materials**

All commercial solvents and reagents were used as received without further purification. Tetraethyl orthosilicate (TEOS), (3-aminopropyl)triethoxysilane (APTES), cetyltrimethylammonium bromide (CTAB) and the dye rhodamine B isothiocyanate (RITC) were purchased from Sigma Aldrich. Distilled water was provided by Merck Millipore and phosphate buffered saline solution was purchased from Thermofisher scientific. For the cells staining, the dyes 4',6-diamidino-2-phénylindole (DAPI) was purchased from Santa Cruz

Biotechnology. The cell lines Hs578T and MCF-10 were kindly offered by the Life and Health Sciences Research Institute (ICVS) – Braga, Portugal.

### ***3.8.2 Preparation of the systems***

#### *Synthesis of the breakable mesoporous organosilica nanoparticles functionalised with rhodamine B isothiocyanate (BMONPs-RITC)*

In a typical procedure, cetyltrimethylammonium bromide (CTAB, 29 mg) was suspended in distilled water (13.5 mL) with a vigorous stirring (750 rpm) at 23 °C and 28 % ammonia was added to have a basic medium (60 µL, pH 9). In a separated vial, APTES (11 µL) was added to a solution of rhodamine B isothiocyanate (RITC, 0.13 mg) in butanol (0.5 mL) and the mixture was stirred at 23 °C during 20 min. In another vial, tetraethyl orthosilicate (TEOS, 26 µL) was added to a solution of the diaminosilane linker (37 mg) in butanol (1 mL) and the mixture was shaken manually to homogenize. The silane solution was then added to the APTES/RITC mixture and the vial was shaken manually to homogenize. The organic solution was eventually added dropwise to the micelles before adding 60 µL more of 28 % ammonia to keep the same pH value in the medium. After stirring during 1d at 23 °C, the material was recovered by means of centrifugation and washing with water and ethanol once each. Eventually, the surfactant was removed through a soxhlet extraction in ethanol at reflux temperature during 4 days and the recovered particles were dried under vacuum.

*Characterisation:* the materials have been characterized by electron microscopy by means of scanning electron microscopy (SEM) and transmission electron microscopy (TEM). Analyses by spectroscopy were also performed such as X-ray photo-electronic spectroscopy (XPS) and IR, as well as nitrogen sorption and zeta potential measurements.

#### *Synthesis of the mesoporous silica nanoparticles functionalized with rhodamine B isothiocyanate (MSNPs-RITC)*

MSNPs-RITC was synthesized by first dissolving cetyl trimethyl ammonium bromide (CTAB; 0.5 g) in a mixture of distilled water (240 mL) and 2 M sodium hydroxide (1.75 mL); the solution was heated to 80°C and stirred vigorously. In a separated vial, APTES (184 µL) was added to a solution of rhodamine B isothiocyanate (RITC, 2.2 mg) in dry ethanol (1,5 mL) and the mixture was stirred at 23 °C during 20 min. In another vial, tetraethyl ortho silicate

(TEOS; 2.5 mL) was dissolved in dry ethanol (1.5 mL) and the solution was added to the APTES/RITC mixture while stirring for 5 more min. Once the temperature of the CTAB solution had stabilized, the ethanol solution containing TEOS/APTES/RITC was added. After 2 h, the solution was cooled down to room temperature and the particles were recovered by means of centrifugation and washing once with ethanol. To remove the surfactant from the pores, the material was refluxed in ethanol overnight with a few drop of hydrochloric acid 37 % and the particles were obtained after centrifugations, washing 3 times with ethanol and drying under vacuum.

*Characterisation:* the materials have been characterized by electron microscopy by means of scanning electron microscopy (SEM) and transmission electron microscopy (TEM). Analyses by spectroscopy were also performed such as X-ray photo-electronic spectroscopy (XPS) and IR, as well as nitrogen sorption and zeta potential measurements.

#### *Loading paclitaxel into BMONPs and MSNPs*

In a typical procedure, BMONPs or MSNPs (10mg) were suspended in PBS at pH 7.4 (10 mL) followed by sonication over 15 min to disperse them. The suspension was then stirred at a medium speed before the addition of 850  $\mu$ L of paclitaxel suspension of 6 mg/mL. The mixture was stirred overnight before a series of centrifugation and washing with PBS at pH 7.4 to remove the drug adsorbed on the outer surface of the particles.

### **3.8.3 *In vitro* experiments**

#### *Cell culture conditions and cell viability assays*

Hs578T and MCF-10 were used in this study as models of human breast carcinoma and human breast epithelial cells, respectively. Hs578T breast carcinoma cells were maintained in DMEM medium (Gibco) supplemented with 10% (v/v) fetal bovine serum (FBS) (Gibco, Invitrogen, USA) and 1% (v/v) penicillin–streptomycin solution (P/S)(Invitrogen, USA). MCF-10 epithelial mammary cells were maintained in DMEM/F-12 medium (Gibco) supplemented with 5% (v/v) FBS, 1% P/S, 1% hydrocortisone (50  $\mu$ g/mL) (Sigma Aldrich, St. Louis, MO, USA), 500  $\mu$ L of insulin solution human (Sigma Aldrich, St. Louis, MO, USA), 50  $\mu$ L cholera toxin (Sigma Aldrich, St. Louis, MO, USA) and 80  $\mu$ L of epidermal growth factor (EGF) per 4 mL of medium (Peprotech, London, UK). Both cell lines were grown at 37 °C and 5% CO<sub>2</sub>.

For the experiments, Hs578T (7500 cells/100  $\mu$ L/well) and MCF-10 (5000 cells/100  $\mu$ L/well) cells were seeded in 96-well plates and incubated at 37 °C in a 5% CO<sub>2</sub> humidified atmosphere for 24 h. In order to assess the effects of the raw materials and DDS, cells were incubated with 0.05 mg/mL and 0.1 mg/mL of the samples in culture medium for 24 h and 48 h. Controls were performed with culture medium alone. To study the effects of paclitaxel (PTX) cells were incubated with 0.017 mg/mL, 0.033 mg/mL, 0.05 mg/mL, and 0.1 mg/mL for 24 h and 48 h. Cell viability was assessed using the Sulforhodamine B (SRB) assay. After each incubation period, the spent media were removed and the cells were fixed with cold 10% trichloroacetic acid (TCA) (xxx) for one hour at 4 °C. Then the cells were stained with 0.4 % SRB (Sigma Aldrich, St. Louis, MO, USA) and the incorporated dye was solubilized with Tris Base (10 mM) (Sigma Aldrich, St. Louis, MO, USA). Absorbance was monitored with a microplate reader at 490 nm. Cell viability was determined as percentage of viability: (OD experiment/OD control)  $\times$  100 (%). Results are presented as mean  $\pm$  standard deviation (SD) of three independent experiments, each in triplicate.

#### *Confocal experiments (procedure used for z-stacking)*

Hs 578T and MCF-10 cell lines were seeded on coverslips in 24-well plates with the density of  $2.5 \times 10^4$  cells/well and incubated at 37 °C in 5% CO<sub>2</sub> atmosphere for 24 h. Spent media were removed, and cells were incubated with 0.05 mg/mL of particles during 4 and 24 h. Cells were washed twice with PBS and fixed with cold metanol during 15 min, washed once with PBS Glicine 10 Mm, washed again twice with PBS and permeabilized with triton x-100 0.1 % for 10 min. Next, and after two washes with PBS, cells were blocked with BSA 5% in PBS during 30 min and then incubated with  $\alpha$ -tubulin antibody (SC23948 Santacruz) diluted in BSA 5% in PBS (1:100) during 2 h at room temperature (RT). In the next step, cells were washed two times with PBS (5 min each) and incubated with the secondary antibody Alexa Fluor 488 goat anti-mouse (A11001, Life Technologies) diluted in BSA 5% in PBS (1:250) during 1 h at room temperature in the dark. Then, cells were washed twice with PBS and the nuclei were stained with DAPI for 10 min. Finally, after two washes with PBS (5 min each) and one wash with sterile water (very quickly), cells were mounted in Permafluor (Thermo Scientific).

Confocal images were acquired in na FV1000 Olympus confocal microscope system equipped with 60 times magnification, numerical aperture 1.35 of Olympus LSM UPLSAPO oil immersion objective lens (Olympus). The rhodamine B isothiocyanate (RITC) grafted on the

particles was excited by a continuous wave (cw) laser at 559 nm while the cells previously co-stained with DAPI (excitation/emission wavelength: 405 nm/461 nm), and Alexa Fluor® 488 dye (excitation/emission wavelength: 488 nm/520 nm) were excited independently at 405, and 488 nm, respectively. The emissions of the particles, DAPI, and Alexa Fluor® 488 dye were collected using their corresponding emission filter. All image processing was done by Fluoview FV1000 software (Olympus). False colour images were adjusted to better distinguish the particles and cellular organelles.

### 3.9 References

1. Latest world cancer statistics Global cancer burden rises to 14.1 million new cases in 2012: Marked increase in breast cancers must be addressed. *International Agency for Research on Cancer - World Health Organization* (2013).
2. Ferlay, J., Soerjomataram, I., Dikshit, R., Eser, S., Mathers, C., Rebelo, M., Parkin, D. M., Forman, D. & Bray, F. Cancer incidence and mortality worldwide: Sources, methods and major patterns in GLOBOCAN 2012: Globocan 2012. *Int. J. Cancer* **136**, E359–E386 (2015).
3. Bray, F., Ren, J.-S., Masuyer, E. & Ferlay, J. Global estimates of cancer prevalence for 27 sites in the adult population in 2008. *Int. J. Cancer* **132**, 1133–1145 (2013).
4. Curado, M. P. Breast cancer in the world: incidence and mortality. *Salud Pública México* **53**, 372–384 (2011).
5. Schiff, P. B., Fant, J. & Horwitz, S. B. Promotion of microtubule assembly in vitro by taxol. *Nature* **277**, 665–667 (1979).
6. Arnal, I. & Wade, R. H. How does taxol stabilize microtubules? *Curr. Biol.* **5**, 900–908 (1995).
7. Amos, L. A. & Löwe, J. How Taxol® stabilises microtubule structure. *Chem. Biol.* **6**, R65–R69 (1999).
8. Howarth, F. C., Calaghan, S. C., Boyett, M. R. & White, E. Effect of the microtubule polymerizing agent taxol on contraction, Ca<sup>2+</sup> transient and L-type Ca<sup>2+</sup> current in rat ventricular myocytes. *J. Physiol.* **516**, 409–419 (1999).
9. Hackett, A. J., Smith, H. S., Springer, E. L., Owens, R. B., Nelson-Rees, W. A., Riggs, J. L. & Gardner, M. B. Two syngeneic cell lines from human breast tissue: the aneuploid mammary epithelial (Hs578T) and the diploid myoepithelial (Hs578Bst) cell lines. *J. Natl. Cancer Inst.* **58**, 1795–1806 (1977).
10. Engel, L. W. & Young, N. A. Human breast carcinoma cells in continuous culture: a review. *Cancer Res.* **38**, 4327–4339 (1978).
11. Lacroix, M. & Leclercq, G. Relevance of Breast Cancer Cell Lines as Models for Breast Tumours: An Update. *Breast Cancer Res. Treat.* **83**, 249–289 (2004).
12. Kresge, C. T., Leonowicz, M. E., Roth, W. J., Vartuli, J. C. & Beck, J. S. Ordered mesoporous molecular sieves synthesized by a liquid-crystal template mechanism. *Nature* **359**, 710–712 (1992).

13. Wang, Y., Zhao, Q., Hu, Y., Sun, L., Bai, L., Jiang, T. & Wang, S. Ordered nanoporous silica as carriers for improved delivery of water insoluble drugs: a comparative study between three dimensional and two dimensional macroporous silica. *Int. J. Nanomedicine* **4015** (2013).
14. Hudson, S. P., Padera, R. F., Langer, R. & Kohane, D. S. The biocompatibility of mesoporous silicates. *Biomaterials* **29**, 4045–4055 (2008).
15. Tao, Z., Toms, B. B., Goodisman, J. & Asefa, T. Mesoporosity and functional group dependent endocytosis and cytotoxicity of silica nanomaterials. *Chem. Res. Toxicol.* **22**, 1869–1880 (2009).
16. Huang, X., Zhuang, J., Teng, X., Li, L., Chen, D., Yan, X., Tang, F. The promotion of human malignant melanoma growth by mesoporous silica nanoparticles through decreased reactive oxygen species. *Biomaterials* **31**, 6142–6153 (2010).
17. Xia, T., Kovoichich, M., Brant, J., Hotze, M., Sempf, J., Oberley, T., Sioutas, C., Yeh, J. I., Wiesner, M. R. & Nel, A. E. Comparison of the Abilities of Ambient and Manufactured Nanoparticles To Induce Cellular Toxicity According to an Oxidative Stress Paradigm. *Nano Lett.* **6**, 1794–1807 (2006).
18. Ray, P. D., Huang, B.-W. & Tsuji, Y. Reactive oxygen species (ROS) homeostasis and redox regulation in cellular signaling. *Cell. Signal.* **24**, 981–990 (2012).
19. AshaRani, P. V., Low Kah Mun, G., Hande, M. P. & Valiyaveetil, S. Cytotoxicity and Genotoxicity of Silver Nanoparticles in Human Cells. *ACS Nano* **3**, 279–290 (2009).
20. Pan, Y., Leifert, A., Ruau, D., Neuss, S., Bornemann, J., Schmid, G., Brandau, W., Simon, U. & Jahnen-Dech, W. Gold Nanoparticles of Diameter 1.4 nm Trigger Necrosis by Oxidative Stress and Mitochondrial Damage. *Small* **5**, 2067–2076 (2009).
21. Croissant, J., Cattoën, X., Man, M. W., Gallud, A., Raehm, L., Trens, P., Maynadier, M. & Durand, J.-O. Biodegradable Ethylene-Bis(Propyl)Disulfide-Based Periodic Mesoporous Organosilica Nanorods and Nanospheres for Efficient In-Vitro Drug Delivery. *Adv. Mater.* **26**, 6174–6180 (2014).
22. Mugabe, C., Liggins, R. T., Guan, D., Manisali, I., Chafeeva, I., Brooks, D. E., Heller, M., Jackson, J. K. & Burt, H. M. Development and in vitro characterization of paclitaxel and docetaxel loaded into hydrophobically derivatized hyperbranched polyglycerols. *Int. J. Pharm.* **404**, 238–249 (2011).
23. Lu, J., Liong, M., Sherman, S., Xia, T., Kovoichich, M., Nel, A. E., Zink, J. I. & Tamanoi, F. Mesoporous Silica Nanoparticles for Cancer Therapy: Energy-Dependent Cellular Uptake and Delivery of Paclitaxel to Cancer Cells. *NanoBiotechnology* **3**, 89–95 (2007).
24. Jia, L., Shen, J., Li, Z., Zhang, D., Zhang, Q., Liu, G., Zheng, D. & Tian, X., In vitro and in vivo evaluation of paclitaxel-loaded mesoporous silica nanoparticles with three pore sizes. *Int. J. Pharm.* **445**, 12–19 (2013).
25. Sun, R., Wang, W., Wen, Y. & Zhang, X. Recent Advance on Mesoporous Silica Nanoparticles-Based Controlled Release System: Intelligent Switches Open up New Horizon. *Nanomaterials* **5**, 2019–2053 (2015).

26. Montcourrier, P., Silver, I., Farnoud, R., Bird, I. & Rochefort, H. Breast cancer cells have a high capacity to acidify extracellular milieu by a dual mechanism. *Clin. Exp. Metastasis* **15**, 382–392 (1997).
27. Glunde, K., Guggino, S. E., Solaiyappan, M., Pathak, A. P., Ichikawa, Y. & Bhujwala, Z. M. Extracellular Acidification Alters Lysosomal Trafficking in Human Breast Cancer Cells. *Neoplasia N. Y. N.* **5**, 533–545 (2003).
28. Cardone, R. A., Casavola, V. & Reshkin, S. J. The role of disturbed pH dynamics and the Na<sup>+</sup>/H<sup>+</sup> exchanger in metastasis. *Nat. Rev. Cancer* **5**, 786–795 (2005).
29. Iessi, E., Marino, M. L., Lozupone, F., Fais, S. & De Milito, A. Tumor acidity and malignancy: novel aspects in the design of anti-tumor therapy. *Cancer Ther* **6**, 55–66 (2008).
30. Kato, Y., Ozawa, S., Miyamoto, C., Maehata, Y., Suzuki, A., Maeda, T. & Baba, Y. Acidic extracellular microenvironment and cancer. *Cancer Cell Int.* **13**, 89–89 (2013).

## Chapter 4

# Encapsulation and *in vitro* delivery of an antibody and a chemotherapeutic agent for cancer treatment

### Abstract

Bioactive molecules have been encapsulated in stimuli-responsive hybrid organic/inorganic nanocapsules through a nanoemulsion method by creating reverse micelles in a water-in-oil phase. Two different stimuli have been explored, which are pH and reduction sensitivity, by the incorporation of a pH-cleavable linker in the one hand and of a reduction sensitive one in the other. Characterisation by scanning electron microscopy and dynamic light scattering enabled to confirm spherical-like shaped materials with a diameter size in the nanometre range. Zeta potential measurements suggested highly negative charges on the surface of the particles. First, an antibody, anti-E6 monoclonal antibody was encapsulated. Besides the confirmation by morphology, size distribution and zeta potential analyses, the particles showed relatively good stability upon suspension in cell culture medium for a short time, then the medium components such as proteins, amino acids or ionic salts seemed to interact with the nanomaterials, likely forming a corona on their surface. Moreover, the particles seemed also to aggregate between each other, resulting in larger size distributions. Furthermore, to enhance the biocompatibility of the nanomaterials for possible *in vivo* studies, they have been functionalised with poly(oxyethylene) also known as poly(ethylene glycol). This process was confirmed by dynamic light scattering and zeta potential characterisations. Eventually, *in vitro* experiments have been performed towards HeLa cells. The experiments were monitored by confocal microscopy with which, it was possible to observe the particles after a fast internalisation which then resulted in their location within the lysosomes. This technique was then extended to the encapsulation of a smaller molecule, Doxorubicin and, from the release profile monitored by fluorimetry, a controllable breaking rate of the nanocapsules was obtained. Furthermore, HeLa cell internalisation studies by confocal microscopy resulted in

images on which the particles were rapidly internalised by the cells, likely within the lysosomes. Eventually, the toxic effect of the system based on the pH-breakable property towards HeLa cells was tested and the results were highly positive.

## 4.1 Introduction

Intracellular delivery of particular proteins has attracted a great deal of attention in nanomedicine for protein or peptide-based nanotherapeutics and several strategies have been undertaken.<sup>1-3</sup> Nevertheless, the efficient delivery of native, functional proteins or enzymes, in an active conformation to the necessary site of action, still remains a challenge. Under physiological conditions, proteins and peptides tend to undergo degradation by proteolytic enzymes or, in the case of the higher-molecular-weight proteins, may be recognised by neutralising antibodies.<sup>4,5</sup> A possible strategy to overcome these limitations consists in shielding the protein in a nanocapsule. This technique provides several advantages such as full protection of the payload and, consequently, its entire stability. Some examples of diverse soft host structures have been reported on nanocapsule systems to deliver proteins into cancer cells. Recently, Yuba *et al.* reported a system composed of pH-sensitive polymer-lipids that they used for antigen delivery for cancer immunotherapy.<sup>6,7</sup> The material is based on fusogenic polymer moieties such as 3-methyl glutarylated poly(glycidol) and 2-carboxycyclohexane-1-carboxylated poly(glycidol), connected to a phosphatidylethanolamine head group. Incorporation of these pH-sensitive polymer-lipids into egg yolk phosphatidylcholine liposomes produce pH-sensitive liposomes which are stable at neutral pH and destabilised in response to very small pH changes in weakly acidic media. Hard host nanoparticles have also been developed for the encapsulation of bioactive macromolecules. Very recently, our group reported the use of hard nanoparticles to effectively encapsulate and deliver into C6 glioma cells highly cytotoxic proteins such as TRAIL Apo2 ligand and onconase. Beside this efficient method, one great advantage of the system is its synergic stimuli-responsive and biodegradability property upon the incorporation of a reduction sensitive organic linker within the framework.<sup>8</sup> More precisely, the organic linker is bis[3-(triethoxysilyl)propyl]disulfide and its structure is represented in **Figure 4.1**.

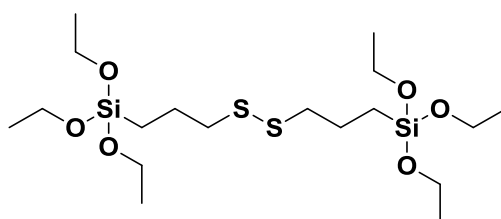


**Figure 4.1** Structure of bis[3-(triethoxysilyl)propyl]disulfide, the reduction-sensitive organic linker incorporated in the nanocapsule framework in previous studies in the group.

In the present chapter, we report the extension of the stimuli-responsive biodegradability of the silica nanocapsules. For this purpose, we describe herein the incorporation of the pH-responsive diiminosilane linker that we used within the mesoporous silica nanoparticles (MSNPs) in **chapters 2 and 3**. The structure of this molecule is recalled in **Figure 4.2**.

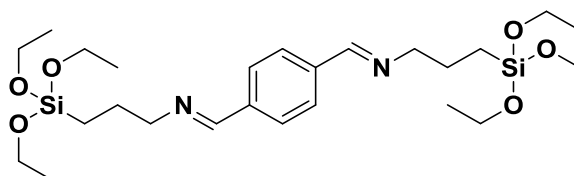


**Figure 4.2** Structure of the diiminosilane, the pH-sensitive organic linker incorporated in the nanocapsule framework in the present studies.

Simultaneously in these works, we also extended the type of encapsulated protein and thus effectively loaded anti-E6 monoclonal antibody (mAB) from mouse papilloma virus. E6 is an oncoprotein from human papillomavirus (HPV) which leads, by its action, to a decrease in p53 tumour suppressor levels. Consequently, cells become cancerous, unable of apoptosis mediated by p53.<sup>9</sup> This mechanism of action is illustrated in **Figure 4.3**.

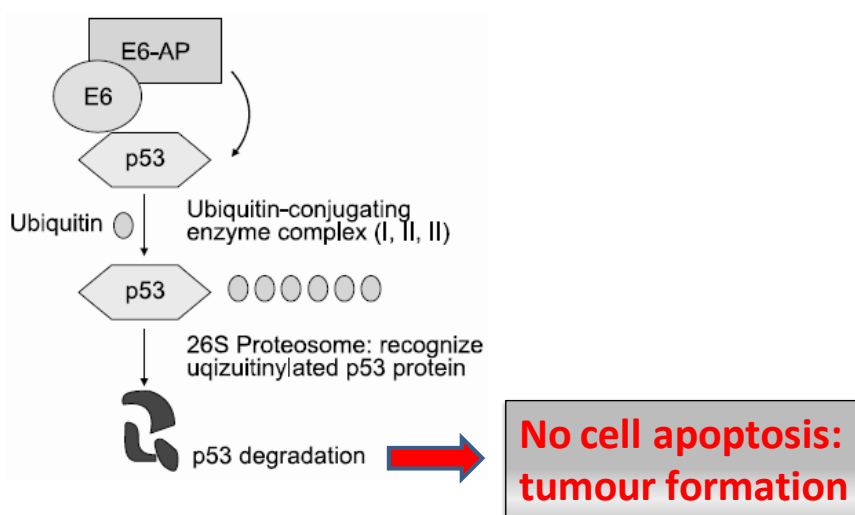


**Figure 4.3** Mechanism of action of E6 to inhibit the effect of p53 in its tumour suppressing action. Figure adapted from reference 9.

mAB antibody, by neutralising E6 leads to p53 reactivation and apoptosis. Some investigations related to the delivery of such an antibody have been reported. We can, for example, find the works conducted by Togtema *et al.* in which they deliver the antibody to transformed cervical keratinocytes through a so called sonoporation technique.<sup>10</sup> The experiments result in the restoration of p53 expression.

In our case, we use the advantages provided by the pH-breakable hard materials to deliver the bioactive macromolecule to Hela cells. As comparisons, we also encapsulated the antibody in the reduction sensitive capsule based on the disulfide function (**Figure 4.1**).

*After these successful encapsulations and deliveries of proteins, another challenge comes up. Is it also possible to effectively encapsulate smaller molecules such as drugs into biodegradable and bio-responsive hard silica nanomaterials and deliver them into cancer cells? And if it is the case, how can it be carried out?*

In **chapter 3**, the use of MSNPs towards drug delivery in the field of cancer therapy was discussed. Due to the small size of some drugs or other payload molecules as compared to that of the pores of MSNPs, many drug delivery systems (DDS) based on MSNPs suffer from leakage issues leading to premature release and thus severe side effects.<sup>11,12</sup> Indeed, as most of the guests are loaded/stored in the pores via non-covalent bonds, the interaction between the host and the guest is not very stable and the payload tend to leak out. Thus, MSNPs often need what is called “gatekeepers” by surface functionalisation<sup>13–17</sup> or outer surface polymer coating such as with poly-L-lysine (PLL) which can induce undesired cytotoxicity.<sup>18,19</sup> To overcome these limitations, the novel systems based on non-porous nanocapsules are attracting a great deal of attention. In such systems, the guest is encapsulated inside a nanoshell as described above for the protein encapsulation systems. This strategy provides several advantages such as full protection of the payload and, consequently, its entire stability, but also the prevention of premature release along the entire circulation of the system until reaching its target *in vivo*.<sup>8</sup> Some examples of diverse soft host structures have been reported on nanocapsule systems to deliver drugs into cancer cells. Ten years ago, Gokhale *et al.* published an article on the encapsulation of Doxorubicin into liposomes using phosphatidylcholine, cholesterol and synthetic tetramyristoyl cardiolipin.<sup>20</sup> Doxorubicin is a potent chemotherapeutic agent commonly used in cancer treatment.<sup>21–25</sup> Hard host nanoparticles have also been developed for the encapsulation of such a drug. An example is

described by Sanyakamdhorm *et al.* in which they encapsulate Doxorubicin and an analogue into chitosan nanoparticles.<sup>26</sup>

However, to the best of our knowledge, no system of drug encapsulation into bio-responsive and breakable hard silica nanocapsules has been yet reported. Thus, encouraged by our novel technology based on the pH-breakable system, we herein rise to this challenge. We have thus effectively encapsulated Doxorubicin into the hybrid nanocapsule which is able to break down upon contact with acidic medium and deliver the loaded drug to provide effective cytotoxicity towards HeLa cells. The system has been designed by incorporating *in situ* the diiminosilane linker within its silica framework during the synthesis. To widen the technology library, the reduction sensitive system based on bis[3-(triethoxysilyl)propyl]disulfide has also been developed.

#### **4.2 Encapsulation of monoclonal anti-E6 antibody**

The encapsulation of monoclonal anti-E6 antibody has been done based on a previous method reported by our group for the encapsulation of other proteins.<sup>8</sup> An aqueous solution of anti-E6 monoclonal antibody from mouse papilloma virus at the concentration of 0.091 mg/mL is entrapped into reverse micelles formed by mixing Triton™ X-100 with n-hexanol and cyclohexane. Tetraethyl orthosilicate (TEOS) is added as silica source, which is combined with the organic diiminosilane linker by 30 mole %. An aqueous solution of 28 % ammonia is added to the mixture as base to trigger the silica hydrolysis and the reaction is allowed to occur over 4 hours at room temperature before precipitating the particles by the addition of acetone. This latter is followed by a series of washing with distilled water to remove the undesirable water-soluble chemicals and with ethanol to remove the organic chemicals. To compare with the previous method, the antibody has also been encapsulated into the disulfide-doped breakable silica shell in the same manner, using bis[3-(triethoxysilyl)propyl]disulfide by 30 mole % as organic moiety. In order to carry out comparison studies with the non-breakable shell which lacks organic moiety, the same procedure has been realised with TEOS by 100 mole %. All this process is illustrated in **Figure 4.4A**. From now on, we will call the capsule as AntiE6@imine-SiO<sub>2</sub>-NCs in the case where the organic linker is diiminosilane, AntiE6@SS-SiO<sub>2</sub>-NCs in that where bis[3-(triethoxysilyl)propyl]disulfide is employed and AntiE6@SiO<sub>2</sub>-NCs for the non-breakable one.

### 4.2.1 Morphology of the resulted particles

A morphological characterisation by scanning electron microscopy (SEM) shows highly monodisperse spherical-like shaped nanoparticles with average diameters of about 80, 60 and 70 nm for AntiE6@imine-SiO<sub>2</sub>-NCs, AntiE6@SS-SiO<sub>2</sub>-NCs and AntiE6@SiO<sub>2</sub>-NCs respectively (Figure 4.4B-D).

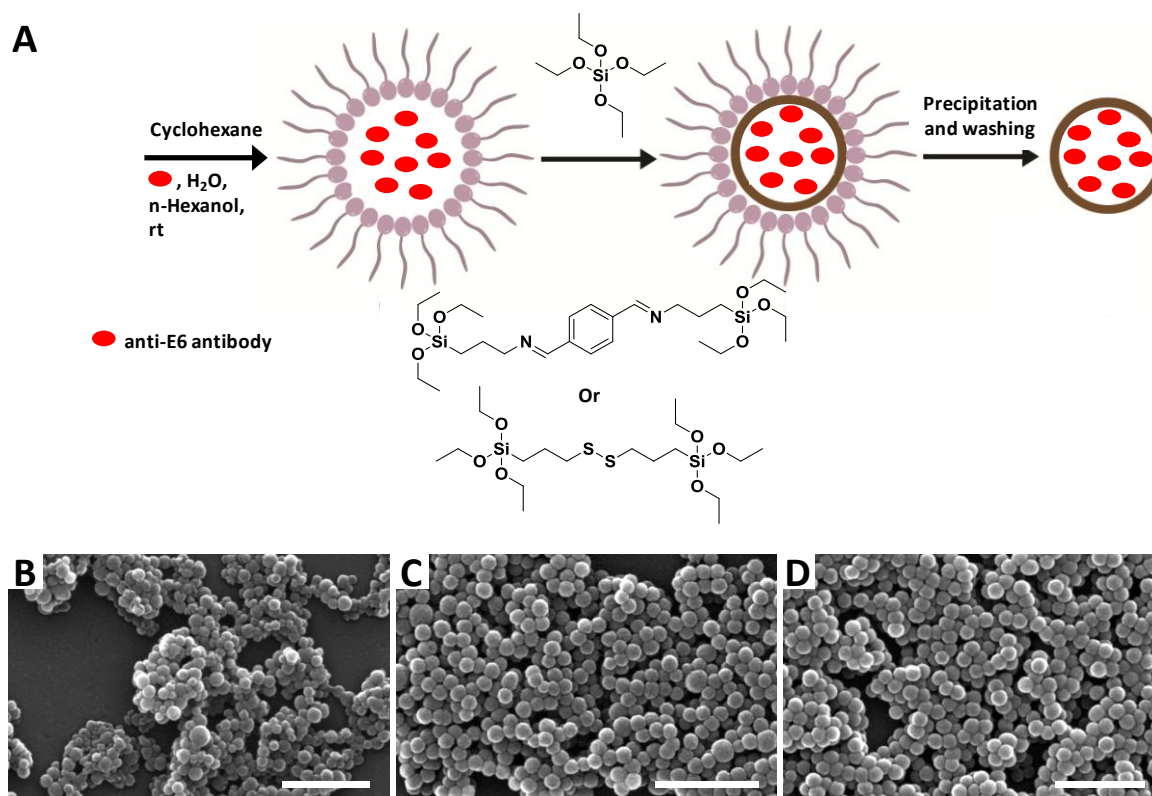


**Figure 4.4** (A) Representative scheme of the synthesis of the breakable silica nanocapsules. SEM images of (B) AntiE6@imine-SiO<sub>2</sub>-NCs, (C) AntiE6@SS-SiO<sub>2</sub>-NCs and (D) AntiE6@SiO<sub>2</sub>-NCs. Scale bar = 400 nm.

Dynamic light scattering (DLS) analysis enables us to determine the size distribution of the capsules in aqueous phase. For this purpose, the particles are dispersed into a phosphate buffered saline (PBS) solution at pH 7.4 in a plastic cuvette and the sample is placed into the DLS device to run the analysis. Mathematic calculations from the software provides size distributions similar to those estimated with SEM, i.e.,  $72.1 \pm 19.0$  nm,  $50.3 \pm 12.5$  nm and  $66.0 \pm 16.8$  nm for AntiE6@imine-SiO<sub>2</sub>-NCs, AntiE6@SS-SiO<sub>2</sub>-NCs and AntiE6@SiO<sub>2</sub>-NCs respectively were recorded (Figure 4.5).

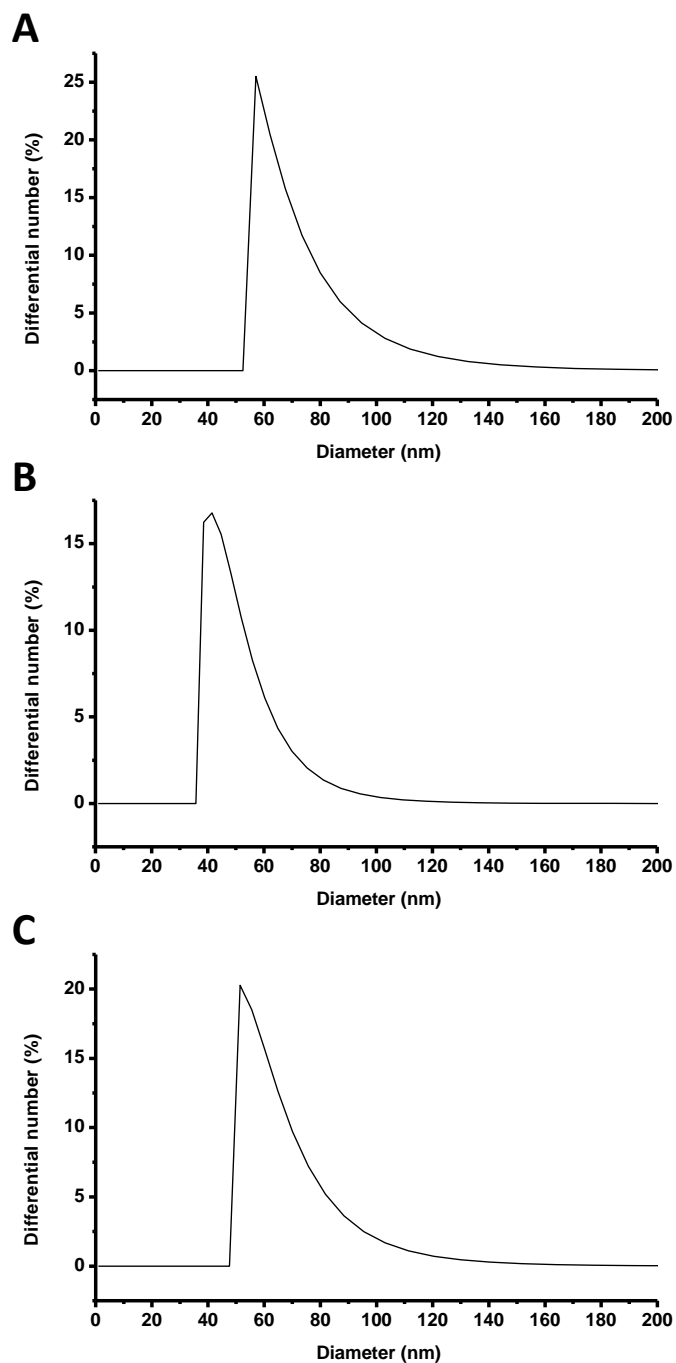


**Figure 4.5** DLS size number distributions of (A) AntiE6@imine-SiO<sub>2</sub>-NCs, (B) AntiE6@SS-SiO<sub>2</sub>-NCs and (C) AntiE6@SiO<sub>2</sub>-NCs. The calculated average sizes are  $72.1 \pm 19.0$  nm,  $50.3 \pm 12.5$  nm and  $66.0 \pm 16.8$  nm for AntiE6@imine-SiO<sub>2</sub>-NCs, AntiE6@SS-SiO<sub>2</sub>-NCs and AntiE6@SiO<sub>2</sub>-NCs respectively.

Zeta potential measurements performed by dispersing the particles into a PBS solution at pH 7.4 indicate highly negative current values for the three capsules. The current values are -

25.38 ± 2.66 mV, -20.25 ± 0.18 mV and -30.14 ± 0.57 mV for AntiE6@imine-SiO<sub>2</sub>-NCs, AntiE6@SS-SiO<sub>2</sub>-NCs and AntiE6@SiO<sub>2</sub>-NCs respectively.

#### ***4.2.2 Colloidal stability in cell culture medium***

In the view of leading studies in biological media with the nanocapsules, investigations on the colloidal stability of those particles in such media are of great importance. Indeed, the physico-chemical properties of nanoparticles can be influenced by the medium in which they are suspended and this property will affect their *in vitro* and *in vivo* behaviours.<sup>27,28</sup> Starting from the PBS solution in which the particles are dispersed to perform DLS and zeta potential analyses in this thesis, this solution is composed of phosphate ions which can be considered as electrolytes. Such electrolytes can interact with the nanoparticles and influence their colloidal stability.<sup>27,28</sup> Several features can be considered in this case, such as inter-particle behaviour resulting from intermolecular and surface forces (e.g. van der Waals (vdW) forces, the repulsive electrostatic double layer (EDL), and structural forces such as depletion attraction). These phenomena can thus explain the small difference observed between the diameter sizes measured by SEM and the size distributions obtained by DLS for our spherical-like shaped nanoparticles. Moreover, the interactions between nanomaterials and biological systems can affect the *in vivo* biocompatibility and toxicity of the materials.<sup>27,29,30</sup> In this sub-chapter, *in vitro* studies will be discussed. Therefore, without considering the complexity of all the phenomena possibly happening inside the cells after the particles internalisation, we will focus on the colloidal behaviour of nanoparticles in cell culture media (CCM). CCM is composed of several components. Among these components, we can find ionic salts which can behave as electrolytes, biomolecules such as amino acids and proteins such as globulins or serum albumin.<sup>27,28</sup> The proteins present in the culture media can interact with the particles by forming a so called corona prior to any contact with cells and such interactions can affect the cell uptake of the particles by, for instance, changing the hydrodynamic radius. Jiang *et al.* illustrate this phenomenon in **Figure 4.6**.<sup>31</sup> The authors quantitatively analysed the adsorption of human transferrin onto small (radius approx. 5 nm) polymer-coated FePt nanoparticles by using fluorescence correlation spectroscopy. They found out that transferrin bind to the negatively charged nanoparticles with an affinity of approximately 26 mM in a cooperative fashion and form a monolayer with a thickness of 7 nm.

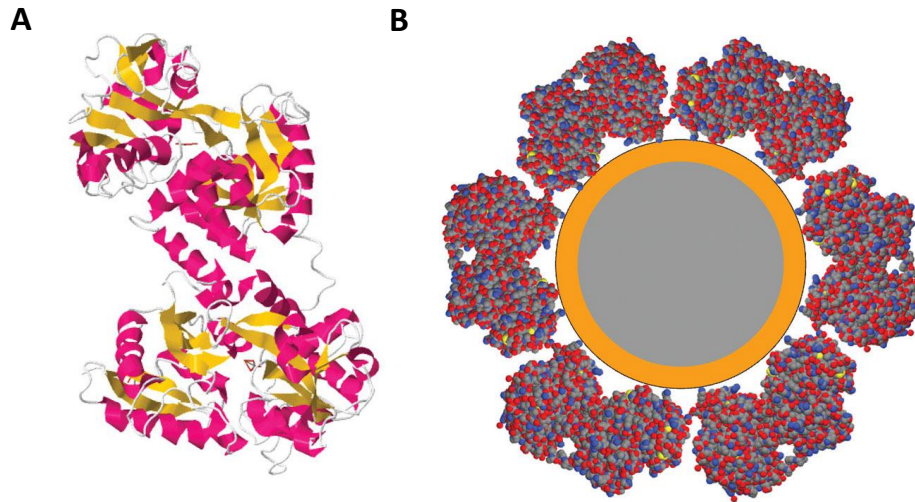


**Figure 4.6** Structural depictions of transferrin (TF) and the protein corona. **(A)** Cartoon representation of the (chicken) TF polypeptide chain (protein database entry 1N04). **(B)** Sketch showing a polymer-coated FePt nanoparticle covered by a monolayer of TF molecules. Figure taken from reference 31.

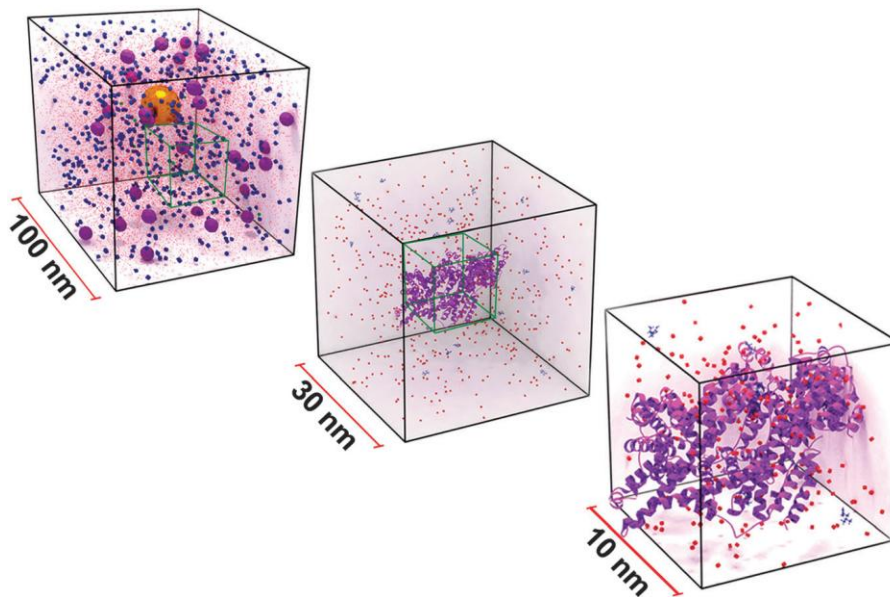


**Figure 4.7** Scaled illustration of a gold nanoparticle suspended in 10% serum-supplemented cell culture medium. The boxes represent the volume of medium at different size scales. The gold nanoparticle can be seen in the  $100 \text{ nm}^3$ , enveloped by serum proteins (violet spheres). Other colours: blue = amino acids, red = ionic salts. Figure taken from reference 28.

Furthermore, by using confocal fluorescence microscopy, they observed that the uptake of FePt nanoparticles by HeLa cells is suppressed by the protein corona compared with the bare nanoparticles. Another article published by *Moore et al.* describes not only the nanoparticle-protein corona but also the interactions of the particles with amino acids and ionic salts present in the CCM.<sup>28</sup> In **Figure 4.7**, the authors illustrate the appearance of a CCM containing spherical gold nanoparticles of 40 nm in diameter, at different size scales ranging from 10 to 100 nm. In that figure, we can see how complex is the environment of the particles upon a suspension in a CCM.

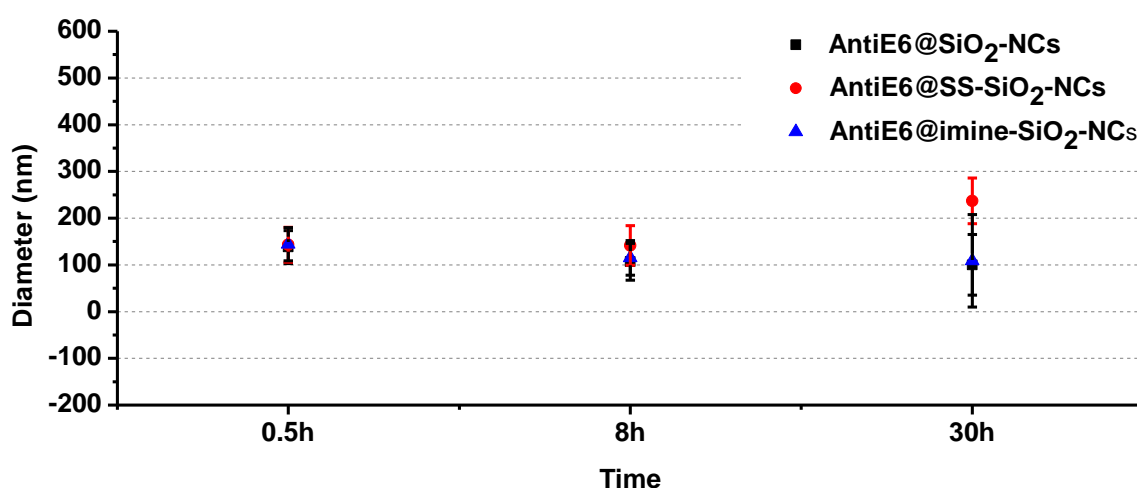


**Figure 4.8** Colloidal stability of AntiE6@NCs in CCM. Dynamic light scattering size number distributions over time of AntiE6@imine-SiO<sub>2</sub>-NCs, AntiE6@SS-SiO<sub>2</sub>-NCs and AntiE6@SiO<sub>2</sub>-NCs upon suspension in CCM.

In our case, to perform the colloidal stability studies of AntiE6@NCs in CCM, the nanocapsules are suspended in such a medium at room temperature without agitation. The size distribution is then measured by DLS at three different times: 30 minutes, 8 and 30 hours and the results are reported in **Figure 4.8**. As we saw in **sub-chapter 4.2.1**, both the diameter size estimated by SEM and the size distribution determined by DLS in PBS at pH 7.4 indicated values below 80 nm for the three particles. In the present study, a size distribution above 100 nm is obtained for all the nanocapsules. This size is relatively constant from time 30 minutes to time 8 hours. However, after 30 hours of suspension, the size variation amplitude is relatively high and a difference up to 100 nm is observed for AntiE6@SS-SiO<sub>2</sub> as compared to the previous times. These results suggest that, as soon as the nanoparticles are

introduced into the CCM, proteins and other biomolecules or ionic salts could cover them to form a corona. This phenomenon could also be accompanied by aggregation between the particles, especially upon a longer duration of suspension.

#### **4.2.3 Biocompatibility enhancement: PEG-5000 post-grafting**

In order to conduct *in vivo* studies at a further stage with these nanocapsules, it is important to investigate some aspects in this respect. Some aspects which need to be considered are biostability, biocompatibility and biodistribution of the nanoparticles. Even though silica nanoparticles are known to be biocompatible, this property can be nuanced depending on the physico-chemical features of the particle. Nevertheless, a very common strategy can be undertaken to effectively enhance the biocompatibility of the materials; it consists in a so called PEGylation technique. Knowing that the biological medium is mainly composed of aqueous phase, polyethylene glycol (PEG), by its hydrophilicity, will enhance the hydrophilicity of the material with which it has been functionalised. The consequence is the biocompatibility enhancement of the material, translated by a longer lifetime in the biological medium or in the circulatory system.<sup>32–36</sup>

We have thus functionalised the outer surface of our nanocapsules with mPEG-silane 5000 by covalent post-grafting method (on the readily synthesised particles). In the view of performing *in vitro* confocal microscopy in a further step, silane-PEG-amine 5000 has also been covalently attached to the outer surface of the materials. The reaction occurs in ethanol and the ratio mPEG-silane 5000/silane-PEG-amine 5000 is set at 8:2 to minimise the presence of possible positive charges on the particles due to protonation on the amine groups. From now on, we will call the corresponding PEGylated nanocapsules as AntiE6@imine-SiO<sub>2</sub>-PEG-NCs, AntiE6@SS-SiO<sub>2</sub>-PEG-NCs and AntiE6@SiO<sub>2</sub>-PEG-NCs. The success of the reaction has been evidenced by DLS and zeta potential analyses. In the one hand, the size distributions provided by DLS show a diameter increase by 17 - 26 nm after the PEGylation process (**Figure 4.9**). This difference is more visible on **Figure 4.9D** where the size distributions before and after the PEGylation process are compared.

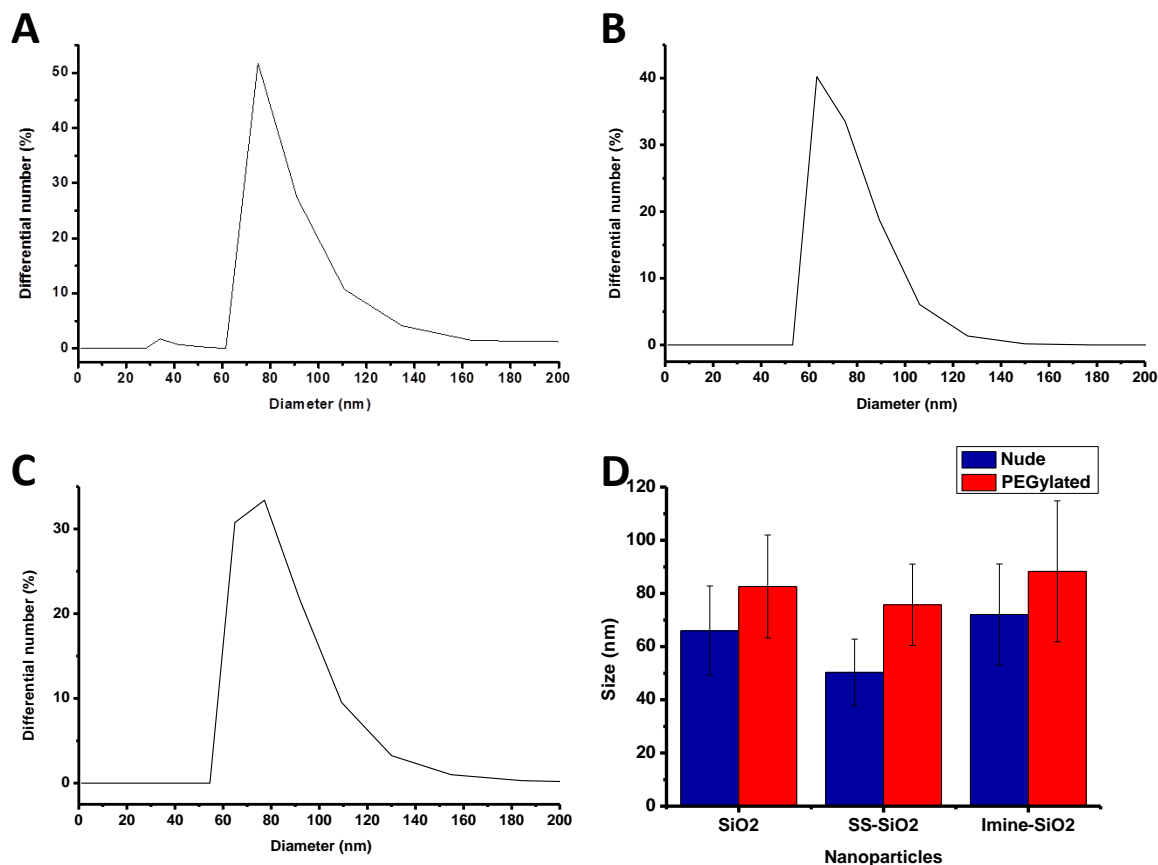


**Figure 4.9** DLS size number distributions of (A) AntiE6@imine-SiO<sub>2</sub>-PEG-NCs, (B) AntiE6@SS-SiO<sub>2</sub>-PEG-NCs and (C) AntiE6@SiO<sub>2</sub>-PEG-NCs. The calculated average sizes are  $88.3 \pm 26.5$  nm,  $75.7 \pm 15.3$  nm and  $82.6 \pm 19.4$  nm for AntiE6@imine-SiO<sub>2</sub>-PEG-NCs, AntiE6@SS-SiO<sub>2</sub>-PEGNCs and AntiE6@SiO<sub>2</sub>-PEG-NCs respectively. (D) Comparison between the size distributions before (blue) and after (red) the PEGylation process.

In the other hand, zeta potential measurements indicate a high difference in the current values. Indeed, this feature goes from highly negative values before the PEGylation reaction to nearly 0 after the process. More precisely, the current values are  $2.96 \pm 2.54$  mV,  $-5.42 \pm 0.95$  mV and  $-2.24 \pm 1.95$  mV for AntiE6@imine-SiO<sub>2</sub>-PEG-NCs, AntiE6@SS-SiO<sub>2</sub>-PEG-NCs and AntiE6@SiO<sub>2</sub>-PEG-NCs respectively. **Figure 4.10** visually evidences this difference. This change in the particles charge is probably due to the fact that the entire surface of the particles has been covered by the PEG which masks the negative charge. Moreover, partial protonation on the amine groups of the silane-PEG-amine could generate some positive charges which then compensate those negative.

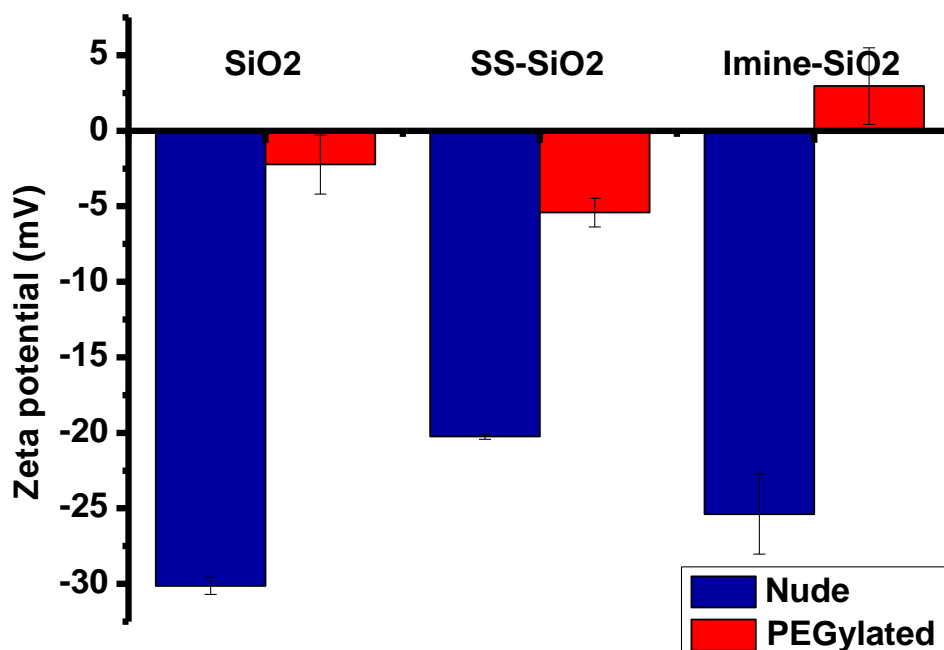


**Figure 4.10** Comparison between the zeta potential of AntiE6@NCs before (**blue**) and after (**red**) the PEGylation process.

#### ***4.2.4 Cell internalisation and localisation studies by confocal microscopy***

Before employing the nanocapsules for their anti-E6 effect, cell internalisation studies have been undertaken. For this purpose, the PEGylated particles have been functionalised with a dye called ATTO™ 425 NHS ester by covalent bond through the amine groups on silane-PEG-amine 5000. The choice of the dye here has been done in order to avoid overlapping with the excitation and emission wavelengths of the dyes used to stain the cells. Regarding the cells, HeLa cells, which are cells taken from a human cervix cancer<sup>37</sup> have been used as a line model. The membrane actin is stained with Alexa Fluor® 647 Phalloidin and the nucleus is not stained because of overlapping excitation/emission issues. The cells are separately incubated with the three nanocapsules at a concentration of 0.05 mg/mL and the samples are analysed by confocal microscopy after 4 and 24 hours. To acquire images in the best conditions, ATTO™ 425 NHS ester is excited at 450 nm while Alexa Fluor® 647 Phalloidin is excited at 650 nm. The resulting images are reported in **Figure 4.11**.

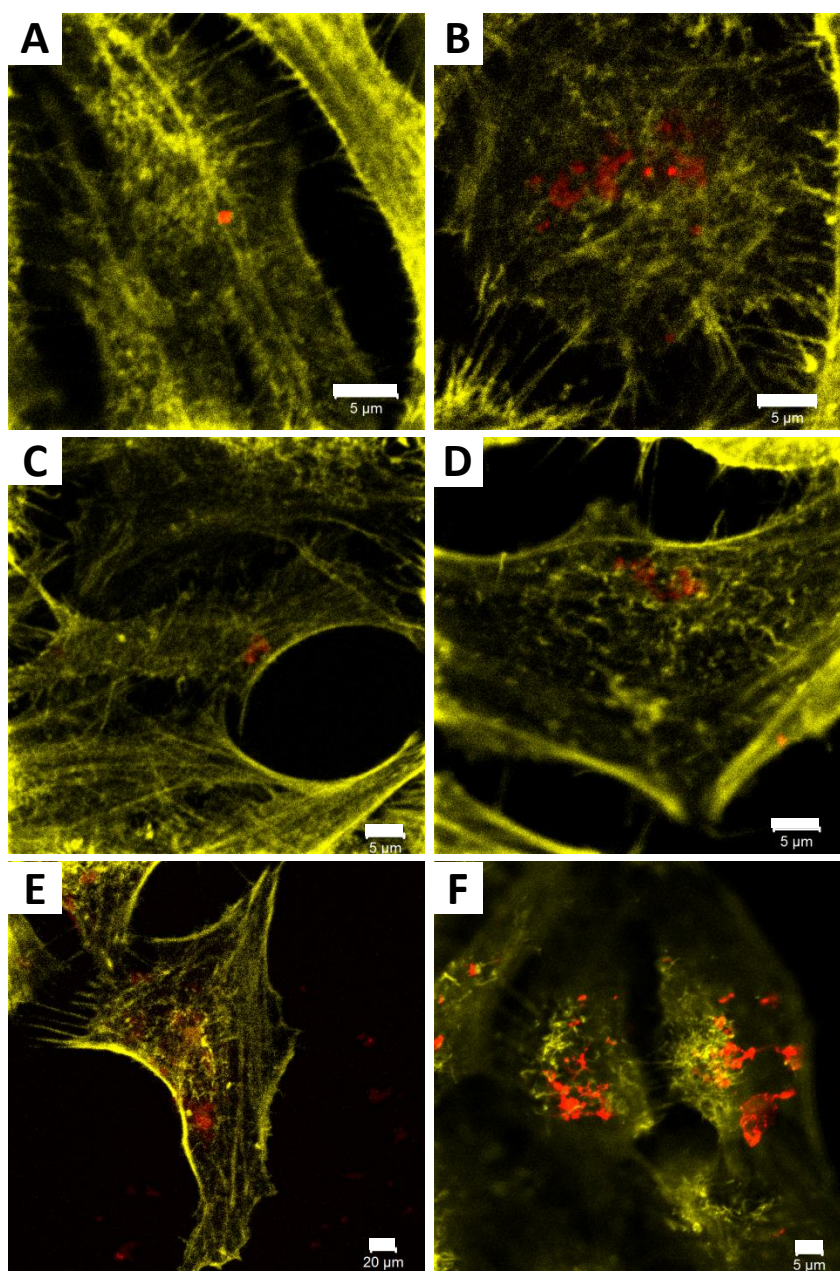


**Figure 4.11** HeLa cells internalisation of the nanocapsules at a concentration of 0.05 mg/mL monitored by confocal microscopy. Images taken upon incubation of the cells with AntiE6@imine-SiO<sub>2</sub>-PEG-NCs for (A) 4 hours and (B) 24 hours, AntiE6@SS-SiO<sub>2</sub>-PEG-NCs for (C) 4 hours and (D) 24 hours, AntiE6@SiO<sub>2</sub>-PEG-NCs for (E) 4 hours and (F) 24 hours. The particles are stained with ATTO™ 425 NHS ester (red) and the cell membrane with Alexa Fluor® 647 Phalloidin (yellow). Scale bar = 5 μm.

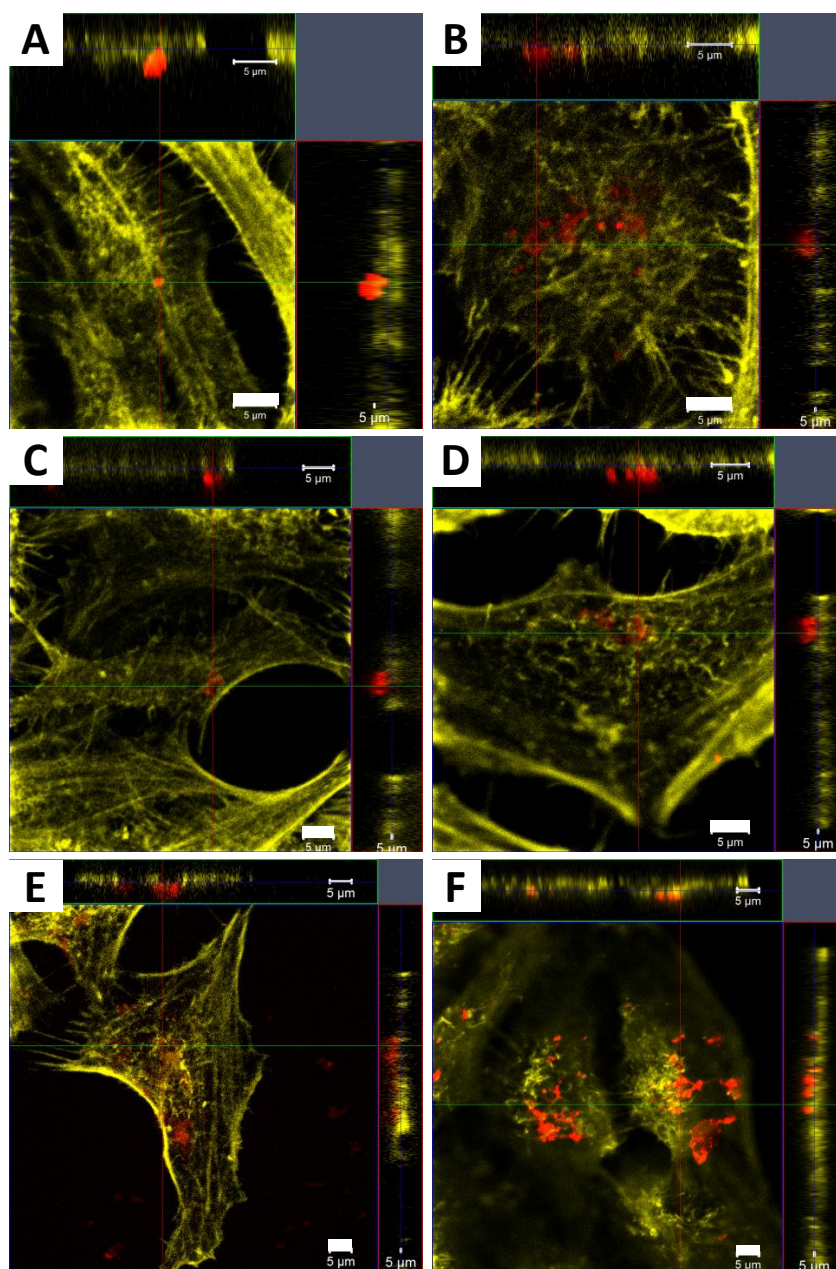


**Figure 4.12** Confocal microscopy on the nanocapsules - Z-stack analysis: images taken upon incubation of HeLa cells with AntiE6@imine-SiO<sub>2</sub>-PEG-NCs for (A) 4 hours and (B) 24 hours, AntiE6@SS-SiO<sub>2</sub>-PEG-NCs for (C) 4 hours and (D) 24 hours, AntiE6@SiO<sub>2</sub>-PEG-NCs for (E) 4 hours and (F) 24 hours, at a concentration of 0.05 mg/mL. The particles are stained with ATTO™ 425 NHS ester (**red**) and the cell membrane with Alexa Fluor® 647 Phalloidin (yellow). Scale bar = 5 μm.

As results, we can see from **Figure 4.11** that, after 4 hours of incubation, a small amount of nanocapsules are internalised and this amount is much higher after 24 hours of incubation. This characteristic is observed with the three particles studied. It is noteworthy to mention that

at the end of the incubation and before analysis with the confocal microscope, the samples are thoroughly washed to avoid the presence of non-internalised particles in the images. Nevertheless, some particles stick on the support (i.e. glass coverslip) and are impossible to remove; these particles are represented by the red spots/area in the empty dark zones in **Figure 4.11E**.

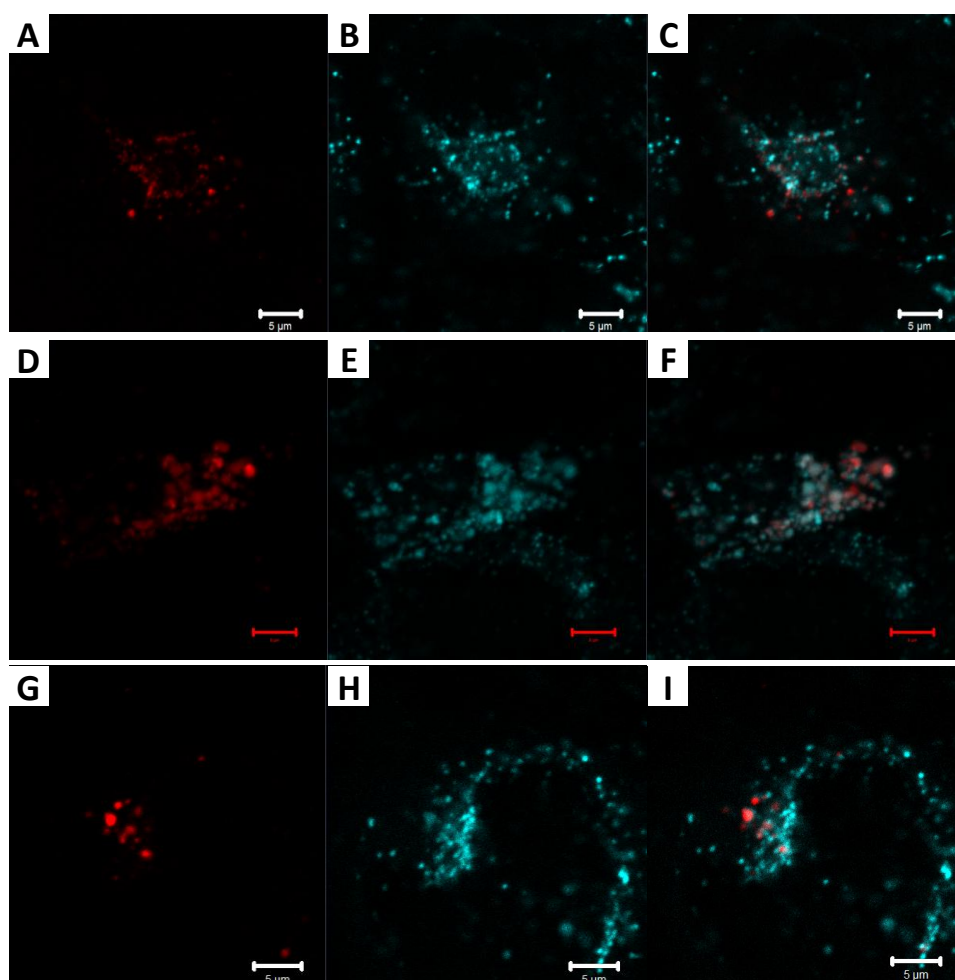


**Figure 4.13.** Co-localisation experiments between the nanocapsules and lysosomes inside HeLa cells. Incubation of the cells with (A-C) AntiE6@imine-SiO<sub>2</sub>-PEG-NCs, (D-F) AntiE6@SS-SiO<sub>2</sub>-PEG-NCs and (G-I) AntiE6@SiO<sub>2</sub>-PEG-NCs, at a concentration of 0.05 mg/mL for 24 hours. (A, D, G) The nanocapsules stained with ATTO™ 425 NHS ester (red), (B, E, H) lysosomes stained with LysoTracker® Red DND-99 (blue), (C, F, I) overlapping evidence between the particles and lysosomes. Scale bar = 5 µm.

To verify that the particles have been internalised by the cells and remain inside, Z-stack analysis has also been performed with the confocal microscope on the same samples and after the same durations of incubation. The results obtained enable us to confirm that the particles are perfectly internalised by the cancer cells and that they are retained inside. Moreover, they seem to be located in the cytoplasm (**Figure 4.12**).

After being taken up by the cells, silica nanoparticles tend to go within the lysosomes.<sup>12</sup> Z-stack analysis has enabled us to suggest that the materials were located in the cytoplasm. To confirm this hypothesis and to determine more precisely the location, we performed a co-localisation experiment. The three labelled particles are thus separately incubated with the cells for 24 hours and the lysosomes are stained with LysoTracker® Red DND-99. During the analysis, ATTO™ 425 NHS ester grafted on the materials are excited at 437 nm while the LysoTracker® Red DND-99 is excited at 577 nm. As we can see on **Figure 4.13**, in the case of the three materials, ATTO™ 425 NHS ester is perfectly overlaid with LysoTracker® Red DND-99, which means that these particles are located within the lysosomes.

Through this sub-chapter, we have seen that it is possible to extend the encapsulation strategy to one more protein, by referring to the previous investigations led in the group. We thus can conclude that, until this report, protein encapsulation into stimuli-responsive, breakable and biodegradable organosilica shell has been a relative straightforward and very efficient strategy. The activity of this newly developed system against HeLa cell line is now under examination. In the next sub-chapter, we describe the extension of such a successful and efficient system to encapsulate smaller molecules such as drugs.

### **4.3 Encapsulation of doxorubicin**

The encapsulation process (Dox@imine-SiO<sub>2</sub>-NCs) has been done following the same procedure as for the antibody. An initial aqueous solution of doxorubicin hydrochloride (Dox.HCl) at the concentration of 2 mg/mL is entrapped into reverse micelles formed by mixing Triton™ X-100 with n-hexanol and cyclohexane. TEOS is added as silica source, which is combined with the diiminosilane linker as organic moiety by 30 mole %. An aqueous solution of 28 % ammonia is added to the mixture as base to trigger the silica hydrolysis and the reaction is allowed to occur overnight at room temperature before precipitating the particles by the addition of acetone. This latter is followed by a series of washing with distilled water to remove the undesirable water-soluble chemicals and with ethanol to remove

the organic chemicals. The encapsulation of the drug into the disulfide-doped breakable silica shell (Dox@SS-SiO<sub>2</sub>-NCs) has been performed in the same manner, using bis[3-(triethoxysilyl)propyl]disulfide by 30 mole % as organic moiety. In order to carry out comparison studies with the non-breakable shell which lacks organic moiety (Dox@SiO<sub>2</sub>-NCs), the same procedure has been realised with TEOS by 100 mole %.

#### 4.3.1 Morphology of the resulted particles

A morphological characterisation by SEM shows highly monodisperse spherical-like shaped nanoparticles with average diameters of about 70, 65 and 80 nm for Dox@imine-SiO<sub>2</sub>-NCs, Dox@SS-SiO<sub>2</sub>-NCs and Dox@SiO<sub>2</sub>-NCs respectively (**Figure 4.14**).

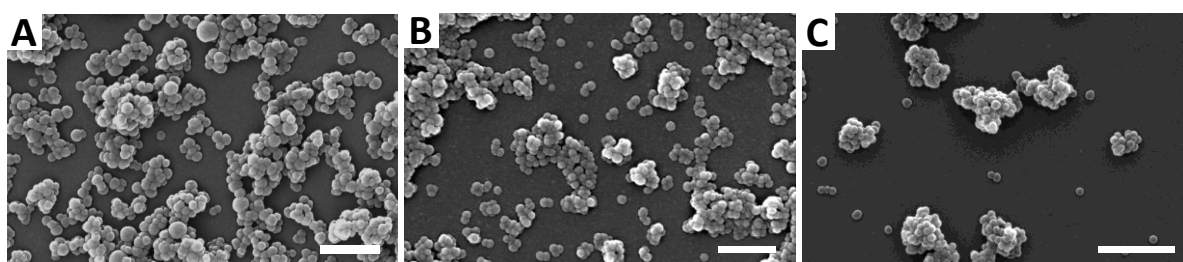


**Figure 4.14** SEM images of (B) Dox@imine-SiO<sub>2</sub>-NCs, (C) Dox@SS-SiO<sub>2</sub>-NCs and (D) Dox@SiO<sub>2</sub>-NCs. Scale bar = 500 nm.

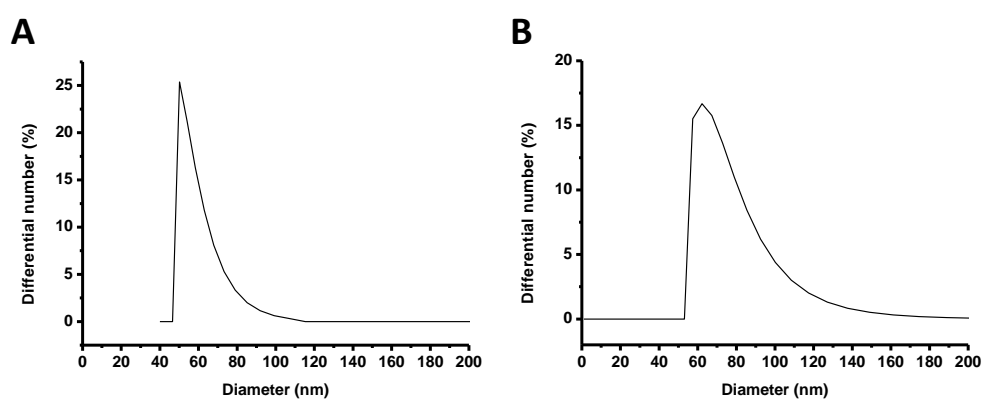


**Figure 4.15** DLS size number distributions of (A) Dox@SS-SiO<sub>2</sub>-NCs and (B) Dox@SiO<sub>2</sub>-NCs. The calculated average sizes are  $59.6 \pm 10.3$  nm and  $77.1 \pm 21.3$  nm for Dox@SS-SiO<sub>2</sub>-NCs and Dox@SiO<sub>2</sub>-NCs respectively.

Determination of the size distribution of the capsules in aqueous phase by DLS in the same manner as for the antibody loaded capsules resulted in similar diameter sizes as estimated by SEM for two samples which are Dox@SS-SiO<sub>2</sub>-NCs and Dox@SiO<sub>2</sub>-NCs showing respectively size distributions of  $59.6 \pm 10.3$  nm and  $77.1 \pm 21.3$  nm (**Figure 4.15**).

However, according to this analysis, Dox@imine-SiO<sub>2</sub>-NCs seem to preferentially disperse into dimers since the size distribution is  $133.3 \pm 9.9$  nm (**Figure 4.16**) which is approximately the double of what was observed with SEM.

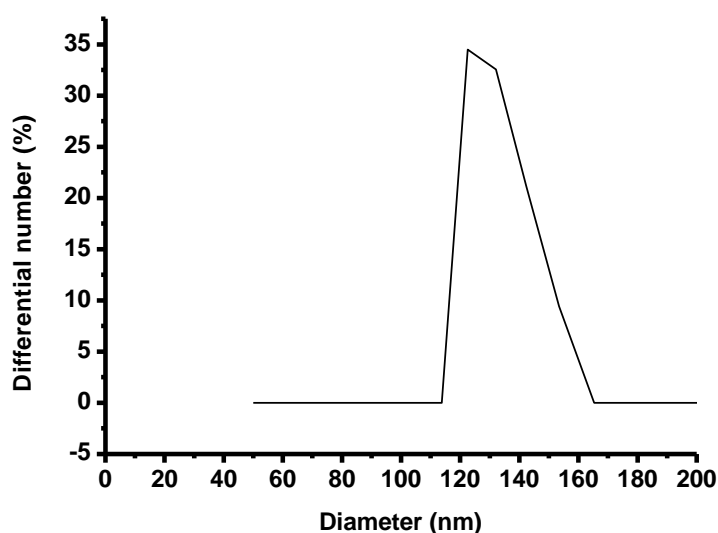


**Figure 4.16** DLS size number distribution of Dox@imine-SiO<sub>2</sub>-NCs. The calculated average size is  $133.3 \pm 9.9$  nm.

Zeta potential measurements performed by dispersing the particles in a PBS solution at pH 7.4 indicate highly negative current values for the three capsules. The current values are -19.04 mV, -24,81 mV and -10,89 mV for Dox@SS-SiO<sub>2</sub>-NCs, Dox@SiO<sub>2</sub>-NCs and Dox@imine-SiO<sub>2</sub>-NCs respectively.

### ***4.3.2 Kinetic studies of the release***

Before moving to the kinetic studies of the release of Doxorubicin (Dox) from the breakable capsules through the stimulus-dependent cleavage of the organic linkers, the particles have thoroughly been washed with distilled water and ethanol as described in sub-chapter **4.3.1**.

After the washing process, the three compounds appeared as more or less pink compounds with the strongest colour and the highest amount of particles observed on Dox@imine-SiO<sub>2</sub>-NCs (**Figure 4.17**).

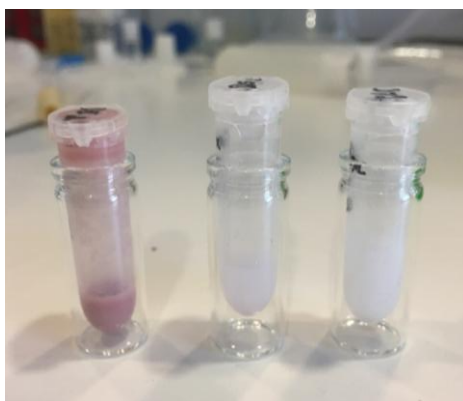


**Figure 4.17** Photos of **(left)** Dox@imine-SiO<sub>2</sub>-NCs, **(middle)** Dox@SS-SiO<sub>2</sub>-NCs and **(right)** Dox@SiO<sub>2</sub>-NCs. All the samples are dispersed in the same volume of distilled water. After the synthesis, the highest amount of particles is obtained with Dox@imine-SiO<sub>2</sub>-NCs.

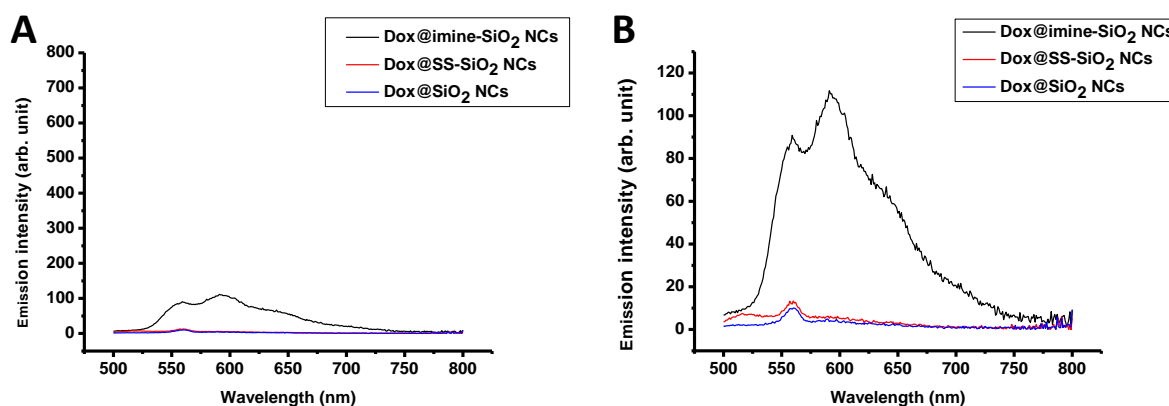


**Figure 4.18** (A) Emission spectra recorded from aqueous supernatants after washing and centrifuging the nanocapsules; (B) zoom on the spectra. Solvent: distilled water;  $\lambda_{exc} = 470$  nm. The Y axis on (A) has been adapted to that of the next figures.

To verify that the colours of the particles are only due to encapsulated Dox and that there was no free drug in solution, the three samples have been vigorously centrifuged and the emission of the supernatant has been measured by fluorimetry. The spectra are reported in **Figure 4.18** and, as evidenced on it, the emission from the three aqueous supernatants is almost non-

existent for an excitation wavelength set at 470 nm. Nevertheless, as already described in **chapter 2**, no matter how strong is the centrifugation, it is impossible to get rid of a few amount of non-precipitating particles. Therefore, even though with a negligible intensity, a little emission is observed as shown in the zoom on **Figure 4.18B**.

The release kinetics of Dox from the pH-responsive nanocapsule has been performed by suspending the particles at a concentration of 0.1 mg/mL in a phosphate saline solution buffered (PBS) at pH 5.5 to simulate the extracellular matrix of the cancer cells. The sample is gently stirred in order to have a controllable release over time and at times 0, 5, 10, 15, 25, 35, 45 minutes, 1, 3, 6, 12 hours, 1 and 2 days, an aliquot is removed, centrifuged over 2 minutes and the emission of the supernatant is measured with a fluorimeter. The excitation wavelength is set at 470 nm. As control experiment, the same procedures with the same particles have been carried out in a PBS solution at pH 7.4 to simulate the physiological medium. For comparison, the stability of the non-breakable nanocapsule has been verified by treating it in the same manner as for the pH-responsive particles.

The results obtained show expected trends for each sample (**Figure 4.19**). When Dox@imine-SiO<sub>2</sub>-NCs is suspended in PBS solution at pH 5.5, a spectrum with a negligible emission intensity is recorded at time 0. Indeed, the emission intensity is almost the same as that from the supernatant obtained just after washing the capsules. After 5 minutes of dispersion, a higher intensity is observed, which then keeps increasing with time before stabilising at times 1 and 2 days. These data are displayed in **Figure 4.19A**. When these same particles are suspended in PBS solution at pH 7.4, the spectra show no particular emission except that similar to that obtained from the supernatant after washing the capsules. No particular evolution of the emission intensity is recorded over time until 1 day of dispersion and, for this reason, the experiment has been stopped after that duration of dispersion (**Figure 4.19B**). Regarding the non-breakable capsules, without any surprise, negligible emission is observed on each spectrum and no particular evolution is noticed from the beginning to 1 day of monitoring. This result is obtained whether at pH 5.5 or 7.4; therefore, the experiment has been stopped at time 1 day in both cases (**Figure 4.19C, D**).

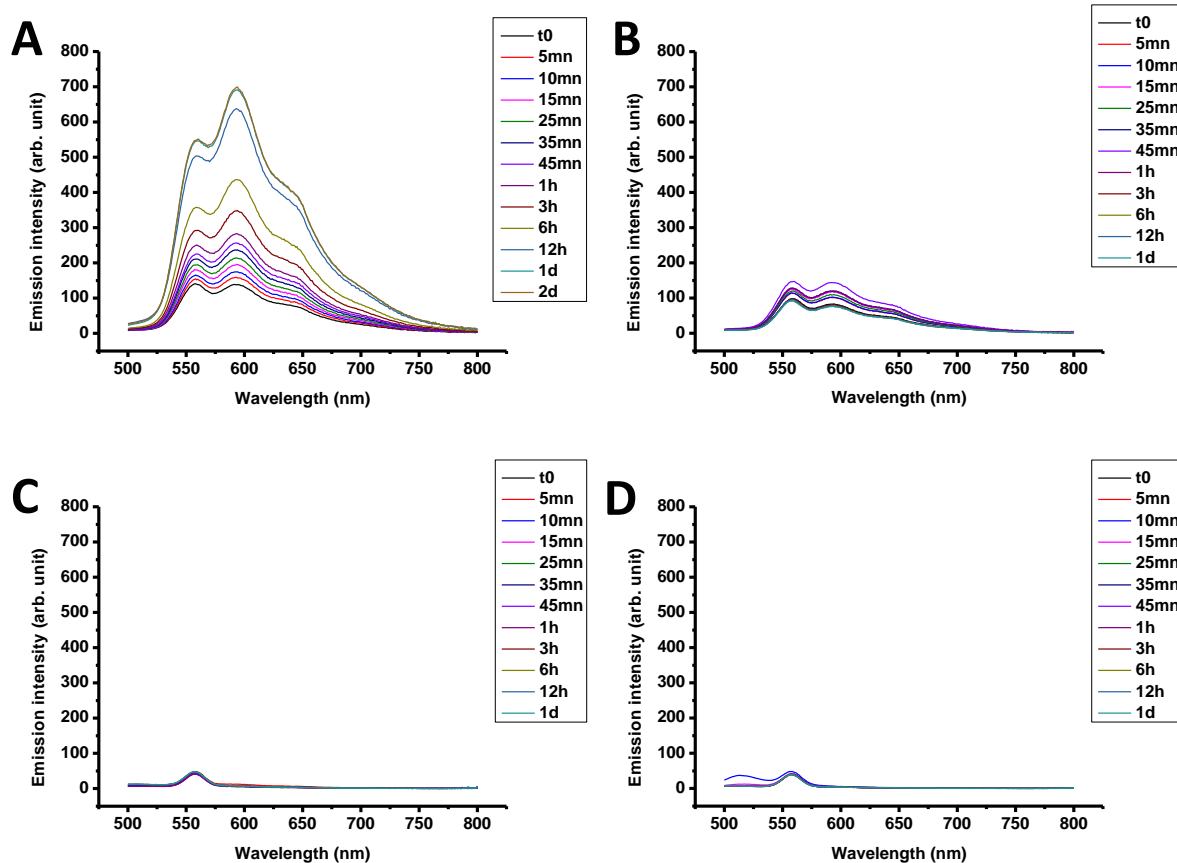


**Figure 4.19** Raw data over time from the emission measurement of the supernatant from suspensions of Dox@imine-SiO<sub>2</sub>-NCs in PBS at (A) pH 5.5 and (B) pH 7.4 and of Dox@SiO<sub>2</sub>-NCs at (C) pH 5.5 and (D) pH 7.4.  $\lambda_{\text{exc}} = 470$  nm.

Regarding the reduction-responsive nanocapsule, the release kinetic study of the loaded drug has been performed by suspending the particles at a concentration of 0.1 mg/mL in a PBS solution containing 10 mM glutathione (GSH) at pH 7.4. This concentration of glutathione has been set to be identical to that found in the cancer cells.<sup>38-40</sup> The sample is gently stirred as in the case of Dox@imine-SiO<sub>2</sub>-NCs and the reaction is monitored at the same time points from time 0 to 2 days in the same way. As control experiment, Dox@SS-SiO<sub>2</sub>-NCs are also dispersed in PBS solution at pH 7.4 without any reducing agent. The reaction is monitored in the same manner but in a larger time interval. As expected, we can see from **Figure 4.20A** that negligible emission is observed on the spectra from the beginning to the end of the experiment upon incubation in PBS solution at pH 7.4. However, against all odds, the same observation is made when the particles are incubated in the same PBS but in the presence of the reducing agent (**Figure 4.20B**).

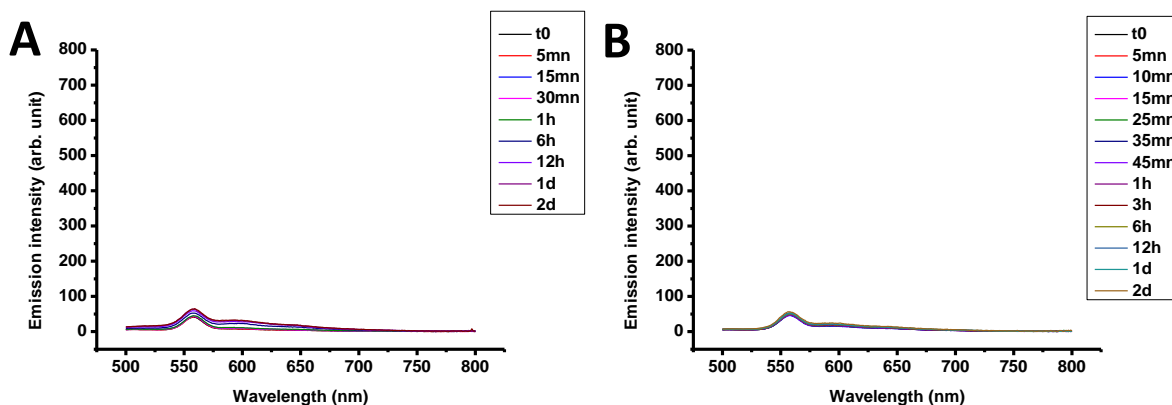


**Figure 4.20** Raw data over time from the emission measurement of the supernatant from suspensions of Dox@SS-SiO<sub>2</sub>-NCs in (A) PBS solution at pH 7.4 and (B) PBS solution at pH 7.4 with GSH 10 mM.  $\lambda_{exc} = 470$  nm.

To verify that the result obtained by incubating Dox@SS-SiO<sub>2</sub>-NCs in the reducing medium is not due to any issue with the reagents or error during the experiment, the capsules themselves have directly been studied. For this purpose, the particles are dispersed in PBS solution at pH 7.4 and the emission from the suspension is measured *in situ* by fluorimetry. As comparison, the same experiment has been performed with Dox@imine-SiO<sub>2</sub>-NCs which, as we can remember, evidenced a clear Dox release over time. Both of the particles are dispersed in the PBS solution at the deliberately high concentration of 0.2 mg/mL to make sure that we could detect the emission. **Figure 4.21** displays the spectra obtained and we can see on it that Dox@imine-SiO<sub>2</sub>-NCs is highly emissive (**Figure 4.21, black curve**) while Dox@SS-SiO<sub>2</sub>-NCs shows negligible emission (**Figure 4.21, red curve**). These data suggest that the encapsulation of Dox.HCl do not occur effectively with the disulfide doped nanocapsule in the conditions explored. Until here, no clear explanation can be done on this issue since a similar study reported by *Sun et al.* on shell-sheddable micelles based on dextran-SS-poly( $\epsilon$ -caprolactone) diblock copolymer for efficient intracellular release of Dox does not mention any interaction between the drug and the disulfide function.<sup>41</sup> Otherwise, the amount of drug loaded into the pH-responsive nanocapsule have been determined to be 10 weight %.

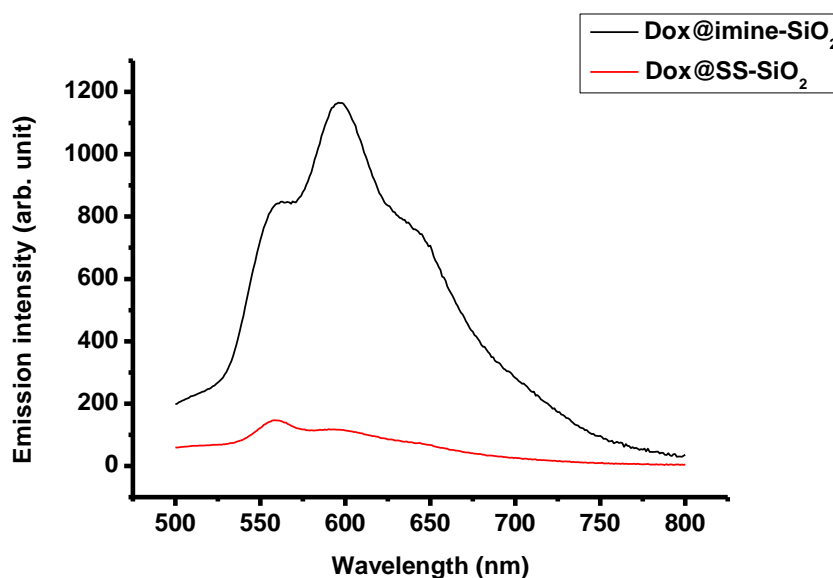


**Figure 4.21** Emission spectra obtained from the dispersion of Dox@imine-SiO<sub>2</sub>-NCs and Dox@SS-SiO<sub>2</sub>-NCs at a concentration of 0.2 mg/mL in PBS solution at pH 7.4.  $\lambda_{exc} = 470$  nm.

To better study the data, the area integration of the emission spectra over time has plotted. The study has been realised only with the pH-responsive material since the reduction-sensitive one did not encapsulate effectively emissive drug. **Figure 4.22A** evidences the comparison of the emission evolution depending on the conditions in which the particles are treated. In the one hand, when Dox@imine-SiO<sub>2</sub>-NCs are dispersed in acidic medium (**Figure 4.22A, black curve**), it releases Dox by 23 % after 5 minutes. The amount of liberated drug then increases with time to reach 41 % after 1 hour and a plateau is obtained at time 1 day where almost the entire quantity of loaded drug was liberated. In the other hand, the suspension in the neutral pH medium does not result in any significant emission from the supernatant. Thus, the area integration profile exhibits a relatively horizontal line along the abscissa axis from time 0 to time 1 day where the experiment has been stopped (**Figure 4.22A, red curve**). Due to residual particles in the supernatant, the curve does not stick on the 0 value but on a higher one, which is still negligible. The maxima of the emission intensity are also displayed in **Figure 4.22B**. As we can see, the profiles obtained by suspending the nanocapsules in pH 5.5 (**Figure 4.22B, black curve**) and in pH 7.4 (**Figure 4.22B, red curve**) media correlate perfectly with their respective area integration analogous.

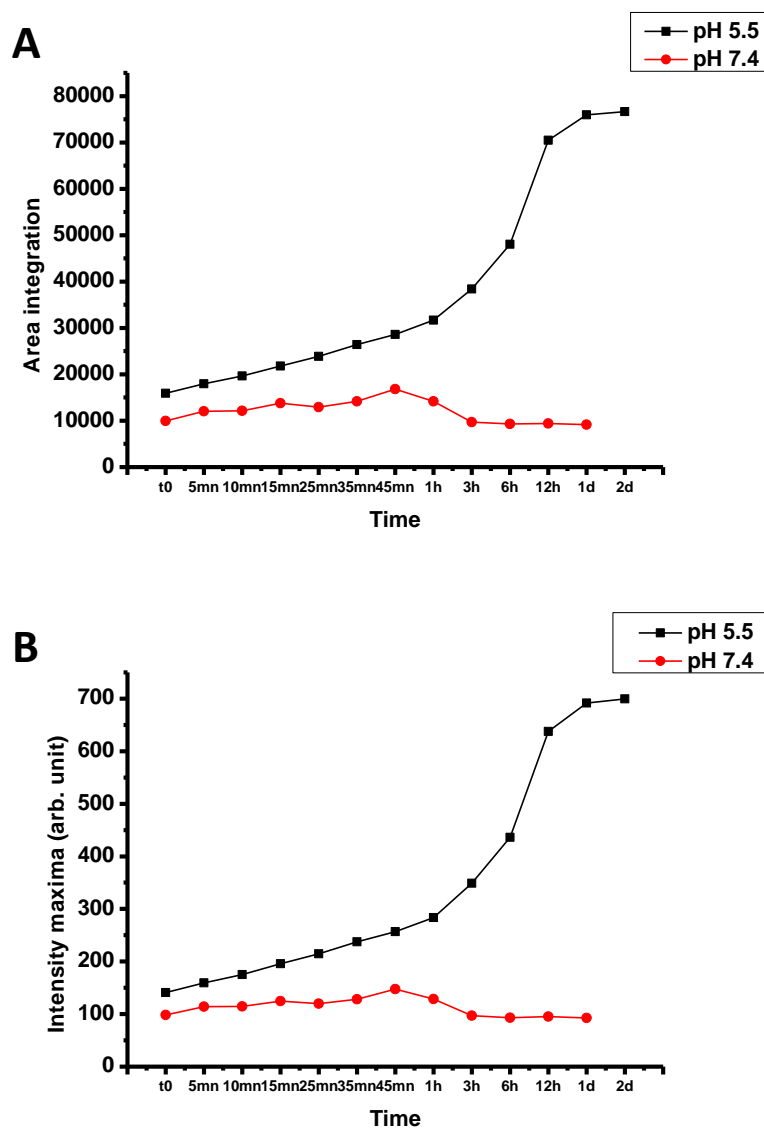


**Figure 4.22** (A) Area integration of the emission over time from the supernatant of a suspension of Dox@imine-SiO<sub>2</sub>-NCs in PBS and (B) the emission maximum intensity over time.

Regarding the non-breakable capsule, both of the area integration of the emission and the intensity maximum over time exhibit a profile with a quasi-horizontal line along the abscissa axis from the beginning to the end of the reaction, i.e. 1 day. This result is independent of the pH of the suspension medium (**Figure 4.23**).

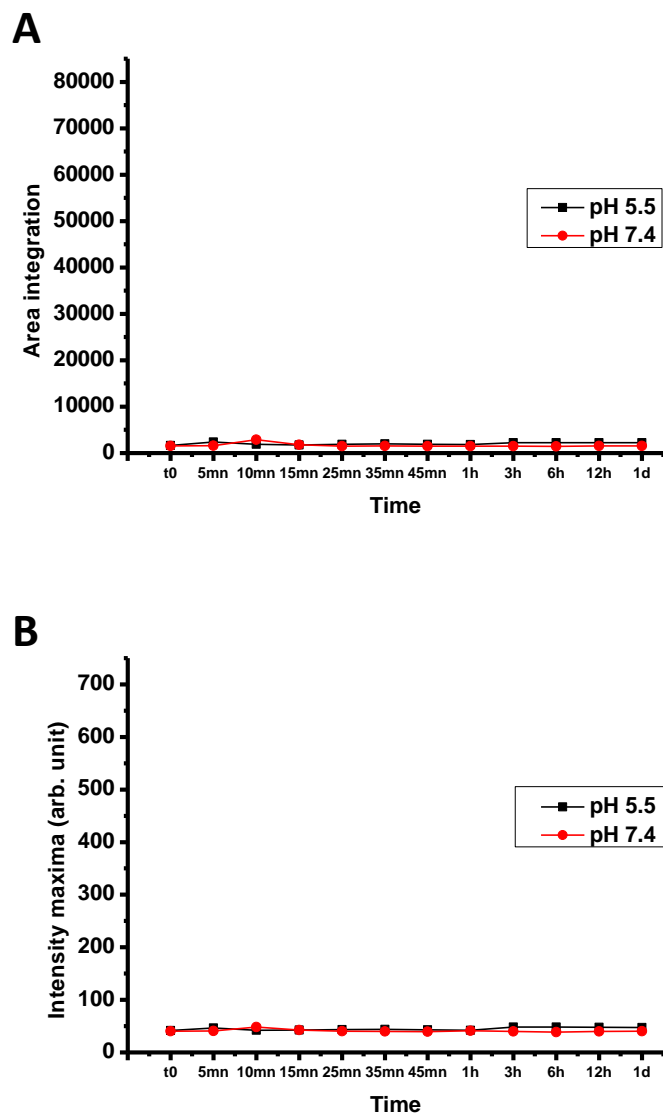


**Figure 4.23** (A) Area integration of the emission over time from the supernatant of a suspension of Dox@SiO<sub>2</sub>-NCs in PBS and (B) the emission maximum intensity over time.

As a conclusion for this part of this sub-chapter, we can say that the encapsulation of Doxorubicin into the imine-doped hybrid organosilica nanocapsule has been a real success. The material is pH-responsive and thus breaks down upon contact with an acidic medium, releasing the drug in a controllable and effective manner. Otherwise, the high stability of the system in the physiological pH has been demonstrated. Furthermore, the non-breakable nanocapsule loaded with the same drug has shown a good stability independently from the pH of the medium and, thus, no drug is released in the conditions explored.

### 4.3.3 Cell internalisation studies by confocal microscopy

To conduct cell internalisation experiments, taking advantage of the fact that Dox is a photoluminescent molecule, the nanocapsules have been used as synthesised. Regarding the cells, HeLa cells have been used as a line model. The membrane actin is stained with Alexa Fluor® 647 Phalloidin and the nucleus is labelled with 4',6-diamidino-2-phénylindole (DAPI). The cells are separately incubated with Dox@imine-SiO<sub>2</sub>-NCs and Dox@SiO<sub>2</sub>-NCs at a concentration of 0.05 mg/mL and the samples have been analysed by confocal microscopy. The incubation time is set for 4 hours to minimise the possible leakage of Dox from the imine-doped nanocapsules due to its breaking. To acquire images in the best conditions, Dox is excited at 455 nm while DAPI and Alexa Fluor® 647 Phalloidin are excited at 405 nm and 650 nm respectively.

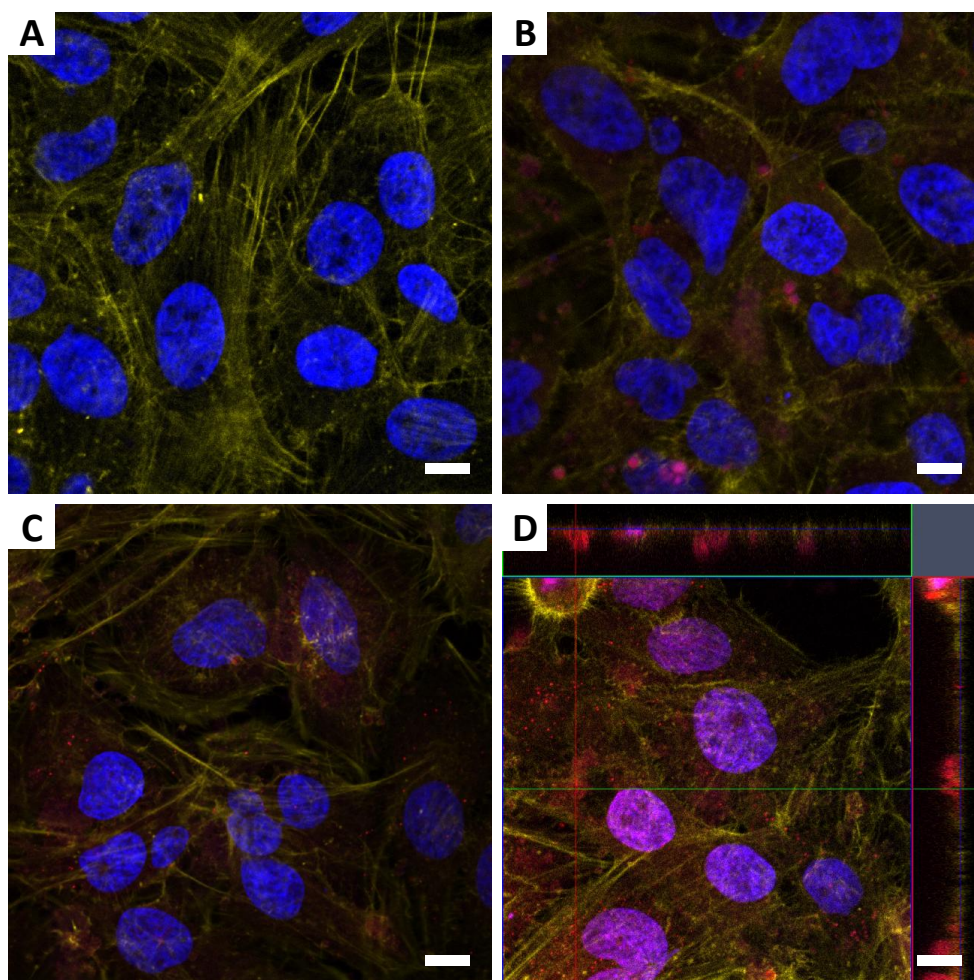


**Figure 4.24** HeLa cells internalisation of the nanocapsules at a concentration of 0.05 mg/mL monitored by confocal microscopy. Images taken upon incubation of the cells for 4 hours with (A) no nanocapsule, (B) Dox@SiO<sub>2</sub>-NCs and (C) Dox@imine-SiO<sub>2</sub>-NCs. (D) Z-stack analysis: image taken

upon incubation of HeLa cells with Dox@imine-SiO<sub>2</sub>-NCs for 4 hours at 0.05 mg/mL. The particles are incubated as synthesized taking advantage of the emission of doxorubicin (**pink/red**) while the cell membrane is stained with Alexa Fluor® 647 Phalloidin (**yellow**) and the nucleus with DAPI (**blue**). Scale bar = 5 μm.

As results, we can see from **Figure 4.24A-C** that, after 4 hours of incubation, some nanocapsules are internalized. This characteristic is observed with both of the particles studied.

To further verify the uptake of the particles, Z-stack analyses have been performed with the confocal microscope on the same samples and after the same duration of incubation. The results obtained enable us to confirm that the particles are perfectly internalised by HeLa cells and that they are retained inside. Moreover, they seem to be located in the perinuclear region of the cytoplasm (**Figure 4.24D**).

#### ***4.3.4 Determining the activity towards cancer cells***

The pH-responsive based nanocapsule technology has been employed to deliver the encapsulated chemotherapeutic agent into cancer cells in order to kill them. For this purpose, the same HeLa cell line as for the confocal microscopy has been used as model. The cells are treated with Dox@imine-SiO<sub>2</sub>-NCs at three different concentrations which are 0.1, 0.5 and 1 mg/mL and the cell viability is determined after 24 and 48 hours. As comparison, the same experiment has been carried out with Dox@SiO<sub>2</sub>-NCs in the same conditions.

**Figure 4.25** illustrates the cell viability profile obtained after 24 hours of incubation. We can see that, upon treatment with 0.1 mg/mL of Dox@imine-SiO<sub>2</sub>-NCs (**Figure 4.25A**), corresponding to 0.01 mg/mL of Dox (**Figure 4.25B**), 81 % of the cells survive. The rate of survival then decreases by increasing the amount of particles, up to 77 % with 1 mg/mL of capsules (0.1 mg/mL of Dox). Regarding Dox@SiO<sub>2</sub>-NCs, the general profile of the cell viability is similar to that observed with the breakable analogue. However, the relative survival rate is always higher, by 8 % in average, than with the breakable particles.

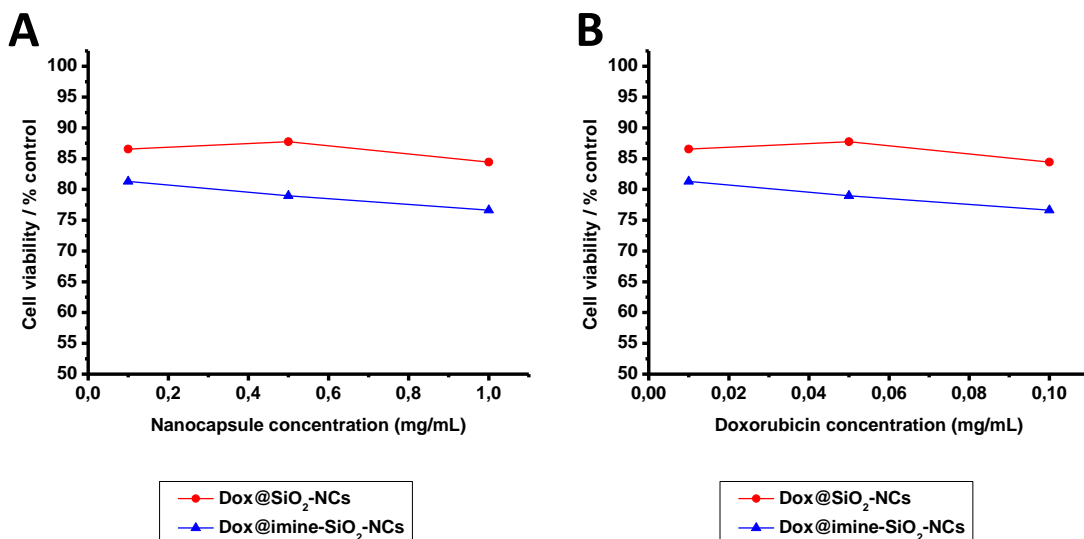


**Figure 4.25** HeLa cell viability tests of doxorubicin loaded nanocapsules – results obtained after 24 hours of treatment. The nanocapsules concentrations used for the experiments are 0.1, 0.5 and 1 mg/mL (A), which correspond to doxorubicin concentrations of 0.01, 0.05 and 0.1 mg/mL (B). Tests performed with alamarBlue assay.

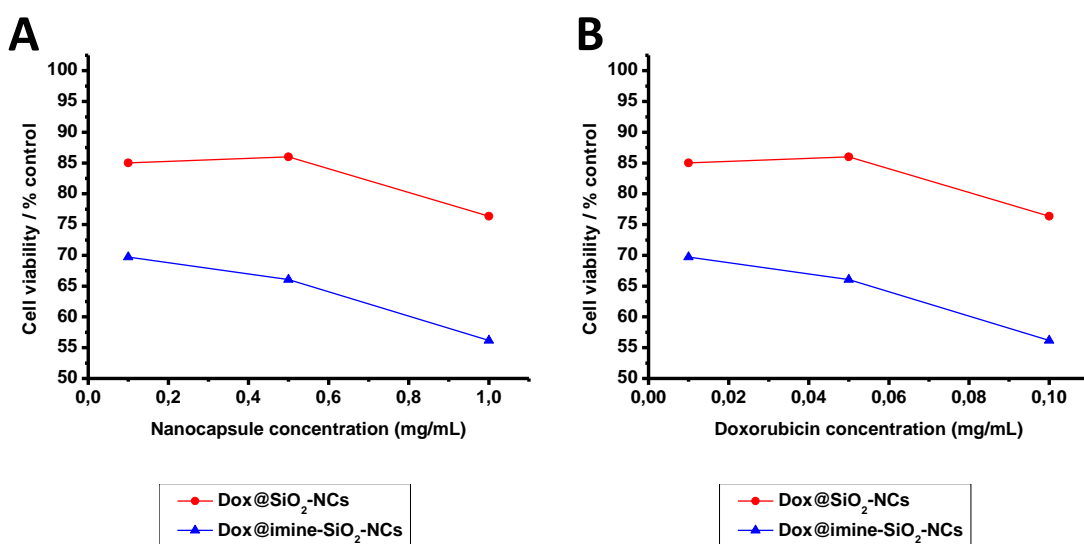


**Figure 4.26** HeLa cell viability tests of doxorubicin loaded nanocapsules – results obtained after 48 hours of treatment. The nanocapsules concentrations used for the experiments are 0.1, 0.5 and 1 mg/mL (A), which correspond to doxorubicin concentrations of 0.01, 0.05 and 0.1 mg/mL (B). Tests performed with alamarBlue assay.

When we focus on the cell viability profiles obtained after 48 hours of incubation (**Figure 4.26**), we can see that the general tendency follows that observed at time 24 hours for each compound. The rate of cell survival keeps decreasing upon treatment with Dox@imine-SiO<sub>2</sub>-NCs and the decrease rate is even higher as compared to that at time 24 hours. Thus, almost 50 % of cells death is observed with 1 mg/mL of nanocapsules (**Figure 4.26A**), which corresponds to 0.1 mg/mL of drug (**Figure 4.26B**). At the same time, the non-breakable system induces also cells death which increases with the concentration. However, the proportion of dead cells is by far lower than in the case of the breakable analogue, displaying up to 20 % of difference in most of the conditions.

Eventually, a further comparison has been performed with a Dox solution prepared from a commercial one at the highest concentration according to the highest nanocapsule concentration and considering the percentage of loading in the nanocapsule (10 weight %). Thus, Dox solution 0.1 mg/mL is used to be in accordance with Dox@NCs of 1 mg/mL.

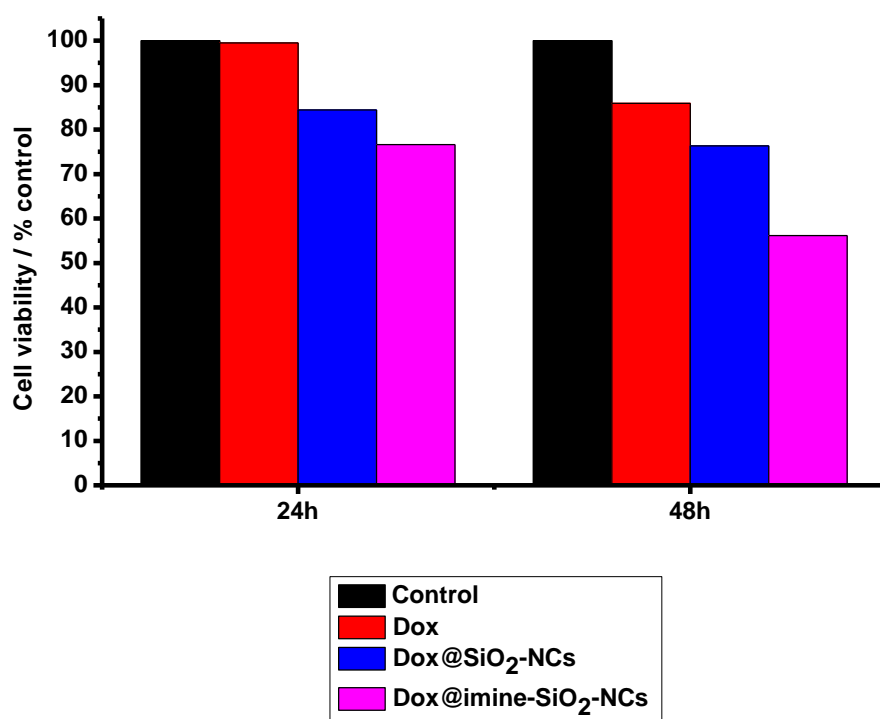


**Figure 4.27** HeLa cell viability tests of doxorubicin loaded nanocapsules and doxorubicin solution. The cells are incubated with the nanocapsules at the concentration of 1 mg/mL and with doxorubicin solution at the concentration of 0.1 mg/mL to be in accordance with the percentage of loading. The cell viability is determined after 24 and 48 hours. Tests performed with alamarBlue assay.

As we can see on **Figure 4.27**, at time 24 hours, while Dox@imine-SiO<sub>2</sub>-Ncs and Dox@SiO<sub>2</sub>-Ncs induce respective cells death of about 23 % and 16 %, Dox solution does not show any cytotoxicity. In the same manner, the tendency after 48 hours of incubation is similar to that after 24 hours and the difference between the three systems is even more remarkable. Thus, almost 50 % and about 24 % of the cells do not survive upon treatment with Dox@imine-SiO<sub>2</sub>-Ncs and Dox@SiO<sub>2</sub>-Ncs respectively, while only 14 % of them die due to the effect of Dox solution. To sum up, at the highest concentration tested (0.1 mg/mL of Dox), the system based on the breakable nanocapsule demonstrates the highest efficiency towards killing HeLa cells.

#### **4.4 Conclusion**

We have been able to extend the reduction sensitive nanocapsule to the pH sensitive one and have successfully encapsulated an antibody. After biocompatibility enhancement by PEGylation process, *in vitro* behaviour studies show a fast internalisation by HeLa cells and retention within the lysosomes. We also have been able to extend such a technology to successfully encapsulate a small drug molecule. The system demonstrates a good stability in physiological conditions and thus enables to avoid premature release of the payload. A rapid internalisation also occurs with HeLa cell line and the particles are retained in the periphery of the nucleus. Eventually, taking advantage of the technology based on the pH-breakability, the nanocapsule can effectively deliver the drug *in vitro* into HeLa cells and leads to the cells apoptosis.

#### **4.5 Experimental section**

##### ***4.5.1 Materials***

All commercial solvents and reagents were used as received without further purification. Tetraethyl orthosilicate (TEOS), atto 425 NHS ester were purchased from Sigma Aldrich. Silane-PEG-amine 5000 was purchased from interchim, mPEG-silane 5000 from Laysan Bio Inc and the anti-E6 antibody from mouse papilloma virus from Merck-Millipore. Doxorubicin hydrochloride solution 2 mg/mL was kindly offered by the institut hospitalo-universitaire de Strasbourg (IHUS)/IRCAD. LysoTracker® Red DND-99, DAPI, alamarBlue assay kit and Alexa Fluor® 647 Phalloidin were purchased from Thermo Fisher Scientific.

### **4.5.2 Instruments**

#### *Scanning electron microscopy (SEM)*

To perform the SEM, the samples were drop-casted onto a round glass coverslip of 12 mm in diameter (purchased from R. Langenbrinck) and allowed to dry at 1 atm and room temperature. Gold (using Emitech K575X peltier cooled, 60 mA) was sputtered on the top of the specimen and the samples were observed with a FEI Quanta FEG 250 SEM (FEI corporate, Hillsboro, Oregon, USA) with an acceleration voltage of 20-30 kV.

#### *Dynamic light scattering (DLS) and zeta potential (ZP)*

DLS and ZP measurements were conducted on a Delsa Nano C Particle Analyzer (Beckman Coulter, Brea, CA, USA; operative wavelength 655 nm). All DLS measurements of the nanoparticles were conducted in water ( $\approx 0.1$  mg/mL), ZP analyses were performed in PBS buffer (pH 7.4;  $\approx 0.1$  mg/mL).

### **4.5.3 Synthesis**

#### *Synthesis of AntiE6@imine-SiO<sub>2</sub>-NCs*

Triton X-100 (1.77mL) and n-hexanol (1.8 mL) were dissolved in cyclohexane (7.5 mL). Separately, 300  $\mu$ L of 0.091 mg/mL aqueous solution of E6 antibody from mouse papilloma virus were mixed with 40  $\mu$ L of tetraethyl orthosilicate (TEOS) and 70.4  $\mu$ L of the diiminosilane. After mixing manually, this mixture was added to the former organic medium. Eventually, 100  $\mu$ L of 28 % ammonia aqueous solution were added and the water-oil emulsion was stirred for 4 hours at room temperature. After that, 20 mL of pure acetone were added in order to precipitate the AntiE6@imine-SiO<sub>2</sub>-NCs and the material was recovered by means of centrifugation and washing six times with water.

#### *Synthesis of AntiE6@SS-SiO<sub>2</sub>-NCs*

Triton X-100 (1.77mL) and n-hexanol (1.8 mL) were dissolved in cyclohexane (7.5 mL). Separately, 300  $\mu$ L of 0.091 mg/mL aqueous solution of E6 antibody from mouse papilloma virus were mixed with 40  $\mu$ L of tetraethyl orthosilicate (TEOS) and 60  $\mu$ L of bis[3-

(triethoxysilyl)propyl]disulfide. After mixing manually, this mixture was added to the former organic medium. Eventually, 100  $\mu$ L of 28 % ammonia aqueous solution were added and the water-oil emulsion was stirred for 4 hours at room temperature. After that, 20 mL of pure acetone were added in order to precipitate the AntiE6@SS-SiO<sub>2</sub>-NCs and the material was recovered by means of centrifugation and washing six times with water.

#### *Synthesis of AntiE6@SiO<sub>2</sub>-NCs*

Triton X-100 (1.77mL) and n-hexanol (1.8 mL) were dissolved in cyclohexane (7.5 mL). Separately, 300  $\mu$ L of 0.091 mg/mL aqueous solution of E6 antibody from mouse papilloma virus were mixed with 70  $\mu$ L of tetraethyl orthosilicate (TEOS). After mixing manually, this mixture was added to the former organic medium. Eventually, 100  $\mu$ L of 28 % ammonia aqueous solution were added and the water-oil emulsion was stirred for 4 hours at room temperature. After that, 20 mL of pure acetone were added in order to precipitate the AntiE6@-SiO<sub>2</sub>-NCs and the material was recovered by means of centrifugation and washing six times with water.

#### *Preparation of AntiE6@(R)-SiO<sub>2</sub>-PEG-NCs*

AntiE6@(R)-SiO<sub>2</sub>-NCs (15 mg) were taken as synthesised and dispersed in dry ethanol (2.5 mL) followed by the additions of mPEG-silane 5000 (8.33 mg) and silane-PEG-amine 5000 (2.08 mg). The mixture was stirred overnight at room temperature (23 °C) before centrifuging and washing the particles 3 times with distilled water and 3 more times with dry ethanol.

#### *Labeling AntiE6@(R)-SiO<sub>2</sub>-PEG-NCs with atto 425 NHS ester*

The readily prepared AntiE6@(R)-SiO<sub>2</sub>-PEG-NCs were entirely dispersed in distilled water (0.5 mL) and atto 425 NHS ester (0.42 mg) was added while covering the reactor with aluminium foil. The mixture was stirred overnight at room temperature (23 °C) before centrifuging and washing the particles 3 times with distilled water and 3 more times with dry ethanol.

#### *Synthesis of Dox@imine-SiO<sub>2</sub>-NCs*

Triton X-100 (7.1 mL) and n-hexanol (7.2 mL) were dissolved in cyclohexane (30 mL). Separately, 1.2 mL of 2 mg/mL aqueous solution of Doxorubicin hydrochloride (Dox.HCl) were mixed with 160  $\mu$ L of tetraethyl orthosilicate (TEOS) and 281.6 mg of the diiminosilane. After mixing manually, this mixture was added to the former organic medium. Eventually, 400  $\mu$ L of 28 % ammonia aqueous solution were added and the water-oil emulsion was stirred overnight at room temperature. After that, 80 mL of pure acetone were added in order to precipitate the Dox@imine-SiO<sub>2</sub>-NCs and the material was recovered by means of centrifugation and washing three times with ethanol and three more with water.

#### *Synthesis of Dox@SS-SiO<sub>2</sub>-NCs*

Triton X-100 (7.1 mL) and n-hexanol (7.2 mL) were dissolved in cyclohexane (30 mL). Separately, 1.2 mL of 2 mg/mL aqueous solution of Doxorubicin hydrochloride (Dox.HCl) were mixed with 160  $\mu$ L of tetraethyl orthosilicate (TEOS) and 240  $\mu$ L of bis[3-(triethoxysilyl)propyl]disulfide. After mixing manually, this mixture was added to the former organic medium. Eventually, 400  $\mu$ L of 28 % ammonia aqueous solution were added and the water-oil emulsion was stirred overnight at room temperature. After that, 80 mL of pure acetone were added in order to precipitate the Dox@SS-SiO<sub>2</sub>-NCs and the material was recovered by means of centrifugation and washing three times with ethanol and three more with water.

#### *Synthesis of Dox@SiO<sub>2</sub>-NCs*

Triton X-100 (7.1 mL) and n-hexanol (7.2 mL) were dissolved in cyclohexane (30 mL). Separately, 1.2 mL of 2 mg/mL aqueous solution of Doxorubicin hydrochloride (Dox.HCl) were mixed with 280  $\mu$ L of tetraethyl orthosilicate (TEOS). After mixing manually, this mixture was added to the former organic medium. Eventually, 400  $\mu$ L of 28 % ammonia aqueous solution were added and the water-oil emulsion was stirred overnight at room temperature. After that, 80 mL of pure acetone were added in order to precipitate the Dox@SiO<sub>2</sub>-NCs and the material was recovered by means of centrifugation and washing three times with ethanol and three more with water.

### *Doxorubicin release studies on Dox@(R)-SiO<sub>2</sub>-NCs*

Dox@(R)-SiO<sub>2</sub>-NCs were dispersed in PBS solution at the concentration of 0.1 mg/mL. The pH of the PBS solution was set at 7.4 or 5.5 according to the desired experiment. In the case of Dox@SS-SiO<sub>2</sub>-NCs, glutathione was added to obtain a final concentration (glutathione) of 10 mM. In all the cases, the mixture was gently stirred and at times 0, 1, 5, 10, 15, 25, 35, 45 minutes, 1, 3, 6, 12 hours, 1 and 2 days, an aliquot was removed, centrifuged and the supernatant was analysed by fluorimetry.

### **4.5.4 In vitro experiments**

#### *AntiE6@(R)-SiO<sub>2</sub>-PEG-NCs and Dox@(R)-SiO<sub>2</sub>-NCs incubation for confocal microscopy experiments*

HeLa cells were seeded onto glass cover slips in a 24-well cell culture plate at a density of 30 000 cells per well and allowed to grow 24 h. Afterwards the media was removed and fresh media containing the particles at a concentration of 40 µg/mL was added to the cells and incubated for 4 and 24 h at 37 °C in a humidified atmosphere with 5% CO<sub>2</sub>. Afterwards, cells were gently washed 5 times with PBS and fixed with 4 % paraformaldehyde (PFA) for 10 min. The PFA was then removed and the cells washed 3 times with PBS. The samples were then incubated with 0.1% Tritton X-100 in PBS for 5 minutes, washed two times with PBS and rinsed with 1% bovine serum albumin (BSA) for 20 minutes. Cells were gently washed with PBS twice. PBS was removed and the cell layer on glass cover slip was directly stained with Phalloidin Alexa Fluor® 647 (Invitrogen), for f-actin/membrane staining, for 20 minutes, in the dark at room temperature, and washed again twice with PBS. The nuclear region was stained with DAPI for 3 minutes. Finally, the cells were washed 3 times with PBS, once with water and then fixed on a glass microscope slide (knittel glass 76\*26mm) with Fluoromount™ aqueous mounting medium and for confocal microscope analysis.

For the lysosomes staining, after that particle incubation was stopped, cells were washed three times with PBS solution. Subsequently 75 nM of LysoTracker® Red DND-99 staining solution in culture media was added, and cells were incubated for 30 minutes followed by another washing process. Fresh culture media was added and imaging was performed directly.

#### *Cell Viability assays with Dox@(R)-SiO<sub>2</sub>-NCs and Dox solutions*

Cell viability was assessed using alamarBlue assay. HeLa cells were seeded onto glass cover slips in a 24-well cell culture plate at a density of 50 000 cells per well and allowed to grow 24 h. Afterwards, the media was removed and fresh media containing the particles at concentrations of 0.1, 0.5 and 1mg/mL were added to the cells. In parallel, the cells were also treated with doxorubicin at 0.1 mg/mL according to the loading percentage in the capsules. The cells were incubated for 24 and 48 h at 37 °C in a humidified atmosphere with 5% CO<sub>2</sub>. After incubation, alamar blue was added to the different well plates (dilution 1:10) and incubated for 4h. The solutions were then transferred into a 96 well plates and the metabolic activity of living cells were testified by the reduction of resazurin (dark blue) in resorufin (pink). The reduction process was recorded at 570 and 600 nm using a VICTOR X5 Multilabel Plate Reader (Perkin Elmer). Each sample was tested in three replicates.

#### 4.6 References

1. Zhou, H., Wu, S., Joo, J., Y., Zhu, S., Han, D. W., Lin, T., Trauger, S., Bien, G., Yao, S., Zhu, Y., Siuzdak, G., Schöler, H. R., Duan, L. & Ding, S. Generation of Induced Pluripotent Stem Cells Using Recombinant Proteins. *Cell Stem Cell* **4**, 381–384 (2009).
2. Schwarze, S. R., Ho, A., Vocero-Akbani, A. & Dowdy, S. F. In Vivo Protein Transduction: Delivery of a Biologically Active Protein into the Mouse. *Science* **285**, 1569 (1999).
3. Shah, A. M. & Mann, D. L. In search of new therapeutic targets and strategies for heart failure: recent advances in basic science. *The Lancet* **378**, 704–712
4. Fu, K., Klibanov, A. M. & Langer, R. Protein stability in controlled-release systems. *Nat Biotech* **18**, 24–25 (2000).
5. Jiskoot, W., Randolph, T., Volkin, D. B., Russell Midd, C., Schöneich, C., Winter, G., Friess, W., Crommelin, D. J. A. & Carpenter, J. F. Protein Instability and Immunogenicity: Roadblocks to Clinical Application of Injectable Protein Delivery Systems for Sustained Release. *J. Pharm. Sci.* **101**, 946–954
6. Yuba, E., Kono, Y., Harada, A., Yokoyama, S., Arai, M., Kubo, K. & Kono, K. The application of pH-sensitive polymer-lipids to antigen delivery for cancer immunotherapy. *Biomaterials* **34**, 5711–5721 (2013).
7. Yuba, E., Harada, A., Sakanishi, Y., Watarai, S. & Kono, K. A liposome-based antigen delivery system using pH-sensitive fusogenic polymers for cancer immunotherapy. *Biomaterials* **34**, 3042–3052 (2013).
8. Prasetyanto, E. A., Bertucci, A., Septiadi, D., Corradini, R., Castro-Hart, P. & De Cola, L. Breakable Hybrid Organosilica Nanocapsules for Protein Delivery. *Angew. Chem. Int. Ed.* **55**, 3323–3327 (2016).
9. Yim, E.-K. & Park, J.-S. The role of HPV E6 and E7 oncoproteins in HPV-associated cervical carcinogenesis. *Cancer Res. Treat.* **37**, 319–324 (2005).

10. Togtema, M., Pichardo, S., Jackson, R., Lambert, P. F., Curiel, L., Zehbe, I. & Rota, R. Sonoporation Delivery of Monoclonal Antibodies against Human Papillomavirus 16 E6 Restores p53 Expression in Transformed Cervical Keratinocytes. *PLoS ONE* **7**, e50730 (2012).
11. Slowing, I., Viveroescoto, J., Wu, C. & Lin, V. Mesoporous silica nanoparticles as controlled release drug delivery and gene transfection carriers. *Adv. Drug Deliv. Rev.* **60**, 1278–1288 (2008).
12. Sun, R., Wang, W., Wen, Y. & Zhang, X. Recent Advance on Mesoporous Silica Nanoparticles-Based Controlled Release System: Intelligent Switches Open up New Horizon. *Nanomaterials* **5**, 2019–2053 (2015).
13. Slowing, I. I., Trewyn, B. G., Giri, S. & Lin, V. S.-Y. Mesoporous Silica Nanoparticles for Drug Delivery and Biosensing Applications. *Adv. Funct. Mater.* **17**, 1225–1236 (2007).
14. Sun, X. Mesoporous silica nanoparticles for applications in drug delivery and catalysis. *Graduate Theses and Dissertations*. Paper 12812 (2012).
15. Cui, Y., Dong, H., Cai, X., Wang, D. & Li, Y. Mesoporous Silica Nanoparticles Capped with Disulfide-Linked PEG Gatekeepers for Glutathione-Mediated Controlled Release. *ACS Appl. Mater. Interfaces* **4**, 3177–3183 (2012).
16. Palanikumar, L., Choi, E. S., Cheon, J. Y., Joo, S. H. & Ryu, J.-H. Noncovalent Polymer-Gatekeeper in Mesoporous Silica Nanoparticles as a Targeted Drug Delivery Platform. *Adv. Funct. Mater.* **25**, 957–965 (2015).
17. Hu, C., Yu, L., Zheng, Z., Wang, J., Liu, Y., Jiang, Y., Tong, G., Zhou, Y. & Wang, X. Tannin as a gatekeeper of pH-responsive mesoporous silica nanoparticles for drug delivery. *RSC Adv.* **5**, 85436–85441 (2015).
18. Li, Q.-L., Sun, Y., Sun, Y.-L., Wen, J., Zhou, Y., Bing, Q.-M., Isaacs, L. D., Jin, Y., Gao, H. & Yang, Y.-W. Mesoporous Silica Nanoparticles Coated by Layer-by-Layer Self-assembly Using Cucurbit[7]uril for in Vitro and in Vivo Anticancer Drug Release. *Chem. Mater.* **26**, 6418–6431 (2014).
19. Mondragón, L., Mas, N., Ferragud, V., de la Torre, C., Agostini, A., Martinez-Manez, R., Sancenon, F., Amoros, P., Pérez-Paya, E. & Orzaez, M. \_ Enzyme-Responsive Intracellular-Controlled Release Using Silica Mesoporous Nanoparticles Capped with  $\epsilon$ -Poly-L-lysine. *Chem. - Eur. J.* **20**, 5271–5281 (2014).
20. Gokhale, P. C., Radhakrishnan, B., Husain, S. R., Abernethy, D. R., Sacher, R., Dritschilo, A. & Rahman, A. An improved method of encapsulation of doxorubicin in liposomes: pharmacological, toxicological and therapeutic evaluation. *Br. J. Cancer* **74**, 43 (1996).
21. Eikenberry, S. A tumor cord model for Doxorubicin delivery and dose optimization in solid tumors. *Theor. Biol. Med. Model.* **6**, 16 (2009).
22. Tacar, O., Sriamornsak, P. & Dass, C. R. Doxorubicin: an update on anticancer molecular action, toxicity and novel drug delivery systems: Doxorubicin cell and molecular biological activity. *J. Pharm. Pharmacol.* **65**, 157–170 (2013).

23. Tian, Y., Li, S., Song, J., Ji, T., Zhu, M., Anderson, G., Wei, J. & Nie, G. A doxorubicin delivery platform using engineered natural membrane vesicle exosomes for targeted tumor therapy. *Biomaterials* **35**, 2383–2390 (2014).
24. Chen, G., Li, D., Li, J., Cao, X., Wang, J., Shi, X. & Guo, R. Targeted doxorubicin delivery to hepatocarcinoma cells by lactobionic acid-modified laponite nanodisks. *New J. Chem.* **39**, 2847–2855 (2015).
25. MacDiarmid, J. A., Langova, V., Bailey, D., Pattison, S. T., Pattison, S. L., Christensen, N., Armstrong, L. R., Brahmabhatt, V. N., Smolarczyk, K. & Harrison, M. T. Targeted Doxorubicin Delivery to Brain Tumors via Minicells: Proof of Principle Using Dogs with Spontaneously Occurring Tumors as a Model. *PLoS One* **11**, e0151832 (2016).
26. Sanyakamdorn, S., Agudelo, D. & Tajmir-Riahi, H.-A. Encapsulation of Antitumor Drug Doxorubicin and Its Analogue by Chitosan Nanoparticles. *Biomacromolecules* **14**, 557–563 (2013).
27. Nel, A. E., Mädler, L., Velegol, D., Xia, T., Hoek, E. M. V., Somasundaran, P., Klaessig, F., Castranova, V. & Thompson, M. Understanding biophysicochemical interactions at the nano–bio interface. *Nat. Mater.* **8**, 543–557 (2009).
28. Moore, T. L., Rodriguez-Lorenzo, L., Hirsch, V., Balog, S., Urban, D., Jud, C., Rothen-Rutishauser, B., Lattuada, M. & Petri-Fink, A. Nanoparticle colloidal stability in cell culture media and impact on cellular interactions. *Chem. Soc. Rev.* **44**, 6287–6305 (2015).
29. Mercer, R. R., Scabilloni, J., Wang, L., Kisin, E., Murray, A. R., Schwegler-Berry, D., Shvedova, A. A. & Castranova, V. Alteration of deposition pattern and pulmonary response as a result of improved dispersion of aspirated single-walled carbon nanotubes in a mouse model. *Am. J. Physiol. - Lung Cell. Mol. Physiol.* **294**, L87–L97 (2008).
30. Kreyling, W. G., Abdelmonem, A., Ali, Z., Alves, F., Geiser, M., Haberl, N., Hartmann, R., Hirn, S., de Aberasturi, D., Kantner, K., Khadem-Saba, G., Montenegro, J.-M., Rejman, J., Rojo, T., de Larramendi, I. R., Ufartes, R., Wenk, A. & Parak, W. J. In vivo integrity of polymer-coated gold nanoparticles. *Nat. Nanotechnol.* **10**, 619–623 (2015).
31. Jiang, X., Weise, S., Hafner, M., Rocker, C., Zhang, F., Parak, W. J. & Nienhaus, G. U. Quantitative analysis of the protein corona on FePt nanoparticles formed by transferrin binding. *J. R. Soc. Interface* **7**, S5–S13 (2010).
32. Otsuka, H., Nagasaki, Y. & Kataoka, K. PEGylated nanoparticles for biological and pharmaceutical applications. *Adv. Drug Deliv. Rev.* **55**, 403–419 (2003).
33. Jokerst, J. V., Lobovkina, T., Zare, R. N. & Gambhir, S. S. Nanoparticle PEGylation for imaging and therapy. *Nanomed.* **6**, 715–728 (2011).
34. Qian, W., Murakami, M., Ichikawa, Y. & Che, Y. Highly Efficient and Controllable PEGylation of Gold Nanoparticles Prepared by Femtosecond Laser Ablation in Water. *J. Phys. Chem. C* **115**, 23293–23298 (2011).
35. Moffatt, S. Nanoparticle PEGylation for Cancer Therapy. *MOJ Proteomics Bioinform* **2**, 37 (2015).
36. Ma, K., Zhang, D., Cong, Y. & Wiesner, U. Elucidating the Mechanism of Silica Nanoparticle PEGylation Processes Using Fluorescence Correlation Spectroscopies. *Chem. Mater.* **28**, 1537–1545 (2016).

37. Scherer, W. F., Syverton, J. T. & Gey, G. O. Studies on the propagation in vitro of poliomyelitis viruses IV. Viral multiplication in a stable strain of human malignant epithelial cells (strain HeLa) derived from an epidermoid carcinoma of the cervix. *J. Exp. Med.* **97**, 695–710 (1953).
38. Maher, P. The effects of stress and aging on glutathione metabolism. *Ageing Res. Rev.* **4**, 288–314 (2005).
39. Lushchak, V. I. Glutathione Homeostasis and Functions: Potential Targets for Medical Interventions. *J. Amino Acids* **2012**, 1–26 (2012).
40. Abdalla, M. Y. Glutathione as potential target for cancer therapy; more or less is good?(mini-review). *Jordan J. Biol. Sci.***4**, 119 (2011).
41. Sun, H., Guo, B., Li, X., Cheng, R., Meng, F., Liu, H. & Zhong, Z. Shell-Sheddable Micelles Based on Dextran-SS-Poly( $\epsilon$ -caprolactone) Diblock Copolymer for Efficient Intracellular Release of Doxorubicin. *Biomacromolecules* **11**, 848–854 (2010).

# Chapter 5

## Instrumental techniques

### Abstract

Knowing the numerous and various types of characterisation which have been performed to well conduct the diverse studies reported in this thesis, it is worth to describe at least the basic principles of the different techniques requested. Thus, in this chapter are first described spectroscopic methods such as NMR, IR, XPS and EDX. This report deals then with the basic principles of some microscopy including SEM, TEM and CLSM, followed by some details about DLS and zeta potential. Eventually, TGA technique is related.

## 5.1 $^1\text{H}$ Nuclear magnetic resonance (NMR) spectroscopy

One of the most used techniques to characterise organic molecules is  $^1\text{H}$  NMR spectroscopy. This technique relies on a magnetic field which enables a sample to absorb an electromagnetic radiation in the radiofrequencies range ( $\lambda \approx 1\text{m}$ ). The absorption depends on the nuclei in the molecule.

Each nucleus has a spin, which describes the surrounding magnetic dipole charge (0, 1/2, 1, 3/2, etc...). Essentially, this spin makes the nuclei behaving as a magnet. Different nuclei can be considered in such an analysis. In this chapter, we will focus on the commonly called “proton” ( $^1\text{H}$ ) nucleus (**Figure 5.A**), which has a spin of 1/2. Upon an external magnetic field  $B_0$ , there are two energy levels called +1/2 (**Figure 5.1B**) and -1/2 (**Figure 5.1C**).

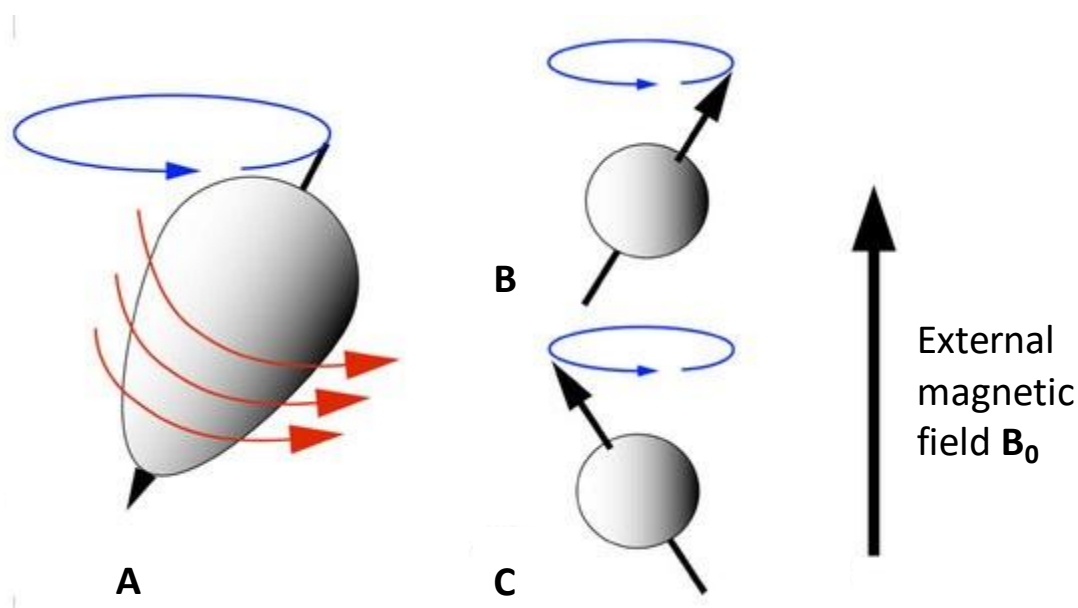


**Figure 5.1** Schematic representation of two energy levels of “proton” upon an external magnetic field application. Figure taken from reference 1.

According to Boltzmann distribution, the energy gap  $\Delta E$  is given by **the equation 5.1** which is displayed below:

$$\Delta E = \left(\frac{h\gamma}{2\pi}\right) B_0 \quad (5.1)$$

In this equation,  $h$  represents the Planck's constant having a value of  $6.62607004 \cdot 10^{-34} \text{ m}^2 \cdot \text{kg} \cdot \text{s}^{-1}$ ) and  $\gamma$  is the gyromagnetic ratio. The latter is described as the ratio of the corresponding magnetic momentum in an atom to its angular momentum (for  $^1\text{H}$  nucleus,  $\gamma =$

$267.513 \text{ rad}\cdot\text{s}^{-1}\cdot\text{T}^{-1}$ ).<sup>1</sup> The equation enables us to notice that  $\Delta E$  is proportional to the magnetic field  $B_0$ .

After establishing this principle, energy can be determined as radiofrequency radiation  $\nu$  in order to get a transition between the spins C and B in a magnetic field. Indeed,

$\Delta E = h\nu$  and, consequently, the radiofrequency radiation can be determined from the following **equation 5.2**:

$$\nu = \left(\frac{\gamma}{2\pi}\right) B_0 \quad (5.2)$$

In this equation,  $\nu$  is given in MHz. For the proton, if  $B_0 = 2.35\text{T}$ ,  $\nu = 100 \text{ MHz}$ . The energy is absorbed by the nucleus which is then shifted to the highest energy state and the spectrum is recorded. This phenomenon is called “resonance”.

Two types of spectrometers exist. We can find, in the one hand, the continuous wave (CW) and, in the other hand, the Fourier transform (FT) devices. In the CW system, a scan is performed through a range of frequencies. The sample is measured with one frequency at a time. The scan of the frequency range results in the generation of a plot of signal intensity (or the absorbed energy) vs. frequency. In the case of the FT spectrometer, the sample is measured with a range of several frequencies at once. The signal decay over time is defined as a so-called “Free Induction Decay” (FID). The generated plot of the signal vs. time is transformed into that of a signal vs. frequency by a FT process. The sample is irradiated with a specified range of frequencies called sweep width for a specified period of time called pulse width. An important feature of a FT technique is the so-called “relaxation time” and it corresponds to the time requested by the sample to go return to its ground state before the next irradiation. The reproducibility of the signal is confirmed by the “relaxation time” feature.

## 5.2 Infrared (IR) spectroscopy

Another very important spectroscopic technique to characterise organic molecules is infrared (IR) spectroscopy, more precisely, mid-infrared spectroscopy. This technique relies on the excitation of vibrational modes of the molecules in the sample. Due to this fact, IR enables the identification of the various chemical bonds and functional groups present in the molecules.<sup>1</sup>

In IR spectroscopy, molecular absorption of electromagnetic radiation in the infrared region leads to transitions between the rotational and vibrational energy levels of the ground

electronic energy state. Due to the fact that transitions between individual rotational states can be measured only in the infrared spectra of small molecules in the gas phase, IR spectroscopy regards firstly molecular vibrations.

In the one hand, a non-linear molecule made up of  $N$  atoms is said to possess  $3N$  degrees of freedom because if the position of each atom were to be described by three coordinates (*e.g.*,  $x$ ,  $y$ , and  $z$  in a Cartesian coordinate system), the position, shape, and orientation of the molecule in three-dimensional space would be completely defined. As a consequence, the molecule has three translational degrees of freedom. Moreover, the rotation of the molecule around the three axes also needs to be considered. Eventually, the remaining  $3N-6$  degrees of freedom correspond to vibrational motions and the molecule is said to have  $3N-6$  normal vibrational modes. We can define these vibrational modes by relating bond stretching and various types of bending vibrations. **Figure 5.2** summarises these different molecular vibrations.

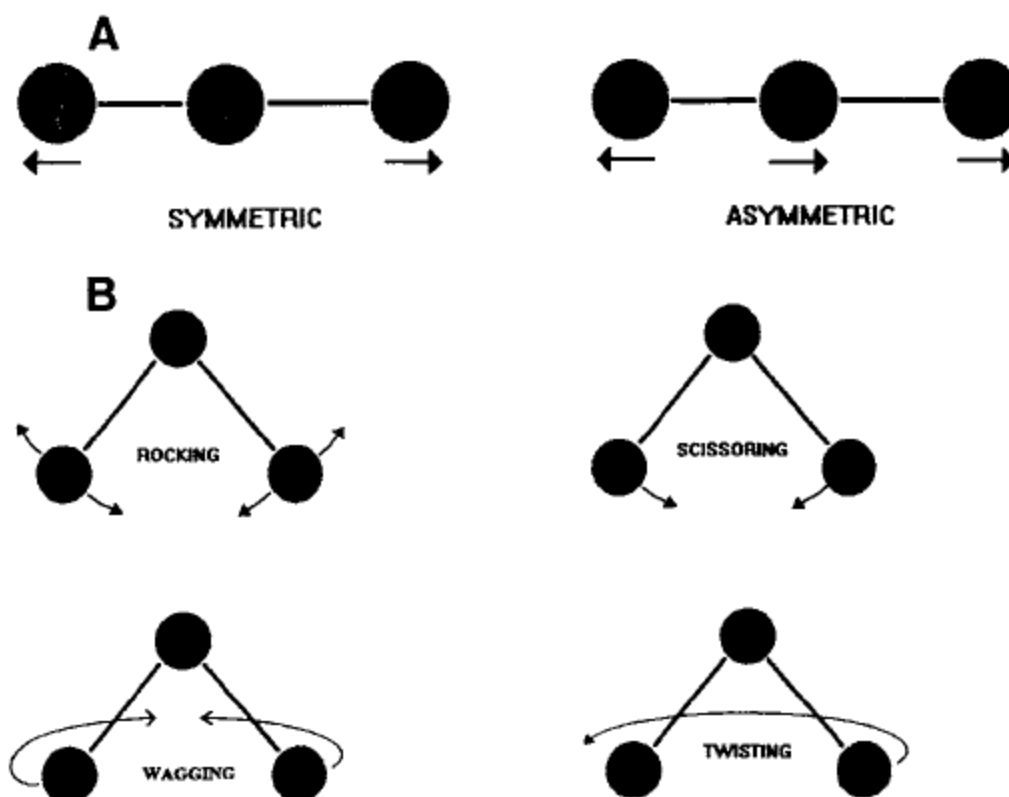


**Figure 5.2** Types of molecular vibrations: (A) stretching vibrations and (B) bending vibrations. Figure taken from reference 1.

In the other hand, for a linear molecule, only two rotational degrees of freedom can be found knowing that rotation around the bond axis cannot occur. As a result, such a molecule shows  $3N-5$  normal vibrational modes. Thus, a simple diatomic molecule represented by A-B has  $(3 \times 2) - 5 = 1$  vibrational mode (stretching along the A-B bond). To a first approximation, the vibration can be described by the model of a harmonic oscillator and the restoring force (F) on the bond is given by Hooke's law (**equation 5.3**), which is displayed below.

$$\mathbf{F} = -\mathbf{kx} \text{ (5.3)}$$

In this law, k represents the force constant of the bond and x the displacement.

This approximation allows the determination of the vibrational frequency  $\nu$  is by the **equation 5.4**.

$$\nu = (1/2\pi)(k/\mu)^{1/2} \text{ (5.4)}$$

where  $\mu$  is the reduced mass of the system, as defined by the following **equation 5.5**:

$$\mu = m_A \cdot m_B / (m_A + m_B) \text{ (5.5)}$$

where  $m_A$  and  $m_B$  are the individual atomic masses of A and B.

The unit of frequency ( $\nu$ ) is reciprocal seconds ( $s^{-1}$ ). However, by convention, band positions in infrared spectra are given in wavenumbers ( $\bar{\nu}$ ), expressed in units of reciprocal centimeters ( $cm^{-1}$ ). This feature is related to the frequency  $\nu$  and, thus, to the wavelength  $\lambda$  by the **equation 5.6**.

$$\bar{\nu} = 1/\lambda \text{ (5.6)}$$

### **5.3 X-ray photoelectron spectroscopy (XPS)**

X-ray photoelectron spectroscopy (XPS) is a surface analysis technique with a very high sensitivity. In the basic principle of XPS, an incident X-ray with energy of 200 - 2000eV is applied and induces the ejection of an electron from the K layer from the atom (1s electron). An electron multiplier detector collects the photoelectron and a spectrometer analyses it in order to acquire the kinetic energy ( $E_k$ ).

The binding energy of the electron ( $E_b$ ) can identify the electron both from its parent element and the atomic energy level. It can be determined from the following **equation 5.7**.

$$E_b = E_{xr} - E_k - W_f \text{ (5.7)}$$

In this equation,  $E_b$  corresponds to the binding energy,  $E_{xr}$  represents the X-Ray energy,  $E_k$  is the kinetic energy of the photoelectron and  $W_f$  the spectrometer work function. Those three parameters are known or can be measured and, as a consequence, the binding energy can easily be determined. The process is illustrated in **Figure 5.3**.

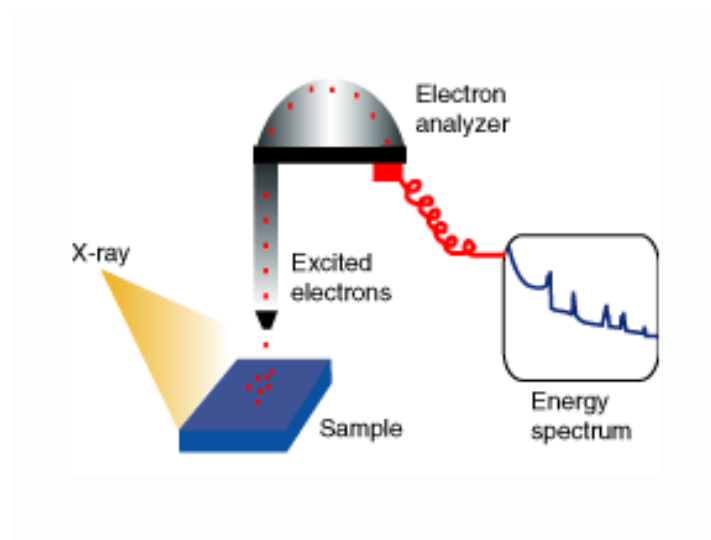


**Figure 5.3** Schematic representation of the principle of XPS. Figure taken from reference 3.

#### **5.4 Electrospray Ionisation-Mass Spectrometry (ESI-MS)**

Chemical compounds can also be characterised by their mass. Different techniques are available. In this chapter, we will focus on ESI-MS because this is the one we used. In ESI-MS, the sample is ionised by an ESI source belonging to a category of ion sources called atmospheric pressure ionization (API). The ions are then transferred to an analyser.

Mass spectrometry measures the mass/charge ( $m/z$ ) ratio of the ions. The mechanism of ESI-MS and the ion source are schematised in **Figure 5.4**.

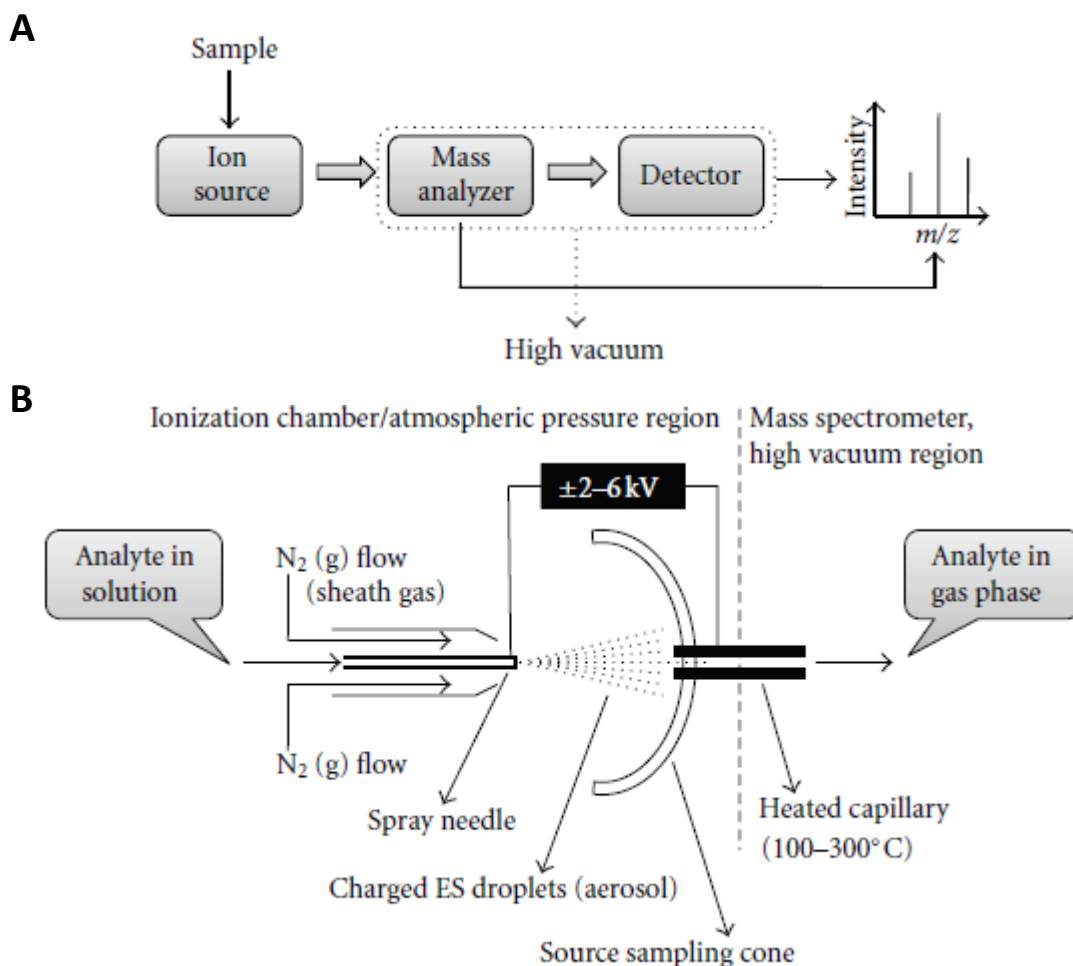


**Figure 5.4** Schematic representations of (A) the mechanism of ESI-MS and (B) the ion source.

In this technique, a strong electric field is applied, under atmospheric pressure, to a liquid passing through a capillary tube with a weak flow. The electric field is promoted by the induction of a potential difference of 2-6 kV between the capillary and the counter electrode; inducing a charge accumulation at the liquid surface located at the end of the capillary, which breaks to form highly charged droplets. Due to charges accumulation at the tip of the needle, the nascent drop tends to elongate until breaking the surface tension and the change of the shape of the profile into the so-called “Taylor cone”, with the appearance of the spray. Due to a coaxial injection of a gas at a low flow rate, the space of the dispersion of the spray can be restricted. The droplets then pass through a heated (100 - 300 °C) capillary transfer to remove the last residual solvent. Consequently, a gas phase ions is produced and dragged to the mass analyser.

## 5.5 Scanning electron microscopy (SEM) and energy-dispersive X-ray spectroscopy (EDX)

### 5.5.1 Scanning electron microscopy (SEM)

Scanning electron microscopy is a microscopic technique which serves to image surfaces by exploiting electronic interactions. In this technology, the sample is scanned with a focused high-energy electron beam to generate a range of signals on the surface. SEM enables the morphologic characterization of solid surfaces. **Figure 5.4** schematically describes the principle of SEM.

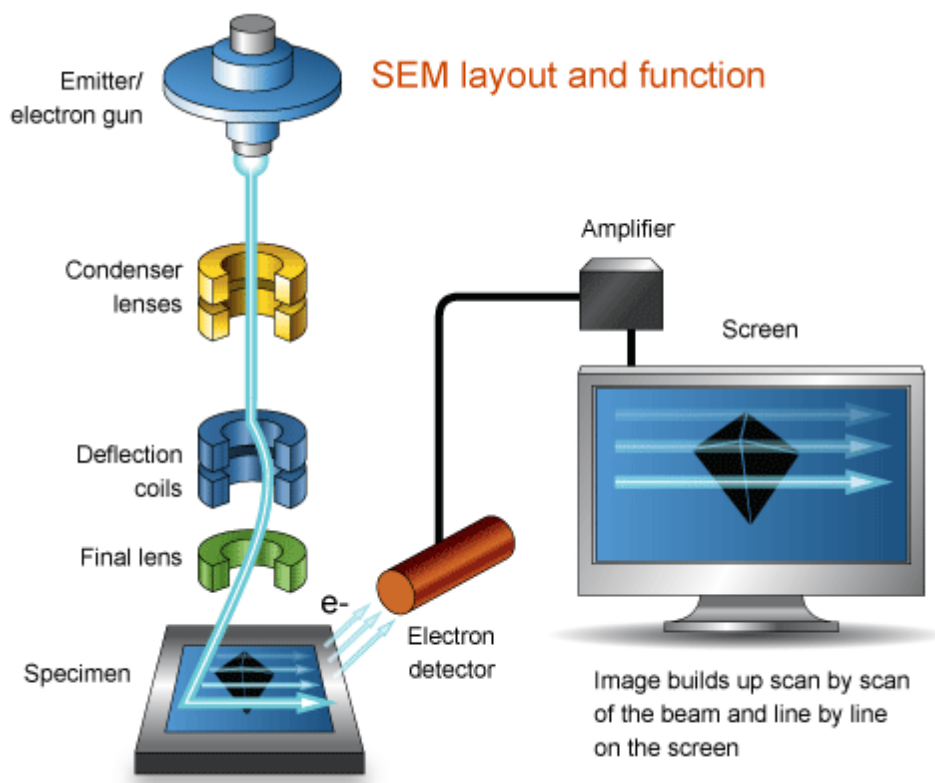


**Figure 5.5** Schematic representation of a SEM and its principle. Figure taken from reference 4.

Electrons called “incident electrons” are generated from an electron gun and typically with an energy range of 1 - 40 keV. The electron gun can be constituted of tungsten hairpin filament (thermionic-based emission), which is heated up to 2500 °C where the energy of the weakest bound electrons exceeds the work function of the material. This phenomenon allows the electron emission or another thermionic emission source such as lanthanum hexaboride or field-emission-sources which use high electric fields between a cathode and an anode, in a

way that if the applied electric field is big enough, the work function of the cathode dramatically decreases and electron emission is possible even at room temperature. The electron beam is then demagnified by electromagnetic condenser lenses (at the numbers of two or three) into a fine probe which is scanned along a selected area of the sample surface in a raster by scan coils. The specimen receives the electrons in a teardrop-shaped volume. The energy of the electron beam, the atomic masses of elements in the specimen and the angle at which the electron beam hits the specimen enables the determination of the overall dimensions of this specimen. Secondary, backscattered and a so-called “Auger” electrons, x-rays and possibly light are produced by the interaction between the electron beam and the specimen and collected by diverse detectors in the specimen chamber.

The type of electrons generally considered for imaging samples are those secondary. They are obtained when the incident electron beam excites electrons in the sample, which then migrate to the surface and escape from the sample, depending on its energy. As the incident energy is very low (typically 40 keV for the maximum), only secondary electrons in the surface environment can leave the sample and produce the output signal. The volume in which those electrons are produced is relatively small, which leads to a high axial resolution, within a few nm. Eventually, the obtained image corresponds to a map formation of the secondary electron density depending on the properties of the sample.

### ***5.5.2 Energy-dispersive X-ray spectroscopy (EDX)***

Energy-dispersive X-ray spectroscopy is a category of spectroscopy which can be coupled with SEM. In SEM, when the excited electrons of specific orbitals return to lower energy states, X-ray signal is generated, producing electromagnetic signal which has a fixed frequency related to the difference in electronic energy levels for a given element. Thus, characteristic X-rays are produced for each element and enables a chemical composition mapping of the sample surface.

### **5.6 Transmission electron microscopy (TEM)**

Transmission electron microscopy (TEM) differs from SEM by its high energy (100 - 300 keV). TEM images the transmission of a beam of electrons through a sample, which is thus placed between the electron source and the detector. Two main types of contrasts can be

observed in the image. Bright areas are provided when the electrons pass through the sample without being scattered, while darker spots are observed when the electron beam is hampered or stopped by other regions of the sample, depending on the electronic density. The way the electrons interact with and are scattered by the sample determines the contrast visualized in the image.

An electron beam is also used in TEM to generate the incident electrons. However, as already said above, higher energy ranging from 100 to 300 keV are requested, by comparison to SEM. The condenser lens is placed before the sample and it simultaneously serves to control the beam parameter, *i.e.* diameter, and to focus the beam onto the sample. After passing through the specimen, the electron beam reaches the objective lens, which generates the first intermediate image of the sample. The resolution of the final image is related to the quality of the first intermediate. Furthermore, this latter is an inverted initial one, which is subsequently magnified by the intermediate lens and a second intermediate image is produced. This feature is eventually collected by the projector lens and the final image is afforded onto a recording device. This principle is illustrated in **Figure 5.5** below.

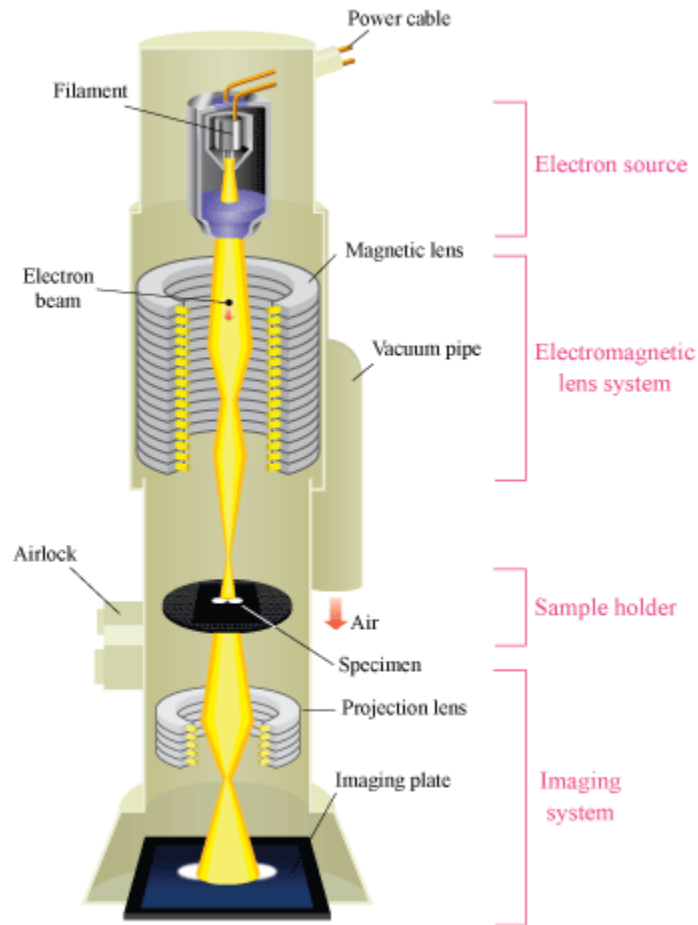


**Figure 5.6** Schematic representation of the principle of TEM. Figure taken from reference 5.

## 5.7 Fluorescence confocal microscopy and z-stack processing

### 5.7.1 Fluorescence confocal microscopy

Fluorescence confocal microscopy or, more precisely, confocal laser scanning microscopy (CLSM) is a widely used optical tool to analyse biological samples nowadays. As illustrated in **Figure 5.7<sup>2</sup>**, the principle of CLSM is composed of different parts.

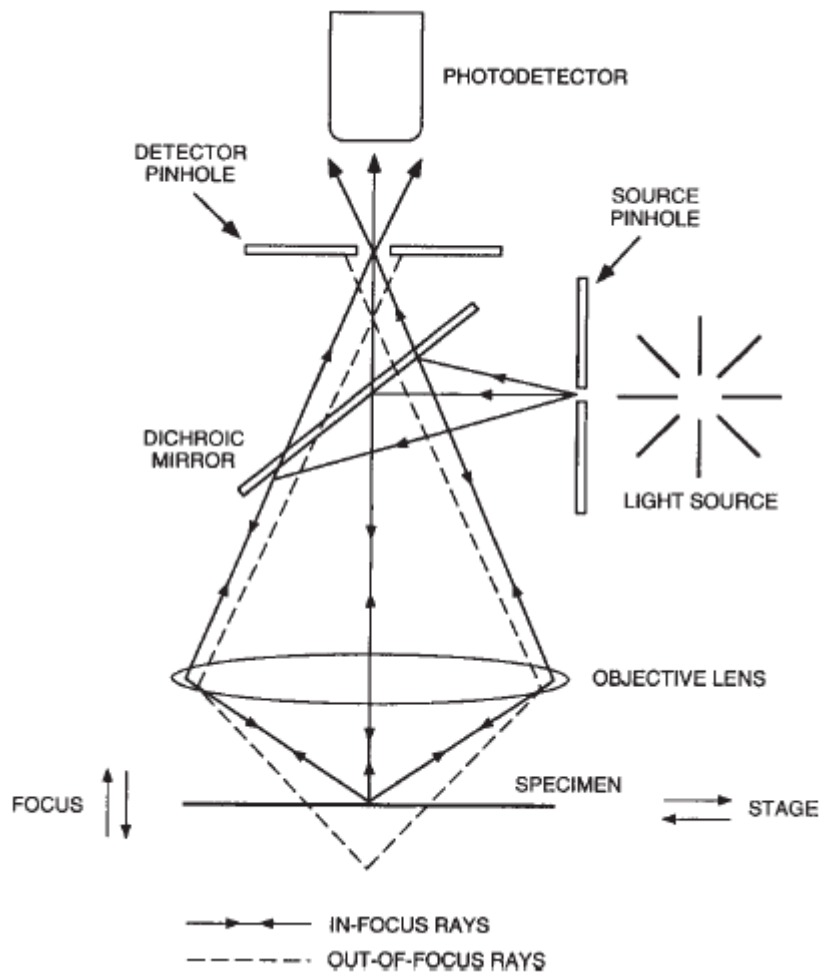


**Figure 5.7** Principle of CLSM. Figure taken from reference 2.

In such a technique, a coherent light coming from the laser system, being the excitation source, travels through a pinhole aperture located in a conjugate plane, also called confocal, with a scanning point on the specimen and a second pinhole aperture positioned in front of the detector. The detector corresponds to a photomultiplier tube. In the ideal case, diffraction limited, secondary fluorescence (also called rays) emitted from points on the specimen (in the same focal plane) pass back through a dichromatic mirror and are focused as a confocal point at the detector pinhole aperture. This is the consequence of the fact that the laser is reflected by the dichromatic mirror and scanned across the specimen in a defined focal plane. The significant amount of out-of-focus rays emission which occurs at points above and below the objective focal plane is not confocal with the pinhole and forms extended airy disks in the aperture plane. Most of this extraneous ray is not detected by the photomultiplier and thus does not contribute to the resulting image because only a small fraction of the out-of-focus

rays emission is delivered through the pinhole aperture. Similar functions are performed to identical components in a widefield epi-fluorescence microscope by some optical elements like dichromatic mirror, barrier filter or excitation filter perform. By refocusing the objective in a confocal microscope, it is possible to shift the excitation and emission points on a specimen to a new plane which becomes confocal with the pinhole apertures of the light source and detector. In the obtained image, a pixel is represented by the detected photon which originates from an illuminated/excited volume element within the specimen. This makes the difference with traditional epi-fluorescence microscope. Scanning over the plane of interest by the laser leads to an entire image pixel-by-pixel and line-by-line, knowing that the relative intensity of detected light represents the brightness of the pixel of the resulting image. The scanning is performed across the sample in the horizontal plane by using one or more oscillating mirrors.

### ***5.7.2 Z-stack processing***

In CLSM, the scan speed can be varied and thus lower scan rate results in a better signal-to-noise ratio and, subsequently, better contrast and higher resolution are afforded. Furthermore, the scan can also be performed through different focal planes on the z-axis. For this purpose, what is needed is just to raise or lower the microscope stage or objective lens. Successive etching processes results in the so-called “z-stack” feature, which can be processed by a software to afford a kind of three dimensional image.

## **5.8 Fluorescence spectroscopy**

Fluorescence spectroscopy is a spectroscopic technique used to characterise luminescent, i.e. fluorescent and/or phosphorescent signals emitted from a given specimen. The basic principle of a fluorimeter, which is the corresponding device, is represented in **Figure 5.7**. Photons, generally generated from a xenon lamp, excite the molecules present in the sample at a certain wavelength by passing through a monochromator. The molecules absorb a part of these photons while the other part is collected by a reference channel. After the excitation step, the molecules return to the ground state by emitting a part of the initially absorbed photons. This emission is luminescent and the corresponding signal is collected at the angle of  $90^\circ$ , pass through a second monochromator to eventually reach a detector. The recorded emission

spectrum represents the wavelength distribution of the emission measured at a single constant excitation wavelength.

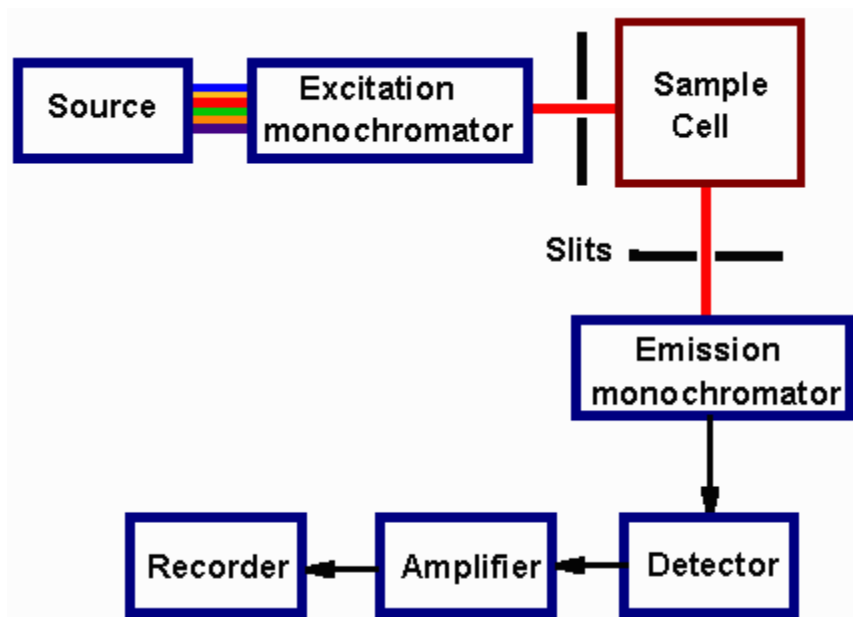


**Figure 5.8** Basic principle of a fluorimeter. Figure taken from reference 6.

### 5.9 Dynamic light scattering (DLS)

Dynamic light scattering (DLS) is a technique used to determine the size of particles in dispersion. The basic principle of a DLS system is described in **Figure 5.9**. When particles are suspended in liquids, they undergo a Brownian motion due to random collisions with solvent molecules. Such a motion induces the diffusion of the particles through the medium.

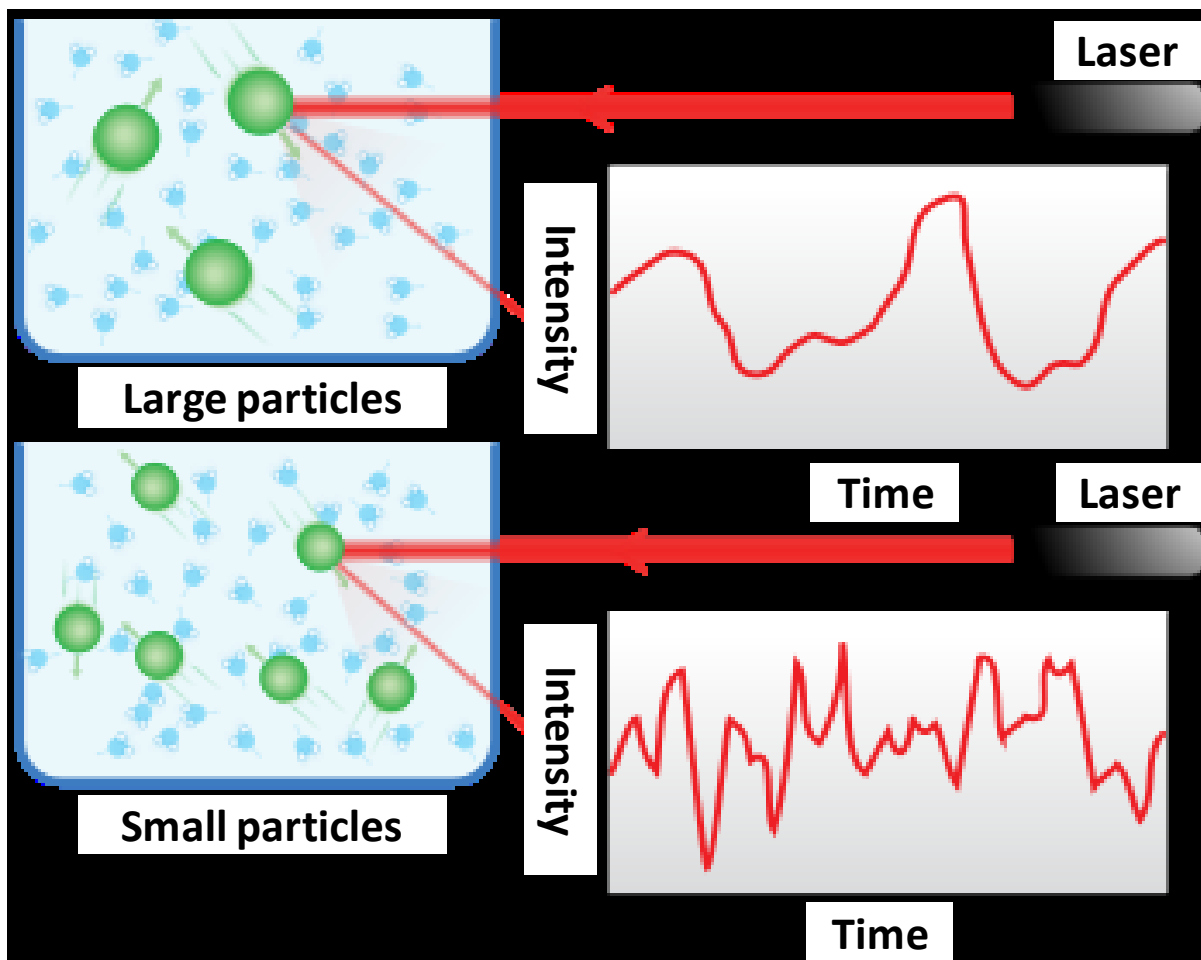


**Figure 5.9** Schematic description of a DLS system. Figure taken from reference 7.

The diffusion coefficient,  $D$ , is inversely proportional to the particle size according to the Stokes-Einstein **equation 5.8** below.

$$D = \frac{kT}{3\pi\eta d} \quad (5.8)$$

In this equation,  $D$  represents the diffusion coefficient,  $k$  the Boltzmann's constant,  $T$  the temperature of the medium, while  $\eta$  corresponds to the viscosity and  $d$  to the hydrodynamic diameter. According to this equation, it is possible to predict that large particles will be associated with relatively small  $D$  and will thus move slowly, while those smaller will induce larger  $D$  and will move faster. Therefore the size of the particles can be calculated by observing their motion and determining their diffusion coefficient in liquid media. Upon a contact with particles, a laser light is scattered in all directions. This scattered light comes from a collection of scattering elements, so that, at each time  $t$ , the intensity is a result of the

interference of light scattered by each element. The relative positions of the elements affect the intensity of the scattered light. If the particles are in motion, the relative positions of particles will change in time and fluctuations in time of the scattered light intensity will thus be observed. The fluctuations of the scattered light intensity are random due to the relatively random character of the particles motion since they are in Brownian motion. Nevertheless, small particles tend to afford fast intensity fluctuations whereas big particles tend to induce slow fluctuations.

The fluctuations of the scattered light are analysed using the so-called “autocorrelation function” (ACF). The ACF is a function which decays as a function of delay time. This function rapidly decays exponentially with a large decay constant for small particles (rapid motion and rapid intensity fluctuations) while, in the case of large particles (slow motion and slow intensity fluctuations), the exponential decays more slowly with a smaller decay constant. The ACF is thus used to determine the diffusion coefficient and, subsequently, the size of the particles. The latter is given in the form of a statistical distribution sorted by scattering intensity, volume or number of particles. The intensity distribution is the directly measured and thus more reliable parameter. This feature is thus the general and most common way used to show DLS data. Nevertheless, it is possible to edit with the software the volume and the number distributions through a calculation from the intensity distribution by using Mie theory.

## **5.10 Zeta potential**

Zeta potential is an analytical technique used for the measurement of the effective electric charge on a particle surface and to quantify the charge stability of colloidal particles. The principle of zeta potential measurement is illustrated in **Figure 5.10**. When a particle has a certain surface charge, it is surrounded by a high concentration of ions of opposite charge near its surface to maintain the electric neutrality. These counter ions form a so-called Stern layer which moves with the particle. In the further environment from the particle, the concentration of the counter ions gradually decreases and the ratio between cations and anions becomes about 1:1. That further layer of ions is called diffuse layer because those ions are diffused. The combination of the Stern layer with the diffuse one is called the electrical double layer. When the particle undergoes a Brownian motion in a medium, they move together with the Stern layer and a part of the diffused layer. The interface between moving and non-moving

ions in the diffused layer is called the slipping plane. Eventually, the potential at the slipping plane versus a point far away from the particle is considered as the so-called zeta potential. Zeta potential measurement is carried out by adding a solution to a cell containing two gold electrodes. When a voltage is applied to the electrode, the particle tends to move onto the electrode with the opposite charge. The particle velocity as a function of voltage is then determined by using a Doppler technique. A laser passes through the sample and, as particles move through the laser beam, the intensity of scattered light fluctuates at a frequency proportional to the particle speed. The measurement of the particle speed at multiple voltages enables the calculation of the zeta potential.

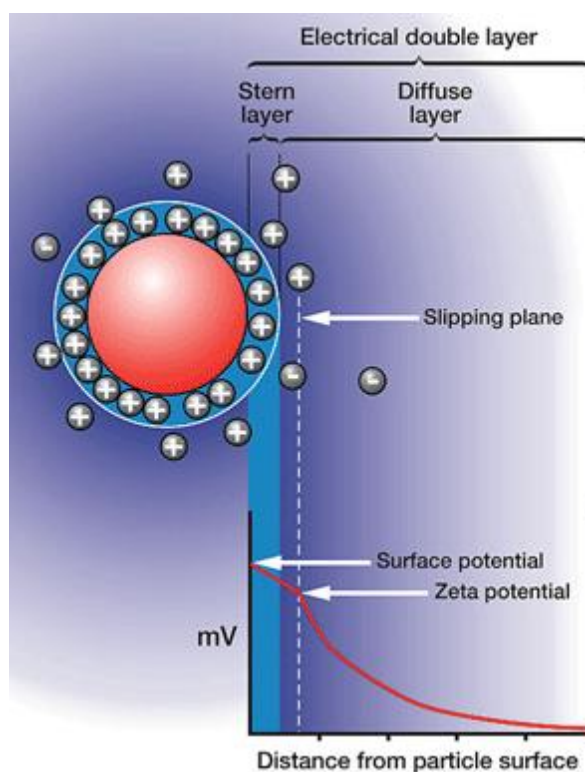


**Figure 5.10** Schematic illustration of the principle of zeta potential measurement. Figure taken from reference 8.

### 5.11 Thermogravimetric analysis (TGA)

Thermogravimetric analysis (TGA) is a technique used to measure mass changes in a chemical compound as a function of the temperature under a controlled atmosphere. In a TGA process, the temperature of the sample is gradually increased by placing it in a furnace, knowing that the weight is measured on an analytical scale located outside of the furnace. In

TGA, a thermal event involving loss of a volatile component induces a mass loss. Chemical reactions, such as combustion, involve mass losses. However, it is not the case for physical changes, such as melting. The obtained thermogram represents the mass of the sample as a function of the temperature or time. The mass loss illustrates thermal transitions in the compound, such as loss of solvent and plasticisers in polymers, water of hydration in inorganic materials and, eventually, decomposition of the compound. All this description is illustrated in **Figure 5.11**.

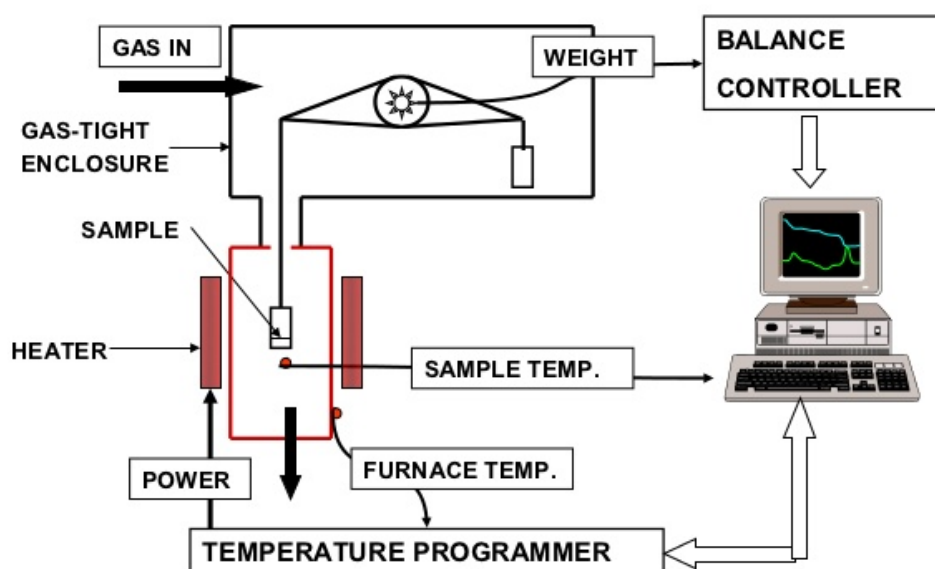


**Figure 5.11** Schematic illustration of a TGA. Figure taken from reference 9.

## 5.12 References

1. Ismail, A. A., van de Voort, F. R. & Sedman, J. in *Techniques and Instrumentation in Analytical Chemistry* (ed. J.R.J. Paré and J.M.R. Bélanger) **Volume 18**, 93–139 (Elsevier, 1997).
2. Paddock, S. W. Principles and practices of laser scanning confocal microscopy. *Mol. Biotechnol.* **16**, 127–149 (2000).
3. <http://www.science.gc.ca/default.asp?lang=En&n=6AA82744-1>
4. <http://www.ammrf.org.au/myscope/sem/practice/principles/layout.php>
5. [http://www.hk-phy.org/atomic\\_world/tem/tem02\\_e.html](http://www.hk-phy.org/atomic_world/tem/tem02_e.html)
6. <http://elchem.kaist.ac.kr/vt/chem-ed/spec/molec/mol-fluo.htm>
7. [https://en.wikipedia.org/wiki/Dynamic\\_light\\_scattering](https://en.wikipedia.org/wiki/Dynamic_light_scattering)
8. <http://www.waterworld.com/articles/print/volume-30/issue-10/>
9. <http://www.slideshare.net/nimmidalwadi5/tga>

# Acknowledgements

The totality of this thesis could not have been done in a proper way without the support from many people; therefore, I write herein some words to acknowledge all these people.

First, I would like to express my acknowledgements to my supervisor, Prof. Luisa De Cola who has kindly accepted my application and given me her confidence to do this PhD thesis in her group. Thank you for giving me these very motivating and ambitious projects. I have learnt many things from you and developed my skills in several instrumental techniques. Thank you for giving me the opportunities to share my knowledges, to learn and get those from scientists from all over the world through different international meetings.

Second, I acknowledge the financial support, which allowed me to lead my thesis from the beginning to the end.

Third, I would like to express my gratitude to the members of the jury for kindly accepting to judge this thesis work. Thank you Dr. Nora Ventosa, thank you Prof. Sylvie Bégin-Colin, thank you Prof. Roberto Corradini.

I would now like to say thank you to all my laboratory members.

Eko, I do not know how to acknowledge you. You did so many things for me; you very kindly took me under your wing, allowing me to get more motivations. I have learnt many things from you, from the scientific point of view as well as from the professional life one. Thank you for everything; honestly, without you, my thesis would have been a bit harder.

Ingrid, ta gentillesse est tellement grande qu'elle devienne apprenante ; elle se voit à travers ton sourire incessant et ta bonne humeur permanente qui apporte toujours du soleil en toute circonstance. Merci pour tous tes conseils et soutien pendant cette thèse, incluant la phase de rédaction. Merci aussi pour tes hospitalités lors des innumérables soirées. Pour la même occasion, je remercie Ondrej pour toute sa gentillesse et fais un gros gros bisou au petit Oli !

Clairounette, je ne sais pas comment te remercier pour tout ton soutien durant ces trois années. Merci pour tous les services que tu m'as rendus, tant du point de vue administratif que de celui de la vie quotidienne dans l'institut. J'ai été extrêmement ravi d'avoir fait ta connaissance et j'en profite pour réaffirmer ma joie d'avoir cotoyé mon pote, Sandro, que j'espère, bien entendu, toujours pouvoir cotoyer à l'avenir.

Ines, vielen dank für alles, for all your help and kindness during all this period.

Dedy, it was great pleasures to have you as colleague and then you have become a friend. Thank you for all your help and advices during this thesis and while I was writing it; thank you for all the moments of laugh that you shared and are still sharing with me. I would say: actually...

Chien-Wei, I have really appreciated to be your colleague and friend. You are a very nice and very kind person and I honestly thank you for all your help and advices in the laboratory as well as in the thesis manuscript.

Ale Bertucci, it has been very nice to know you, very nice and funny to have drinks with you, to speak French with you. Thank you for all these moments and I hope that you will keep your French vocabulary forever.

Loïc ! Tu es un gars ultra-cool, toujours souriant et très calme. C'était un grand plaisir de te retrouver dans le même groupe après t'avoir cotoyé dans le laboratoire du Dr. Alexandre Specht quelques années plus tôt.

Sere, tu es une très bonne amie et je suis très ravi d'avoir fait ta connaissance. Tu es une personne adorable, toujours souriante et de bonne humeur. Ton énergie débordante a toujours été là pour me tirer vers le haut, à aller changer d'air quand il le faut. Merci pour ton amitié et bon courage pour la fin de ta thèse, c'est bientôt fini. BOH

Alberto, mon frère ! Tu es un ami qu'il est impossible d'oublier. Tu es extrêmement gentil et tu es toujours prêt à rendre service. Merci pour tout ton soutien et toute cette période qui m'a permis de travailler dans la joie et la bonne humeur. Merci, monsieur ! Begueheh

John, mon frère ! You are a very good person; it has been very nice to know you within this last year. Thank you very much for all your help, especially for those related to the things in KIT. I also wish you a good luck and a very good pathway for your PhD thesis. Bwe

Amparo, thank you for all your kindness; I remember how nicely I was welcome on the day of my interview and when you made the labtour for me. Thank you very much also for all your help and advices, especially regarding science.

Leti, you are an amazing person, always smiling and always ready to play basketball; thank you for all these moments.

Camilla, thank you for your kindness and permanent smile during your visit in this group and good luck for your thesis. Bwe

Rémi, tu es quelqu'un de très gentil et toujours prêt à rendre service. Merci pour tout, en particulier, pour tes hébergements lors de soirées un peu arrosées.

Mike, s'il te plait, donne-moi la liste de ce qui serait à la hauteur des remerciements que je pourrais faire à ton égard, compte tenu de toute l'aide que tu m'as apportée durant cette thèse. Ton aide m'a été d'une énorme utilité tant dans la vie professionnelle que dans le quotidien. A côté de cela, tu es un ami très adorable, très calme et toujours prêt à rendre service. Merci pour tout et bon courage pour la suite de ta thèse. Tcha

I also acknowledge the rest of my laboratory team for different kinds of help and advices. Among them, there are Fede, Simone, Nadia, Yevhen, Giuseppe, Pengkun, Ale aliprandi, Matteo, Céline, Luca, Nina, Etienne, Damiano, Veronika, Leana, Bea, Becky, Vito, Maurizio, Angélique and Stephan.

Thank you my collaborators, especially those from ICVS in Braga (Portugal) and, in particular, Natalia, for all the work that you did for me and for your kindness, your permanent smile as well; thank you very much.

I will never forget all the help, support and advices from the other members of the institute; among them: Eloïse, Thomas, Vincent, Elena, Yann, Paul, Marian, Jean-Louis, Mihail, Annette, Stefano, Ania, Philippe, Fabrice, Thierry, Fabien, Fabienne, Muriel, Nathalie, Corrine; the FRC team: Yahia, Elisabeth, Cécile, Jean.

Thank you to my football team for all the games but also for different help and advices. Thank you Thibault, Hadi, Oussama, Seb, Ed, Paul, Jorge, Akihiro, Jérémy, Tommaso, Matteo and the list can go on forever...

Thank you to the former neighbour group for the different discussions, laughs and advices during the daily life. Thank you Emilie, Amélie, Raghavan, Viktoria, Alka and the list can keep ongoing...

I also would like to acknowledge the laboratory team, which supported me during my university pathway for internships. Thus, thank you, Alex, Elena, Joan, Eric, Jean-François, Jean-pierre, Maurice. Thank you Alain, Marion, Marie-Charlotte, Cyril, Sasha, Mathias.

During my thesis, I had the opportunity to regularly meet and talk with some Nobel laureates working in the institute; I would thus like to thank Prof. Jean-Marie Lehn and Prof. Jean-Pierre Sauvage for their permanent smile and kindness.

I would like to express a particular acknowledgement to Prof. Mir Wais Hosseini, who supported me a lot during my university pathway, from personal point of view as well as professional one. Thank you very much.

A présent, je voudrais adresser de chaleureux remerciements aux amis et anciens collègues de l'extérieur de l'institut.

Tout d'abord, merci à mes amis de la licence et de master.

En particulier, un énorme MERCI à Thomas, le tonton ! Tu es une personne avec un très bon cœur, tu es plus qu'un ami, tu es de la famille, un tonton. C'est un énorme plaisir de t'avoir parmi mes entourages proches. De plus, tu es toujours là pour rendre service et tu m'en as

beaucoup rendu. Notamment, merci pour la chambre que tu m'as attribuée dans ton appart et, à propos, je fais un clin d'œil à tata Yulia qui est tout aussi formidable que toi.

Dimby, merci pour ton aide durant les années licence et master, les périodes de révisions/examins ; merci aussi pour toutes les périodes de rire avec ta débilité, on ne va quand même pas pousser mémé dans les orties gggggggggggg. Je te souhaite un grand succès pour ta vie professionnelle.

S'il y a un ami pour voir lequel on serait prêt à payer sans compter, il s'agit du Vieux Mouss. Wullah Mouss, on ne va pas se mentir ni tergiverser, tu as la class. Tu es vraiment une personne formidable, remplie de gentillesse et tu m'as rendu beaucoup de services, souvent sauvé lorsque j'en avais besoin. Merci aussi pour toutes ces années remplies de rire, d'excuses/justifications de dernière minute de ta part. Non mais t'sais pourquoi ? Tchaaaaaaaaaaaaaaaaaaaaa !!!!!!!!!!!!!!!!!!!!!!!

Jo le DJ, mon frère. Merci d'avoir toujours été à mes côtés, dans les moments de joie comme dans les plus difficiles. Merci d'être dans la famille. Même si on se donne rarement de nouvelle, je sais que je peux toujours compter sur toi en toutes circonstances. Merci pour tout ça.

M. Vogt, merci pour toutes ces années de soirées et d'hébergements qui m'ont assez souvent aidé à changer d'air.

Je remercie aussi les amis qui m'ont aidé à rendre les périodes de révisions plus faciles durant les années licence en fournissant les cours dont ils disposaient déjà. Merci notamment à Yusuf, Mouss, Brahim, cousin Patrick et Emra.

Avant de fermer cette partie dédiée aux remerciements. Je tiens tout particulièrement à remercier une personne très importante dans mon entourage ; il s'agit du Docteur Meilleur Ami. Même jusqu'à la fin de ma vie, je ne te remercierai jamais assez pour tout ce que tu as fait pour moi depuis le début de mon cursus universitaire en chimie, ça fait bientôt 10 ans maintenant. Comme je n'aurais jamais assez de place pour tout citer. Je raccourcirais en disant : merci pour tout ton soutien matériel comme moral durant toutes ces années. Tous tes

services sur lesquels je sais que je peux toujours compter, ta patience, ton extrême gentillesse, tous les moments de joie, de rire et pour ton soutien dans les moments difficiles et même ceux très difficiles. A part cela, en tant que scientifique et collègue durant tout le cursus universitaire, jusqu'à la fin de cette thèse, je te remercie aussi pour les différents conseils et discussions scientifiques. Wullah ladim, tu es le meilleur des meilleurs amis, bien que, par timidité, tu aies du mal à avouer ma drôlerie ; par ailleurs, pour la même occasion, je fais un petit clin d'œil à TchaEda qui essaye de te raisonner à ce propos. Begueheeeeeeeeeeh ?!?!?!

Je voudrais, à présent, fermer cette partie en adressant mes remerciements les plus chaleureux à ma famille sans laquelle ce parcours que j'apprécie énormément n'aurait tout simplement pas été possible. Merci à ma mère Nadine, mon père Manu, mon frère Willy, mes sœurs Fransga et Elodie ainsi que tout le reste de ma famille que je ne puis citer ici.

# Curriculum Vitae

**Ricardo Totovao**  
6, rue Sainte Odile  
67120 Molsheim  
Tel : +33 (0) 6 08 46 40 31

Born on the 09/13/1987  
Single  
Driving licence and car owner  
E-mail : [totovao@unistra.fr](mailto:totovao@unistra.fr)  
French citizen

---

## EDUCATION

---

### 2013-2017:

**PhD THESIS IN BIOMATERIALS CHEMISTRY: *STIMULI-RESPONSIVE HYBRID ORGANIC/INORGANIC NANOPARTICLES FOR BIOMEDICAL APPLICATIONS*, LABORATOIRE DE CHIMIE ET DES BIOMATERIAUX SUPRAMOLECULAIRES, Prof. Luisa DE COLA, INSTITUT DE SCIENCE ET D'INGENIERIE SUPRAMOLECULAIRES (ISIS) – UNIVERSITE DE STRASBOURG (UDS)-CNRS**

Biomaterials, supramolecular and molecular chemistry: mesoporous organosilica nanoparticles, shells and surfaces

Stimuli-responsive and biodegradable systems

Bio-active molecules (drugs), proteins and gene (siRNA) delivery into cancer cells

Biomedical applications (cancer treatment)

*In vitro* experiments

Use/knowledges of/on different analysis instruments: nuclear magnetic resonance (NMR) and Fourier transform infrared (FTIR) spectroscopies, mass spectrometry, thermogravimetric analysis (TGA), fluorimetry, confocal microscopy, scanning electron microscopy (SEM), scanning transmission electron microscopy (STEM), transmission electron microscopy (TEM), energy-dispersive X-ray (EDX) spectroscopy, X-ray photoelectron spectroscopy (XPS), ultra-violet-visible (UV-Vis) spectroscopy

Frequent powerpoint presentations in front of the group or other audiences

Visit of some collaborator groups abroad as well as some pharmaceutical companies

Attendance of different international congress and related meetings

Attendance of numerous conferences/talks given by researchers from all over the world

### 2011-2013:

**MASTER'S DEGREE IN MOLECULAR AND SUPRAMOLECULAR CHEMISTRY (CMS), UNIVERSITE DE STRASBOURG (UDS)**

Research Master's degree

Very developed teaching of organic and inorganic chemistry

Teaching of the basics of X-Ray crystallography and supramolecular chemistry

Practices in physical chemistry (High Performance Liquid Chromatography-HPLC, Gas Chromatography-GC) and in chemical synthesis (organic and inorganic)

9 months internships in a research laboratory (3 during the first year and 6 during the second year)

### 2007-2011:

**LICENCE EN CHIMIE, EQUIVALENT OF A BACHELOR'S DEGREE IN CHEMISTRY, UDS**

Teaching of the basics of chemistry, including organic (reactivity and mechanisms), inorganic (organometallic chemistry and catalysis) and analytical (HPLC, GC, and mass spectrometry)

Practices in physical chemistry (electrochemistry, UV-Visible, NMR)

and synthetic chemistry (organic and inorganic)

### 2006:

**BACCALAUREAT SCIENTIFIQUE, EQUIVALENT OF A-LEVEL IN SCIENCE, Lycée Henri Meck, Molsheim, France**

---

## PRACTICE EXPERIENCES

---

**2013:**

**INTERNSHIP AT THE LABORATORY OF FUNCTIONAL CHEMO-SYSTEMS (LFCS), Dr. Alain WAGNER, FACULTE DE PHARMACIE, UDS-CNRS** (as part of the CMS Master's degree, 6 months)  
Organic chemistry for pharmaceutical applications, development of cleavable linkers for applications in proteomics

**2012:**

**INTERNSHIP AT THE LABORATOIRE DE DERMOTICHIMIE, Prof. Jean-Pierre LEPOITTEVIN, FACULTE DE CHIMIE, UDS-CNRS** (as part of the CMS Master's degree, 3 months)  
Organic chemistry for biological applications, synthesis and studies of molecules in view of <sup>13</sup>C isotopic substitutions

**2011:**

**INTERNSHIP AT THE LABORATOIRE DE CONCEPTION ET APPLICATION DE MOLECULES BIOACTIVES, Dr. Alexandre SPECHT, FACULTE DE PHARMACIE, UDS-CNRS** (1 month)  
Organic chemistry for pharmaceutical applications  
Observation internship on my own initiative

---

**TEACHING/SUPERVISION AND RELATED EXPERIENCES**

---

**2013-2016:**

High school students supervision during their internship in the group  
Welcoming audiences (students and every audience from all ages) and organizing laboratories visits on open days

**2015 February-April:**

Supervision of experimental classes for bachelor students (2<sup>nd</sup> year) at the faculty of chemistry

---

**INTERNATIONAL CONGRESSES AND RELATED MEETINGS**

---

**2016 August:**

**BIOINTERFACES INTERNATIONAL 2016, University of Zürich, Zürich (Switzerland)** (1 week)  
Engineering Smart Surfaces / Bioinspired Responsive Interfaces  
Smart (Drug) Delivery Systems, Biomaterials, Medical Devices & Implants  
New Antibacterial Interface and Detection Strategies, Novel Interfacial Concepts in Bioanalytics & Diagnostics  
Progress in Biointerface Characterization and Imaging Methodologies  
Regenerative Medicine

**2015 August:**

**ADVANCED MATERIALS WORLD CONGRESS, Stockholm (Sweden), Helsinki (Finland)** (1 week)  
Nanomaterials and nanotechnology, biomaterials and biodevices, smart energy technologies, computational materials, biosensors and bioelectronics  
Poster presentation: stimuli-responsive hybrid organic/inorganic mesoporous silica nanoparticles for nanomedicine

**2015 June-July:**

**10<sup>th</sup> INTERNATIONAL SYMPOSIUM ON MACROCYCLIC AND SUPRAMOLECULAR CHEMISTRY, Strasbourg (France)** (1 week) (550 participants)  
Organized by Prof. Luisa DE COLA (my supervisor) and her group  
**Personally involved in the organizing committee**

**2015 February:**

**TRAINING SCHOOL ON EM AND CRYOEM@TECHNION, Technion-Israel Institute of Technology, Haifa (Israel)** (1 week)  
Course on electron and cryo-electron microscopy in general

**2014 June:**

**GRONINGEN-STRASBOURG SYMPOSIUM, Strasbourg (France) (2 days)**

Symposium organized between Prof. Luisa DE COLA group (Université de Strasbourg, France), Prof. Ben L. FERINGA and Prof. Katalin BARTA (University of Groningen, The Netherlands)

Poster presentation: nano-materials for bio-applications

---

**SKILLS ON TECHNICAL INSTRUMENTS**

---

Very good practice skills on **SEM, STEM, EDAX (EDX), TGA, FTIR, FL3 (fluorimeter), NMR**

Good practice skills on **TEM**

Good skills in analyzing data from **confocal microscope, XPS, mass spectrometer** and **all the instruments cited above**

---

**LANGUAGES, COMPUTER SOFTWARES AND OTHER SKILLS**

---

**French:** as being afrench citizen

**English:** fluent in written and spoken, including scientific vocabulary, main language used in the current group

**German:** read, written and spoken (A level)

**Malagasy:** native language

Very well able to **collaborate** with other scientists in different projects, from inside the group as well as from outside and from different fields (chemists, biologists, biophysicists, researchers from a hospital – IRCAD) and different countries

Good knowledges on office software applications (word processor, spreadsheet, powerpoint, excel...)

Comfortable with the use of chemistry softwares (NMR notebook, Chembiodraw, Origin...)

---

**INTERESTS**

---

Astronomy, music, cinema, sport (practiced within the university): football, basketball, english boxing, travelling.

# Stimuli-responsive breakable hybrid organic/inorganic silica nanoparticles for biomedical applications

## Résumé

Pour pallier le problème d'efficacité de la plupart des médicaments disponibles sur le marché aujourd'hui, lié à des manques de spécificité et de solubilité, notamment dans le cadre du traitement du cancer, la nanomédecine, via les nanoparticules présente une alternative de grande importance. Dans ce domaine, les nanoparticules de silice ont récemment attiré une énorme attention de la part des scientifiques. Cependant, des problèmes d'élimination liés à la solidité du matériau entravent aujourd'hui sa traduction clinique. Afin d'élucider cette problématique, nous présentons, dans cette thèse, l'utilisation de nanoparticules de silice hybrides dont l'une est mésoporeuse et l'autre sous forme de nanocapsule dépourvue de porosité. Les particules qui sont sphériques ont été préparées en incorporant un groupement imine dans leur charpente afin de les rendre sensibles au pH bas, sachant que les tissus cancéreux présentent une certaine acidité par comparaison aux tissus sains. Les matériaux préparés se montrent particulièrement sensibles aux milieux acides similaires aux conditions dans les milieux cancéreux. Dans le même temps, ces particules exposent une bonne stabilité en milieu à pH neutre similaire aux conditions physiologiques. Des études *in vitro* réalisées avec la particule mésoporeuse sur une lignée de cellule cancéreuse issue du sein humain démontrent une bonne et rapide internalisation. De plus, lorsque le matériau est chargé avec un médicament hydrophobe très puissant utilisé dans le traitement du cancer du sein, le système en résultant indique une efficacité de grande ampleur en tuant une forte majorité des cellules cancéreuses, contrairement au système basé sur la particule non cassable et au médicament isolé. Parallèlement, les nanocapsules chargées avec un autre agent anticancéreux se montrent particulièrement cytotoxiques vis-à-vis de cellules cancéreuses très communes et qui l'internalisent de manière très rapide.

## Résumé en anglais

To overcome the limitations of most of the drugs available nowadays on the market due to their lack of solubility and specificity in cancer treatment for instance, nanomedicine plays an emerging role as an alternative. In that field, nanoparticles are endowed with several advantages, leading them to be highly considered for drug delivery systems preparation. In this respect, silica nanoparticles have recently a great deal of attention from the scientists. Nevertheless, some issues related to the *in vivo* elimination of silica materials represent the main obstacle impeding their clinical translation. To elucidate this problematic, we report, in this thesis, the use of breakable hybrid organosilica nanoparticles where one is mesoporous and the other one consists in a nanocapsule without porosity. Such materials have been prepared by incorporating an imine-based linker in the particles framework in order to make them pH-responsive. The advantage of the pH sensitivity relies on the fact that cancerous media present certain acidity as compared to those healthy. The particles exhibit a high pH sensitivity where, at low pH, they fully break down, while a good stability is observed in physiological conditions. Furthermore, *in vitro* studies performed with a drug delivery system based on the mesoporous particle and a highly hydrophobic drug show a remarkable efficiency towards a cancer cell line from human breast, which moreover, rapidly internalises the material. The nanocapsule loaded with a hydrophilic drug also demonstrates a fast internalisation towards a commonly used cancer line which does not resist to the system and thus dies by a very high rate.